The Trigger Tracker and a Monte Carlo Study of the $B_s^0 \to J/\psi\,\eta'$ Decay in the LHCb Experiment

---

Dissertation

zur

Erlangung der naturwissenschaftlichen Doktorwürde
(Dr. sc. nat.)

vorgelegt der
Mathematisch-naturwissenschaftlichen Fakultät
der

Universität Zürich

von

Dmytro Volyanskyy

aus
Ukraine

Promotionskomitee

Prof. Dr. Ulrich Straumann (Vorsitz)
Dr. Jeroen van Tilburg

Zürich 2007

To my parents

Abstract

The LHCb experiment, which is currently under construction at the Large Hadron Collider (CERN, Geneva), is designed to study *CP* violation and find rare decays in the *B* meson system. An important element of the LHCb tracking system is the Trigger Tracker, which covers a sensitive surface of about 7.7 m^2 with silicon microstrip detectors. This dissertation is dedicated to this part of the LHCb spectrometer. In particular, the detector design, its main characteristics, the main results from the R&D programme and the quality assurance programme for detector modules are discussed. In addition, the XML-based detector description of the Trigger Tracker for the Monte Carlo simulation of the LHCb experiment is presented.

Also, this dissertation presents the analysis of the $B_s^0 \to J/\psi\,\eta'$ decay based on the full Monte Carlo simulation. By measuring the time-dependent *CP* asymmetry arising in this channel, the B_s^0 weak mixing phase ϕ_s, which refers to the CKM angle χ, can directly be extracted without theoretical uncertainties. Since ϕ_s is expected to be very small in the Standard Model, the measurements of this phase will provide a sensitive probe for contributions from New Physics beyond the Standard Model. In this dissertation, the reconstruction and selection of $B_s^0 \to J/\psi\,\eta'$ events at LHCb using the decay channels $J/\psi \to \mu^+\mu^-$ and $\eta' \to \rho^0(\pi^+\pi^-)\gamma$ is described. Finally, the sensitivity of the LHCb detector to measure ϕ_s with this decay mode is presented.

Zusammenfassung

Das LHCb Experiment am Large Hadron Collider (CERN, Genf) welches momentan im Aufbau ist, wurde für die Untersuchung von *CP* Verletzung konstruiert und dient zur Beobachtung von seltenen Zerfällen von B Meson. Ein wichtiges Element des LHCb Spurrekonstruktionssytems ist der Triggertracker mit einer Sensorfläche von rund 7.7 m^2, bestehend aus Silicon Microstrip Detektoren. Diese Dissertation konzentriert sich auf diesen Teil des LHCb Spektrometers. Im Speziellen werden das Detektrodesign, dessen Charakterisik, die ausschlaggebenden Resultate des R&D Programms und die Qualitätssicherungsprogramme für den Detektor besprochen. Zusätzlich wird die auf XML basierende Detektorbeschreibung des Triggertracker für die Monte Carlo Simulation des LHCb Experiments präsentiert.

Desweiteren beinhaltet diese Dissertation die Analyse des Zerfalls $B_s^0 \to J/\psi\,\eta'$ basierend auf einer reinen Monte Carlo Simulation. Die schwache B_s^0 Mischungsphase ϕ_s kann mittels der Messung der zeitabhängigen *CP* Assymetrie, welche in diesem Zerfallskanal auftritt, ohne theoretische Unsicherheiten bestimmt werden. Da das Standardmodel eine sehr kleine Phase ϕ_s voraussagt, bietet die Bestimmung dieser Phase eine gute Möglichkeit, Beiträge von neuer Physik zu suchen. In dieser Dissertation ist die Rekonstruktion des Mesons $B_s^0 \to J/\psi\,\eta'$ am LHCb mittels der Zerfallskanäle $J/\psi \to \mu^+\mu^-$ und $\eta' \to \rho^0(\pi^+\pi^-)\gamma$ untersucht. Schliesslich wird die Sensitivität des Detektors bei der Bestimmung der Phase ϕ_s über die oben erwähnten Zerfallskanäle präsentiert.

Contents

Introduction

One of the fundamental problems of modern physics is the imbalance between matter and antimatter observed in our Universe. According to the Standard Model – the modern theory used to describe particle interactions – matter and antimatter should have been created in equal amounts shortly after the Big Bang. However, there is no evidence that antimatter is present in our Universe at all. Everything around us is made of matter, including our bodies. If there would be antimatter somewhere in the Universe, then at the border between the “world” and “antiworld” particles and antiparticles would annihilate releasing huge amounts of energy. Today we do not see any sign which indicates that such processes take place.

On the other hand, if matter and antimatter annihilate leaving behind nothing except energy, then it is quite strange that there is anything left at all after the Big Bang. Therefore, many scientists believe that shortly after the Big Bang a small excess of particles over antiparticles was created, and as a result, just a tiny fraction of the matter has survived after annihilation. If this is true, then just a small excess of particles would be enough to build our inconceivable Universe. It is believed by many physicists that our Universe has been saved due to this tiny asymmetry between the matter and antimatter.

The concept of symmetry is the basis of modern physics. Each conservation law in physics is strongly linked to a symmetry. There are three discrete symmetry transformations in particle interactions [1]: charge conjugation (C), parity operation (P) and time reversal (T). Charge conjugation revers all charges and all the internal quantum numbers. It results in replacing a particle by its antimatter counterpart. Parity operation or space reversal makes a reflection of the coordinate system through the origin and as a result, it changes the sign of any polar vector. Time reversal changes the direction of time and reverses time derivatives. Finally, all these three discrete symmetry transformations are united into the Schwinger-Luders-Pauli theorem, also known as CPT theorem, which states that the CPT transformation should be a valid symmetry transformation in any local field theory. This means that the combined transformation of time reversal, charge conjugation, and space reversal in any particular order is an exact symmetry of any interaction and that all physical laws must be invariant under these three symmetry transformations. The CPT symmetry is a fundamental symmetry of physical laws. Physicists once believed that each of these three symmetries is conserved. However in 1957, C. Wu and her collaborators found a clear violation of parity conservation in the β decay of Cobalt-60 [2]. During the same time the violation of C symmetry was also observed in weak interactions. This was first demonstrated by physicists at the University of Liverpool studying the decay of muons to electrons and antimuons to positrons and then analysing the polarisation of the electrons and positrons. It was found that muons decayed to left-handed electrons but not to right-handed electrons, and that antimuons decayed to right-handed positrons but not to left-handed positrons. When C and P violation were first observed, it was expected that the combined CP symmetry would still be preserved. The violation of CP symmetry implies the violation of T symmetry in order to conserve CPT. However, CP symmetry was found to be violated at a small level in the weak interactions of kaons in 1964 by J. Cronin and V. Fitch and collaborators, for which they won the Nobel Prize in physics in 1980 [3]. All experiments designed to test CPT symmetry have found no evidence for its violation.

In 1967, academician A. Sacharov included CP violation as one of three conditions necessary for the matter-antimatter imbalance [4]. So CP violation is closely related to this fundamental problem of modern physics. The Standard Model can accommodate CP violation, but it does not explain it. Today this is still an open question on which modern physics cannot give an answer.

In the weak interaction, CP violation can be easily accessed in decays of particles involving a bottom quark, so-called B hadrons, where the amplitudes of the CP asymmetries are higher than in the kaon sector. Recently, CP violation has been experimentally detected in decays of B mesons. The first measurements have been made in 2001 using the decay $B_d^0 \rightarrow J/\psi K_s^0$ by the two experiments at the B factories, BaBar (at SLAC, USA) and Belle (at KEK, Japan) [5, 6].

In order to perform precise measurements of CP violation, physicists need to produce large amounts of B mesons and accurately reconstruct their decays into specific final states. The first can be achieved by colliding particles accelerated to high energies in a collider facility, while the second can be achieved by building an excellent detector. Today BaBar and Belle experiments are already making important measurements of CP violation. However, their disadvantage is that they are unable to produce the heavier types of B mesons, namely B_s^0 mesons. In contrast, the proton-antiproton collider at FNAL (USA) called Tevatron can produce all types of B hadrons. Therefore, the CDF and DØ experiments, currently running at this collider, are reconstructing the decays of various B hadrons. However, in order to improve the current results in the B_d^0 sector and to perform precise measurements of CP violation in the B_s^0 meson sector, a higher collision energy, resulting in a larger production b quarks, and higher luminosity is required.

The Large Hadron Collider, which is currently under construction at CERN (European Organisation for Nuclear Research), will be the world's most powerful particle collider in terms of energy and luminosity. It will collide two proton beams with a centre-of-mass energy of $\sqrt{s} = 14\,\mathrm{TeV}$. The collision energy is roughly seven times more than that at the Tevatron. This will allow to produce large amounts of B hadrons and as a result, physicists will be able to measure CP violation in the B meson sector with high accuracy and study rare decays of B hadrons. This will provide a powerful test of the Standard Model and increase the discovery potential for New Physics. The Large Hadron Collider is scheduled to start mid-2008. It will host several particle physics experiments. One of them is LHCb, designed to make precision studies of CP violation and rare decays in the B meson system.

To achieve the physics goals the LHCb detector must have a high-quality particle identification, excellent decay time and mass resolutions and high trigger efficiencies. A crucial role in precise B hadron reconstruction is played by the tracking system which has to reconstruct the particle trajectories, measure their momenta and determine the interaction point and decay vertices. The Trigger Tracker is an important element of the LHCb tracking system. The construction of this part of the LHCb detector and its simulation are described in this dissertation. Another important topic of this dissertation is the analysis of the $B_s^0 \to J/\psi\,\eta'$ decay at LHCb based on a full Monte Carlo simulation of the experiment. According to the Standard Model, the CP asymmetry arising in this channel is tiny and hence, any observation of CP asymmetry significantly larger than the Standard Model expectation would be an indication of New Physics. Therefore, by measuring the CP asymmetry in this decay channel it will be possible to carry out a sensitive test of the Standard Model.

This dissertation is organised as follows:

In **Chapter 1**, a brief introduction into the Standard Model and an overview of CP violation is given. Thereafter, the physics of B mesons and CP asymmetries arising in their decays are considered.

In **Chapter 2**, a brief description of the Large Hadron Collider is given. Thereafter, the design of the LHCb experiment including its different subdetectors and the trigger system are discussed.

In **Chapter 3**, the purpose and requirements of the Trigger Tracker are considered first. Then, a general description of silicon microstrip detectors, which is the basic detector technology of the Trigger Tracker, is given. Next, the detector design and its main characteristics are discussed. Finally, a brief overview of the R&D programme performed for the Trigger Tracker is presented.

In **Chapter 4**, the quality assurance programme for the Trigger Tracker detector modules performed in the burn-in test-stand is described. First, the main goals and the measurement programme of this test are discussed. Then, the experimental setup and software used to perform these measurements are considered. Finally, a selection of the obtained results is presented.

In **Chapter 5**, the Monte Carlo simulation of the Trigger Tracker is considered. First, an overview of the simulation and reconstruction software in the LHCb experiment is given. Then, the XML-based detector description of the Trigger Tracker is discussed in detail. The results of the validation tests are presented in the end.

In **Chapter 6**, the reconstruction of the $B_s^0 \to J/\psi\eta'$ decay at LHCb based on a full Monte Carlo simulation using the decay channels $J/\psi \to \mu^+\mu^-$ and $\eta' \to \rho^0(\pi^+\pi^-)\gamma$ is described. By measuring the time-dependent *CP* asymmetry arising in this channel, the B_s^0-$\bar{B}_s^0$ mixing phase ϕ_s, which refers to the CKM angle χ, can be extracted without theoretical uncertainties. The sensitivity of the LHCb detector to measure the ϕ_s with this decay mode is presented in the last section of this chapter.

Finally, the dissertation is concluded with a summary.

Foreword

The contents of this dissertation describes my research activities during three and a half years, in which I worked on the LHCb experiment as a Ph.D. student. During this time, I have been strongly involved in projects dedicated to the LHCb Trigger Tracker. The design and construction of this detector is the main responsibility of the LHCb group at the University of Zürich.

In 2003 and 2004, I was involved in the R&D programme for silicon microstrip detectors of the Trigger Tracker. I participated in the testing of various prototypes of silicon microstrip detectors using a pulsed infra-red laser. In addition, I participated in tests of prototype detector modules at the X7 test-beam facility at CERN. The results of these investigations were used to determine the final design of the silicon microstrip detectors for the Trigger Tracker and to verify the expected performance of the detector.

After the start of the series production of the Trigger Tracker detector modules in 2005, I was involved in the quality assurance programme carried out in the “burn-in” test stand. The main goal of this project was to investigate the long-term behaviour of the detector modules at different thermal conditions, study their electrical characteristics and search for defective channels. I was responsible for the development of the software to control the readout electronics, the high voltage power supply, the chiller, and the temperature and humidity sensors. This was done using the LabView programming language, allowing to perform the burn-in programme fully automatically. Temperature cycling, measurements of sensor leakage currents as a function of the applied bias voltage, pedestal data taking and pulse shape scans were done without any need for operator intervention. I have also significantly contributed to the processing and analysis of the acquired data.

In order to understand the physics reach of the experiment, I have performed the analysis of the $B_s^0 \to J/\psi(\mu^+\mu^-)\ \eta'(\rho^0(\pi^+\pi^-)\gamma)$ decay channel based on the full Monte Carlo simulation of the LHCb experiment. This was the main topic of my Ph.D. thesis work. For this decay mode, I have developed an event selection algorithm in C++. I have optimised simultaneously the requirements on the selection variables used in this analysis to separate signal events from the background. Next, I have investigated the events that passed through the final selection requirements. The quality of reconstruction in terms of mass, vertex and decay time resolutions has been studied and the event yield and background pollution for this decay mode at LHCb has been estimated. The determination of the LHCb's sensitivity to measure ϕ_s with this decay was the last step of this analysis.

In parallel to the activities described above, I was responsible for the detector description of the Trigger Tracker for the LHCb Monte Carlo simulation. In 2005, using the XML language I have written a detailed description of the detector geometry and of the structure. This is used as input for reconstruction applications and for the GEANT4 toolkit to perform a realistic Monte Carlo simulation of the LHCb detector.

Chapter 1

CP violation and *B* meson physics

1.1 Standard Model basics

The Standard Model of particle physics [7, 8] is a theory describing the smallest constituents of matter, and their interactions through the electromagnetic, weak, and strong, fundamental forces. It provides an elegant theoretical framework which has successfully passed all precision tests so far. Experiments have verified its predictions to incredible precision, and all the particles predicted by this theory have been found, except one, the Higgs boson, which still needs to be discovered experimentally. However, this theory does not explain everything. For example, the gravitational interaction is not included in the Standard Model. Also, this theory contains 19 free parameters[1], whose values must be determined experimentally. Therefore, the Standard Model cannot be presented as the final theory of elementary particles. It is generally believed to be part of a some grand unified theory which unifies all the fundamental forces.

The Standard Model consists of elementary particles grouped into two different classes: fermions and bosons. Fermions have half-integer spin. They obey the Pauli exclusion principle, which states that no two identical fermions in a system may occupy the same quantum state at the same time. Particles with integer spin are bosons and in contrast to fermions they may share the same quantum state at the same time. In the Standard Model, the Glashow-Salam-Weinberg (GSW) model of electroweak interactions, describing the electromagnetic and weak forces, is combined with the theory of Quantum Chromodynamics (QCD), describing the strong force. All of these theories are gauge theories, meaning that they model the forces between fermions by coupling them to bosons. These mediating bosons are referred to as gauge bosons. Hence, in the Standard Model, fermions

---

[1] These include three independent interaction strengths and a *CP*-violating parameter for the strong interaction, six quark masses and four parameters to describe how they are mixed by the weak interaction, three charged-lepton masses, the $W^{\pm}$ and Higgs boson masses [7].

Table 1.1: *The Standard Model interactions, their coupling constants and corresponding gauge bosons.*

Interaction	Coupling constant, α_i	Gauge boson name	Symbol
Strong	$O(1)$	gluon	g
Electromagnetic	$O(10^{-2})$	photon	γ
Weak	$O(10^{-6})$	W^+, W^-, Z^0 weak bosons	$W^\pm$, Z^0

are particles that make up matter and gauge bosons are particles that transmit forces. The fundamental forces in the Standard Model, their coupling constants[2] and corresponding gauge bosons are listed in Table 1.1.

There are two different types of elementary fermions: quarks and leptons. Each fermion has a corresponding antiparticle with opposite charge quantum numbers, but with equal mass and lifetime, according to *CPT* symmetry. Quarks and leptons can be split into three generations with increasing mass. Each generation consists of two quarks and two leptons. This results in six different quark flavours: up (u), down (d), strange (s), charm (c), bottom (b) and top (t). Quarks are the only fundamental particles that interact through all four of the fundamental forces. Each quark has a fractional electric charge, Q, which is either $Q = +2/3$ or $Q = -1/3$. The former are called up-type quarks (u, c, t), the latter, down-type quarks (d, s, b). For the up-type quarks the weak isospin, T_z, equals +1/2, and for down-type quarks T_z equals –1/2. In case of leptons, each generation consists of a charged lepton and its corresponding neutrino — a particle with no electric charge and a very small mass. Leptons do not participate in the strong interaction. In total there are three known flavours of leptons: electron (e), muon (μ) and tau (τ). The list of known fermions is presented in Table 1.2.

In contrast to leptons, quarks cannot exist as free particles. They are always confined inside particles called hadrons. This important property of quarks is called confinement. However, the heaviest quark, t, decays into lighter quarks and W boson before it can form a hadron. Therefore, there are no hadrons containing a top quark in Nature. Confinement exists due to the strong interaction between the quarks described in QCD. This theory is based on a gauge symmetry group called $SU(3)$. The group has eight generators, resulting in the existence of eight strong force carriers, called gluons. According to the theory, every quark has an additional quantum number, called colour charge, which can take three values: red, green and blue. The corresponding antiquarks have the opposite anticolours. A quark can change its colour by exchanging a gluon with another quark. A gluon is a vector gauge massless boson that mediates the strong interaction. According to QCD,

---

[2] A coupling constant for each force is a dimensionless constant, which determines the relative strength of interaction.

Table 1.2: *The fundamental fermions in the Standard Model. For each fermion listed there is a corresponding antiparticle with opposite charge quantum numbers. Values are obtained from Ref. [9].*

Fermion type	Name	Symbol	Electric charge	Mass
Generation 1				
Lepton	electron	e	–1	0.511 MeV
Lepton	electron neutrino	ν_e	0	< 3 eV
Quark	up	u	+2/3	1.5–4 MeV
Quark	down	d	–1/3	4–8 MeV
Generation 2				
Lepton	muon	μ	–1	106 MeV
Lepton	muon neutrino	ν_μ	0	< 0.19 MeV
Quark	charm	c	+2/3	1.15–1.35 GeV
Quark	strange	s	–1/3	80–130 MeV
Generation 3				
Lepton	tau	τ	–1	1.78 GeV
Lepton	tau neutrino	ν_τ	0	< 18.2 MeV
Quark	top	t	+2/3	174.3 GeV
Quark	bottom	b	–1/3	4.1–4.4 GeV

hadrons are colour-neutral objects meaning that they have no net colour charge. It implies the non-observability of free quarks. Since quarks carry colour they are confined within colour-singlet bound states by the strong force. However, it should be mentioned that in case of small distances the strong force between quarks decreases. It becomes arbitrarily weak and asymptotically converge to zero. This property is known as asymptotic freedom. This is a feature of QCD. Asymptotic freedom implies that in high–energy scattering the quarks move within hadrons, as free particles.

According to the quark model, there are two types of hadrons: baryons and mesons. Baryons are fermions, which are build from three quarks, each having a different colour charge. They always carry an additive quantum number, called baryon charge (B). For the proton and neutron, which are the building blocks of the atomic nucleus and therefore, are well-known examples of baryons, this quantum number is equal to 1. Hence, each quark has $B = 1/3$. In contrast to baryons, mesons are bosons. They are build from a quark–antiquark pair with opposite colour. As a result, they have an integer spin of either 0 or 1, i.e. either the quark and antiquark have opposite spin, or the quark and antiquark have parallel spin. Mesons have a baryon number equal to 0. The most common mesons are pions and kaons. They have the lowest masses and live long enough to be detected directly by the tracks they leave behind in a particle physics detector.

In the Standard Model, the electromagnetic force acts on all particles with non-zero electrical charge through the exchange of a massless particle, called the photon. The weak interaction affects all left-handed leptons and quarks or right-handed antileptons and antiquarks. This type of interaction is mediated by heavy gauge bosons — $W^{\pm}$, Z^0. It results in a different range of these interactions. For the electromagnetic force the range of interaction is infinitive (because of massless photon, which transmits the force) and for the weak force the range of interaction is about $10^{-18}\,\mathrm{cm}$ (since the mass of the weak force carriers is of the order of $80\,\mathrm{GeV}/c^2$)[3].

One of the most interesting effects of the weak force is flavour changing. This unique feature results that a down-type quark can emit a W^- or absorb a W^+ boson and convert into a superposition of up-type quarks. Conversely, an up-type quark can emit a W^+ or absorb a W^- boson and convert into a superposition of down-type quarks.

Due to the weakness of the weak interaction, weak decays are much slower than strong or electromagnetic decays. For example, an electromagnetically decaying neutral pion lives about 10^{-16}s, while a weakly decaying charged pion has a lifetime of about 10^{-8}s. However, eventually physicists discovered that at very short distances of about $10^{-18}\,\mathrm{m}$ the strength of the weak interaction is comparable to that of the electromagnetic. In the GSW theory, the electromagnetic and weak forces have been unified into a single electroweak interaction. The group symmetry of the electromagnetic interactions, $U(1)_{em}$, appears in the Standard Model as a subgroup of $SU(2)_L \times U(1)_Y$, which describes electroweak interaction. In order to be able to unify these forces it was necessary to introduce another particle – the Higgs boson. If the electroweak theory based on $SU(2)_L \times U(1)_Y$ would have an excellent symmetry, then it would require zero masses for the $W^{\pm}$, Z^0 bosons just as for photon. This obviously contradicts the different range of interactions observed for the electromagnetic and weak forces. In the Standard Model, the phenomenon of spontaneous symmetry breaking (SSB) describe the difference between the masses of $W^{\pm}$, Z^0 and photon. It is accomplished by introducing a non-gauge Higgs boson, which still needs to be experimentally detected. Through SSB, the quarks and leptons acquire their masses from the Yukawa coupling to the Higgs field. It should be noted that the resulting mass eigenstates of the quarks are not the same as the eigenstates of the weak interaction. The weak eigenstates of quarks can be presented as a superposition of the mass eigenstates. This phenomenon is described by the Cabibbo-Kobayashi-Maskawa (CKM) quark mixing matrix. A more detailed description of the CKM matrix will be given in the next section.

---

[3] This range is dictated by the uncertainty principle, since the $W^{\pm}$ bosons are virtual bosons, existing only within the time frame allowed by the uncertainty principle.

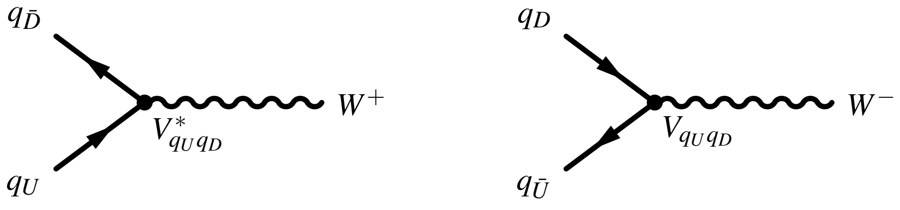

Figure 1.1: *Charged-current quark level interaction and its charge-conjugated process, where* $q_U \in (u,c,t)$, $q_D \in (d,s,b)$, $q_{\bar{U}} \in (\bar{u},\ \bar{c},\ \bar{t})$, $q_{\bar{D}} \in (\bar{d},\ \bar{s},\ \bar{b})$. *The charge-current coupling is represented by* $V_{q_U q_D}$ *and its complex-conjugate* $V^*_{q_U\ q_D}$.

1.2 *CP* violation in weak interactions

1.2.1 Quark mixing and parametrization of the CKM matrix

As mentioned before, the weak interaction has a unique feature to change the quark flavour, resulting in transitions between down-type quarks and up-type quarks. This phenomenon is called quark mixing. It should be noted that only the charged current of the weak interaction, mediated by the $W^{\pm}$ bosons, can change the flavour of quarks. Another carrier of the weak interaction, the Z^0 boson, which is referred to as the neutral current, cannot change the flavour of quarks. The absense of flavour changing neutral currents is explained by the Glashow-Iliopoulos-Maiani (GIM) mechanism [10]. Figure 1.1 illustrates a Feynman diagram of the charged current quark-level interactions.

The quark mixing process can be described by the charged-current interaction Lagrangian in terms of the mass eigenstates:

$$L^{CC}_{int} = -\frac{g_2}{\sqrt{2}}(\bar{u},\bar{c},\bar{t})_L\,\gamma^{\mu}\,V_{\text{CKM}}\begin{pmatrix} d \\ s \\ b \end{pmatrix}_L W^{\dagger}_{\mu} + \text{h.c.} \tag{1.1}$$

where the gauge coupling g_2 is related to the gauge group $SU_L(2)$, γ^{μ} are the Dirac matrices and the $W^{\dagger}_{\mu}$ fields describe the charged W bosons. V_{CKM} is the CKM quark mixing matrix, which connects the electroweak eigenstates (d',s',b') of the down, strange and bottom quarks with their mass eigenstates (d,s,b), through the following relation:

$$\begin{pmatrix} d' \\ s' \\ b' \end{pmatrix} = V_{CKM}\begin{pmatrix} d \\ s \\ b \end{pmatrix} = \begin{pmatrix} V_{ud} & V_{us} & V_{ub} \\ V_{cd} & V_{cs} & V_{cb} \\ V_{td} & V_{ts} & V_{tb} \end{pmatrix}\begin{pmatrix} d \\ s \\ b \end{pmatrix}. \tag{1.2}$$

This matrix was introduced in 1973 by M. Kobayashi and T. Maskawa, adding one generation to the matrix previously introduced by N. Cabibbo. This is a 3 × 3 unitarity matrix.

Each element of the matrix is the relative amplitude for the different quark–quark couplings to the $W^{\pm}$ bosons. In other words, the square of each element of the CKM matrix $|V_{qq'}|^2$ is proportional to the probability of a transition from one quark q to another quark q'. The Standard Model does not predict the values of individual elements of the CKM matrix. They need to be determined from weak decays of the relevant quarks.

A complex $n \times n$ unitarity matrix contains n^2 independent parameters. Since the matrix describes an interaction of $2n$ quarks, $2n-1$ parameters are needed to describe the quark fields. Therefore, the total number of physically independent parameters which parameterise the matrix is:

$$n^2 - (2n-1) = (n-1)^2$$

This number can be presented as the sum of $n(n-1)/2$ parameters describing the mixing angles between generations, and $(n-1)(n-2)/2$ parameters, which are the complex phases[4]. In case of three generations ($n=3$), the CKM matrix contains four independent parameters: three Euler angles and one complex phase, which is the source of *CP* violation in the Standard Model.

The relative strength of *CP* violation in the Standard Model is given by the Jarlskog parameter [11], J_{CP}, which is defined as:

$$J_{CP} = \pm Im(V_{ik}V_{jl}V_{il}^{*}V_{jk}^{*}) \;\; (i \neq j, l \neq k). \tag{1.3}$$

The *CP* violation effect is expected to be small, since the Standard Model predicts $J_{CP} = O(10^{-5})$. This means that any experimental observation of a *CP* asymmetry greater than the Standard Model prediction is an indication of New Physics.

There are several parametrisations of the CKM matrix. One of them is the so-called Chau–Keung parametrisation used by the Particle Data Group [9], where the CKM matrix is presented in the following way:

$$V_{CKM} = \begin{pmatrix} c_{12}c_{13} & s_{12}c_{13} & s_{13}e^{-i\delta_{13}} \\ -s_{12}c_{23} - c_{12}s_{23}s_{13}e^{i\delta_{13}} & c_{12}c_{23} - s_{12}s_{23}s_{13}e^{i\delta_{13}} & s_{23}c_{13} \\ s_{12}s_{23} - c_{12}c_{23}s_{13}e^{i\delta_{13}} & -c_{12}s_{23} - s_{12}c_{23}s_{13}e^{i\delta_{13}} & c_{23}c_{13} \end{pmatrix}. \tag{1.4}$$

with $c_{ij} = \cos\theta_{ij}$ and $s_{ij} = \sin\theta_{ij}$, where $i, j = 1,\ 2,\ 3$ is the index of generations. The Euler angles θ_{ij} may be chosen such that $0 \leq \theta_{ij} \leq \pi/2$, and the phase δ_{13} such that $0 \leq \delta_{13} < 2\pi$. This parametrisation has the advantage that each of the rotation angles θ_{ij}, relates to the mixing of two specific generations.

---

[4] This is due to the fact that an orthogonal $n \times n$ matrix contains $n(n-1)/2$ independent rotation angles. Hence, for a complex unitary matrix the number of independent phases is $(n-1)^2 - n(n-1)/2 = (n-1)(n-2)/2$.

In 1983, Wolfenstein proposed another parametrisation [12] based on experimental results. It takes into account the observation that the diagonal elements of the CKM matrix are close to 1 and off-diagonal elements of the matrix are progressively smaller. This hierarchy can be formalised by defining λ, A, ρ and η through

$$\lambda = s_{12}, \qquad A = s_{23}/\lambda^2, \qquad \rho + i\eta = s_{13}e^{i\delta_{13}}/A\lambda^3. \tag{1.5}$$

The parameter λ is the sine of the Cabbibo angle λ = sin $\theta_C \simeq 0.22$. The parameter A, is approximately equal to 0.8 and $\sqrt{\rho^2+\eta^2} \approx 0.4$. The elements of the CKM matrix in the Wolfenstein parameterisation are expressed in powers of λ. The CKM matrix gets the following form:

$$V_{CKM} = \begin{pmatrix} 1-\frac{1}{2}\lambda^2 & \lambda & A\lambda^3(\rho - i\eta) \\ -\lambda & 1-\frac{1}{2}\lambda^2 & A\lambda^2 \\ A\lambda^3(1-\rho-i\eta) & -A\lambda^2 & 1 \end{pmatrix} + O(\lambda^4). \tag{1.6}$$

Clearly, *CP* violation implies that $\eta \neq 0$, keeping the matrix complex. Especially the physics in the B_s^0 sector requires a more precise approximation of the CKM matrix elements. The higher-order terms up to $O(\lambda^5)$ are presented as:

$$\begin{pmatrix} -\frac{1}{8}\lambda^4 & 0 & 0 \\ A^2\lambda^5(\frac{1}{2}-\rho-i\eta) & -\frac{1}{8}\lambda^4(1+4A^2) & 0 \\ \frac{1}{2}A\lambda^5(\rho+i\eta) & A\lambda^4(\frac{1}{2}-\rho-i\eta) & -\frac{1}{2}A^2\lambda^4 \end{pmatrix} + O(\lambda^6). \tag{1.7}$$

1.2.2 Unitarity triangles

The unitarity of the CKM matrix ($V_{CKM}V_{CKM}^\dagger = V_{CKM}^\dagger V_{CKM} = 1$) implies nine relations between its elements. Three of them are constraints on the diagonal elements, which can be written as $\sum_j |V_{ij}|^2 = 1$ for each generation i. This implies that the sum of all couplings of any of the up-type quarks to all the down-type quarks is the same for all generations. This effect is known as the weak universality and was introduced by N. Cabibbo in 1967. The remaining six constraints can be written in the form $\sum_k V_{ik}V_{jk}^* = 0$ $(i \neq j)$. These orthogonality relations can be presented in the complex plane as triangles. The shape of each unitarity triangle is different, but they all have the same area, which is directly related to the size of *CP* violation in the Standard Model. Among the six triangles there are only two which have sides of the same order in λ. The other four triangles are squashed, because they have one side which is significantly less than other sides in the triangle. The non-squashed unitarity triangles are shown in Fig. 1.2. As can be seen, the triangles can be described by four angles: α, β, γ and χ. The first three angles are defined as:

$$\alpha = \arg\left(-\frac{V_{td}V_{tb}^*}{V_{ud}V_{ub}^*}\right) \quad , \quad \beta = \arg\left(-\frac{V_{cd}V_{cb}^*}{V_{td}V_{tb}^*}\right) \quad , \quad \gamma = \arg\left(-\frac{V_{ud}V_{ub}^*}{V_{cd}V_{cb}^*}\right) \quad . \tag{1.8}$$

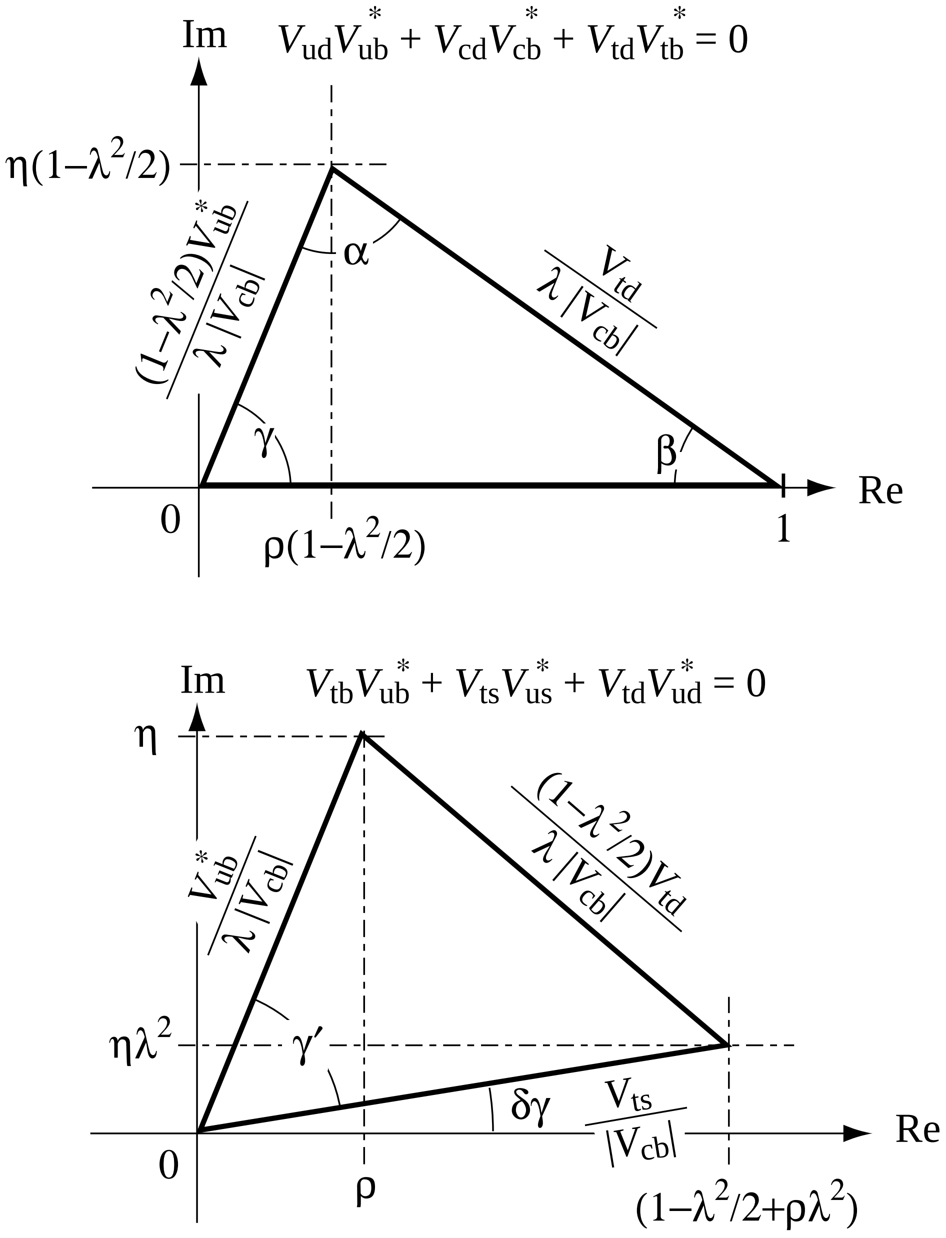

Figure 1.2: *The non-squashed unitarity triangles in the complex plane. Here, the angle χ is indicated as the angle $\delta\gamma$.*

The fourth angle, χ, is a one of the main topics of this dissertation. It is given by:

$$\chi = \arg\left(-\frac{V_{cb}V_{cs}^*}{V_{tb}V_{ts}^*}\right) \quad . \tag{1.9}$$

It originates from the so-called *bs* squashed triangle, which is defined by the following relation:

$$V_{ub}V_{us}^* + V_{cb}V_{cs}^* + V_{tb}V_{ts}^* = 0. \tag{1.10}$$

This triangle has two sides of order λ^2 and one side of order λ^4 :

$$V_{cb}\, V_{cs}^* \backsim O(\lambda^2) \quad , \quad V_{tb}\, V_{ts}^* \backsim O(\lambda^2) \quad , \quad V_{ub}\, V_{us}^* \backsim O(\lambda^4) \quad .$$

Clearly, the angle χ defined as the angle between the $V_{cb}\, V_{cs}^*$ and $V_{tb}\, V_{ts}^*$ sides must be of order $\lambda^2 \approx$0.04. Therefore, experimental measurements of this angle will provide a sensitive test of the CKM picture. Using the Wolfenstein parameterisation, the angle χ can be defined as:

$$\chi = \arg[\,1-\lambda^2(\frac{1}{2}-\rho-i\eta)+O(\lambda^4)] \approx \lambda^2\, \eta \approx \arg(V_{ts})-\pi. \tag{1.11}$$

As follows, the angle χ represents the phase of V_{ts} in the Wolfenstein parameterisation. Likewise, the angles β and γ can be presented as phases of V_{td} and V_{ub}, respectively.

In order to test the Standard Model description of *CP* violation based on the CKM matrix, it is important to measure all angles of the CKM unitary triangles. This would allow to overconstrain the CKM matrix and would improve our understanding of flavour physics. Moreover, it would provide a search for physics beyond the Standard Model. Measurements of all angles of the CKM unitary triangles can be performed through the decays of *B* mesons.

1.3 The *B* meson system

B mesons are bound states of the heavy $\bar{b}$ antiquark and a lighter *u*, *d*, *s* or *c* quark forming B_u^+, B_d^0, B_s^0 or B_c^+ mesons respectively. Similarly, the antiparticle of the *B* meson is made up of a *b* quark and a $\bar{u}$, $\bar{d}$, $\bar{s}$ or $\bar{c}$ antiquark. In total there are four types of neutral *B* mesons (B_d^0, $\bar{B}_d^0$, B_s^0 and $\bar{B}_s^0$) and four types of charged *B* mesons (B_u^+, B_u^-, B_c^+, and B_c^-). According to the *CPT* theorem, the *B* meson and its corresponding *B* antimeson have the same mass and lifetime. The general characteristics of these particles are summarised in Table 1.3. The B_d^0 meson was the first *B* meson which was experimentally observed. It was discovered in 1981 by the CLEO and CUSB experiments [13, 14]. The latest *B* meson found was the B_c^+ which was detected by the CDF experiment in 1998 [15]. The properties of *B* mesons were investigated in many particle physics experiments. It is still one of the main goals of current research programmes in High Energy Physics. Due to the existence of weak interactions, the *B* mesons are unstable particles with relatively long lifetimes.

Table 1.3: *Types of B mesons and their general characteristics. For each B meson listed there is a corresponding antiparticle with opposite electric charge. Values are obtained from Ref. [9].*

B-meson	Quark content	Electric charge	Mass (MeV)	Lifetime (ps)
B_u^+	$\bar{b}u$	+1	5279.0 ± 0.5	1.671 ± 0.018
B_d^0	$\bar{b}d$	0	5279.4 ± 0.5	1.536 ± 0.014
B_s^0	$\bar{b}s$	0	5369.6 ± 2.4	1.461 ± 0.057
B_c^+	$\bar{b}c$	+1	6400 ± 400	0.46 ± 0.03

1.3.1 Mixing of neutral B mesons

One of the most interesting properties of the neutral B mesons is their mixing, which has been discovered in the B_d^0 sector by the ARGUS experiment in 1987 [16]. In this process a neutral B meson oscillates from its particle state to its antiparticle state and vice versa. The mixing can only occur through weak interactions. The corresponding Feynman diagrams are illustrated in Fig. 1.3.

The state of a neutral B meson observed at time t after the creation at time $t = 0$ can be described by a superposition of the two flavour states:

$$|\psi(t)\rangle = a(t)|B_q^0\rangle + b(t)|\bar{B}_q^0\rangle \quad , \tag{1.12}$$

where $|B_q^0\rangle = |\bar{b}q\rangle$, $|\bar{B}_q^0\rangle = |b\bar{q}\rangle$ and $q \in (s,d)$. The time evolution of such a state is determined by the time-dependent Schrödinger equation:

$$i\frac{\mathrm{d}}{\mathrm{d}t}\begin{pmatrix} a(t) \\ b(t) \end{pmatrix} = H_q \begin{pmatrix} a(t) \\ b(t) \end{pmatrix} \quad . \tag{1.13}$$

The effective Hamiltonian, H_q, is presented by a 2×2 matrix[5] and can be written in terms of Hermitian matrices M_q and Γ_q in the following way:

$$H_q = M_q - \frac{i}{2}\Gamma_q = \begin{pmatrix} M_0^q & M_{12}^q \\ M_{12}^{q*} & M_0^q \end{pmatrix} - \frac{i}{2}\begin{pmatrix} \Gamma_0^q & \Gamma_{12}^q \\ \Gamma_{12}^{q*} & \Gamma_0^q \end{pmatrix} \quad . \tag{1.14}$$

The M_q and Γ_q are known as the mass and decay width matrices describing the dispersive and absorptive parts of the B_q^0–$\bar{B}_q^0$ mixing respectively. As CPT symmetry guarantees the same masses and equal decay width for B_q^0 and $\bar{B}_q^0$ mesons, the diagonal elements in the M_q

---

[5] The effective Hamiltonian is not Hermitian, since otherwise the mesons would only oscillate and not decay.

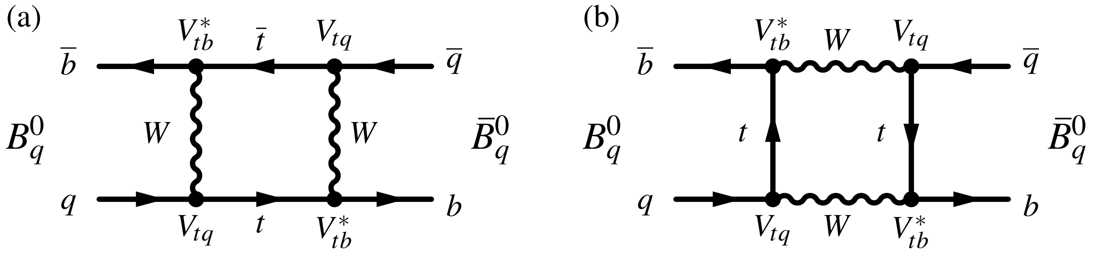

Figure 1.3: *Feynman box diagrams illustrating B_q^0–$\bar{B}_q^0$ mixing, where $q \in (s,d)$. The charge-conjugated process for $\bar{B}^0 \rightarrow B^0$ is obtained by replacing all quarks by antiquarks (and vice versa) and taking the complex-conjugates of the CKM elements.*

and Γ_q matrices are identical. The off-diagonal terms arise from $\Delta B = 2$ flavour-changing transitions with virtual (M_{12}^q) or real intermediate states (Γ_{12}^q) and are particularly important in the discussion of *CP* violation.

Diagonalizing (1.14), one can get the mass eigenstates and the corresponding eigenvalues of the effective Hamiltonian. The eigenstates are defined as:

$$|B_H^q\rangle = p|B_q^0\rangle - q|\bar{B}_q^0\rangle \quad , \quad |B_L^q\rangle = p|B_q^0\rangle + q|\bar{B}_q^0\rangle \quad , \tag{1.15}$$

where B_H^q is the *heavy* mass eigenstate and B_L^q is the *light* mass eigenstate. The corresponding eigenvalues are given as:

$$\begin{aligned} |\lambda_H^q\rangle &= (M_0^q - \frac{i}{2}\Gamma_0^q) - \frac{q}{p}(M_{12}^q - \frac{i}{2}\Gamma_{12}^q) \quad , \\ |\lambda_L^q\rangle &= (M_0^q - \frac{i}{2}\Gamma_0^q) + \frac{q}{p}(M_{12}^q - \frac{i}{2}\Gamma_{12}^q) \quad . \end{aligned} \tag{1.16}$$

The variables p and q, satisfying $|p|^2 + |q|^2 = 1$, describe the transformation from the flavour basis into the mass basis. Their ratio can be obtained by the diagonalisation of the effective Schrödinger equation and is defined as:

$$\frac{q}{p} = -\sqrt{\frac{2M_{12}^{q*} - i\Gamma_{12}^{q*}}{2M_{12}^q - i\Gamma_{12}^q}} \quad . \tag{1.17}$$

The mass difference, ΔM_q, and the decay width difference, $\Delta\Gamma_q$, between the heavy and light eigenstates of the neutral B meson are given by

$$\begin{aligned} \Delta M_q &= M_H^q - M_L^q \quad , \\ \Delta\Gamma_q &= \Gamma_H^q - \Gamma_L^q \quad , \end{aligned} \tag{1.18}$$

such that ΔM_q is positive by definition, while the sign of $\Delta\Gamma_q$ needs to be experimentally determined. The average mass and decay width of the heavy and light eigenstates are simply defined as

$$\begin{aligned} M_q &= \frac{M_H^q + M_L^q}{2} \quad , \\ \Gamma_q &= \frac{\Gamma_H^q + \Gamma_L^q}{2} \quad . \end{aligned} \tag{1.19}$$

It should be mentioned that the ΔM_q parameter is the frequency of the B_q^0–$\bar{B}_q^0$ oscillations, while the average number of oscillations before decay is given by the oscillation parameter, x_q, determined in the following way:

$$x_q = \frac{\Delta M_q}{\Gamma_q} \tag{1.20}$$

The time dependence of the mass eigenstates is given by the following relations:

$$|B_H^q(t)\rangle = e^{-(iM_H^q + \Gamma_H^q/2)t}|B_H^q(0)\rangle \quad , \quad |B_L^q(t)\rangle = e^{-(iM_L^q + \Gamma_L^q/2)t}|B_H^q(0)\rangle \tag{1.21}$$

Substituting (1.15) into (1.21) one can obtain the time-evolution of an initially pure $|B_q^0\rangle$ and $|\bar{B}_q^0\rangle$ state:

$$\begin{aligned} |B_q^0(t)\rangle &= g_+^q(t)|B_q^0\rangle + \frac{q}{p}g_-^q(t)|\bar{B}_q^0\rangle \quad , \\ |\bar{B}_q^0(t)\rangle &= g_+^q(t)|\bar{B}_q^0\rangle + \frac{p}{q}g_-^q(t)|B_q^0\rangle \quad , \end{aligned} \tag{1.22}$$

where:

$$g_\pm^q(t) = \frac{1}{2}(e^{-(iM_L^q + \Gamma_L^q/2)t} \pm e^{-(iM_H^q + \Gamma_H^q/2)t}) \quad . \tag{1.23}$$

The first term, $g_+^q(t)$, describes the process when the flavour states remain unchanged, while the second term, $g_-^q(t)$, describes their oscillation into each other. The corresponding time-dependent probability of these processes is proportional to

$$|g_\pm(t)|^2 = \frac{e^{-\Gamma_q t}}{2}[\cosh(\frac{\Delta\Gamma_q}{2}t) \pm \cos(\Delta M_q t)] \quad . \tag{1.24}$$

It should be noted that B_q^0–$\bar{B}_q^0$ oscillations have been investigated in many particle physics experiments. However, the oscillations in the B_d^0 system are much better studied than those in the B_s^0 sector. B_s^0–$\bar{B}_s^0$ oscillations were recently observed by the CDF and DØ experiments [17, 18]. The oscillation frequency is found to be $\Delta M_d = 0.507 \pm 0.005$ ps^{-1} for the B_d^0 system and $\Delta M_s = 17.4^{+0.3}_{-0.2}$ ps^{-1} for the B_s^0 system according to the latest published results. The oscillations in the B_s^0 sector are much more rapid than in the B_d^0 system. The $\Delta\Gamma_d/\Gamma_d$ parameter is very small (below 1%) in the B_d^0 system and can be neglected. In contrast, $\Delta\Gamma_s/\Gamma_s$ is considerably larger and is approximately equal to 0.1 within the Standard Model. These width differences are caused by the existence of final states to which both B_q^0 and $\bar{B}_q^0$ mesons can decay. Such decays involve $\bar{b} \to \bar{c}c\bar{q}$ quark level transitions. In Section 6.1.1, the physics of the $\bar{b} \to \bar{c}c\bar{s}$ quark-level transition is described in detail. The current status of the B_q^0–$\bar{B}_q^0$ mixing measurements is summarised in Ref. [19].

1.3.2 *CP* violation in B meson decays

The weak decays of the B mesons can be classified into three types: leptonic, semileptonic and non-leptonic transitions. Almost all of them have a rather small branching fraction of $O(10^{-3} - 10^{-9})$. The leptonic modes $B_u^- \to \ell^- \ \bar{\nu}_\ell$ and their charge-conjugated processes (where ℓ can be e or μ) are very hard to detect experimentally due to impossibility to reconstruct neutrinos. The semileptonic decays of B mesons provide the best experimental probes for the CKM matrix elements V_{ub} and V_{cb}. They are caused by $b \to u\ell \ \bar{\nu}_\ell$ and $b \to c\ell \ \bar{\nu}_\ell$ quark-level transitions.

The non-leptonic B meson decays play an important role in the Standard Model description of *CP* violation. At the quark level, these decays are $b \to q\bar{q}_1 q_2$ quark-level transitions, with $q_1 \in (u,c)$, $q_2 \in (d,s)$ and $q \in (u,c)$. They can be divided into three classes: decays receiving both "tree" and "penguin" contributions, pure "tree" decays and pure "penguin" decays. There are two types of penguin topologies: gluonic (QCD) and electroweak (EW) penguins. The leading-order Feyman diagrams describing these topologies can be found in Ref. [20].

In order to analyse non-leptonic B decays theoretically, it is necessary to use low-energy effective Hamiltonians, which are expressed using the operator product expansion. This allows to separate the short-distance contributions, which are described by the perturbative Wilson coefficient functions $C_k(\mu)$, from the long-distance contributions, which are described by the non-perturbative hadronic matrix elements $< f|Q_k(\mu)|i >$. Hence, the effective Hamiltonian for $|\Delta B| = 1$ transitions has the following form:

$$H_{eff} = \frac{G_F}{\sqrt{2}} \sum_{j=u,c} V_{jq}^* V_{jb} \left(\sum_{k=1}^{2} C_k(\mu) Q_k^{jq} + \sum_{k=3}^{10} C_k(\mu) Q_k^{q} \right) \ , \tag{1.25}$$

where $q \in (d,s)$, μ=$O(m_b)$ is a renomalization scale, the Q_k^{jq} are four quark operators, k distinguishes between tree contributions ($k = 1,2$), QCD ($k = 3,4,5,6$) and EW ($k = 7,8,9,10$) penguin operators. The V_{jq}^* and V_{jb} are the corresponding CKM matrix elements and G_F is the Fermi coupling constant, which describes the interaction after "integrating out" the W boson at the renormalisation scale μ. The calculation of such low-energy effective Hamiltonians can be found in Ref. [21].

Time dependent decay rates

The time-dependent decay amplitudes of a pure B_q^0 or $\bar{B}_q^0$ state into a final state are defined as:

$$A_f = \langle f|T|B_q^0\rangle \quad , \quad \bar{A}_f = \langle f|T|\bar{B}_q^0\rangle \quad , \tag{1.26}$$

where T is the transition matrix. Analogously, the decay amplitudes $A_{\bar{f}}$ and $\bar{A}_{\bar{f}}$ for the charge-conjugated final state $\bar{f}$ can be written. The total decay amplitudes A_f and $\bar{A}_{\bar{f}}$ can be written as the sum of the contributing diagrams

$$A_f = \sum_k A_k e^{i\delta_k} e^{i\phi_k} \quad , \quad \bar{A}_{\bar{f}} = \sum_k A_k e^{i\delta_k} e^{-i\phi_k} \quad , \tag{1.27}$$

where A_k is a real number. The strong phase, δ_k, is identical for both B_q^0 and $\bar{B}_q^0$, since the strong interaction does not violate *CP* symmetry. The weak phase, ϕ_k, changes sign under *CP* conjugation.

Taking into account the time evolution of the initially pure $|B_q^0\rangle$ and $|\bar{B}_q^0\rangle$ states defined in (1.22) the time-dependent amplitude of the $B_q^0 \to f$ and $\bar{B}_q^0 \to f$ processes are found to be:

$$\begin{aligned} A[B_q^0(t) \to f] &= \langle f|T|B_q^0(t)\rangle = g_+^q(t) A_f + \frac{q}{p} g_-^q(t) \bar{A}_f \quad , \\ A[\bar{B}_q^0(t) \to f] &= \langle f|T|\bar{B}_q^0(t)\rangle = g_+^q(t) A_f + \frac{p}{q} g_-^q(t) \bar{A}_f \quad . \end{aligned} \tag{1.28}$$

The corresponding decay rates to *CP* conjugated states f and $\bar{f}$ are defined as:

$$\Gamma_{B_q^0 \to f}(t) = |\, A[B_q^0(t) \to f]\, |^2 \quad , \quad \Gamma_{\bar{B}_q^0 \to f}(t) = |\, A[\bar{B}_q^0(t) \to f]\, |^2 \quad , \tag{1.29}$$

and can be written in the following way:

$$\begin{aligned} \Gamma_{B_q \to f}(t) &= \left|A_f\right|^2 \left(|g_+(t)|^2 + |\lambda_f|^2 |g_-(t)|^2 + 2\mathrm{Re}[\lambda_f g_+^*(t) g_-(t)]\right) \quad , \\ \Gamma_{B_q(t) \to \bar{f}}(t) &= \left|\bar{A}_{\bar{f}}\right|^2 \left|\frac{q}{p}\right|^2 \left(|g_-(t)|^2 + |\bar{\lambda}_{\bar{f}}|^2 |g_+(t)|^2 + 2\mathrm{Re}[\bar{\lambda}_{\bar{f}} g_+(t) g_-^*(t)]\right) \quad , \\ \Gamma_{\bar{B}_q \to f}(t) &= \left|A_f\right|^2 \left|\frac{p}{q}\right|^2 \left(|g_-(t)|^2 + |\lambda_f|^2 |g_+(t)|^2 + 2\mathrm{Re}[\lambda_f g_+(t) g_-^*(t)]\right) \quad , \\ \Gamma_{\bar{B}_q \to \bar{f}}(t) &= \left|\bar{A}_{\bar{f}}\right|^2 \left(|g_+(t)|^2 + |\bar{\lambda}_{\bar{f}}|^2 |g_-(t)|^2 + 2\mathrm{Re}[\bar{\lambda}_{\bar{f}} g_+^*(t) g_-(t)]\right) \quad . \end{aligned} \tag{1.30}$$

The parameters λ_f and $\lambda_{\bar{f}}$ and $\bar{\lambda}_{\bar{f}}$ are defined as:

$$\lambda_f = \frac{q}{p}\frac{\bar{A}_f}{A_f} \quad , \quad \lambda_{\bar{f}} = \frac{q}{p}\frac{\bar{A}_{\bar{f}}}{A_{\bar{f}}} \quad , \quad \bar{\lambda}_{\bar{f}} = \frac{1}{\lambda_{\bar{f}}} \quad . \tag{1.31}$$

The functions governing the time evolution in (1.30) are given by:

$$\begin{aligned}
|g_\pm(t)|^2 &= \frac{1}{4}\left(e^{-\Gamma^q_H t} + e^{-\Gamma^q_L t} \pm 2e^{-\Gamma_q t}\cos\Delta M_q t\right) \\
&= \frac{e^{-\Gamma_q t}}{2}\left(\cosh\frac{\Delta\Gamma_q t}{2} \pm \cos\Delta M_q t\right) \quad , \\
g^*_+(t)g_-(t) &= \frac{1}{4}\left(-e^{-\Gamma^q_H t} + e^{-\Gamma^q_L t} + 2ie^{-\Gamma_q t}\sin\Delta M_q t\right) \\
&= \frac{e^{-\Gamma_q t}}{2}\left(\sinh\frac{\Delta\Gamma_q t}{2} + i\sin\Delta M_q t\right) \quad . \qquad (1.32)
\end{aligned}$$

Types of *CP* violation in *B* meson decays

There are three different categories of *CP* violation in *B* meson decays, which can be classified in a model-independent way:

- ***CP* violation in decay**. This type of *CP* violation occurs in both charged and neutral *B* meson decays, when the amplitude for a decay and its *CP* conjugated process have different magnitudes, i.e.:

  $$\left|\frac{\bar{A}_{\bar{f}}}{A_f}\right| \neq 1 \quad . \qquad (1.33)$$

  As shown in (1.27), the decay amplitudes can be written in terms of strong and weak phases. *CP* violation of this type will not occur unless if there are at least two amplitudes with different weak phases and different strong phases. In other words, direct *CP* violation can occur when there are at least two decay amplitudes which contribute to the same final state. Recently, this kind of *CP* violation has been experimentally observed in the $B^0_d \to K^+\pi^-$ decay and in the $B^0_d \to \pi^+\pi^-$ decay by the BaBar and Belle experiments [22, 23].

- ***CP* violation in mixing**. In contrast to *CP* violation in decay, this type of *CP* violation occurs only in the neutral system, when the two neutral mass eigenstates cannot be chosen to be *CP* eigenstates. When *CP* symmetry is conserved, the mass eigenstates must be *CP* eigenstates. In that case the relative phase between M^q_{12} and Γ^q_{12} vanishes in (1.17). The condition to have indirect *CP* violation is:

  $$\left|\frac{q}{p}\right| \neq 1 \quad . \qquad (1.34)$$

  This type of *CP* violation arises when the oscillation probabilities of $B^0_q \to \bar{B}^0_q$ and $\bar{B}^0_q \to B^0_q$ are not the same. *CP* violation in mixing has been observed unambiguously in the neutral kaon system. For the neutral *B* system, this effect is very small (of the order of 10^{-2}) and can be observed for instance in semileptonic decays.

- ***CP* violation in the interference between decays with and without mixing**. This kind of *CP* violation arises only in the neutral system. Even if *CP* symmetry would be conserved in the decay amplitudes and in the mixing, the *CP* violation may still be observed in the interference between $B_q^0 \to f$ and $B_q^0 \to \bar{B}_q^0 \to f$ processes. This occurs when there is a relative phase between the mixing parameter q/p and the decay amplitudes $\bar{A}_f/A_f$. The effect is proportional to the imaginary part of λ_f defined in (1.31). Therefore, the condition for the presence of this type of *CP* violation is:

  $$\mathrm{Im}(\lambda_f) \neq 0 \quad . \tag{1.35}$$

  This kind of *CP* violation requires that the B_q^0 and $\bar{B}_q^0$ mesons decay into the same final state, $|f\rangle$.

CP violation in B_q^0 meson decays into *CP* eigenstates

CP violation in decays of B_q^0 mesons into a *CP* self-conjugated final states $|f\rangle$ can be easily described. By definition: the final state $|f\rangle$ is a *CP* eigenstate if it satisfies the relation

$$(CP)|f\rangle = n_f|\bar{f}\rangle = n_f|f\rangle \quad , \tag{1.36}$$

where $n_f = \pm\, 1$ is the *CP* eigenvalue of the final state. In this case, the time-dependent *CP* asymmetry can be defined as

$$A_{CP}(t) = \frac{\Gamma(\bar{B}_q^0(t) \to f) - \Gamma(B_q^0(t) \to f)}{\Gamma(\bar{B}_q^0(t) \to f) + \Gamma(B_q^0(t) \to f)} \quad . \tag{1.37}$$

Substituting (1.32) into (1.30) and putting the corresponding algebraical expressions for the transition rates into (1.37) one can write the time-dependent *CP* asymmetry in the following way[6]:

$$A_{CP}(t) = -\frac{A_{CP}^{\mathrm{decay}} \cos(\Delta M_q t) + A_{CP}^{\mathrm{interfer}} \sin(\Delta M_q t)}{\cosh(\Delta\Gamma_q t/2) + A_{\Delta\Gamma_q} \sinh(\Delta\Gamma_q t/2)} \quad , \tag{1.38}$$

where A_{CP}^{decay} and $A_{CP}^{\mathrm{interfer}}$ are the contributions of *CP* violation in decay and *CP* violation in the interference between decays with and without mixing. They are given in terms of λ_f as

$$A_{CP}^{\mathrm{decay}} = \frac{1 - |\lambda_f|^2}{1 + |\lambda_f|^2} \quad , \quad A_{CP}^{\mathrm{interfer}} = -\frac{2\,\mathrm{Im}\lambda_f}{1 + |\lambda_f|^2} \quad . \tag{1.39}$$

---

[6] It assumes that $q/p = 1$, since *CP* violation in mixing is small in the *B* system.

The term, $A_{\Delta\Gamma_q}$, is related to the presence of $\Delta\Gamma_q$, which is negligible in the B_d^0 system and may be sizeable in the B_s^0 system. It is given as

$$A_{\Delta\Gamma_q} = -\frac{2\,\mathrm{Re}\lambda_f}{1+|\lambda_f|^2} \quad . \tag{1.40}$$

The observable $A_{\Delta\Gamma_q}$ is not independent of A_{CP}^{decay} and $A_{CP}^{\mathrm{interfer}}$, since they are related by

$$|A_{CP}^{\mathrm{decay}}|^2 + |A_{CP}^{\mathrm{interfer}}|^2 + |A_{\Delta\Gamma_q}|^2 = 1 \quad . \tag{1.41}$$

According to Ref. [24], the parameter λ_f can be presented as:

$$\lambda_f = n_f e^{-i\phi_q} \frac{\sum\limits_{j=u,c} V_{jq}^* V_{jb} < f|Q^{jq}|\bar{B}_q^0 >}{\sum\limits_{j=u,c} V_{jq} V_{jb}^* < f|Q^{jq}|\bar{B}_q^0 >} \quad ,$$

where ϕ_q is the weak mixing phase of the B_q^0–$\bar{B}_q^0$ oscillation and $< f|Q^{jq}|\bar{B}_q^0 >$ are the hadronic matrix elements. However, if the decay $B_q^0 \to f$ is dominated by a single CKM phase, as in case of a $\bar{b} \to \bar{c}c\bar{s}$ quark-level transition (see Section 6.1.1), then the hadronic matrix elements cancel, and λ_f can be written in the simple form

$$\lambda_f = n_f e^{-i(\phi_q - \phi_D)} \quad , \tag{1.43}$$

where ϕ_D is a weak decay phase, which is equal to 0 for the $\bar{b} \to \bar{c}c\bar{r}$ $(r \in (d,s))$ quark-level transitions in the Wolfenstein parametrisation. In this case

$$\lambda_f = n_f e^{-i\phi_q} \quad . \tag{1.44}$$

Substituting (1.44) into (1.39) and (1.40) one can get

$$A_{CP}^{\mathrm{decay}} = 0 \quad , \quad A_{CP}^{\mathrm{interfer}} = n_f \sin\phi_q \quad , \quad A_{\Delta\Gamma_q} = -n_f \cos\phi_q \quad . \tag{1.45}$$

As can be seen, due to the dominance of a single CKM phase, there is no contribution from *CP* violation in decay. Only *CP* violation in the interference between decays with and without mixing can appear. The corresponding *CP* asymmetry directly measures the weak mixing phase ϕ_q. As a result, the time-dependent *CP* asymmetry can be written in the following way:

$$A_{CP}(t) = -\frac{n_f \sin\phi_q \sin(\Delta M_q t)}{\cosh(\Delta\Gamma_q t/2) - n_f \cos\phi_q \sinh(\Delta\Gamma_q t/2)} \quad . \tag{1.46}$$

The weak mixing phase of the B_q^0–$\bar{B}_q^0$ oscillation, ϕ_q, is given in terms of CKM elements as:

$$\phi_q = 2\,\arg[V_{tq}^* V_{tb}] \quad . \tag{1.47}$$

In the B_s^0 system, ϕ_s is directly related to the CKM angle χ. It can be shown using the Wolfenstein expansion up to $O(\lambda^6)$ and taking into account (1.11) :

$$\phi_s = 2\,\arg[V_{ts}^* V_{tb}] \approx -2\,\lambda^2 \eta \approx -2\chi \quad . \tag{1.48}$$

Analogously, in the B_d^0 sector it can be found that $\phi_d \approx 2\beta$.

Therefore, if a B_q^0 meson decays into a *CP*-pure eigenstate and the decay exists due to a $\bar{b} \to \bar{c}c\bar{s}$ quark-level transition, then by measuring the time-dependent *CP* asymmetry arising in this decay, it is possible to extract directly ϕ_q without any theoretical uncertainties. As a consequence, the CKM angles β (in the B_d^0 system) and χ (in the B_s^0 system) can be easily evaluated. There are two so-called "gold-plated" decays[7] allowing to extract these CKM angles: $B_d^0 \to J/\psi K_s^0$ and $B_s^0 \to J/\psi\phi$. Both exist due to the $\bar{b} \to \bar{c}c\bar{s}$ quark-level transition and therefore, are dominated by a single CKM phase. However, in the $B_s^0 \to J/\psi\phi$ channel the B_s^0 decays into two vector mesons. In such a case, there can be opposite contributions from both the *CP* even and *CP* odd decay amplitudes and thus, an angular analysis is required to disentangle them. In this dissertation, an analysis of the $B_s^0 \to J/\psi\eta'$ decay at LHCb based on a full Monte Carlo simulation is described. This decay is also existing due to the $\bar{b} \to \bar{c}c\bar{s}$ quark-level transition and therefore, can be used to extract ϕ_s (angle χ). Its branching fraction is approximately three times less than for the $B_s^0 \to J/\psi\phi$ decay, however the advantage is that the final state of this decay is a pure *CP* eigenstate, since it has a well defined *CP* eigenvalue of $+1$. As a result, no angular analysis is required. In Chapter 6, the physics of the $B_s^0 \to J/\psi\eta'$ decay, its selection and sensitivity of the LHCb detector to measure the ϕ_s with this decay mode are described.

---

[7] They have a rather large branching fraction of the order of 10^{-3} and can be easily measured experimentally.

Chapter 2

The LHCb experiment at the LHC

The European Organisation for Nuclear Research (CERN) is the world's largest particle physics laboratory [25], situated near Geneva on the border between France and Switzerland, at the foot of the Jura mountains. Since its foundation in 1954, CERN provides physicists with the facilities needed to study elementary particles. Currently, CERN is building the world's largest accelerator – the Large Hadron Collider (LHC) – in collaboration with over two thousand physicists from 34 countries, universities and laboratories. This facility allows physicists to perform sensitive tests of the Standard Model and to look for New Physics. The LHC will host several particle physics experiments, and LHCb is one of them. First in this chapter, a brief overview of the LHC is given. Thereafter, the design of the LHCb experiment including its different subdetectors and trigger system is described.

2.1 The Large Hadron Collider

The LHC [26] is a proton–proton (pp) collider with a centre-of-mass energy of $\sqrt{s} = 14\,\mathrm{TeV}$. At such a high energy, new elementary particles beyond the Standard Model predictions might be discovered. For example, particles predicted by supersymmetry (SUSY) might be detected. The Higgs boson – the only particle in the Standard Model that has not yet been observed – is also expected to be produced and detected at the LHC. In any case, this collider will generate many B hadrons that will allow physicists to perform high-precision measurement of CP violation in the B meson sector and to study rare decays of B hadrons. In addition, the LHC will be used to study the behaviour of nuclear matter at extreme energy densities in heavy-ion collisions and the formation of the quark-gluon plasma. These studies will be done in dedicated runs, when the LHC will be filled with heavy ions (e.g. Pb). The LHC is scheduled to start operating at a low energy in an engineering run in November 2007. The first pp collisions at nominal energy will take place mid-2008.

The LHC is located underground in a 27 km circumference tunnel. This tunnel was formerly used to house the Large Electron Positron collider (LEP). The new accelerator consists of two separate beam pipes, in which two proton beams are accelerated in opposite directions to an energy of 7 TeV. Before reaching that energy, the protons will pass through several preaccelarators. The Super Proton Synchrotron (SPS) is used at the last stage of preaccelaration. It increases the energy of protons up to 450 GeV and injects them into the LHC.

At the LHC, a magnetic field of 8.34 T is needed to maintain the orbit of the protons at an energy of 7 TeV. To reach such a high magnetic field, the two beam pipes are enclosed within superconducting magnets providing opposite magnetic fields. The superconducting magnets are positioned inside a cryostat containing superfluid helium with a temperature of 1.9 K.

A proton needs $90\,\mu$s to travel once around the collider. At the LHC, the protons are "bunched" together into 2 808 bunches, each bunch consisting of 10^{11} protons. The time interval between two consecutive bunches is 25 ns. The bunch crossing frequency of $\nu = 40\,\text{MHz}$ sets the basic clock frequency for the detector electronics. However, some bunches will be empty due to the filling procedure. The average bunch crossing frequency of filled bunches is $\nu_{\text{filled}} = 30\,\text{MHz}$.

The total cross section of pp interactions can be presented as the sum of an elastic and an inelastic part. Elastic pp interactions leave the colliding particles intact. These interactions are usually not seen in the detector, since the protons escape through the beam pipe. Inelastic pp interactions lead to the creation of various particles that pass through the detector. According to Ref. [27], the expected inelastic cross section at $\sqrt{s} = 14\,\text{TeV}$ is $\sigma_{pp}^{\text{inel}} = 80\,\text{mb}$, while the total cross section is $\sigma_{pp}^{\text{tot}} = 100\,\text{mb}$. The total number of inelastic pp collisions over a given time interval $[t_1, t_2]$ is given by

$$N_{pp} = \sigma_{pp}^{\text{inel}} \int_{t_1}^{t_2} L\mathrm{d}t \quad , \tag{2.1}$$

where L is the luminosity at the crossing point. The luminosity depends on the compactness of the beam, the ability of the magnets to focus the beams at the interaction point, the bunch crossing frequency and the number of particles in the bunches. The design luminosity of the LHC is $L = 10^{34}\,\text{cm}^{-2}\text{s}^{-1}$. However, during the first few years after the startup the LHC will run at a lower luminosity of $L = 10^{33}\,\text{cm}^{-2}\text{s}^{-1}$. The proton beams are stored for 7 hours in the collider. Afterwards, they are dumped and the LHC is refilled. During storage the luminosity exponentially decreases with a characteristic lifetime of 10 hours. The Poisson-distributed number of inelastic collisions per filled bunch crossing for a given instantaneous luminosity has a mean of

$$\bar{n}_{pp} = \frac{L\sigma_{pp}^{\text{inel}}}{\nu_{\text{filled}}} \quad . \tag{2.2}$$

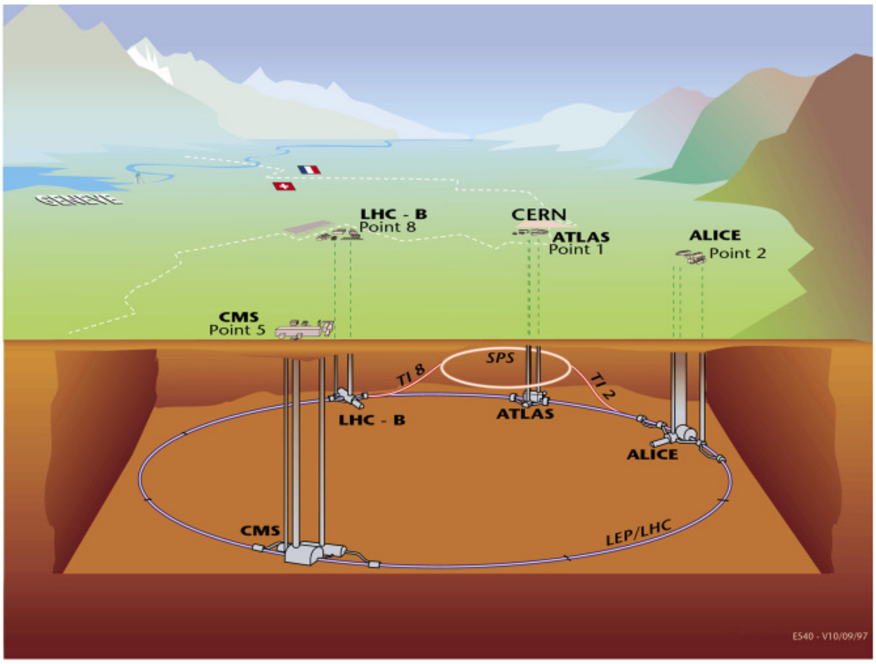

Figure 2.1: *The LHC complex with its four main experiments.*

It is approximately equal to 27 at the LHC design luminosity.

Figure 2.1 illustrates the overall view of the LHC complex together with its four main experiments. In total, there are six detectors which are being constructed at the LHC. All of them are located in large caverns excavated at the LHC's interaction points. These are:

- ATLAS [28] and CMS [29]. Both are central detectors having broad physics programs including the search for the Higgs boson and for SUSY particles. They also plan to study B physics and many other interesting phenomena.
- ALICE [30]. This detector is specifically designed to investigate the behaviour of nuclear matter at the extreme energy densities in heavy-ion collisions and the formation of the quark-gluon plasma.
- LHCb [31]. This detector is dedicated to the study of CP violation and rare decays in the B system. Its design is discussed in the next section.
- TOTEM [32] and LHCf [33]. These are much smaller projects, which share the interaction point with CMS and ATLAS detectors, respectively. The TOTEM detector is designed to measure the total cross section, elastic scattering and diffractive processes at the LHC. The LHCf detector focuses on studying the particles generated in the forward region of collisions. Its main purpose is to precisely measure the pion

production cross section near zero degrees through the measurement of photons produced in neutral pion decays. This measurement is crucial for the simulation of particle showers in the atmosphere induced by high-energy cosmic rays.

2.2 The LHCb detector

The LHCb detector will exploit the large number of B hadrons produced at the LHC to study CP violation and rare decays in the B meson system with a very high precision. Other physics topics (e.g., Higgs and charm physics) will be investigated to a smaller extent. The detector is designed and constructed by a collaboration consisting of around 500 physicists, technicians and engineers from 47 universities and laboratories from 15 countries.

For the precise reconstruction of the B hadrons it is important to have a good vertex resolution in order to separate the B decay vertex from the production vertex. Multiple pp collisions within the same bunch crossing (so-called pile-up) can significantly complicate the identification of the B decay vertex and its corresponding production vertex. Therefore, the LHCb experiment will operate at an average luminosity of only $2\times10^{32}\,\mathrm{cm}^{-2}\mathrm{s}^{-1}$, fifty times less than the design luminosity of the LHC. This is achieved by defocusing the proton beams at the interaction point, reducing the mean number of inelastic pp collisions per filled bunch crossing from 27 to 0.53. In addition, the particle multiplicity will be lower, making the reconstruction of tracks easier. Another benefit of running at a moderate luminosity is the reduction of radiation damage on the detectors and readout electronics. In LHCb, all subdetectors are designed to cope with a luminosity of $5\times10^{32}\,\mathrm{cm}^{-2}\mathrm{s}^{-1}$. This leaves room for running at slightly higher luminosities.

The estimates for the $b\bar{b}$ production cross section in pp collisions at $\sqrt{s} = 14\,\mathrm{TeV}$ have large uncertainties. In this dissertation, it is assumed to be $\sigma_{b\bar{b}} = 500\ \mu\mathrm{b}$ [27]. This value is a conservative estimate. The integrated luminosity defined as $L^{\mathrm{int}}_{\mathrm{year}} = \int L\ dt$ after one nominal year of 10^7 s is $2\,\mathrm{fb}^{-1}$. Hence, the number of $b\bar{b}$ pairs produced in the LHCb experiment during a nominal year is expected to be $\sigma_{b\bar{b}} \times L^{\mathrm{int}}_{\mathrm{year}} = 10^{12}$.

2.2.1 General layout

Since $b\bar{b}$ hadrons at the LHC will be predominately produced at low polar angles in the same forward cone (see Fig. 2.2), the LHCb detector is designed as a single-arm, forward spectrometer with an angular coverage from 10 mrad to 300(250) mrad in the horizontal (vertical) plane. The first design of the detector, described in the Technical Proposal [27], was approved in September 1998. Between 2001 and 2003, several optimisations were made to reduce the material budget and to improve the trigger performance of

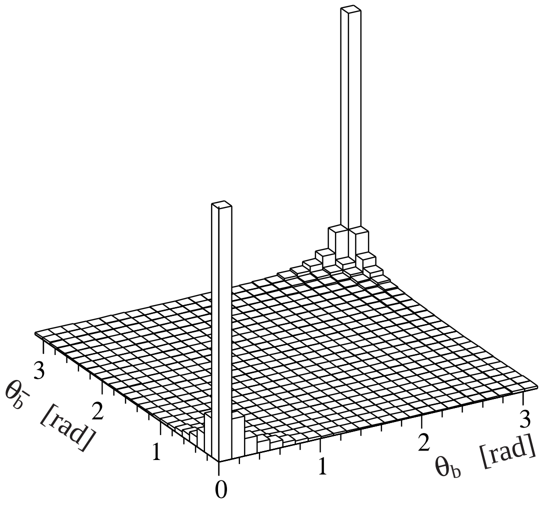

Figure 2.2: *Polar angle θ of b and $\bar{b}$ hadrons at the LHC. The polar angle is defined with respect to the beam axis in the pp centre-of-mass system.*

the detector. The optimised design of the LHCb experiment is described in Ref. [31]. The detector setup presented in this dissertation refers to this design.

Figure 2.3 illustrates the LHCb experimental setup shown in the vertical plane. A right-handed coordinate system is adopted such that the z axis points from the Vertex Locator towards the muons stations and the vertical axis y points upwards. The x axis points to the right when looking into the negative z direction. The dimensions of the detector are roughly equal to $x \times y \times z = 6\,\mathrm{m} \times 5\,\mathrm{m} \times 20\,\mathrm{m}$.

In LHCb, all subdetectors can be divided into tracking detectors used to reconstruct the trajectories of a charged particles, and particle identification (PID) detectors used to identify the different particle types:

- **Tracking detectors**: Vertex Locator (VELO), Trigger Tracker, Magnet, Tracking stations (T1–T3).
- **Particle identification detectors**: Ring Imaging Cherenkov counters (RICH1 and RICH2), Scintillating Pad/Preshower Detector (SPD/PS), Electromagnetic Calorimeter (ECAL), Hadronic Calorimeter (HCAL) and the Muon system (M1–M5 stations).

The beam pipe traverses the whole detector except the VELO which is enclosed in a vacuum vessel. In the next sections, each part of the detector is briefly described.

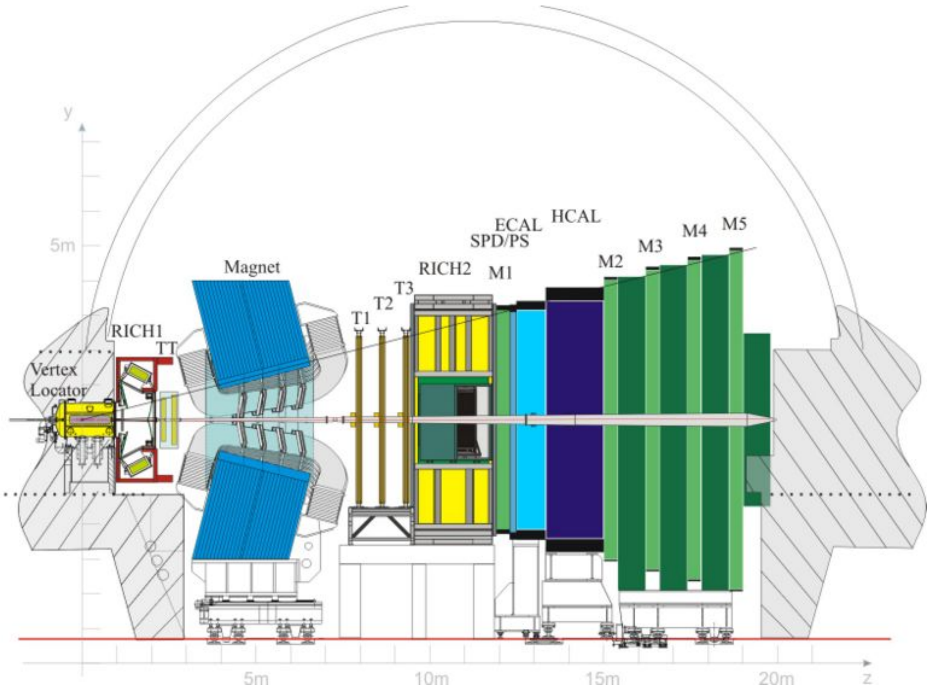

Figure 2.3: *The LHCb detector shown in the vertical plane.*

2.2.2 Vertex locator

The Vertex Locator [34, 31] provides precise measurements of tracks close to the pp interaction region. These tracks are used to reconstruct the location of the production and decay vertices of B hadrons, providing accurate measurements of their decay times. The VELO contains 21 stations of silicon microstrip detectors positioned along and perpendicular to the beam axis. Figure 2.4 illustrates a cross section of the VELO and the pp interaction region as seen from above. In each station, two types of silicon microstrip detectors are used: one measures the r coordinate with circular strips centred around the beam axis and the other measures the azimuthal ϕ coordinate with radial strips. Figure 2.5 shows the half-disc sensors. The sensors are based on single-sided, n-on-n technology with a thickness of $220\,\mu$m. They are separated from the beam vacuum by a thin aluminium foil, which shields the electronics against RF pickup from the LHC beams and prevents outgassing of the sensors into the beam vacuum.

The r sensors directly give a projection in the $r-z$ plane, in which the tracks with a high impact parameter relative to the production vertex can be easily identified. This feature is exploited by the LHCb trigger, which first reconstructs all tracks in the $r-z$ projection to estimate their impact parameter, and afterwards reconstructs only the ones with a large impact parameter in three dimensions by including the ϕ sensors. This strategy

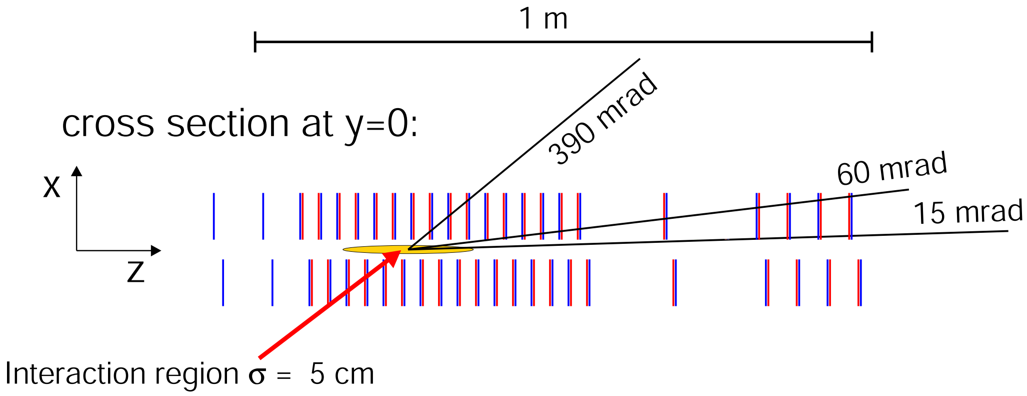

Figure 2.4: *Setup of the stations in the VELO.*

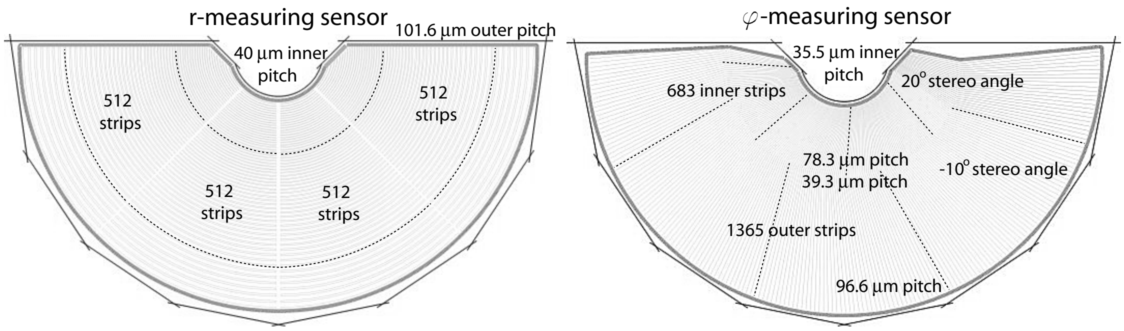

Figure 2.5: *Layout of the r- and ϕ-measuring sensors. The r-measuring sensors are divided into four sections of 45°. The ϕ-measuring sensors have an inner section with strips under a stereo angle of 20° and an outer section with strips under a stereo angle of –10°. Both r- and ϕ-measuring sensors have a varying strip pitch to provide a more homogeneous occupancy.*

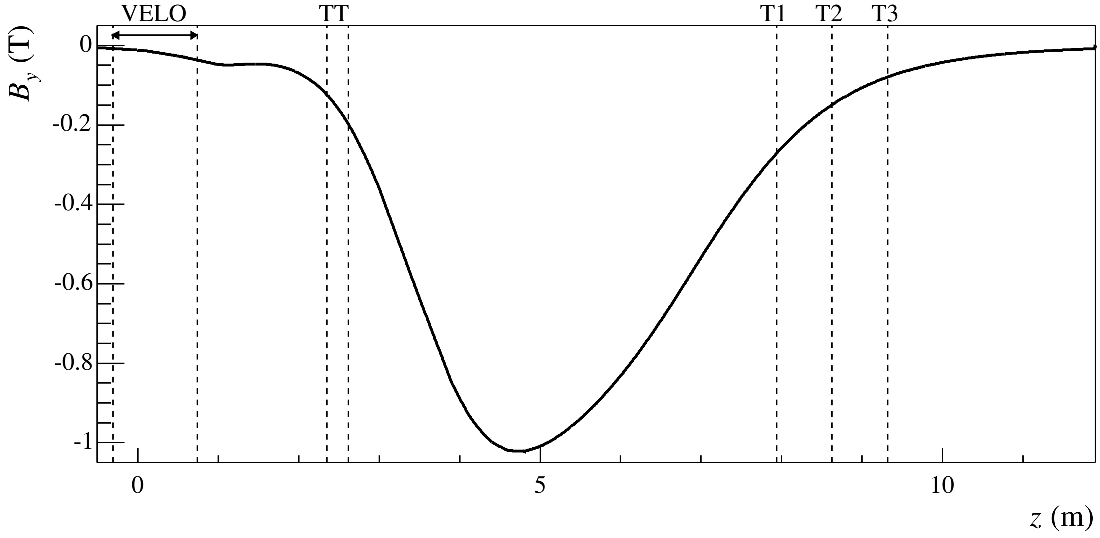

Figure 2.6: *The main component of the magnetic field strength (B_y) along the z axis.*

decreases the processing time.

In order to reduce the error on the reconstructed position of the vertices, the silicon sensors should be located as close to the pp interaction region as possible. In the VELO, the sensitive area of the silicon sensors starts at 8 mm from the beam axis. This is much smaller than the aperture of 3 cm required by the LHC during injection and therefore the sensors must be retractable. This is achieved by mounting the detectors inside a vacuum vessel with a Roman pot system to be able to move the two detector halves away from the beam during beam injection and to avoid radiation damage.

2.2.3 Magnet

In order to be able to measure the momentum of tracks, the LHCb detector houses a magnet [35]. Its aperture defines the acceptance of the experiment. The momentum of charged particles is obtained their curvature in the field of the magnet. The difference between the track slope in the VELO and the track slope in the tracking stations T1–T3 is inversely proportional to the particle's momentum [36]. The bending power of the magnet is characterised by the total integrated field, which is $\int B dl = 4.2\,\mathrm{T\,m}$. Figure 2.6 illustrates the strength of the main component of the magnetic field as a function of z coordinate.

2.2.4 Trigger Tracker

The Trigger Tracker is located just in front of the entrance of the magnet. Its main purpose is to add momentum information to charged particles. This information is used by the LHCb trigger system to make a decision. In addition, the Trigger Tracker aids to reconstruct the trajectories of long-lived neutral particles (such as K_s^0 and Λ) which may decay outside the VELO acceptance. It also estimates the momentum for particles which are bent out of the LHCb acceptance before reaching the tracking stations T1–T3. The Trigger Tracker is one of the main topics of this dissertation. Its design and main characteristics of this subdetector are described in the next chapters.

2.2.5 Tracking stations

The three tracking stations T1–T3 are located downstream of the spectrometer magnet at equidistant positions along the beam line. They represent the final part of the LHCb track reconstruction system. The deflection of the tracks at these stations is used to measure their momentum. In addition, the T stations measure the direction of track segments before the RICH2 detector, which is used as an input for the particle identification algorithms. Each T station consists of an Inner Tracker covering the innermost region around the beam pipe and an Outer Tracker covering the outer part of the tracking stations. Figure 2.7 shows a sketch of the front view of a tracking station giving the overall dimensions of the active area.

Inner Tracker

In each tracking station, the Inner Tracker (IT) [37] covers a cross-shaped area around the beam pipe with silicon microstrip detectors. Although the IT covers only 1.3% of the sensitive surface of the tracking stations, approximately 25% of all charged particles originated from the *pp* interaction point that reach the tracking stations will pass through the IT [37]. Charge particle fluxes of about $1.5\times10^5\,\mathrm{cm}^{-2}\mathrm{s}^{-1}$ are expected in the innermost region of the IT. The average hit occupancy in the IT is expected to be less than 2% [38].

There are four separate IT boxes in each T station: above, below, left and right of the beam pipe. They provide electrical and thermal shielding for the silicon sensors and readout electronics. The IT box contains four detection layers of silicon microstrip detectors with a *x*–*u*–*v*–*x* topology: the first and the last layer have vertical strips, while the second and third have strips which are rotated by an angle of $+5^\circ$ and -5°, respectively.

The silicon sensors for the IT contain 384 strips with a pitch of $198\,\mu$m. They have a length of 11.0 cm and a width of 7.8 cm. The sensors are assembled onto one-sensor ladders (used in the top/bottom boxes) and onto two-sensor ladders (used in the left/right

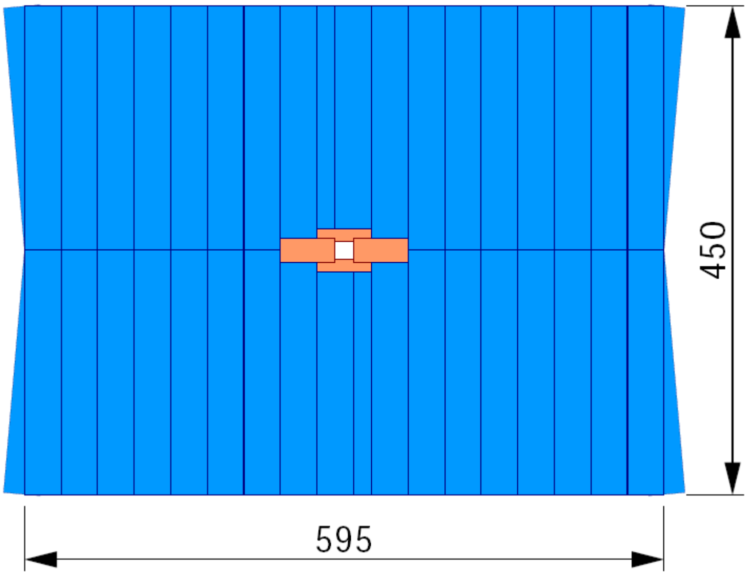

Figure 2.7: *Front view of a tracking station. Dimensions are given in cm. In the centre the four IT boxes surrounding the beam pipe hole are visible.*

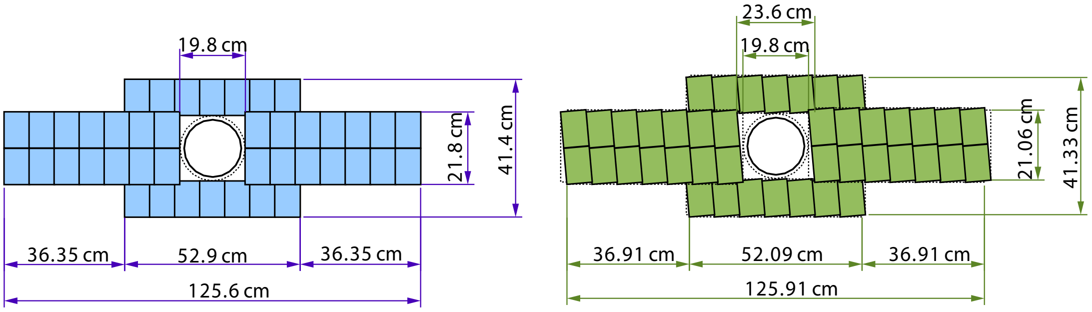

Figure 2.8: *Layout of an IT x and u layer with the silicon sensors. Dimensions refer to the sensitive surface covered by the IT. In the centre a cross section of the beam pipe is drawn.*

boxes) that are connected to a readout hybrid. In order to ensure an acceptable signal-to-noise performance, the sensor thickness was chosen to be 320μm for one-sensor ladders and 410μm for two-sensor ladders. The layout of the x and u detection layers with the silicon sensors is shown in Fig. 2.8.

Outer Tracker

In the T stations, the Outer Tracker (OT) [39] covers the large area outside of the IT acceptance with gas-filled straw tubes with an inner diameter of 5 mm serving as drift cells. The advantage of this technology is the rather low cost with a good spatial resolution. The drift cells, which contain an anode wire in the middle to collect the signal, are assembled in modules with a width of 34 cm. These are the building blocks of the OT detection layer. As for the IT, each OT station consists of four detection layers arranged in the same x–u–v–x configuration. The selected gas is the mixture Ar(70%)/CO_2(30%), which gives a maximal drift time of 42 ns [40]. A spatial resolution better than 200 μm was obtained in a test beam experiment.

2.2.6 RICH detectors

Often, in order to reconstruct interesting B meson decays, it is necessary to separate pions from kaons. For example, the selection of $B_s^0 \to D_s^{\mp} K^{\pm}$ decays, allowing to measure the CKM angle γ, requires the rejection of $B_s^0 \to D_s^- \pi^+$ decays, which have the same topology. Additionally, the identification of kaons from the accompanying B hadron decay allows to tag the flavour of the B meson.

The LHCb particle identification system comprises two Ring Imaging Cherenkov detectors [41]: RICH1 and RICH2. These detectors are based on the Cherenkov effect, which is explained as follows. When a charged particle traverses a medium with a velocity larger than the speed of light in that medium, it emits electromagnetic radiation. The velocity of the particles can be found by measuring the angle, θ_{C}, between the Cherenkov photon and the direction of the particle using the relation

$$\cos\theta_{\mathrm{C}} = \frac{1}{n\beta} \quad ,$$

where $\beta = v/c$ is the particle's velocity and n is the refraction index of the medium. Particles start to emit Cherenkov radiation with a velocity $\beta > 1/n$. Knowing the particle's velocity and momentum one can determine its mass and as a result, its identity.

The RICH1 detector is located between the VELO and the Trigger Tracker. It covers the full LHCb acceptance and uses aerogel with $n = 1.03$ and C_4F_{10} gas with $n = 1.0014$ as radiators. This provides identification of charged particles with momenta from 1 to

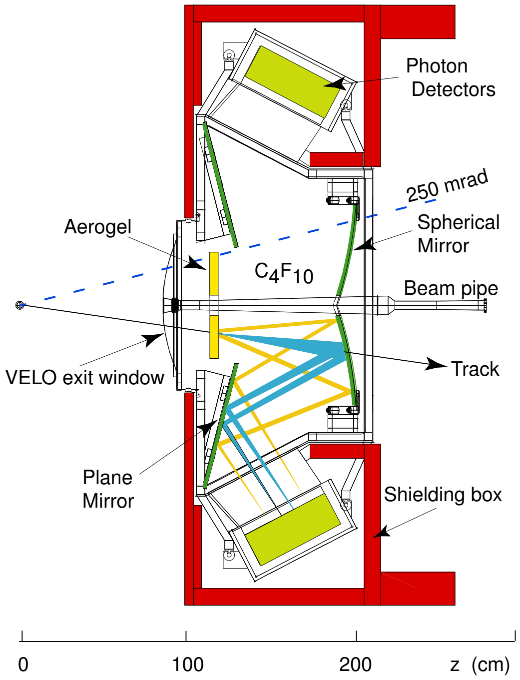

Figure 2.9: *Vertical cross section of the RICH1 detector.*

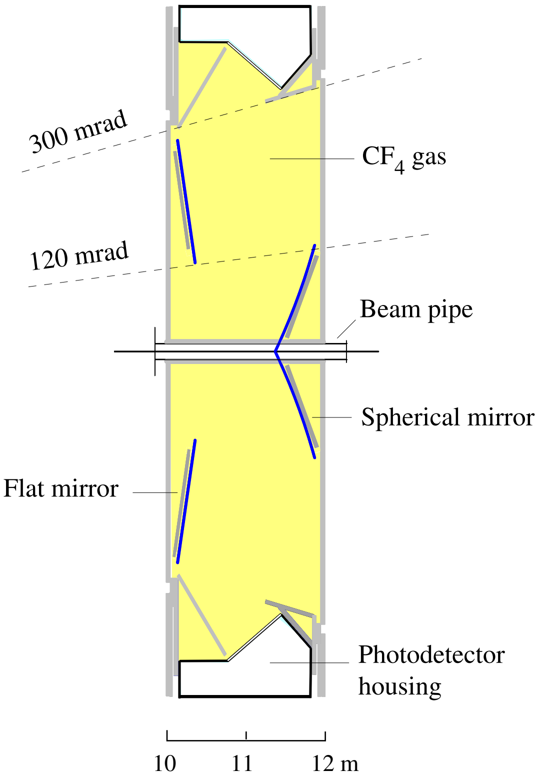

Figure 2.10: *Horizontal cross section of the RICH2 detector.*

65 GeV/c. The RICH2 detector is located directly behind the T stations and has a limited acceptance of ±25 mrad to ±120 mrad (horizontal) and ±100 mrad (vertical). This detector allows to perform identification of charged particles with a momentum from around 15 GeV/c up to and beyond 100 GeV/c using CF_4 gas with n =1.0005. In both RICH detectors the focusing of the Cherenkov light is accomplished using a combination of spherical and flat mirrors to guide the image out of the acceptance to the Hybrid Photon Detectors (HPD's). RICH1 has a vertical optical layout symmetry, while RICH2 has a horizontal optical layout symmetry. The mirror system projects the light cones as rings onto the plane of HPD's. The projected image has a granularity of 2.5 mm ×2.5 mm. The radius of each ring gives a measure for the Cherenkov angle, θ_C. In order to identify charged particles, a global likelihood analysis is performed on the observed pattern of photons. Figure 2.9 and Figure 2.10 illustrate the layout of the RICH1 and RICH2 detectors.

2.2.7 Calorimeters

The main purpose of the calorimeter system [42] is to provide identification of neutral particles, electrons and hadrons for the trigger and the offline analysis. In LHCb, the calorimeters are located between the first and the second muon station. By absorbing the particles, they measure their energy and position. In the material of the calorimeter system, a shower of secondary particles is produced by each incident particle. The ionisations induced by these showers excite the atoms in the scintillating material of the calorimeters resulting in the emission of scintillation light. The total amount of scintillation light is a measure of the particle's energy. The LHCb calorimeter system consists of a Scintillating Pad/Preshower detector (SPD/PS), an Electromagnetic Calorimeter (ECAL) and Hadronic Calorimeter (HCAL). They are described hereafter.

Scintillating Pad/Preshower Detector

The SPD/PS detector consists of a lead plate with a thickness of 12 mm that is sandwiched between two almost identical detection layers of rectangular scintillator pads. The total sensitive area of the SPD/PS detector is 7.6 m wide and 6.2 m high. The purpose of the first layer, called SPD, is to distinguish electrons from photons. It relies on the fact that electrons are charged particles which produce ionisation as opposed to photons. The lead plate, located directly behind SPD, is used to initiate the electromagnetic shower, which is then detected by the second detection layer, called PS. The PS discriminates between electrons and hadrons. The scintillator pads in the SPD/PS system have a thickness of 15 mm. They are subdivided into an inner, middle and outer section, each having a different granularity to obtain roughly the same hit occupancy throughout the detector. In each pad, the scintillator light is collected by a wavelength shifting (WLS) fibre and directed to multianode photomultipliers located outside the detector acceptance.

Electromagnetic Calorimeter

The ECAL is placed at 12.5 m from the pp interaction point, directly behind the SPD/PS system. This subdetector is used to perform the identification and reconstruction of photons and electrons via their electromagnetic showers. The ECAL is based on the shashlik calorimeter technology, which implies a sampling structure of 2 mm thick lead sheets interspersed with 4 mm thick scintillator plates, read out by WLS fibres. This calorimeter technology provides a good energy resolution, fast response time and acceptable radiation resistance. The segmentation of the ECAL scintillator plates follows that of the SPD/PS. The energy resolution is $\sigma(E)/E = 10\%/\sqrt{E} \oplus 1.5\%$, where E is the energy expressed in GeV and $\oplus$ means addition in quadrature.

Hadronic Calorimeter

The HCAL is located behind the ECAL and is used to identify hadrons via their interactions with the detector material. In principle, hadrons may start to shower already in the ECAL. Nevertheless, they are fully absorbed inside the HCAL, where they deposit most of their energy. As for the ECAL, the HCAL has a sampling structure consisting of 16 mm thick iron sheets and 4 mm thick scintillating tiles. The overall detector thickness is 1.2 m. The tiles are placed parallel to the beam direction, in a staggered arrangement. The expected energy resolution is $\sigma(E)/E = 80\%/\sqrt{E} \oplus 10\%$.

2.2.8 Muon detector

The identification of muons is a fundamental aspect in LHCb, since these particles are present in the final states of many B decay channels. Moreover, muons from semi-leptonic B decays provide a tag of the initial flavour of accompanying B hadron. These particles possess a unique property: a very high penetrative power. Muons are the only charged particles likely to penetrate the LHCb calorimeter system. They are identified by the muon system [43] consisting of five stations – M1 in front of the SPD/PS and M2–M5 behind the calorimeters, intervaled with iron shielding plates with a thickness of 80 cm. In the trigger algorithm, high-momentum muons are found by selecting particles which pass all five muon stations. The position of M1 is motivated by the need to decrease the error on the momentum measurement due to scattering of charged particles in the material of the calorimeter system. The slope of the track between M1 and M2 is used to estimate the momentum of tracks assuming that the particle originated from the pp interaction point. In the offline reconstruction, tracks found in the T stations are extrapolated to the muon stations to verify the muon hypothesis.

All muon stations cover the full LHCb acceptance with multiwire proportional chambers (MWPC's), divided into four regions with different pad granularity. The dimensions of the pads decrease towards the inner regions to obtain a constant hit occupancy throughout the station. The MWPC's collect the signal within 20 ns. In the innermost region of M1, the MWPC's are equipped with a triple-GEM foil to cope with the higher radiation load. The M1 station contains only two layers of MWPC's to reduce the material budget before the calorimeter system, while the other four stations contain four detection layers.

2.2.9 Trigger system

With a bunch crossing frequency of 40 MHz, it is impossible to record all events, since it would lead to a huge amount of data that cannot be stored. Furthermore, most recorded events are not interesting for physics studies, since at the average luminosity of LHCb there will be about 10 MHz of crossings with “visible pp interactions”[1], which is expected to contain a rate of about 100 kHz of $b\bar{b}$ pairs only. In order to select only those events that are of interest for B physics studies and to reduce the event rate to an acceptable level a trigger system is developed. The LHCb trigger [44, 45] exploits the fact that B hadrons are long-lived particles with a relatively large mass. It is based on a two-level system described hereafter.

The Level-0 trigger

The first level, Level-0, is implemented in hardware. Its main purpose is to select the events containing particles with a high transverse energy, E_T. Due to the relatively large mass of a B hadron, the presence of high-E_T decay products is one of the main signatures of a decay of a B hadron. Also, the Level-0 is used to reject busy events for which the reconstruction would take a long time. The Level-0 uses information from the pile-up system, the calorimeter system and the Muon detector. The Level-0 decision unit (L0DU) combines the output from these three components and issues the final trigger decision of this level. The latency of the Level-0 trigger, which is the time elapsed between a pp interaction and the arrival of the Level-0 trigger decision at the frond-end electronics, is fixed to $4\,\mu$s. This time includes the time-of-flight, cable length and all other delays in the frond-end electronics leaving only $2\,\mu$s for the actual processing of the data in the Level-0 to derive a decision. The Level-0 output rate is 1 MHz.

The pile-up system detects bunch crossings with multiple pp inelastic interactions (i.e. multiple primary vertices). This system is part of the VELO and consists of two planes of silicon sensors with circular strips (the r-measuring sensors). Crossings with two or more visible pp interactions are identified with an efficiency of 60% and a purity of about 95%. The output of the pile-up system to the L0DU consists of two event variables: the number of tracks from a second pp interaction and the pile-up system hit occupancy. An event is rejected when the hit multiplicity is larger than 112 or when the number of tracks used to reconstruct the second pp interaction is greater than 3.

The calorimeter system gives the L0DU the highest-E_T hadron, electron, photon and π^0 candidates, the total energy deposited in the calorimeter and SPD multiplicity. The Level-0 accepts an event if it contains an electron with $E_\mathrm{T} > 2.6\,\mathrm{GeV}$, a hadron with $E_\mathrm{T} > 3.5\,\mathrm{GeV}$, a photon with $E_\mathrm{T} > 2.3\,\mathrm{GeV}$ or neutral pion with $E_\mathrm{T} > 4.0\,\mathrm{GeV}$. There is a veto on the event if the sum of the total energy in the calorimeter is below 5.0 GeV. In addition, the event is rejected if the SPD multiplicity is larger than 280.

The Level-0 trigger considers the two muon tracks with the largest transverse momentum, p_T, found in the Muon detector. These two highest-p_T muon candidates are sent to

---

[1] These are defined as pp interactions that produce at least two charged particles with a sufficient number of hits to be reconstructed in the detector.

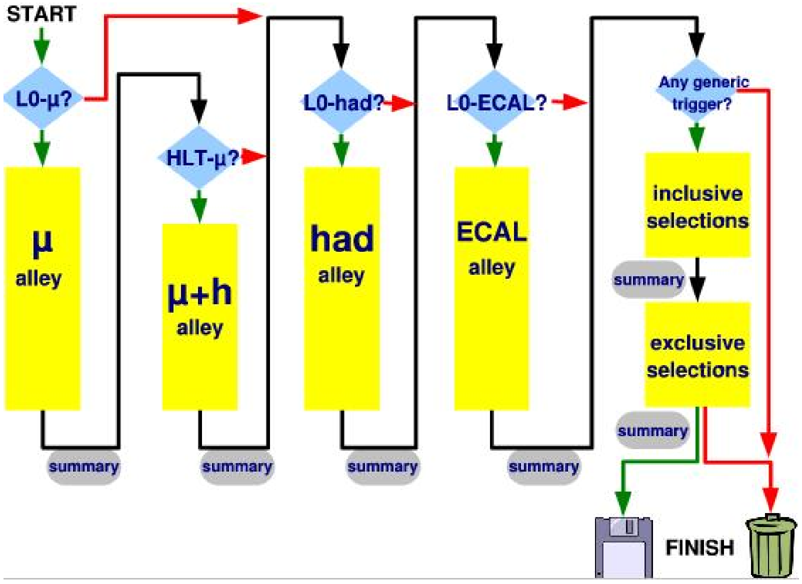

Figure 2.11: *Flow-diagram of the different trigger sequences in the HLT. Diamonds indicate where the trigger decisions are taken, while squares represent the reconstruction algorithms.*

the L0DU. An event is accepted when it contains a muon with $p_\mathrm{T} > 1.3\,\mathrm{GeV}/c$ or when the sum of the p_T of the two muons is greater than $1.5\,\mathrm{GeV}/c$.

The High Level trigger

All Level-0 accepted events are passed on to the High Level Trigger (HLT), which reduces the rate down to 2 kHz by using data of all subdetectors. This software trigger runs on the event-filter farm composed of about 1800 CPU nodes. The generic HLT algorithms refine the selections on the candidates found by the Level-0 trigger. A schematic view of the different trigger sequences in the HLT is shown in Fig. 2.11. At the first stage, the HLT checks whether the Level-0 decision was based on the calorimeter system or on the Muon detector. As shown in Fig. 2.11, the HLT is separated into four independent trigger streams, so-called alleys: the muon alley, the muon and hadron alley, the hadron alley, and the electromagnetic alley. In each alley an event should pass through the following consecutive steps:

- First, it is necessary to confirm the Level-0 decision for selected events by matching the Level-0 candidates to a track segment in at least one tracking subdetector.
- Second, a fast finding track algorithm using information from only the VELO and Trigger Tracker is run to localise production vertices of a B hadrons and to find

tracks with a large p_{T} and large impact parameter with respect to the production vertex.

- Then, a search for B hadron decay vertices and a more precise measurement of the p_{T} using the T stations is done.
- Finally, selection requirements specific to the alley are applied.

Most events that passed through the Level-0 are only selected due to one Level-0 candidate, and hence will only be processed by one alley. Around 15% of the events that passed through the Level-0 are selected by multiple candidates and as a result will pass more than one alley in the HLT.

In the muon alley an event is selected when it contains two muon candidates with an invariant mass above 2.5 GeV, or when the invariant mass of the two muon tracks is larger than 0.5 GeV and the impact parameter of both is larger than 100 μm. Events with a single muon can also pass the muon alley if the muon has a $p_{\mathrm{T}} > 3.0\,\mathrm{GeV}$ and the impact parameter significance $\mathrm{IP}/\sigma_{\mathrm{IP}} > 3$. Overall, the muon alley triggers events at a rate of about 1.5 kHz.

The muon and hadron alley is run when the event is selected by the Level-0 muon trigger, but did not pass through the muon alley of the HLT. In this alley, the algorithm selects those events which have a muon and a hadron track with a high impact parameter and a relatively high p_{T}. The exact requirements are not defined yet.

If the event is selected by the Level-0 hadron trigger, then the HLT hadron alley is executed. Events with a single hadron are selected by the alley if the hadron has a $p_{\mathrm{T}} > 2.5\,\mathrm{GeV}$ and an impact parameter larger than 150 μm. If there are two hadrons in the event, then one of them should have a $p_{\mathrm{T}} > 1.1\,\mathrm{GeV}$ and the other should have a $p_{\mathrm{T}} > 0.9\,\mathrm{GeV}$, while the impact parameter should be more than 150 μm for both. The hadron alley triggers events at a rate of about 4 kHz.

The electromagnetic alley is currently under development. It process the events selected by the Level-0 electromagnetic trigger. For the time being this alley requires one track and one calorimeter object (electron or photon) above a certain transverse momentum and energy.

Each alley produces summary information which is written to storage for accepted events. This summary contains information of all tracks and vertices which have triggered the event. The combined output rate of events accepted by the alleys is around 10 kHz. If the event is selected by at least one alley, then it is processed by the inclusive selections, where specific resonances are reconstructed and selected, and it is processed by the exclusive triggers, which are used to fully reconstruct the B hadron final state. The inclusive and exclusive selections reduce the 10 kHz input rate down to around 2 kHz. At this rate the data is written to storage for further analysis. The average event size is estimated to be around 30 kBytes.

Chapter 3

The Trigger Tracker in LHCb

In the original design of the LHCb detector presented in Ref. [27], the main tracking system consists of eleven tracking stations located between the VELO and the calorimeter system. Later, simulations with this design showed that the particle reconstruction efficiency was rather poor due to hadronic interactions with the material of the detector. It became clear that the material budget of the detector had to be reduced. Therefore, the LHCb collaboration decided to build only three tracking stations (T1–T3) after the magnet and one tracking station (Trigger Tracker) before the magnet. Simulations with this optimised design showed the positive effect of these changes on the performance of the detector as presented in Refs. [31, 46].

The Trigger Tracker is part of the LHCb Silicon Tracker project, together with the Inner Tracker that covers the innermost part of tracking stations T1–T3. Both subdetectors are large-surface single-sided silicon microstrip detectors, which have almost identical readout electronics and infrastructure systems such as high voltage, low voltage and cooling. Around 30 physicists from 5 universities and laboratories from 4 countries are currently involved in the LHCb Silicon Tracker project.

This chapter is dedicated to the Trigger Tracker. First, the purpose and requirements of this subdetector are considered. Second, a general description of silicon microstrip detectors is given. Then, the detector design and its main characteristics are discussed. Finally, a brief overview of the R&D programme performed for the Trigger Tracker is presented.

3.1 Purpose and main requirements

The Trigger Tracker is located between the RICH1 and the magnet at 2485 mm from the *pp* interaction region. As was mentioned in Chapter 2, this subdetector is used:

- **in the HLT** to assign a rough momentum estimate to the tracks. It relies on the presence of a low integrated magnetic field of $\sim 0.15\,\mathrm{T\,m}$ (see Fig. 2.6) between the VELO and the Trigger Tracker.

- **in the offline analysis** to reconstruct trajectories of long-lived neutral particles that decay outside of the VELO acceptance and to reconstruct trajectories of low-momentum particles that are bent out of the detector acceptance before reaching the tracking stations T1–T3.

The Trigger Tracker is constructed entirely using silicon microstrip detectors based on single-sided, *p*-on-*n* technology. These detectors provide a good spatial resolution, which is needed to estimate the particle's momentum especially in regions of relatively low magnetic field, where the deflection of high-momentum tracks is small.

The Trigger Tracker must meet the following requirements:

1. **A low material budget** to minimise multiple scattering and secondary interactions of particles with the material of the detector. This is required to obtain an excellent momentum resolution for charged particles and a high track reconstruction efficiency.

2. **A strip occupancy not exceeding a few percent** to provide a high track finding efficiency.

3. **An acceptable signal-to-noise performance** to guarantee a good single-hit reconstruction efficiency.

4. **A spatial hit resolution of around 50 μm** to ensure an accurate measurement of the track coordinates.

5. **An acceptable radiation hardness** to prevent damage of the silicon microstrip detectors and readout electronics due to the high radiation dose in the LHCb environment[1].

6. **A shaping time of the front-end electronics below 25 ns** to avoid the reconstruction of tracks originating from previous bunch crossings.

7. **A minimal number of readout channels** to keep cost of the detector as low as possible.

---

[1] For ten years of operation at nominal LHCb luminosity, a 1-MeV neutron equivalent fluence of about 5×10^{13} per cm^2 is expected in the innermost region of the Trigger Tracker [47].

Some of these requirements are contradictory. For example, a low material budget requires the thickness of the silicon microstrip detectors to be small. On the other hand, an acceptable signal-to-noise performance requires the silicon detectors to be thick in order to produce enough signal. Furthermore, a fast shaping time of the front-end electronics leads to a large Johnson noise that directly affects the signal-to-noise performance (see Section 3.2.2). Also, a low occupancy and a high spatial hit resolution requires short strips with a small pitch. Clearly, this leads to the existence of a large number of read-out channels, which disagrees with the last requirement. Therefore, in order to find the optimal detector parameters for the Trigger Tracker, a broad R&D programme has been performed (see Section 3.4).

3.2 Silicon microstrip detectors

Modern silicon microstrip detectors can determine the passage of a particle through the detector with an accuracy of a few microns. They are radiation-hard detectors with a small thickness and a fast response time compared to other detector technologies. Therefore, silicon microstrip detectors are widely used in particle physics experiments.

3.2.1 Principles of operation

Silicon, a semiconductor, can be fabricated as n-type with a surplus of electron sites in the crystal lattice, and as p-type with a deficit of electron sites in the crystal lattice. In the n-type semiconductor, the electrons act as free charge carriers, while the positively charged holes act as free charge carriers in the p-type semiconductor. When a p-type semiconductor is joined together with an n-type semiconductor, a p-n junction is formed. At this junction, electrons start to diffuse into the p-region and holes into the n-region, where they recombine. This migration leaves a region of net charge of opposite sign on each side, called the depletion region. As a consequence, an electric field directed from the n-side towards the p-side appears in this region. It forms an electrical barrier of the order of a few hundred millivolts, which prevents further diffusion of carriers between the p-type and n-type semiconductors. The depletion region is a nonconducting layer, which is almost fully depleted of charge carriers. By manipulating this non-conductive layer, p-n junctions are commonly used as diodes.

When an ionising particle passes through a silicon layer it creates electron-hole pairs. In the depletion region, these charge carriers are accelerated in the electric field and generate an electric current which can be detected. However, the detection efficiency is rather limited due to the small thickness of the depletion region which is usually about a few μm. The charge carriers created in the non-depleted region by the ionising particle recombine with free carriers and cannot be detected. By applying a reverse-bias voltage to the p-n

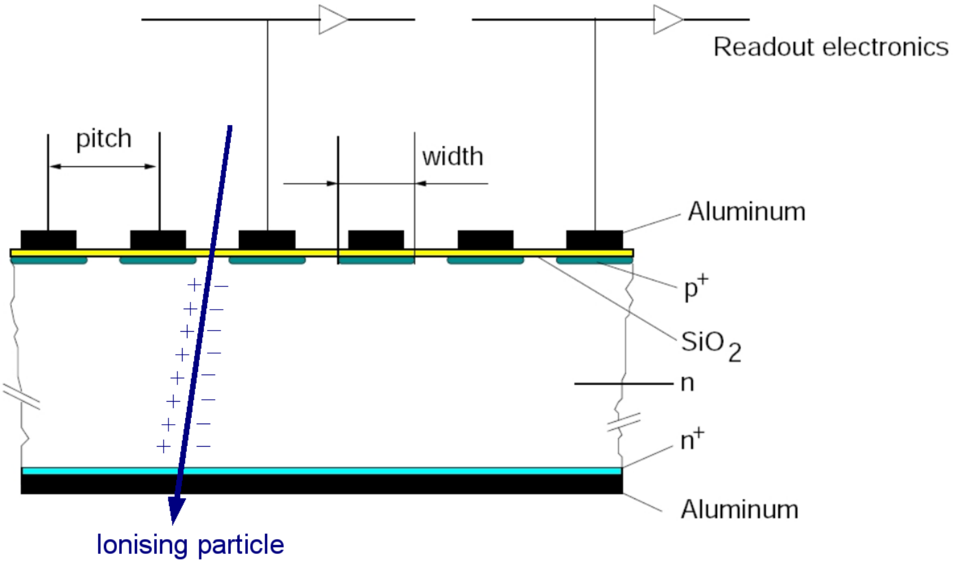

Figure 3.1: *A cross section of a single-sided silicon microstrip detector. Typical dimensions for these detectors are the following: the strip pitch varies between 20 μm and 250 μm, the strip width varies between 10 μm and 70 μm and the thickness varies between 200 μm and 1000 μm. The exact parameters of the silicon microstrip detectors used in the LHCb Trigger Tracker are given in the Section 3.3.1.*

junction, the depletion region can be increased to the full thickness of the silicon layer. This significantly improves the detection capability.

The single-sided silicon microstrip detectors used in the LHCb Trigger Tracker are 500 μm thick *p*-*n* junction diodes operating with reverse-bias voltage. In order to measure the position of the particle intersection with the detector with high precision, one side of these detectors is segmented into many parallel strips which are read out individually. Figure 3.1 illustrates a cross section of such a device. As can be seen, the strip geometry is formed by *p*-type implants on the upper side. The bulk material of the detector is a high-resistivity *n*-type silicon wafer. The *p*-*n* junction is formed between the segmented implants and the bulk. In the detector, the holes are collected by the negatively charged *p*-type strips, while the electrons are collected by the positively charged aluminium backplane. An additional n^+ layer on the backplane enables a high ohmic contact between the silicon bulk and the aluminium. The front-end electronics is connected to the aluminium strips located just above the *p*-type strips, which are separated by a thin isolating layer consisting of SiO_2 and Si_3N_4 (AC coupling). This dielectric structure introduces a coupling capacitance on the detector that prevents saturation effects in the readout electronics which exist due to high leakage currents[2]. The holes collected by the *p*-type strip induce

---

[2] This current flows through the *p*-*n* junction mostly due to the thermal excitations of electrons.

a measurable charge on the corresponding aluminium strip which is then processed by the readout electronics. The reverse bias is applied by grounding the p-type strips and supplying a positive voltage to the backplane.

3.2.2 Signal and Noise generation

Signal

The mean energy required to produce an electron-hole pair in silicon is 3.62 eV. The energy deposited by a minimum ionising particle (MIP) traversing a silicon layer follows a Landau distribution. According to the Bethe-Bloch formula for energy loss of ionising particles, the mean value for the energy loss of a MIP traversing silicon bulk is 270 eV/μm. This means, that around 37 000 electron-hole pairs will be created by a MIP passing through 500 μm of silicon.

After the generation of electron-hole pairs by the ionising particle, the created charge carriers drift towards the anode (backplane) or the cathode (p-strips). During their drift, electrons and holes do not exactly follow the electric field lines, since they are diffused by multiple collisions in the crystal lattice. The drift time of the carriers (i.e. the charge collection time) can be calculated as:

$$t_{\mathrm{drift}} = \frac{d_{\mathrm{drift}}}{v_{\mathrm{drift}}} = \frac{d_{\mathrm{drift}}}{\mu(|\vec{E}|,T)\cdot|\vec{E}|} \quad , \tag{3.1}$$

where d_{drift} is the drift length in the silicon bulk, v_{drift} is the drift velocity of the charge carriers, which is equal to the product of the electric field strength, $|\vec{E}|$, and the mobility of the charge carrier, μ. The latter depends on the electric field strength and the temperature of the silicon. For an electric field strength of 0.5 V/μm at a temperature of 10° C, the mobility of electrons and holes is 7×10^5 μm^2 V^{-1}ns^{-1} and 2.5×10^5 μm^2 V^{-1}ns^{-1}, respectively. For a drift length of 500 μm this results in a drift time of 7.1 ns for electrons and 20 ns for holes [48, 49].

According to the Shockley-Ramo theorem [50], the induced current on the detector electrodes due to the movement of the carriers can be calculated as:

$$I = q\vec{v}_{\mathrm{drift}}\cdot\vec{E}_w \quad , \tag{3.2}$$

where $\vec{E}_w$ is the weighting field which describes the geometrical coupling between the moving carrier and the corresponding electrode. The drift velocity $\vec{v}_{\mathrm{drift}}$ for both electrons and holes depends on the location of the charge carrier, which consequently depends on time: $\vec{v}_{\mathrm{drift}} = \vec{v}_{\mathrm{drift}}(\vec{x}(t))$. The induced current is much smaller in case the MIP traverses the detector in the interstrip region than in case it traverses the detector in the region below the strip, since the drift velocity of the created carriers is much larger in the region below the strip than in the interstrip region [49]. Typical values of the induced current on the detector electrodes are around few hundred nanoamperes.

Noise

Since there is no charge multiplication in a silicon microstrip detector, it is necessary to minimise the noise in the readout electronics in order to provide an efficient signal detection. The two main noise contributions for silicon microstrip detectors are:

- **Thermal or Johnson noise**. This noise is typical for any resistor. It is generated by the thermal agitation of electrons in a conductor. The variance of the noise potential for a conductor with a resistance R can be given by

  $$U^2_{\text{thermal}} = 4kTR\Delta f \quad , \tag{3.3}$$

  where k is the Boltzmann constant, T is the resistor's temperature and Δf is the bandwidth over which the noise is measured.

  In case of silicon microstrip detectors, the noise is measured by a charge-sensitive amplifier in number of electrons. Therefore, the noise is typically presented in terms of equivalent noise charge (ENC), which is given as:

  $$\text{ENC}_{\text{thermal}} = C_{\text{T}} \cdot U_{\text{thermal}} = 2C_{\text{T}}\sqrt{kTR\Delta f} \quad . \tag{3.4}$$

  As can be seen, the power of the thermal ENC linearly depends on the total capacitance C_{T} at the input of the charge amplifier. Obviously, in order to decrease the noise level one should try to reduce the capacitance, which means reducing the length of the readout strips. Another way to suppress this noise is to make the signal response slower. This allows to decrease the bandwidth and thus the thermal noise.

- **Shot noise**. This noise, which occurs in any electronic device, originates from random fluctuations of the electric current in a conductor. It is caused by the fact that the current is carried by discrete charges. In a silicon microstrip detector, shot noise is generated by a leakage current flowing through the *p*-*n* junction. Therefore, the leakage current must be minimised to decrease the noise in the detector. Shot noise is a statistical process following a Poisson distribution. The current fluctuations have a standard deviation of

  $$\sigma_I = \sqrt{2eI\Delta f} \quad , \tag{3.5}$$

  where I is the average leakage current.

3.3 Trigger Tracker detector design

3.3.1 Detection layers and detector modules

The Trigger Tracker consists of four planar detection layers of silicon microstrip sensors that cover the complete LHCb acceptance of 300 mrad in the horizontal plane, and

Table 3.1: *Basic parameters of the silicon sensors used in the Trigger Tracker.*

Technology	p^+-on-n
Thickness	$500\,\mu$m
Overall width	96.344 mm
Overall length	94.326 mm
Active width	93.906 mm
Active length	91.6 mm
Number of readout strips	512
Readout strip pitch	$183\,\mu$m
Implant strip width	$46\,\mu$m
Aluminium strip width	$58\,\mu$m

250 mrad in the vertical plane. As in the IT and OT, the layers are arranged according to the x–u–v–x configuration: the first and the last layer have vertical strips (x layers), while the second (u layer) and third (v layer) have strips which are rotated by an angle of $+5^\circ$ and -5°, respectively. In contrast with the T1–T3 stations, the four detection layers of the Trigger Tracker are assembled into two pairs — TTa and TTb half-stations — separated by a gap of 27 cm along the beam axis. This design allows to perform rough measurement of the slope of charged particles after RICH1. The first two layers (TTa) are centered around z=2350 mm downstream of the pp interaction region, while the last two layers (TTb) are centered around z=2620 mm. A detailed description of the detector layout can be found in Ref. [51].

The basic detector unit of the Trigger Tracker is the half-module. It is a ladder consisting of seven $500\,\mu$m thick silicon sensors and a baseplate located at one end of the half-module to support the readout hybrids. The baseplate is made out of aluminium nitride to match the thermal expansion coefficient of the baseplate to the sensors. To provide mechanical stability two carbon fibre rails are glued along the sensor edges. A Kapton cable runs over the back of the half-module to supply the sensors with bias voltage. The silicon sensors used in the Trigger Tracker are purchased from Hamamatsu Photonics (Shizuoka, Japan). Their basic parameters are summarised in Table 3.1.

Charge particle fluxes of about $5\times10^5\,\mathrm{cm}^{-2}\mathrm{s}^{-1}$ are expected in the innermost region of the Trigger Tracker around the beam pipe, while at the edge of the detector it is predicted to be 100 times less. By bonding the strips on adjacent sensors the half-module are segmented into several readout sectors. This allows to limit the hit occupancy and to decrease the total load capacitance at the input of a readout amplifier. There are two different types of half-modules: LMK and LM half-modules. The LMK half-modules are placed in the innermost part of the detector around the beam pipe, where the occupancy is highest. In these half-modules, the seven silicon sensors are electronically divided into three independent readout sectors: an outer four-sensor long readout sector, an intermediate two-sensor long readout sector and an inner readout sector consisting of a single silicon sensor. The LM half-modules are placed outside the beam pipe region. These half-modules are electronically divided into two readout sectors: an outer four-sensor long readout sector and an inner three-sensor long readout sector. The 512 strips of each readout sector are independently read out by a front-end hybrid located at the end of the half-module. This leads to two (three) stacked readout hybrids for the LM (LMK) half-module. Each readout hybrid consists of four Beetle chips and several blocking capacitors and resistors, seated on a polyimide print. The prints are laminated on a substrate: aluminium nitride ceramics for the lowest level and copper plates for the upper levels. The staggered readout hybrids are separated by 2.5 mm high copper supports for thermal conductance. The four-sensor readout sectors are directly connected to their front-end readout hybrids via pitch adapters[3]. In order to connect the three-sensor and two-sensor readout sectors of the LM and LMK half-modules to the corresponding readout hybrids an interconnect Kapton cable with a length of 39.1 cm is used. A similar cable but with a length of 58 cm is employed to connect the one-sensor readout sectors of the LMK half-modules to their readout hybrids. The interconnect Kapton cable has a thickness of 0.010 cm and a width of 6 cm and carries 512 signal lines with a fan-in section which reduces the sensor pitch of $183\,\mu$m to the $112\,\mu$m pitch of the cable. An isometric drawing of the LM half-module is shown in Fig. 3.2, while Fig. 3.3 illustrates a cross section of the interconnect Kapton cable. Photographs of assembled LM and LMK half-modules can be seen in Fig. 3.4 and Fig. 3.5.

The total load capacitance at the input of the readout amplifiers depends on the length of the readout strips and on the length of the connected cable. Table 3.2 lists the total load capacitance for the different readout sectors.

In order to cover the full height of the Trigger Tracker in the areas to the left and to the right of the beam pipe, two half-modules are glued together. The resulting full module consists of 14 silicon sensors and is equipped on both ends with readout hybrids, which are situated outside the active area of the experiment. In TTa, both detection layers consist of 14 full modules and two half-modules positioned above and below beam pipe. In TTb, 16 full modules plus two half-modules above and below beam pipe cover each of the two detection layers. Figures 3.6 and 3.7 illustrate the layout for each of the four detection layers of the Trigger Tracker, where the different readout sectors along the detector modules are indicated by different shadings.

Since the overall width of the silicon sensors is 96.344 mm and their active area is only 93.906 mm, there is a 1.219 mm wide inactive region on each side of the sensor, which is where the guard and bias rings are located. In order to avoid dead regions in

---

[3] Ceramic pitch adapters are used to convert the input pitch of the Beetle chips to the strip pitch of the sensors and the pitch of interconnect Kapton cables.

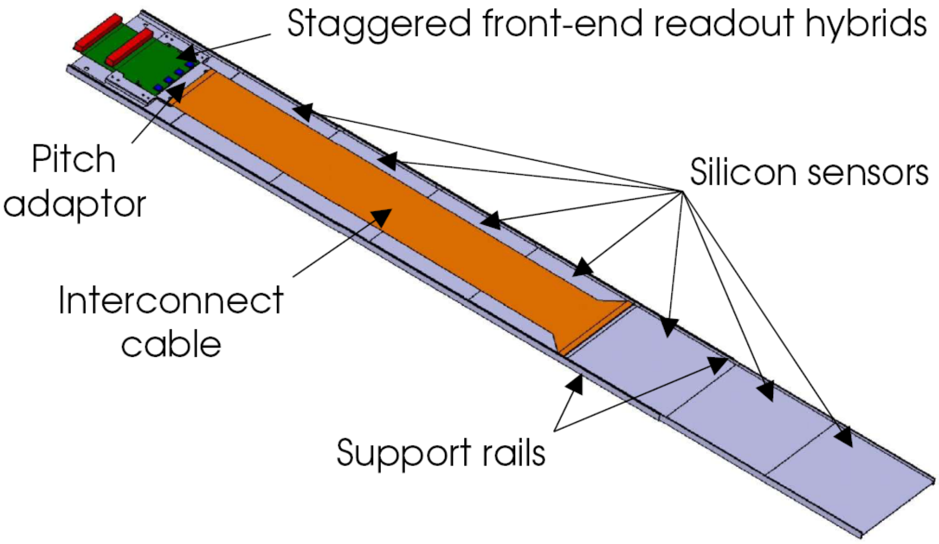

Figure 3.2: *Isometric view of an LM half-module. For a LMK half-module, there are three staggered readout hybrids and two interconnect Kapton cables employed to read out the two-sensor and one-sensor long readout sectors.*

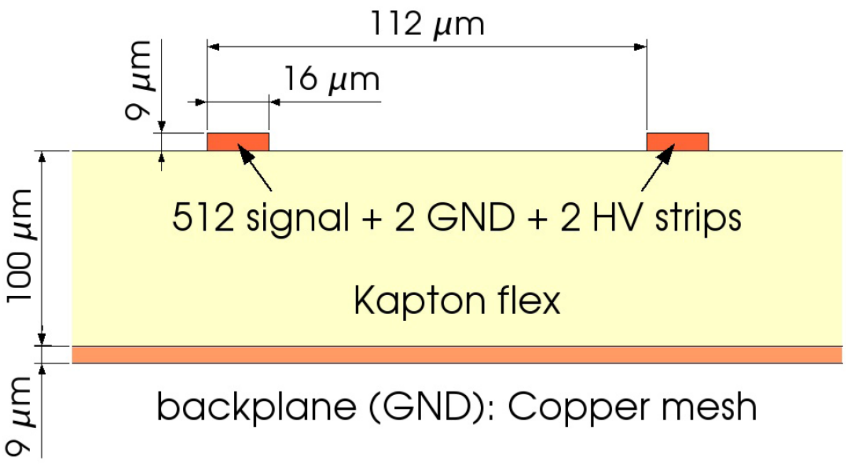

Figure 3.3: *Cross section of an interconnect Kapton cable.*

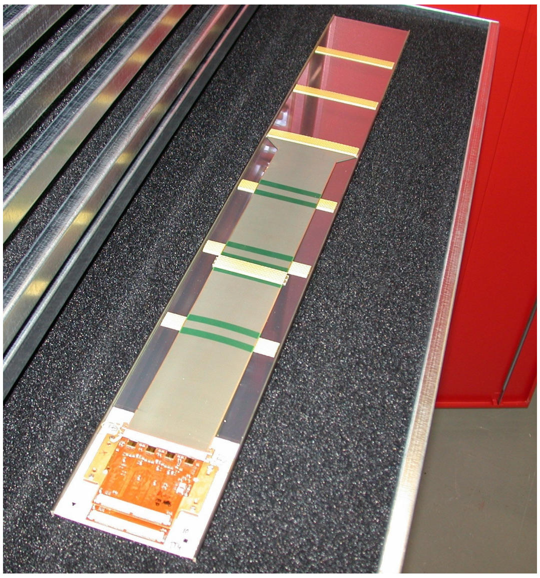

Figure 3.4: *Photograph of an assembled LM half-module.*

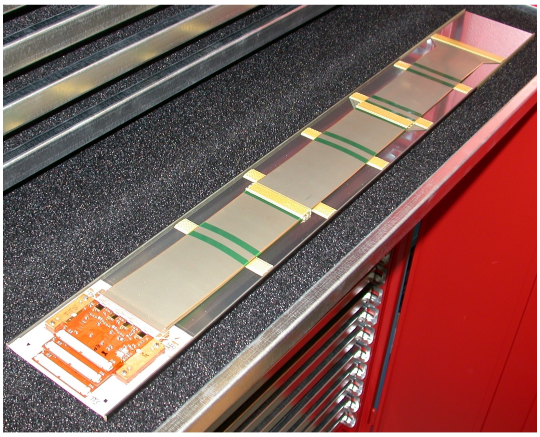

Figure 3.5: *Photograph of an assembled LMK half-module.*

Table 3.2: *Total load capacitance for different readout sectors. Here, the length of the readout strips for a single silicon sensor is assumed to be 9.44 cm. This is a conservative estimate for the physical length of the sensor [52].*

Readout sector	Readout strip length [cm]	Cable length [cm]	Capacitance [pF]
four-sensor	37.76	—	54.9
three-sensor	28.32	39.1	57.3
two-sensor	18.88	39.1	44.1
one-sensor	9.44	58.0	38.4

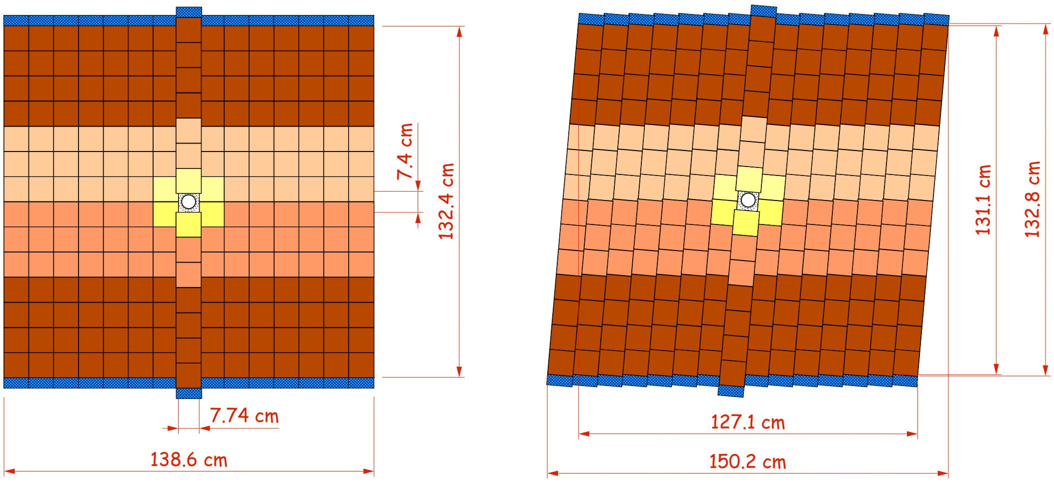

Figure 3.6: *Layout of the x (left) and u (right) layers of TTa as seen from the back.*

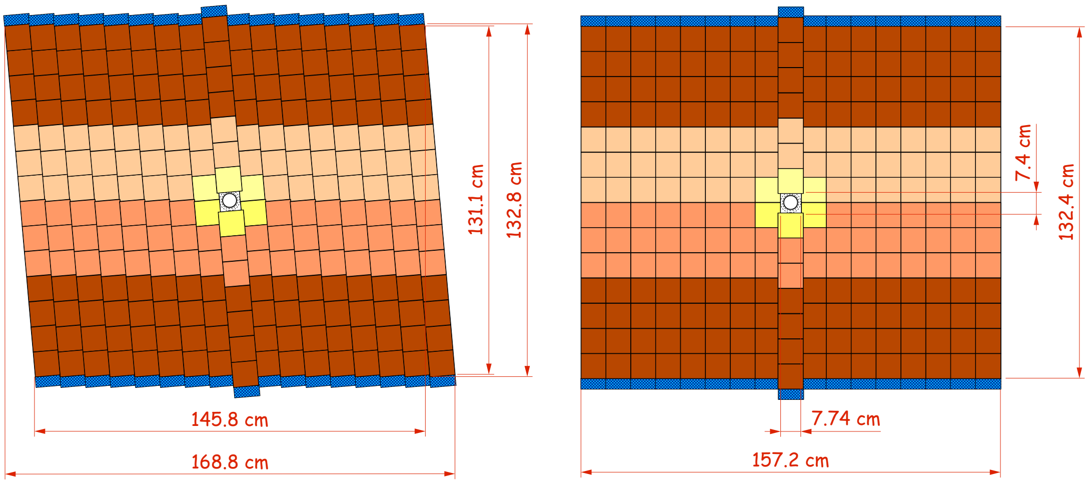

Figure 3.7: *Layout of the v (left) and x (right) layers of TTb as seen from the back.*

the detector acceptance, adjacent modules within a detection layer are staggered. The two innermost half-modules directly above and below the beam pipe have an overlap of 9.5 mm with the neighbouring full modules as measured from edge to edge of the active area. The overlap for the other full modules is 3.5 mm for the first three full modules to the left and to the right of the beam pipe and 4.0 mm for full modules farther away from the beam axis. The distance in z between adjacent full modules within a detection layer is 4.5 mm with the exception of the two half-modules above and below the beam pipe which

Table 3.3: *Main detector parameters of the Trigger Tracker.*

Number of silicon sensors	896
Number of the LM half-modules	104
Number of the LMK half-modules	24
Number of readout sectors	280
Number of readout channels	143 360
Total active area (including overlaps)	7.7 m^2

are positioned 12 mm apart from the neighbouring full modules. Table 3.3 lists the main detector parameters of the Trigger Tracker.

3.3.2 Detector box

The silicon microstrip detectors should be kept at a temperature below 5° C in order to keep leakage currents at an acceptable level. Therefore, the detection layers of the Trigger Tracker are enclosed in a common thermally-insulating box that also provides electrical and optical shielding and mechanical support.

An accurate positioning of the silicon modules inside the detector box is achieved by mounting the baseplate of each half-module onto a balcony. The balconies are 135 mm long, 85 mm wide and 5 mm thick aluminium blocks which are located outside of the detector acceptance. They are vertically mounted onto the cooling plate. Hence, the balconies provide thermal contact between the readout hybrids and the cooling plate.

In the Trigger Tracker, there are in total four cooling plates which are placed at the top and at the bottom and are attached to the outer walls of the detector box. The cooling plate is an 8 mm thick aluminium plate with a dimension of 897 mm×348 mm containing the cooling ducts in which the liquid coolant C_6F_{14} is circulating at a temperature of $-15°$ C. Figure 3.8 shows an isometric drawing of the cooling plate.

To increase the efficiency of the cooling of the detector volume, the Trigger Tracker contains four additional cooling elements which are made out of copper with a cooling duct length of about 6 m. They are attached to the left and right side walls of the detector box. In addition, the box is continuously flushed with dry nitrogen to avoid condensation on the cold surface.

The insulating walls of the detector box are manufactured out of 40 mm thick Airex foam that is clad with Kevlar and aluminium foils on both sides. Insulation around the beam pipe hole is provided by a so-called beam pipe jacket that consists of the same

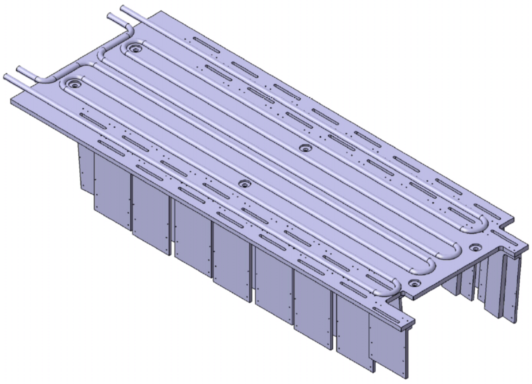

Figure 3.8: *Isometric view of the cooling plate. The balconies that are vertically mounted onto the cooling plate are displayed.*

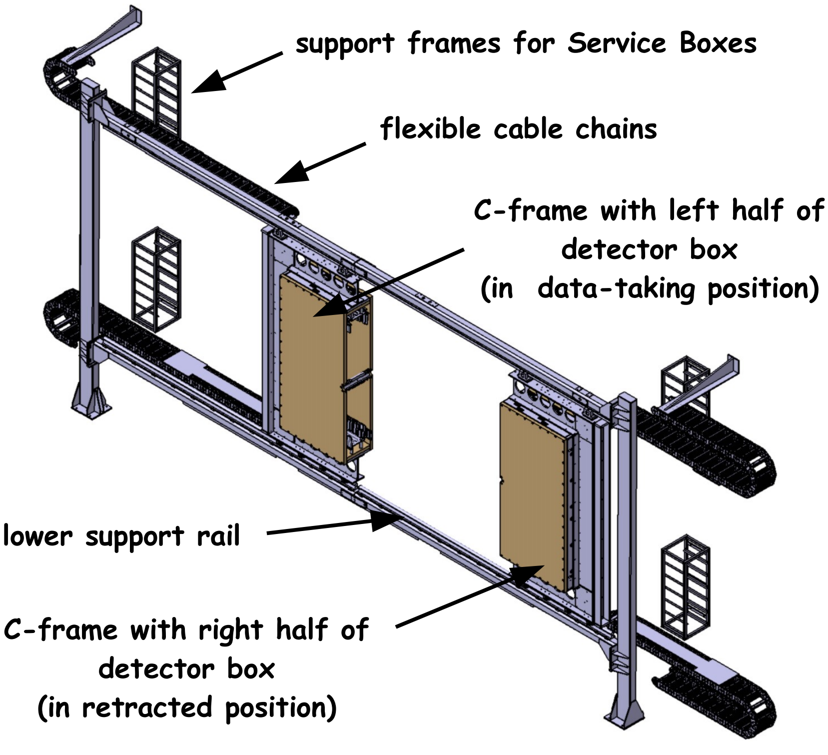

Figure 3.9: *Isometric view of the Trigger Tracker box. The flexible cable chains used to bring signals from the readout hybrids to the service boxes, where they are further processed, are displayed.*

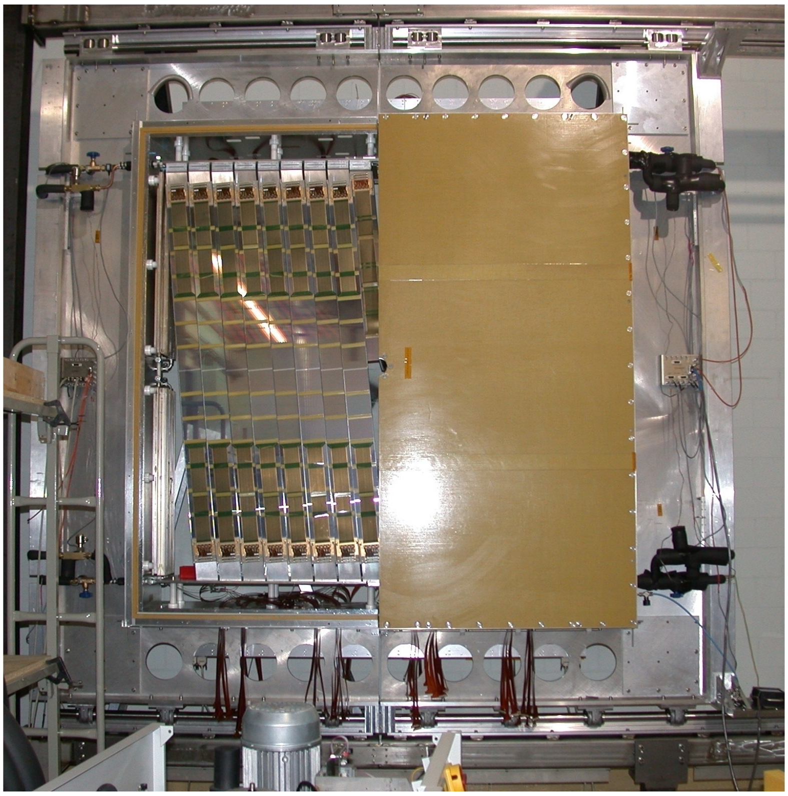

Figure 3.10: *Photograph of front view of the Trigger Tracker with an assembled u-layer.*

material as the walls. The side walls of the box are made out of honeycomb structures with aluminium covers.

The Trigger Tracker frame is located completely outside the LHCb acceptance and is made out of aluminium with a thickness of 1.5 cm. It consists of two C-shaped frames used to support the whole detector box. They are mounted onto precision support rails positioned above and below the detector. The C-frames are supported at the bottom by ball bearings. Hence, the Trigger Tracker can horizontally be split into two movable halves which can be retracted away from the LHC beam pipe as shown in Fig. 3.9. This is needed for detector maintenance.

It should be noted that the Trigger Tracker follows the beam pipe inclination of 3.6 mrad. Its total weight excluding supporting rails and flexible cable chains is approximately 500 kg. Figure 3.10 illustrates a photograph of the front view of the Trigger Tracker with an assembled u-layer.

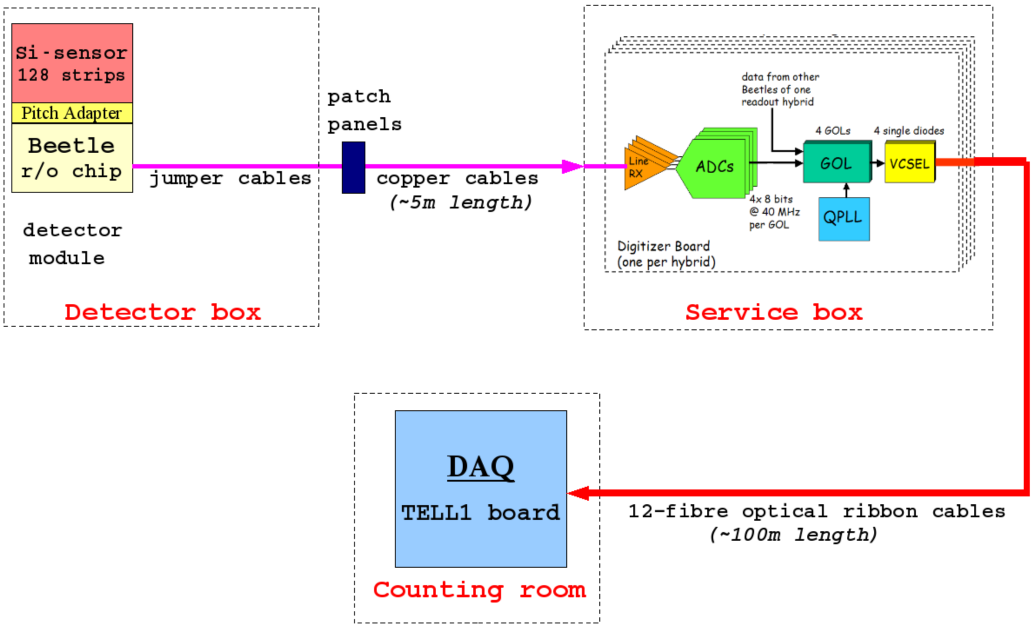

Figure 3.11: *The readout scheme of the Trigger Tracker.*

3.3.3 Readout electronics

The Beetle front-end chip [53] has been developed by the ASIC-laboratory of the University of Heidelberg for the LHCb experiment and is used to read out the silicon microstrip detectors in the VELO, Trigger Tracker and IT. The Beetle has been designed in 0.25 μm CMOS technology and complies to the requirements of the LHCb trigger and readout scheme. The chip is radiation hard to an accumulated dose of more than 100 Mrad. It integrates 128 channels, each consisting of a low-noise, charge-sensitive preamplifier, a CR-RC pulse shaper and a pipelined buffer. The shaper output is sampled with the LHC bunch crossing frequency of 40 MHz into the analogue pipeline memory of the Beetle, where the charge information for each channel of the last 160 bunch crossings is stored. Four ports of the Beetle allow to read out the multiplexed analogue data from all 128 channels within 900 ns, compatible with a maximum Level-0 trigger rate of 1.1 MHz. The chip provides a signal rise time well below 25 ns and as a result, the signals can be associated to their corresponding bunch crossings. The remainder of the peak voltage after 25 ns can be adjusted to less than 30% for load capacitances below 35 pF [53].

Trigger Tracker readout scheme is shown in Fig. 3.11. The 50 cm long jumper cables[4] are used to connect the readout hybrids to the patch panels located outside the detector

---

[4] These are flexible double-layer 0.25 mm thick cables that are made out of polymide.

box. From here, the analogue output data of the Beetle is transmitted via approximately 5 m long low-mass copper cables to a service box that is located close to the detector in an area of moderate radiation load. In the service box, the analogue data is first amplified by line receivers and then, is digitised using fast 8-bit ADCs operating at 40 MHz. At the next stage, the digital data is transmitted to Gigabit Optical Link (GOL) chips [54], which are radiation-hard gigabit serialisers developed at CERN. The laser driver in the GOL chip controls a VCSEL diode which transmits the digitised and multiplexed data at 1.6 Gbit/s via optical fibres. Commercial 12-fibre optical ribbon cables are used to bridge the approximately 100 m distance to the LHCb counting room, where an optical receiver card carrying a commercial 12-channel parallel optical receiver and commercial Gbit demultiplexers provides the interface to the TELL1 readout board. The TELL1 is the data acquisition board of the LHCb experiment, which provides data formating, event synchronisation, a large network interface buffer and other features.

In total, 48 TELL1 boards and 24 service boxes are used to read out the Trigger Tracker. A single TELL1 board can process the data from 6 readout hybrids (i.e. from 24 Beetles). Each service box contains 12 digitiser boards. Each of them processes the analogue data from one readout hybrid (i.e. from 4 Beetle chips). The digitiser board contains four circuit blocks, each consisting of four line receivers, four ADCs, one GOL, one VCSEL and a QPLL clock clean-up circuit. Other elements of the service box are the backplane, which provides regulation of the supply voltages and distribution of the signals to the digitiser boards, and the control card that serves as the interface to the TFC and ECS systems[5]. A detailed description of the readout scheme of the Trigger Tracker and its main characteristics can be found in Ref. [48].

3.4 Overview of the R&D programme

In order to verify the detector concept, to optimise detector parameters and to develop the detector mechanics, an extensive R&D programme has been performed within the Silicon Tracker project. In 2003, many efforts have been made to optimise the parameters of silicon sensors and front-end electronics. Several prototype modules of single-sided silicon microstrip detectors with different sensor thicknesses, strip lengths and implant width over pitch ratios have been tested in a laboratory setup at the University of Zürich using a pulsed infra-red laser, which allows to generate charges at well-defined positions in the silicon sensors. In these studies, described in Ref. [55], the signal pulse shapes and the charge collection efficiencies of the prototype modules have been investigated as a function of different detector designs, operational parameters and the position of the

---

[5] The Timing and Fast Control (TFC) network provides the clock and the trigger signals for the LHCb detector electronics. The Experiment Control System (ECS) allows to set and read back setting of the LHCb detector electronics.

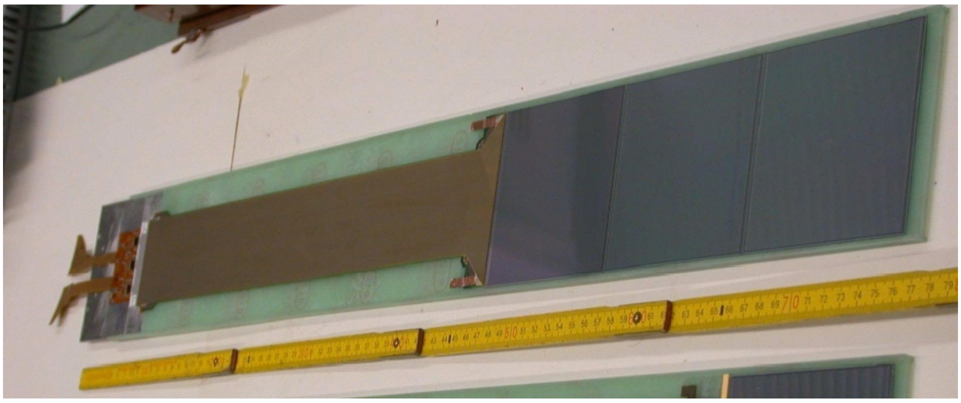

Figure 3.12: *The CMS3+Flex prototype module.*

laser beam. Later, these prototype modules have been tested at the X7 test-beam facility at CERN using a 120 GeV/c π^- beam. In this experiment, described in Ref. [56], the charge loss in the interstrip region, the signal-to-noise performance and the hit finding efficiency as a function of the interstrip position have been investigated in addition to the pulse shapes. These studies allowed to define the final thickness and the geometry of the silicon sensors for the Trigger Tracker and Inner Tracker.

Before starting the series production of the Trigger Tracker detector modules it was very important to verify the performance of the three-sensor long readout sectors of the LM half-modules, which are read out via a 39.1 cm long interconnect Kapton cables. As shown in Table 3.2, these readout sectors have the largest capacitance and thus, the largest expected noise. Therefore in 2004, a prototype module, CMS3+Flex, has been constructed, consisting of three 500 μm thick silicon sensors bonded together and read out via a 39.1 cm Kapton cable (see Fig. 3.12). The properties of this prototype module are described in Ref. [57]. In this section, the measurements performed on the CMS3+Flex module in a laser test stand and at the X7 test-beam facility at CERN using a 120 GeV/c π^- beam are briefly described.

3.4.1 Laser tests

Initial tests on the CMS3+Flex module were performed at the University of Zürich in an infra-red laser test stand. A detailed description of the setup and the results obtained in these measurements can be found in Ref. [57]. The setup comprises a pulsed 1064 nm laser diode, which allows to generate a charge inside the silicon bulk, focusing optics, which give a spot size of 13 μm, and a stepper motor, which permits the movement of the laser spot across the sensor with a minimal step size of 5 μm. The wavelength of the laser diode correspond to a photon energy of 1.165 eV which is very close to the value

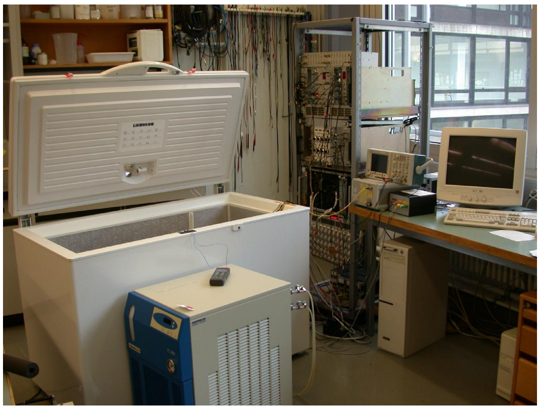

Figure 3.13: *Photograph of the laser test stand setup.*

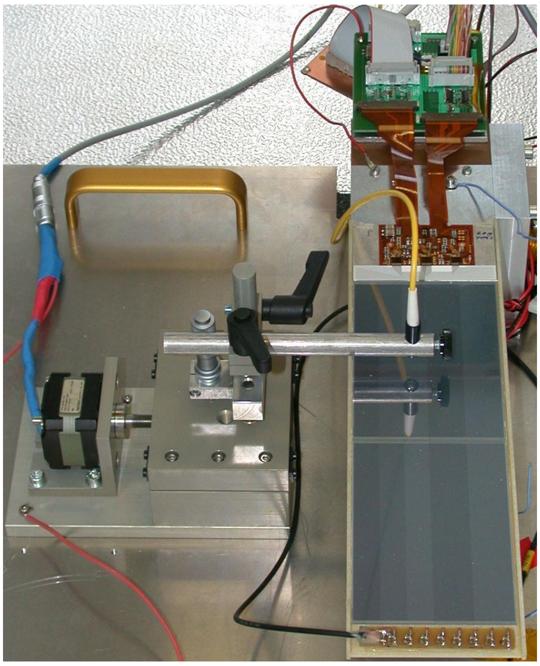

Figure 3.14: *Inside view of the freezer. On the left side is the stepper motor with the optical unit. On the right side is a test module consisting of two silicon sensors.*

of the band gap of silicon[6]. In order to provide optical shielding and a good thermal and electrical insulation from the external environment, the setup consists of a commercial freezer, which houses the prototype modules, the stepper motor and the focusing optics. A picture of the laser test stand is shown in Fig. 3.13, while Fig. 3.14 shows the inside view of the freezer. Similar setups have been widely used in the construction and testing of silicon microstrip detectors [58, 59].

At the start of the measurements the CMS3+Flex module was checked for disconnected or noisy channels. At the next step, a bias voltage scan was performed in order to investigate the dependence of the amplitude of the pulse on the applied bias voltage. For each bias voltage setting, the pulse shape scan was done by taking several runs with different delay times between the trigger signal and the Beetle sampling time, around the rough position of the signal maximum. A parabolic fit was then made to the resulting distribution of the average signal amplitude versus the delay time and the amplitude of

---

[6] If the photon energy would be higher, then the laser beam would not penetrate the full thickness of the sensor, since the photons would be immediately absorbed. The chosen wavelength of the laser allows to penetrate the full thickness of the sensor and uniformly produce charge along the beam. By tuning the intensity of the laser it is possible to change the amount of the produced charge.

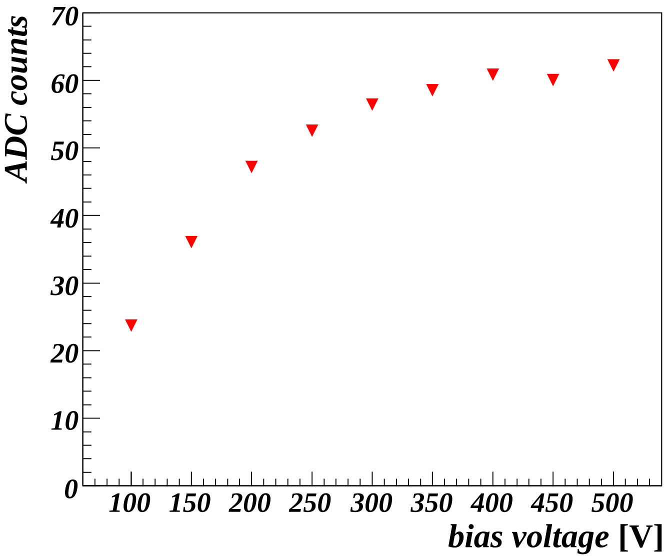

Figure 3.15: *Amplitude of the signal pulse as a function of bias voltage for the CMS3+Flex module.*

the pulse was extracted. Its dependence on the applied bias voltage is shown in Fig. 3.15. As can be seen, the signal plateau starts around 350 V. This is 110 V larger than the depletion voltage of this sensor determined from measurements of the detector capacitance as a function of the applied bias voltage [60]. This is consistent with results of previous measurements [55]. According to them, it is necessary to bias the silicon sensor around 100 V above full depletion in order to ensure full charge collection.

At the next step of the measurements, a series of pulse shape scans was performed varying the delay between the trigger signal and the Beetle sampling time in order to investigate the dependence of the pulse shape on the bias voltage, the Beetle shaping time and the position of the laser spot. A programmable parameter V_{fs} allows to adjust the signal shaping time of the Beetle chip within a certain range. Larger values of V_{fs} correspond to longer signal shaping times, while lower values of V_{fs} correspond to faster signal shaping. Examples of the obtained pulse shapes with the fastest and slowest shaping time corresponding to a V_{fs} of 0 mV and 1000 mV, respectively, can be seen in Fig. 3.16 and Fig. 3.17. The observed increase in the signal amplitude between these two scans agrees within 10% with the expected increase due to the change in gain of the Beetle preamplifier between these two V_{fs} settings [53]. In these plots the signals on the neighbouring strips are shown in addition to the signal on the strip illuminated by the laser. As in previous measurements [55, 56] it can be seen that the signals on the neighbouring strips have a different time dependence than the main strip. Both, the signal maximum and the undershoot occur earlier in time than for the main strip. This cross talk has been reproduced in a

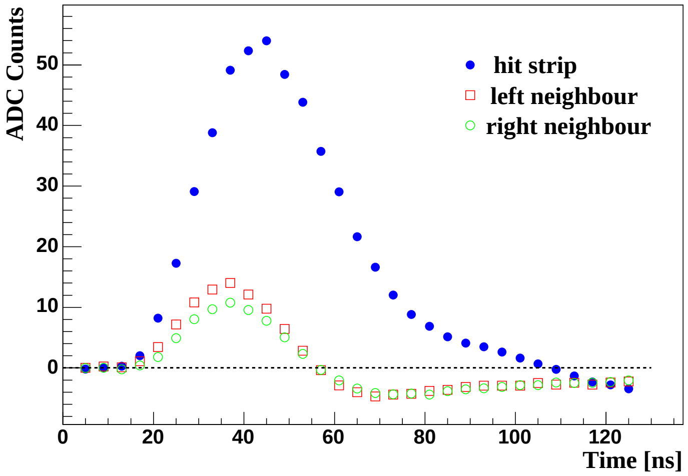

Figure 3.16: *Pulse shape scan for the CMS3+Flex module with the laser beam near the strip, bias voltage of 450 V and* $V_{\mathrm{fs}} = 0$ *mV.*

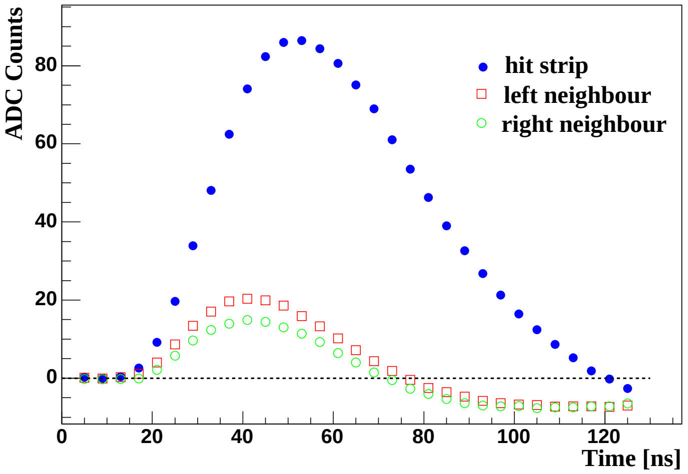

Figure 3.17: *Pulse shape scan for the CMS3+Flex module with the laser beam near the strip, bias voltage of 450 V and* $V_{\mathrm{fs}} = 1000$ *mV.*

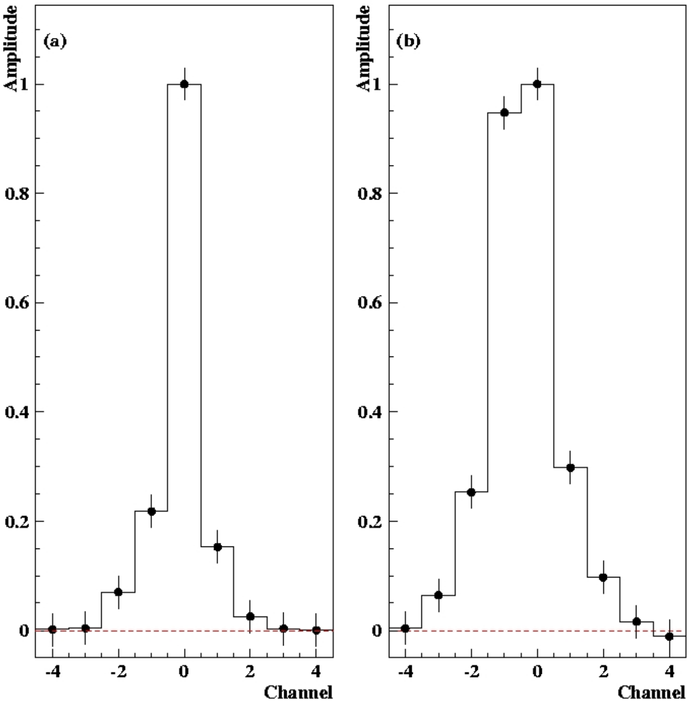

Figure 3.18: *Charge deposition shapes for the CMS3+Flex module with bias voltage of 450 V and* $V_{\rm fs} = 400$ *mV: (a) for near-strip data and (b) for mid-strip data.*

detector simulation [49] and has been shown to be due to capacitive coupling between the readout strips. The signal on the left neighbour is slightly larger than the signal on right neighbour, because the laser beam was positioned on the left side of the illuminated strip, allowing some charge sharing to this strip to occur in addition to the capacitive coupling.

In the final experiment, the level of signal cross talk is determined by the charge on the neighbouring strips at the time of the signal maximum on the illuminated strip. Figure 3.18 illustrates the relative signal amplitudes obtained when the laser beam was positioned close to the readout strip (near-strip data) and when the laser beam was positioned in the central region in between two readout strip (mid-strip data). As in previous studies [55, 56] it can be seen that the relative size of the shoulders is larger for the mid-strip data than for the near-strip data.

An important characteristic of the pulse shape for the operation of the detector in the LHC environment is the fraction of the signal left in the subsequent bunch crossing, i.e. 25 ns after the signal maximum — the signal remainder. Simulation studies have shown that a remainder below 50% is required for the Trigger Tracker. Another important characteristic of the pulse shape is the rise-time which is defined as the time from 10% to 90% of the signal maximum. Both were investigated in the laser test as a function of

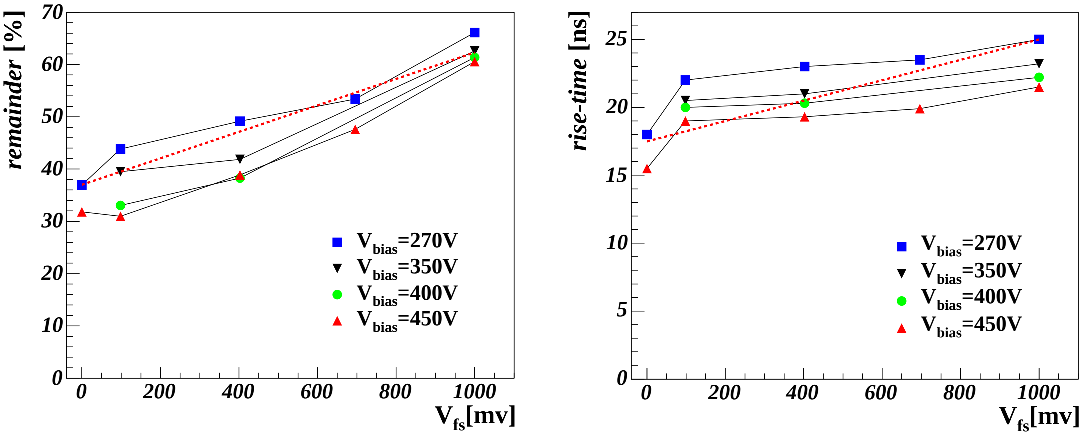

Figure 3.19: *Signal remainder (left) and rise-time (right) as a function of shaping time and bias voltage for the CMS3+Flex module. The dashed line shows the expected dependence from the measurements in Ref. [53].*

the Beetle shaping time and the bias voltage. Figure 3.19 illustrates the measured signal remainder and the rise-time as a function of the V_{fs} settings for different bias voltages. The dashed line in these figures is the expectation from front-end measurements described in Ref. [53], which were made with discrete capacitances and a δ function input signal[7]. As can be seen the signal remainder decreases as the bias voltage increases. This is due to the fact that at higher bias voltages the charge collection is faster. As expected, the remainder increases significantly with increasing V_{fs}. The smallest remainder of 31% was found for a bias voltage of 450 V and $V_{\mathrm{fs}} = 0$ mV. As in Ref. [55], the measurements of the signal remainder are found to be slightly better than expected from the front-end measurements. As can be seen the rise-time decreases with higher voltages, which is again due to the higher electric field in the sensor that results in a faster charge collection. For all settings the rise-time is less than 25 ns, meaning that no signal should be observed in the previous bunch crossing.

3.4.2 Beam test

Further measurements on the CMS3+Flex module were performed at the X7 test-beam facility at CERN, using a 120 GeV/c π^- beam. The CMS3+Flex module and other prototypes were installed in a light-tight detector box, together with a beam telescope consisting of four double-sided silicon microstrip detectors that allowed to determine the impact

---

[7] In Ref. [53] measurements were made with a load capacitance up to 50 pF. Therefore, it was necessary to extrapolate the results to the 57 pF load capacitance of the CMS3+Flex module.

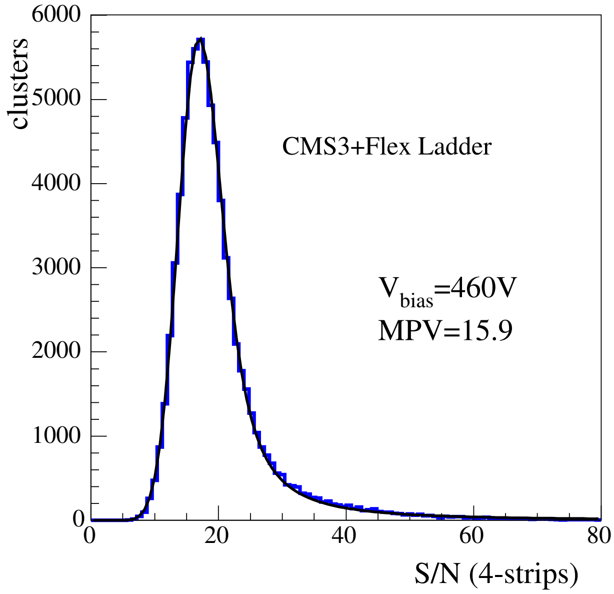

Figure 3.20: *S/N distribution fitted with a Landau distribution convolved with a Gaussian for the CMS3+Flex module.* V_{fs} *was set to 400 mV.*

point of the π^- tracks on the prototype modules with a resolution of around 14 μm. As a result, a study of the detector performance as a function of the particle impact point relative to the readout strips was performed. A detailed description of the test-beam setup and of the obtained results can be found in Ref. [61].

The goal of this test was to investigate the pulse shapes of the prototype modules, their signal-to-noise (S/N) performance and the hit finding efficiency. The results of the pulse shape studies in terms of the signal remainder and the rise-time were found to be fully consistent with the corresponding results obtained in the laser test. The S/N distribution obtained for the CMS3+Flex module is shown in Fig. 3.20. The "signal" was determined as the sum of the ADC counts on the four strips closest to the predicted particle impact point from the beam telescope, while the "noise" was taken as the single strip noise. The charge produced by a MIP traversing a silicon sensor is proportional to its energy loss, which follows a Landau distribution, while the noise variations can be well approximated by a Gaussian distribution. Therefore, the S/N distribution was fitted with a Landau distribution convolved with a Gaussian which has a standard deviation depending on noise contributions [62]. The S/N value was extracted as the most-probable value obtained from the fit. It is equal to 15.9 for the CMS3+Flex module. This result was obtained for $V_{\mathrm{fs}} = 400$ mV, which was found to be the most appropriate setting for the Beetle shaping time, providing a signal remainder below 50%, while limiting the Johnson noise which

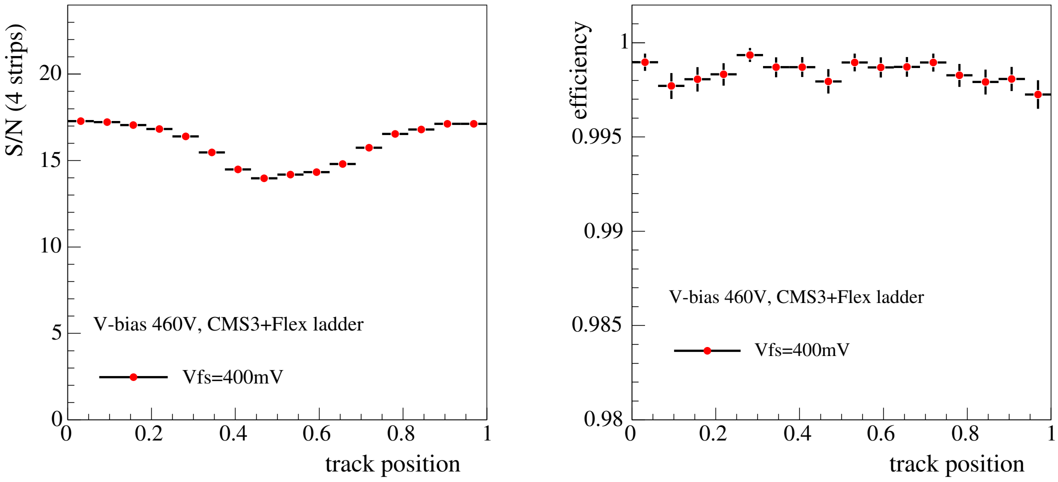

Figure 3.21: *Most probable S/N values (left) and hit finding efficiency (right) for the CMS3+Flex module as a function of the relative interstrip position of the track impact point on the sensor.*

occurs due to the high bandwidth, i.e. fast shaping (see Section 3.2.2).

The most-probable S/N values and the hit finding efficiency for the CMS3+Flex module as a function of the relative interstrip position of the track impact point on the sensor are shown in Fig. 3.21. As in previous measurements [63, 56] a substantial dip in S/N is observed in the region in between two readout strips. This effect has been seen for all tested detectors and is mainly attributed to a loss of charge carriers at the boundary between the silicon bulk and the isolating layer consisting of SiO_2 and Si_3N_4 in between two readout strips. It cannot be solved by applying a higher electric field. It was found that the relative size of the charge loss in the interstrip region is a function of the sensor geometry and depends roughly linearly on the ratio $(p-w)/t$, where t is the sensor thickness, p and w are the readout pitch and the strip width [64]. Despite the signal loss, the S/N value in the interstrip region is well above 10, which is the critical value below which the hit finding efficiency is known to be degraded [63]. Therefore, the hit finding efficiency is approximately equal to 99.8% across the entire interstrip region.

The measurements on the CMS3+Flex module in the laser test stand and at the X7 test-beam facility at CERN have tested the detector performance of the three-sensor long readout sectors, read out via a 39.1 cm long Kapton cable. The obtained results in terms of S/N and hit finding efficiency demonstrate a high detection capability of these detectors. The pulse shape characteristics meet LHCb's specifications.

Chapter 4

Quality Assurance programme for the Trigger Tracker detector modules

The series production of the Trigger Tracker detector modules was launched in September 2005 and was completed in December 2006. Including 15% spares, 148 half-modules have been produced: 116 LM half-modules and 31 LMK half-modules. A rigorous quality assurance (QA) programme has been performed to ensure that the detectors meet the mechanical and electrical requirements and to study their characteristics. All silicon sensors were qualified by the manufacturer and were additionally verified at the University of Zürich. These tests included optical inspections, measurements of the full depletion voltage and of the leakage current, searches for defective strips and metrological measurements. The quality of the sensors was found to be excellent and a very good agreement between the results obtained at the University of Zürich and the data provided by the manufacturer was observed [65]. All readout hybrids also underwent a series of control checks provided by the vendor and a further 96 hours burn-in programme, which included measurements of the power consumption of all chips, different readout tests and searches for dead channels [66]. The QA programme also included measurements of the positioning of the silicon sensors on assembled half-modules. The positioning accuracy was found to be around $8\,\mu$m, which is much better than the expected spatial resolution of about $50\,\mu$m.

A crucial role in the QA programme for the Trigger Tracker detector modules was played by the comprehensive “burn-in” test, through which each half-module passed at least once during its assembly. This chapter is dedicated to this test. First, the main goals and the measurement programme of the burn-in test are considered. Then, the experimental setup and software used to perform these measurements are described. Finally, a selection of the results is presented.

4.1 The burn-in test: goals and procedure

The production of LM (LMK) half-modules proceeded in two (three) stages. During the first production step the seven silicon sensors and the lowest readout hybrid were placed on an assembly template, the two carbon fibre rails were glued along the sensor edges, the bias voltage cable was connected to the sensors, and the readout strips and the ground connections of the four-sensor readout sectors were bonded. After this stage, the four-sensor sector was fully operational. At the next production step, the readout hybrid and a 39.1 cm long interconnect Kapton cable for the three-sensor and two-sensor readout sectors of the LM and LMK half-modules were mounted and the sensors within these sectors were bonded together. After this step, the assembly of a LM half-module was completed. For the LMK half-modules, the third (and the last) production stage was performed to attach and bond the readout hybrid and a 58 cm long interconnect Kapton cable of the one-sensor readout sector. The half-modules underwent a burn-in programme after each production step, since on a fully assembled half-module it is impossible to access, and thus to repair a lower readout hybrid.

The goal of the burn-in test was to investigate the long-term behaviour of the half-modules at different thermal conditions, to study their electrical characteristics and to search for defective channels. Moreover, this test also helped to gain experience in the use of the LHCb electronics, since it employs prototypes of readout components which will be used in the final experiment. The standard burn-in programme included:

- **Temperature cycling**. During the test, the burn-in box was several times cooled down to a temperature of around $+5^\circ$ C and warmed up to room temperature. This allowed to check the operation of the detectors at different thermal conditions. During the cycling, the half-modules were continuously biased at 500V and the leakage current for each readout sector was monitored as a function of temperature and time.

- **IV scans**. The leakage currents were additionally measured as a function of the applied bias voltage at cold and warm temperature. These measurements provide a search for the breakdown voltages of the silicon sensors.

- **Pedestal runs**. In order to investigate the noise performance of the detectors, pedestal runs were repeatedly taken at cold and warm temperatures.

- **Pulse shape scans**. Measurements of the signal pulse shapes were performed at both temperatures using an internal test pulse implemented in the Beetle readout chip and using an array of infra-red laser beams that permitted to generate charges at predefined locations on each readout sector. This allowed to verify the optimal timing settings of the readout electronics, extract the signal remainder for each readout chip and study this characteristic as a function of the temperature.

- **Charge collection scans**. At both temperatures bias voltage scans were made using the laser system to investigate the dependence of the signal amplitude on the applied bias voltage. This allowed to determine the operational voltage for each readout sector from the obtained charge collection efficiency curve.

Clearly, a huge amount of resources would be needed to carry out this measurement programme for each half-module manually. Therefore, many efforts have been made to automate the burn-in test stand. Finally, the burn-in programme was running fully automatically. This was achieved by using the LabView programming language [67]. This allowed to perform extensive and uninterrupted measurement programmes which were running even overnight and over the weekends. The need for operator intervention was limited to searching of defective channels at the beginning and at the end of the test and to exchanging the half-modules. A typical burn-in programme took around 37 hours and its time table is shown in Table 4.1. As can be seen the duration of one temperature cycle is about three hours, with the exception of the two last cycles during which the IV, pulse shape and bias voltage scans were done at warm and at cold temperature. For half-modules tested over the weekends, the measurement programme was extended to up to 70 hours by including additional temperature cycles. The collected data for each half-module was analysed and the results were stored in a central production database [68, 69].

4.2 Experimental setup and software

Up to four half-modules were tested in parallel in a light-tight and thermally insulating box which is shown in Fig. 4.1. It has a similar but down-sized layout as the Trigger Tracker detector box. The half-modules are fixed onto so-called balconies which are vertically mounted onto a cooling plate containing cooling ducts in which liquid C_6F_{14} is circulating as a coolant.

In order to investigate temperature and humidity during the temperature cycling, there are several temperature and humidity sensors inside the box: three temperature sensors are located on the cooling plate at equidistant positions along the cooling ducts, three temperature and humidity sensors are fixed on a thin rod allowing to measure the temperature and humidity in the top, in the middle and in the bottom of the box, along the tested half-modules. The two temperature sensors mounted on the inside and the outside wall of the box were used to study the thermal insulating capability of the walls. Additional temperature and humidity sensors located outside the box were employed to monitor the ambient temperature and humidity. The temperature sensors used in the burn-in test stand are DS1820 digital thermometers manufactured by Dallas Semiconductor (Dallas, USA), while the humidity sensors are HIH–3610 sensors manufactured by Honeywell (Morristown, USA). They were controlled and read out via a HA5 1–Wire host adapter manufactured by Point Six Inc. (Lexington, USA), which is directly connected to the serial port

Table 4.1: *Task list of typical measurement programme in the burn-in test stand.*

Time [h:min]	Action
00:00	set 500V
00:00	Pedestal run
00:00	Cool down
03:00	Pedestal run
03:05	Warm up
06:00	Pedestal run
06:05	Cool down
09:00	Pedestal run
09:05	Warm up
12:00	Pedestal run
12:05	Cool down
15:00	Pedestal run
15:05	Warm up
18:00	Pedestal run
18:05	Cool down
21:00	Pedestal run
21:05	Warm up
24:00	Pedestal run
24:05	Cool down
27:00	Pedestal run
27:05	Pulse shape scan
27:30	Bias voltage scan
30:00	set 500V
30:00	IV scan
30:30	set 500V
31:00	Pedestal run
31:05	Warm up
34:00	Pedestal run
34:05	Pulse shape scan
34:30	Bias voltage scan
37:00	set 500V
37:00	IV scan
37:30	set 500V

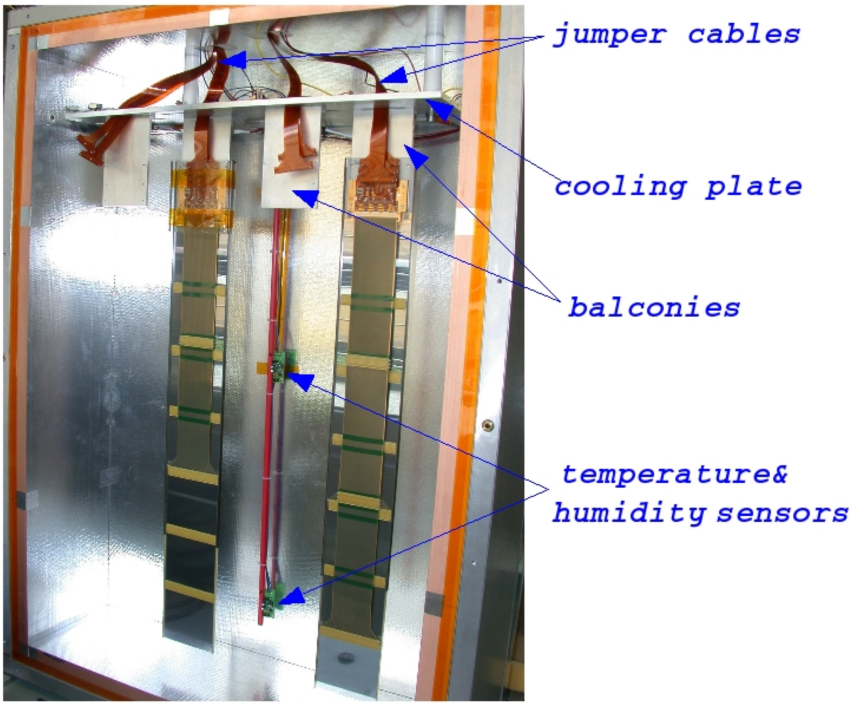

Figure 4.1: *Box of the burn-in test stand with two mounted half-modules. The front wall of the enclosure is not shown in order to display the interior of the box.*

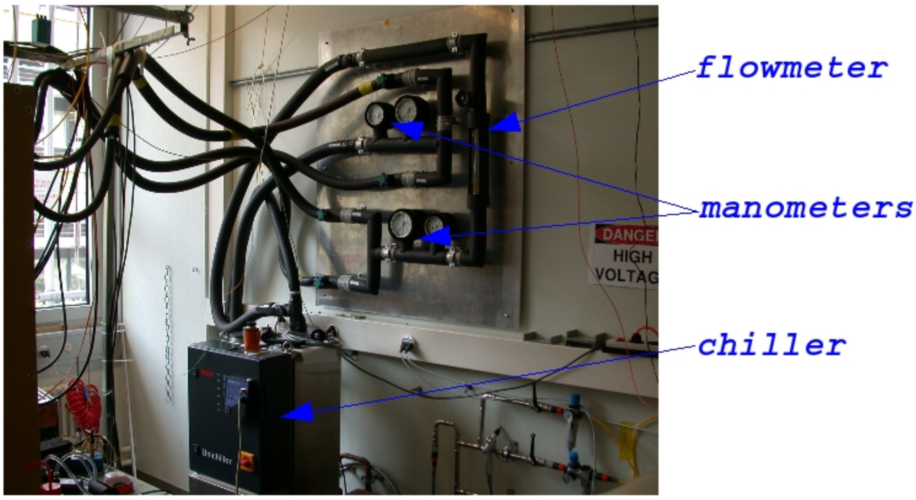

Figure 4.2: *Overview of the cooling system of the burn-in test stand.*

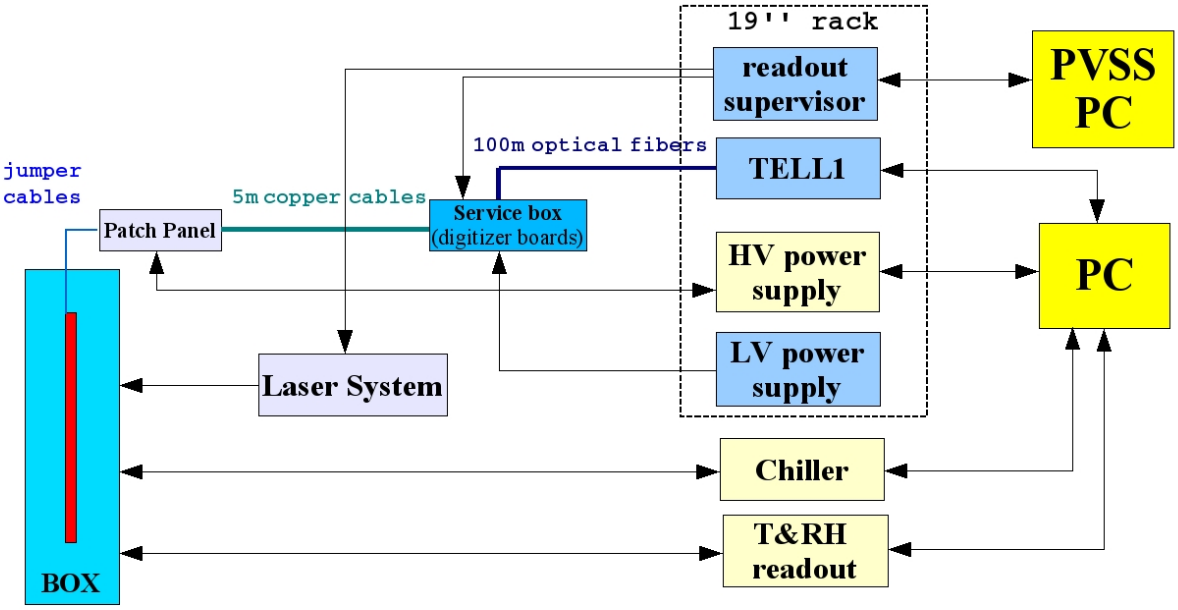

Figure 4.3: *Sketch of the burn-in test stand.*

of the PC. In order to cool down the box, the burn-in test stand is equipped with a chiller manufactured by Peter Huber Kältemaschinenbau GmbH (Offenburg, Germany). This device is connected to the box via thermally isolated hoses. As in the final experiment, the chiller was operated with C_6F_{14} as coolant. It was found that approximately one hour was needed to cool down the box from room temperature to around $+5^\circ$ C. This was achieved by setting the fluid temperature in the chiller to -20° C. The cooling system of the burn-in test stand (see Fig. 4.2) also includes manometers and a flowmeter to control and monitor the flows "in" and "out" of the chiller.

The bias voltage for the half-modules was provided by a EHQ 8006-F high voltage power supply manufactured by ISEG Spezialelektronik GmbH (Rossendorf, Germany). The supply contains 4 modules, each consisting of 8 independent channels in which a voltage of up to 600V can be set. Each channel of the power supply is equipped with a switch allowing to set a limit of up to 2 mA on the leakage current of the silicon sensors. Using approximately 5m long cables, the power supply is connected to patch panels located at the top of the burn-in box, where the high voltage is further distributed to the half-modules. The low voltage for the detector electronics is provided by a custom built 5V/50A power supply. Both power supplies are mounted in a 19" rack which also houses a 9U VME crate containing a TELL1 board and a readout supervisor [70]. The latter is a module of the LHCb TFC system, which is used to distribute the trigger signals to the digitiser boards and to the laser system in the burn-in test stand. It is controlled via

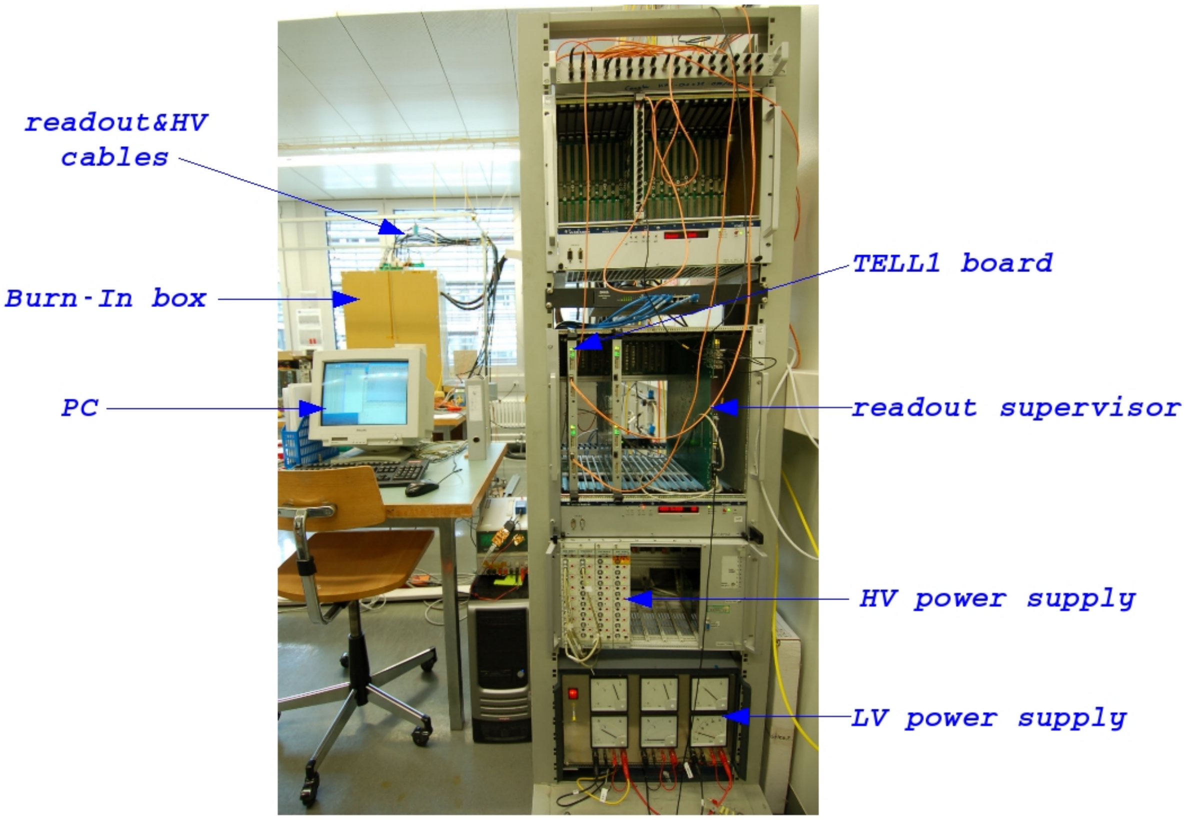

Figure 4.4: *Photograph of some components of the burn-in test stand.*

PVSS [71] running on a dedicated Linux PC. The TELL1 board is interfaced to standard Gigabit Ethernet network equipment providing up to four Gigabit Ethernet links. An overview of the burn-in stand components is shown in Fig. 4.3, while Fig. 4.4 shows a photograph of some of its components.

The custom made laser system of the burn-in stand consists of a pulsed 1064 nm laser diode with 30 mW power output and a beam splitter, which allows to split the laser beam input into eight outputs. This is needed to supply signals to all tested readout sectors simultaneously. The laser diode is triggered by the orbit signal, which is used in the readout supervisor to synchronise all TFC functions[1]. The spot size of the laser beam is about 1.6 mm allowing to illuminate eight readout strips on each readout sector. The laser beam is transmitted to the detectors via plain fibres, which are inserted into dedicated holes in the front wall of the box as shown in Fig. 4.5.

The burn-in test stand including the data taking was controlled by a LabView pro-

---

[1] The orbit signal will be used to mark a full turn in the LHC.

Figure 4.5: *Front wall of the burn-in box together with an array of plain fibres, which are inserted into dedicated holes to supply laser beams to all tested readout sectors simultaneously.*

gramme running on a Linux PC (see Fig. 4.6). It is steered by a script file in which the task list of the measurement programme is coded. This LabView programme sends the corresponding commands at the right time to LabView sub-programmes that control the readout system and the slow control components, such as high voltage power supply, chiller and temperature and humidity sensors. The graphical user interfaces of these sub-programmes are shown in Fig. 4.7 and Fig. 4.8. Each of them consists of many other LabView programmes which are used to control each component of the burn-in stand individually. The temperature and humidity sensors directly communicate with a LabView programme via a 1–Wire interface, while the chiller communicates via an RS–232 interface. The high voltage power supply is controlled via a PCI interface to CAN-bus using several C programmes. These were implemented into a dedicated LabView programme

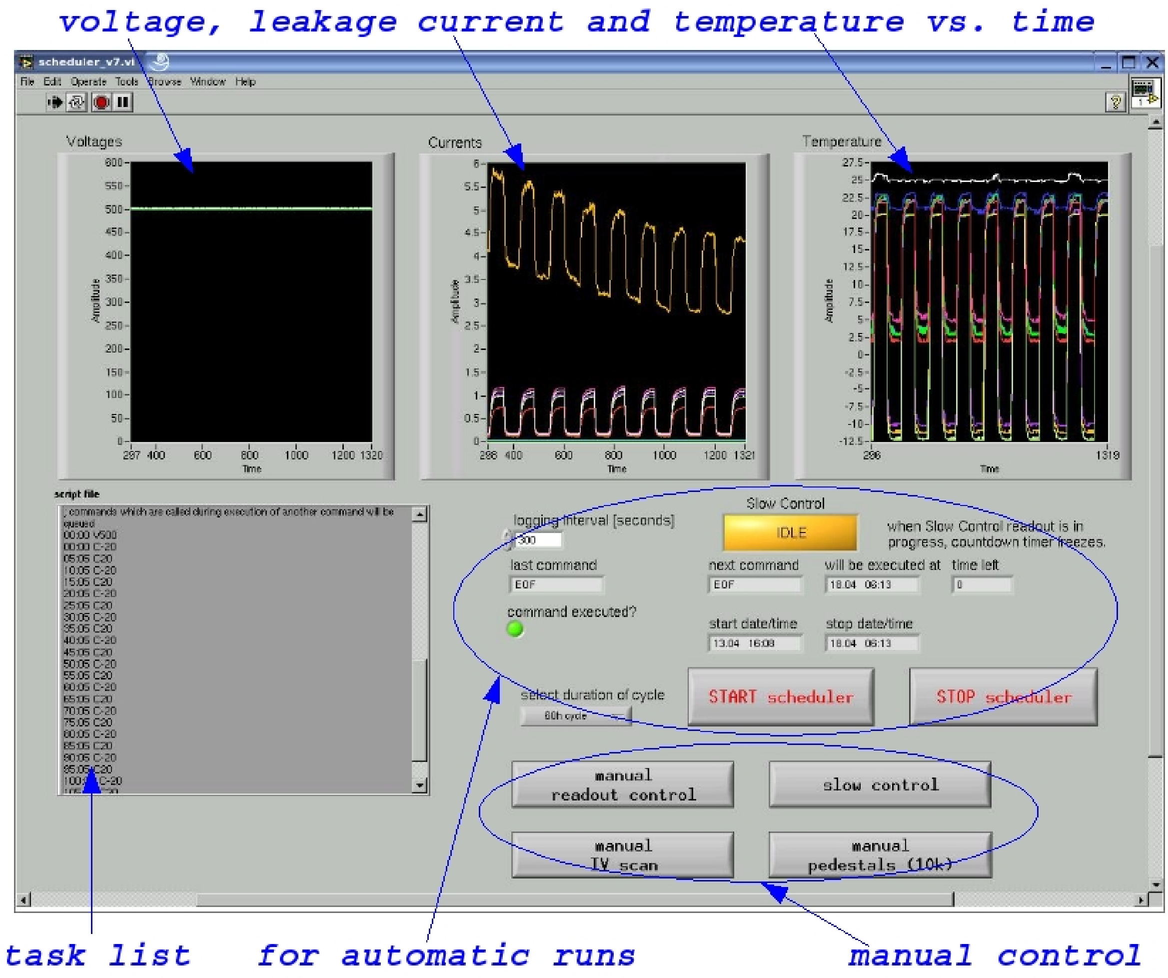

```
; commands which are called during execution of another command will be
queued
00:00 V500
00:00 C-20
05:05 C20
10:05 C-20
15:05 C20
20:05 C-20
25:05 C20
30:05 C-20
35:05 C20
40:05 C-20
45:05 C20
50:05 C-20
55:05 C20
60:05 C-20
65:05 C20
70:05 C-20
75:05 C20
80:05 C-20
85:05 C20
90:05 C-20
95:05 C20
100:[illegible] C-20
```

logging interval [seconds]: 300

when Slow Control readout is in progress, countdown timer freezes.

last command: EOF

next command: EOF

will be executed at: 18.04 08:13

time left: 0

command executed?

start date/time: 13.04 16:08

stop date/time: 18.04 08:13

select duration of cycle: 80h cycle

Figure 4.6: *User interface of the main LabView programme allowing to perform an automatic measurement programme in the burn-in test stand.*

by making use of a special feature referred to as the Call Library Function Node [72]. This mechanism allows to access external code via Dynamic Link Libraries (DLLs), which are usually called shared libraries. The same mechanism was used to control the readout system. The Beetle readout chips of the tested half-modules, the digitiser boards and the control card in the service box are controlled via an I^{2}C interface using several C programmes, which were implemented into LabView using DLLs. In addition, the C programme allowing to read out the raw data from the TELL1 board was executed via a system call introduced into another C programme, which was called by LabView via DLL.

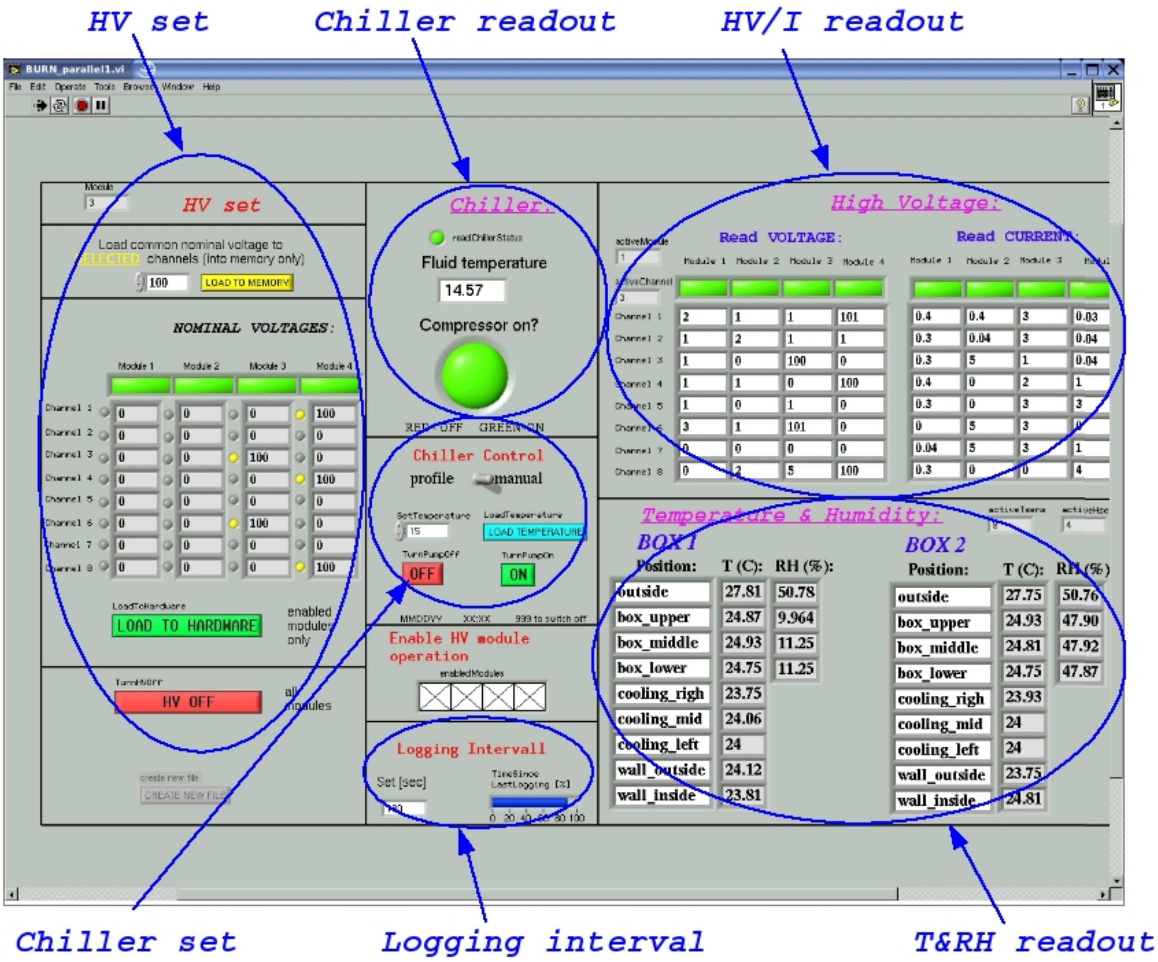

Module: 3

Load common nominal voltage to SELECTED channels (into memory only): 100

enabled modules only

all modules

	Module 1	Module 2	Module 3	Module 4
Channel 1	0	0	0	100
Channel 2	0	0	0	0
Channel 3	0	0	100	0
Channel 4	0	0	0	100
Channel 5	0	0	0	0
Channel 6	0	0	100	0
Channel 7	0	0	0	0
Channel 8	0	0	0	100

Fluid temperature: 14.57

profile / manual

SetTemperature: 15

Set [sec]: 180

activeModule: 1

activeChannel: 3

Read VOLTAGE:

	Module 1	Module 2	Module 3	Module 4
Channel 1	2	1	1	101
Channel 2	1	2	1	1
Channel 3	1	0	100	0
Channel 4	1	1	0	100
Channel 5	1	0	1	0
Channel 6	3	1	101	0
Channel 7	0	0	0	0
Channel 8	0	2	5	100

Read CURRENT:

	Module 1	Module 2	Module 3	Modul
Channel 1	0.4	0.4	3	0.03
Channel 2	0.3	0.04	3	0.04
Channel 3	0.3	5	1	0.04
Channel 4	0.4	0	2	1
Channel 5	0.3	0	3	3
Channel 6	0	5	3	0
Channel 7	0.04	5	3	1
Channel 8	0.3	0	0	4

activeTemp: 8

activeHse: 4

BOX 1

Position:	T (C):	RH (%):
outside	27.81	50.78
box_upper	24.87	9.964
box_middle	24.93	11.25
box_lower	24.75	11.25
cooling_righ	23.75	
cooling_mid	24.06	
cooling_left	24	
wall_outside	24.12	
wall_inside	23.81	

BOX 2

Position:	T (C):	RH (%)
outside	27.75	50.76
box_upper	24.93	47.90
box_middle	24.81	47.92
box_lower	24.75	47.87
cooling_righ	23.93	
cooling_mid	24	
cooling_left	24	
wall_outside	23.75	
wall_inside	24.81	

Figure 4.7: *User interface of the LabView programme for the slow control system of the burn-in test stand.*

Slow control data[2] was recorded every 5 minutes by a dedicated LabView programme. This allowed to monitor the current status of the burn-in stand and of the tested half-modules. The data acquisition of the test stand was running stably within at least several days. This has provided the possibility to carry out uninterrupted and automatic measurement programmes for the Trigger Tracker detector modules.

---

[2] This includes the temperature and humidity inside and outside the box, the fluid temperature in the chiller, the voltage and the leakage current in each channel of the power supply and the Linux time stamp.

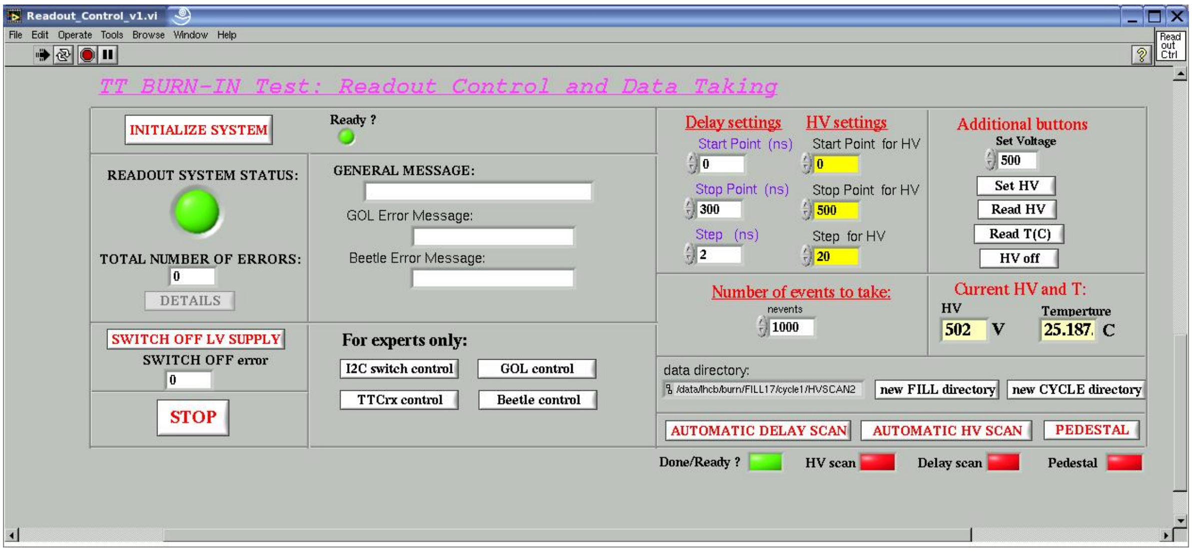

TOTAL NUMBER OF ERRORS: 0

SWITCH OFF error 0

GENERAL MESSAGE:

GOL Error Message:

Beetle Error Message:

Start Point (ns) 0

Stop Point (ns) 300

Step (ns) 2

Start Point for HV 0

Stop Point for HV 500

Step for HV 20

Set Voltage 500

nevents 1000

HV 502 V

Temperture 25.187 C

data directory: /data/lhcb/burn/FILL17/cycle1/HVSCAN2

Figure 4.8: *User interface of the LabView programme allowing to control the readout system of the burn-in test stand.*

4.3 A selection of the results

4.3.1 Fraction of defective channels

In general, three main types of defective channels of silicon microstrip detectors can be distinguished:

- **Interrupts**. These channels are interrupted due to breaks in the pitch adapter traces, missing wire bonds between a pitch adapter and a sensor or between two sensors and breaks in the aluminium strips.
- **Shorts**. This kind of defects appears when there is an ohmic connection between neighbouring channels. This can occur in the pitch adapter, wire bonds or sensors.
- **Pinholes**. These are ohmic contacts between the p-type implant and its corresponding aluminium strip. They appear due to the defects in the isolating layer consisting of SiO_2 and Si_3N_4.

As mentioned above, a searching of defective channels has been done by an operator for each tested half-module at the beginning and at the end of the burn-in programme. The defective channels were identified by analysing strip noise and pulse shapes. A clear tag for identification of interrupted channels is their low noise which is due to the reduced

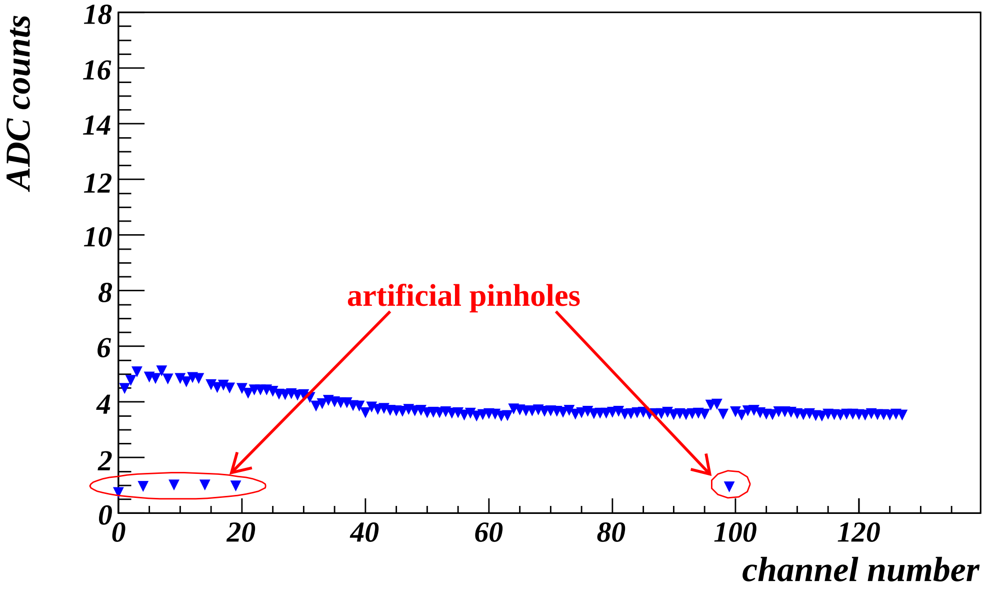

Figure 4.9: *Root-mean-square of the noise distribution for each of the 128 channels on a Beetle chip obtained with an open box. Channels with artificially introduced pinholes can be easily distinguished.*

load capacitance. In addition, these channels produce a too high amplitude of an internal test pulse. This is again due to the reduced load capacitance, that directly increases gain in the amplifier. Shorted channels were identified as pairs of adjacent channels both having too small amplitude of the internal test pulse. This can be explained by the fact that the gain in the amplifier decreases for such channels due to the increased load capacitance. When there is only one channel with a too small amplitude of the test pulse, then this channel was recognised as a failed readout channel in the Beetle chip. In order to find pinholes it was necessary to take a pedestal run with an open box. The light shining onto the silicon sensors generates leakage currents, which flow through the readout electronics when a pinhole is present. Even without applying any bias voltage to the silicon sensors, these leakage currents are so large that they saturate the front-end amplifier and as a consequence, the noise for such channels decreases significantly, as can be seen in Fig. 4.9. This gives a clear tag for the identification of pinholes.

In total, 209 defective channels were found after the testing of all produced half-modules (about 166 000 readout channels in total):

- **83 interrupts**;
- **74 shorted channels**;

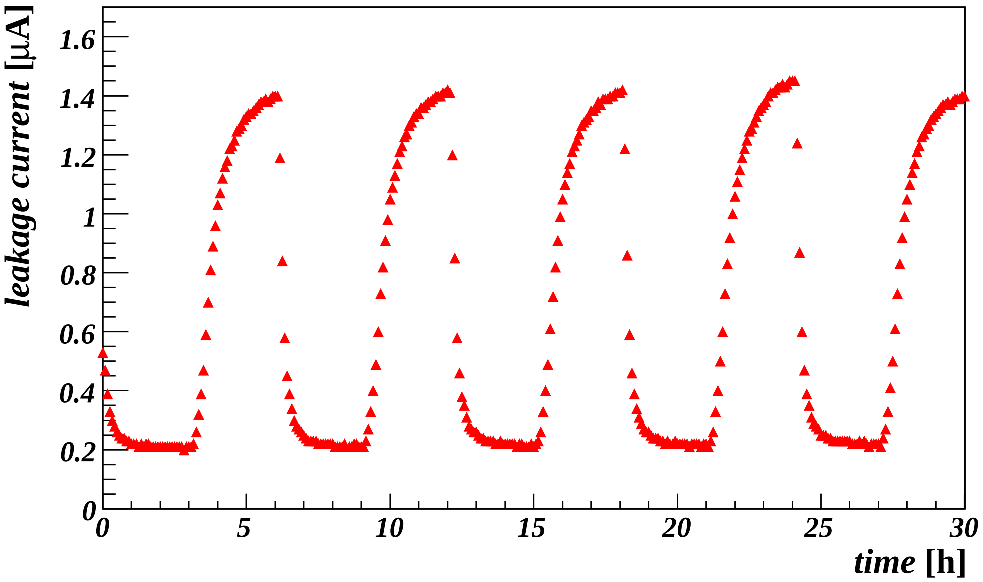

Figure 4.10: *Leakage current for the four-sensor readout sector as a function of time measured during the burn-in programme.*

- **35 pinholes**;
- **17 failed readout channels**.

As a result, the fraction of defective channels for the Trigger Tracker detector modules is about 0.13%.

4.3.2 Leakage currents

As mentioned in Section 4.1, the half-modules in the burn-in stand were continuously biased at 500V and the leakage current for each readout sector was monitored as a function of temperature and time. Figure 4.10 illustrates an example of the leakage current for the four-sensor readout sector as a function of time. The periodic variation of the leakage current observed in this picture is because of the temperature cycling performed in the burn-in stand between room temperature and $+5^\circ$ C. As noted in Section 3.2.1, the leakage current flowing through a *p*-*n* junction arises mostly due to the thermal excitations of electrons. Therefore, it strongly depends on temperature.

The leakage current for each readout sector was also investigated as a function of the applied bias voltage. The current-voltage characteristic (IV) curves were measured at cold

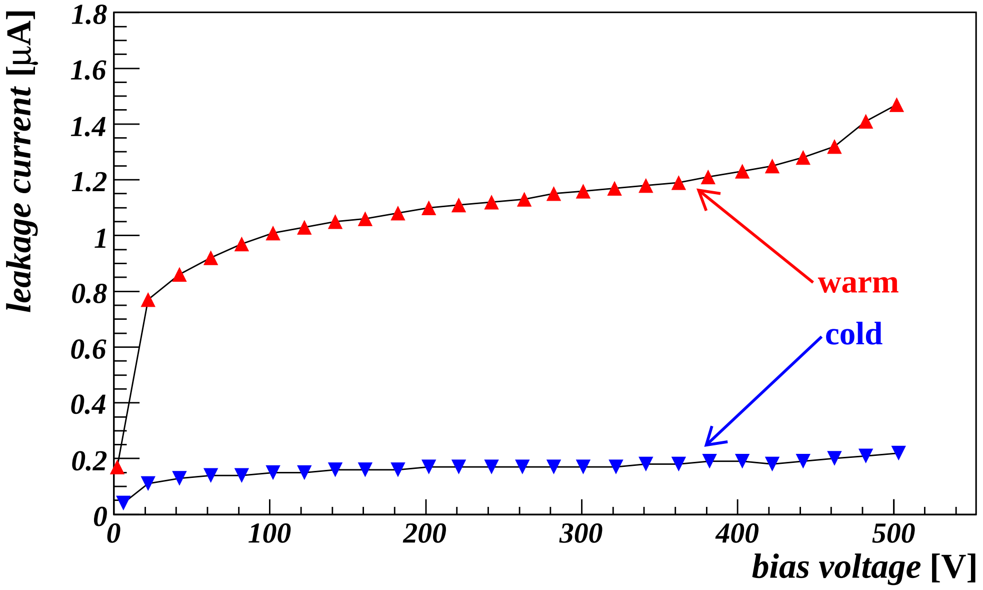

Figure 4.11: *Leakage current for the four-sensor readout sector as a function of the applied bias voltage at cold and warm temperature.*

and warm temperature. An example can be seen in Fig. 4.11. Almost all the obtained IV curves have a plateau, since the detectors exhibit the characteristic curve of a diode. As expected, the highest leakage current at 500V was obtained for the four-sensor readout

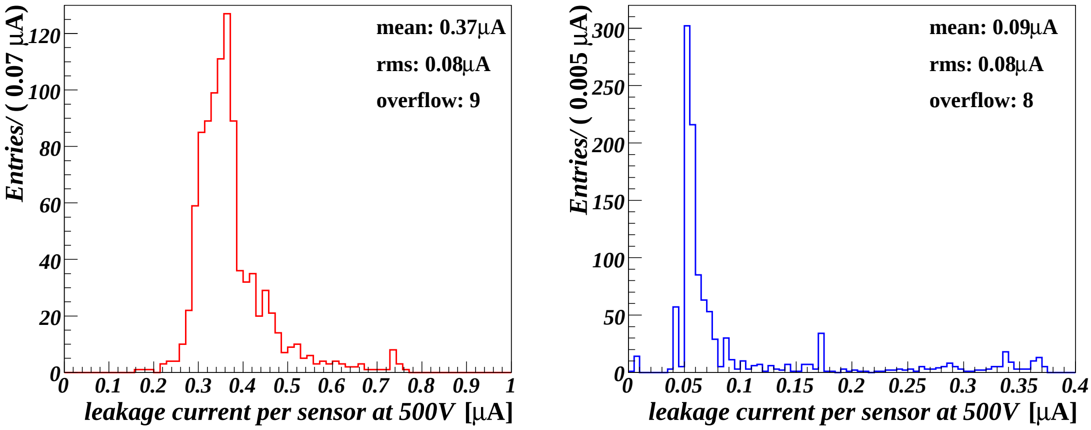

Figure 4.12: *Leakage current at 500V per silicon sensor at warm (left) and cold (right) temperature.*

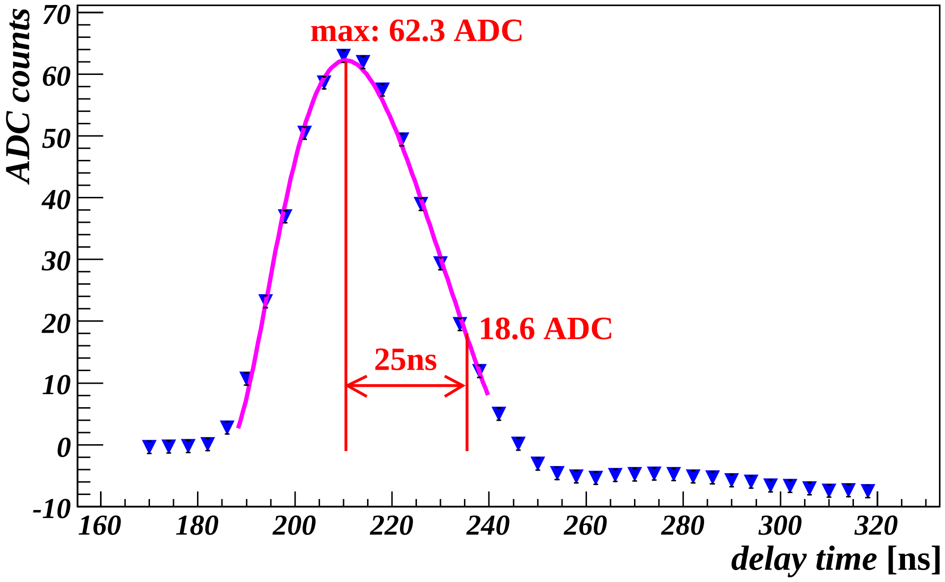

Figure 4.13: *Pulse shape of the Beetle readout chip fitted with the function defined in (4.1).*

sectors (on average 1.5μA at warm temperature and 0.4μA at cold temperature), while the lowest leakage current was obtained for the one-sensor readout sectors (on average 0.3μA at warm temperature and below 0.01μA at cold temperature). Several readout sectors were found to have a higher leakage current. Most of them have a breakdown below 500V. The half-modules containing such readout sectors will be used as spares.

Figure 4.12 illustrates the distributions of leakage currents at 500V per silicon sensor at warm and cold temperatures, as retrieved from the all obtained IV curves. As can be seen, the leakage current per silicon sensor at room temperature has a mean of 0.37μA, while at cold temperature it is approximately four times less.

4.3.3 Pulse shape scans

One of the most important characteristics of the detectors is the signal remainder. As explained in Section 3.4.1, this is the fraction of the signal that is left 25 ns after the signal maximum, i.e. the fraction of the signal which will appear in the subsequent bunch crossing. In order to study this characteristic and to test the functionality of the Beetle readout chips, the signal pulse shapes were measured[3] using an internal test pulse implemented

---

[3] As described in Section 3.4.1, the pulse shape scans are performed by varying the delay between the trigger signal and the Beetle sampling time.

in the Beetle readout chip and using an array of infra-red laser beams, as mentioned before. To extract the remainder, the obtained pulse shapes were fitted using the following function:

$$f(t) = A \cdot \left(\frac{(t-t_0)^2}{2 \cdot \tau^2} - \frac{(t-t_0)^3}{6 \cdot \tau^3} \right) \cdot e^{\frac{t-t_0}{\tau}} \quad , \tag{4.1}$$

where A is the amplitude of the signal, τ is the time constant describing the width of the signal and t_0 is the parameter describing the time-offset of the pulse with respect to the delay time between the trigger signal and the Beetle sampling time. An example of a measured pulse shape fitted with this function can be seen in Fig. 4.13.

Figure 4.14 shows the distributions of the remainders for the four-sensor readout sectors which were measured at warm and cold temperature using the laser system. As can be seen, the signal remainder is much larger at warm temperature than at cold. The same effect was observed for all readout sectors. This can be explained by the fact that at cold temperature the Beetle signal gets faster. It was found that the gain of the Beetle preamplifier increases at cold temperature. In addition, it was observed that the Beetle internal test pulses create broader pulse shapes than the laser beams. As a consequence, the remainder gets larger for the pulse shapes created by the Beetle internal test pulses, as can be seen in Fig. 4.15. This effect is not understood. However, the remainder is well-below 50% in both cases and as a result, meets the requirement for the Trigger Tracker. A detailed study of the characteristics of the detector pulse shape measured in the burn-in stand for all tested half-modules can be found in Ref. [69].

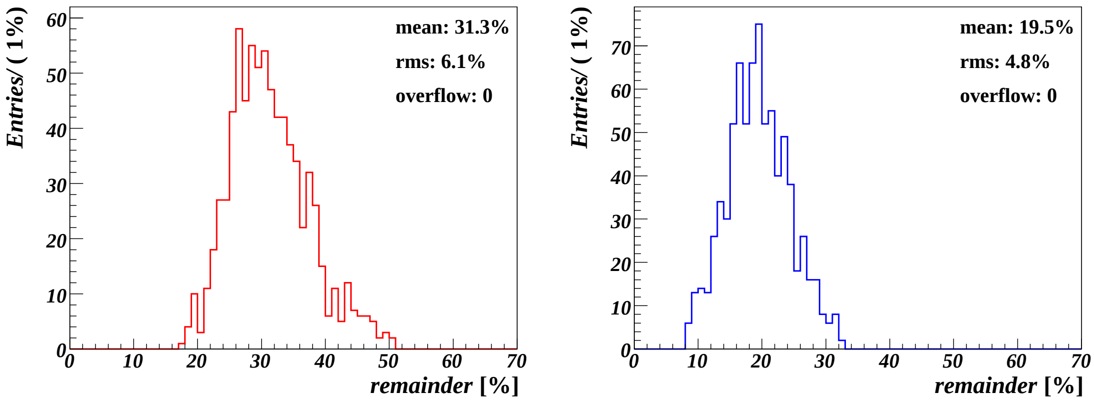

Figure 4.14: *Remainder for the four-sensor readout sectors extracted from the pulse shape scans which were measured at warm (left) and cold (right) temperature using the laser system.*

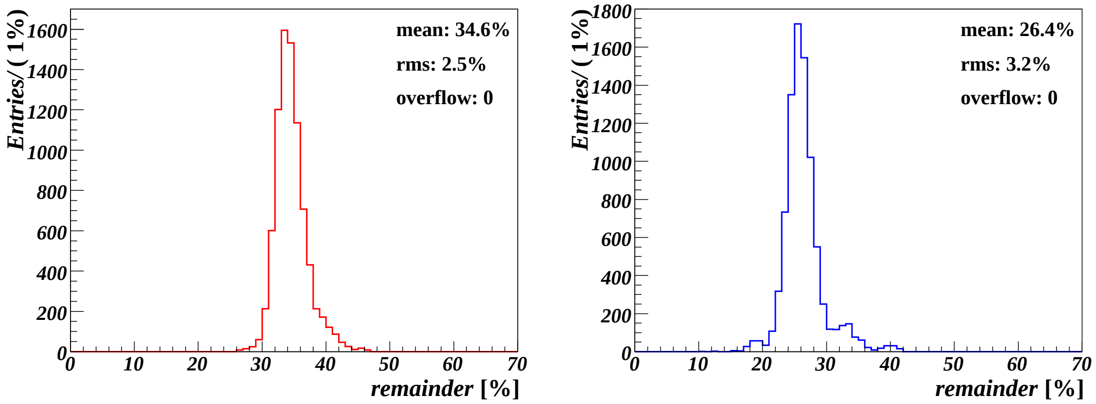

Figure 4.15: *Remainder for the four-sensor readout sectors extracted from the pulse shape scans which were measured at warm (left) and cold (right) temperature using the Beetle internal test pulses.*

4.3.4 Noise performance

As mentioned before, pedestal runs were repeatedly taken at 500V, at cold and warm temperatures to study the noise performance of the detectors. In each readout channel, the raw noise was calculated as the root-mean-square of the ADC distribution obtained with 10 000 events. A common mode correction was performed to suppress common mode (CM) noise. This noise results in a common shift of the ADC values in the readout channels, which is nearly the same for all channels within the same area. The CM noise arises for example due to pickup of external signals by the detector or readout electronics. Other sources can be power supply variations in the Beetle chip or similar effects in the analog readout chain. More information about CM noise and the CM correction procedure can be found in Ref. [73]. Examples of the raw and CM corrected noise extracted from the pedestal run measured at warm temperature for 128 channels of a Beetle readout chip of a four-sensor readout sector are shown in Fig. 4.16.

Figures 4.17 – 4.20 show the CM corrected noise for different readout sectors at warm and cold temperature. These are the distributions of the mean values of the CM corrected noise extracted from the 128 channels of each tested Beetle chip, which were obtained by analysing all pedestal runs for all tested half-modules. As can be seen for all readout sectors the CM corrected noise in ADC counts is approximately 8% lower at warm temperature than at cold. As explained in the previous section, the Beetle signal gets faster at cold temperature, resulting in a larger Johnson noise. Underflows in the distributions for the four-sensor readout sectors are due to a broken readout chip for which a very low noise was measured.

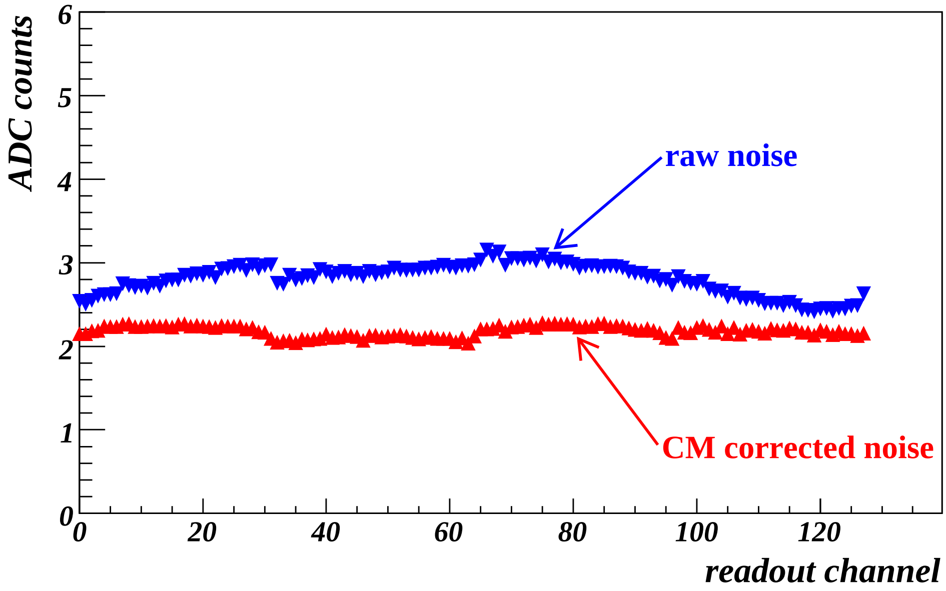

Figure 4.16: *Raw and CM corrected noise extracted from the pedestal run measured at warm temperature for 128 channels of a Beetle readout chip of a four-sensor readout sector.*

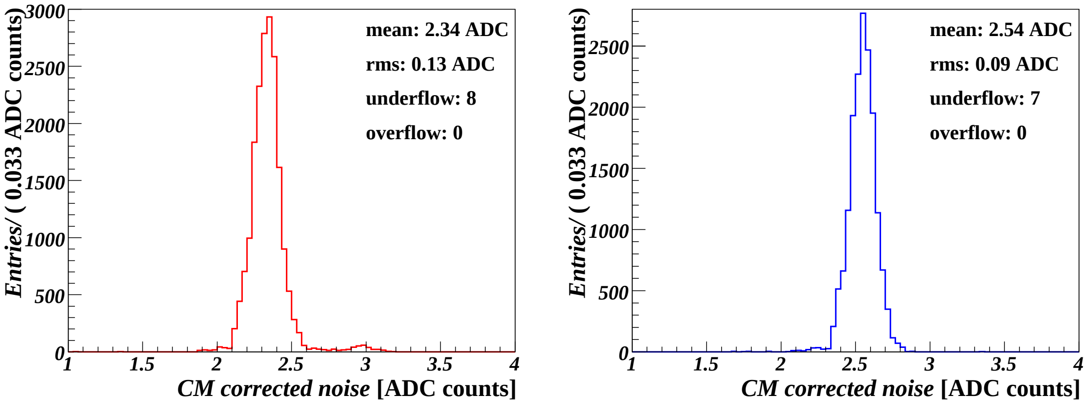

Figure 4.17: *CM corrected noise for the four-sensor readout sectors at warm (left) and cold (right) temperature.*

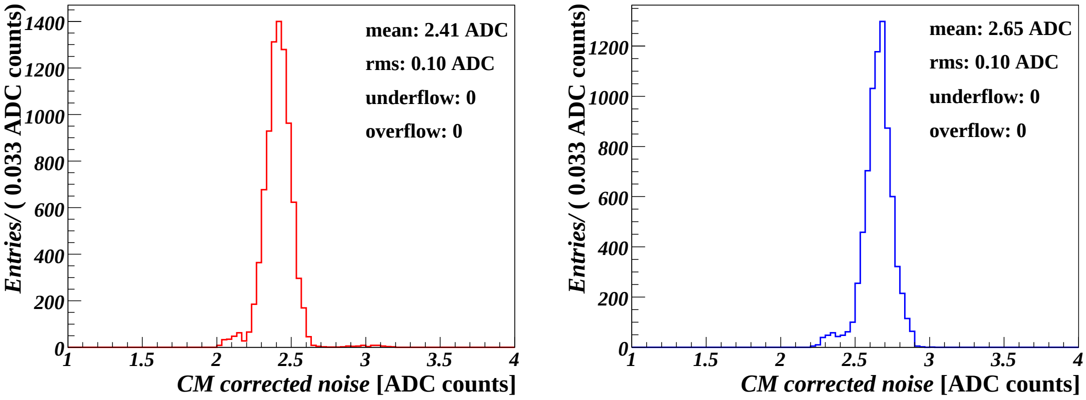

Figure 4.18: *CM corrected noise for the three-sensor readout sectors at warm (left) and cold (right) temperature.*

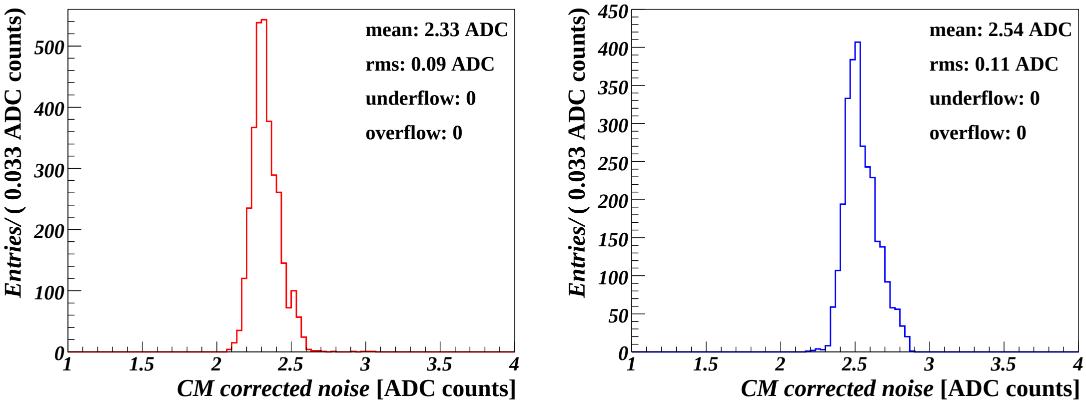

Figure 4.19: *CM corrected noise for the two-sensor readout sectors at warm (left) and cold (right) temperature.*

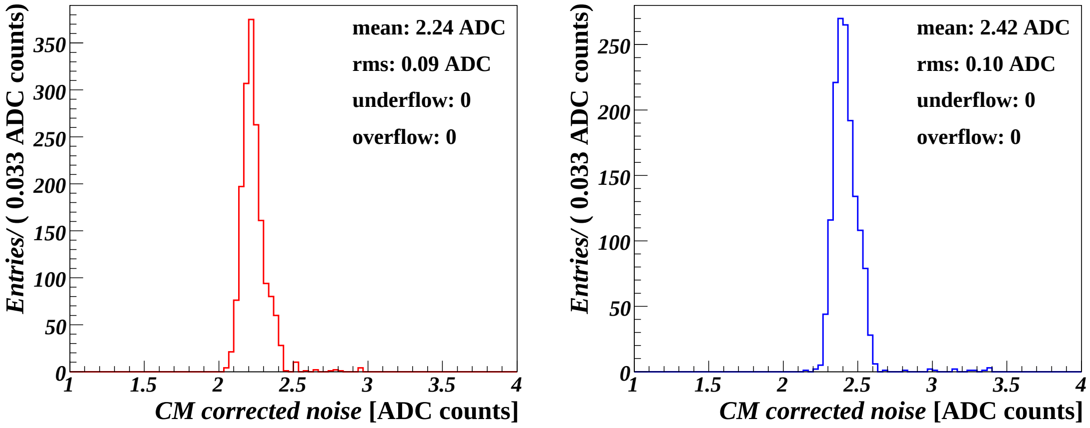

Figure 4.20: *CM corrected noise for the one-sensor readout sectors at warm (left) and cold (right) temperature.*

Chapter 5

Monte Carlo simulation of the Trigger Tracker

Due to its complexity, many years of research and development are required to design and build a particle physics detector. During this time, Monte Carlo simulations are essential to estimate the performance of the detector and to develop the required software. By comparing different detector setups, it is possible to optimise many design parameters. During the running phase of the experiment Monte Carlo simulations will be used for efficiency studies that rely on comparisons between simulated data and real data from the experiment.

In general, a Monte Carlo method is a numerical method based on a stochastic (i.e. non-deterministic) technique. It allows to solve different quantitative problems by the simulation of random variables. This method is widely applied to perform simulations of any process whose development is influenced by random factors.

In order to perform a realistic Monte Carlo simulation of a particle physics experiment, an accurate description of the detector geometry and structure is required. First, in this chapter an overview of the simulation and reconstruction software in the LHCb experiment is given. Then, the XML-based detector description of the Trigger Tracker is discussed in detail. Finally, the results of validation tests are presented.

5.1 Monte Carlo simulation in LHCb

The Monte Carlo simulation of the LHCb experiment is performed by software based on the object-oriented (OO) architecture of GAUDI [74]. In this framework, which is written in C++, there is clear distinction between data objects on one side and algorithms and tools that manipulate these objects on the other side. GAUDI provides several services (e.g. data access) needed in the algorithms. All LHCb software applications are embedded in the GAUDI framework. They perform different tasks, such as: event generation, detector simulation, digitisation, trigger, reconstruction, and event selection. The successive stages in the simulation and reconstruction are briefly described below, together with their GAUDI applications.

- **Event generation**. First, it is necessary to simulate the physics processes that take place in pp collisions at a centre-of-mass energy of $\sqrt{s} = 14\,\text{TeV}$. This is done by the PYTHIA programme [75]. Since pp interactions at such a high energy are dominated by QCD effects, PYTHIA simulates the QCD short-distance, perturbative processes describing the scattering of the partons inside the protons and the QCD long-distance, non-perturbative processes between the incoming protons and outcoming particles. Multiple pp collisions in the same bunch crossing, so-called pile-up events, are also generated. The output of this programme consists of the outcoming particles, represented by their momentum vectors. The decay of the B hadrons is controlled by a specialised software package, EVTGEN [76]. Both, PYTHIA and EVTGEN programs are steered by a GAUDI-based application called GAUSS [77].
- **Detector simulation**. Second, the tracking of the generated particles through the detector is simulated. It is performed by the GEANT4 toolkit [78], which is also controlled by GAUSS. The evolution of particles in the detector, including the magnetic field influence, the interactions of the particles with the detector material and the decay of the remaining long-lived particles (such as K_s^0 and Λ) are simulated by this application.
- **Digitisation**. Third, the response of the detector electronics is simulated by a GAUDI application called BOOLE [79]. At this step, the hits, deposited by the particles in the sensitive elements of the detector, are digitised into electrical signals. Electronic noise, cross talk and spill-over[1] effects are taken into account. BOOLE also simulates the Level-0 decision unit, since it is part of the readout hardware. The simulated response for each subdetector is calibrated using test beam data. The output of BOOLE has the same format as the data that will come out of the detector.
- **Trigger simulation**. At the next step, the HLT is executed. For real data, the same HLT algorithms will run on a dedicated processor farm, together with the online reconstruction software, which allows to get the information required for the trigger decision. Therefore, the HLT trigger software can be presented as part of the reconstruction job.

---

[1] Due to the collection time of some detectors and due to slow particles giving hits in the subsequent bunch crossing, the detector response may span more than 25 ns – the time interval between two consecutive bunch crossings at 40 MHz. This effect is referred to as spill-over.

- **Reconstruction**. After a positive trigger decision, the BRUNEL application [80] is used to process all the data obtained from the detector. It associates hits from the different subdetectors to form tracks and performs particle identification. The same programme will be used for real data.
- **Physics analysis**. Finally, the event selection is performed by the DAVINCI application [81], which provides all the necessary tools for this purpose. It assigns particle identifications to tracks and calorimeter clusters, as will be described in Section 6.3. Consequently, it forms particle candidates from tracks and clusters. DAVINCI also performs primary vertex reconstruction and provides flavour tagging.

In addition, the events and the geometry of the detector can be displayed using the visualisation application PANORAMIX [82].

It should be noted that for the last three steps the simulated events are treated in the same way as if they would be obtained from real data. In the LHCb event model, there is a clear separation between the Monte Carlo data and the reconstructed data.

5.2 Detector description software

One of the most important components of the LHCb software is the detector description, which is shared among all applications, including simulation, reconstruction, analysis and visualisation. The GAUDI framework is used to store, access and process all data related to the description of the detector.

The overall structure of the detector description is shown in Fig. 5.1. It can be seen that GAUDI algorithms access data through a transient representation of the persistent detector description database. Conversion to other representations (e.g. graphical views, GEANT4 geometry description) is performed by conversion services. The detector description database (XmlDDDB) contains all information about the physical and logical description of the detector. It is implemented using the Extensible Markup Language (XML) [83] which allows to describe the detector in a consistent and coherent manner. The XML data can be easily translated into different formats using specific tools (e.g. XSLT processors). The detector description is divided into three parts:

- **Geometry.** This part is used for the geometry tree description. It describes a hierarchy of *logical* and *physical volumes*. A logical volume contains information about the shape, dimensions and material content of a detector object. However, it does not have any information about its absolute position in the LHCb coordinate system. A physical volume is a logical volume that has been positioned inside another logical volume. Hence, a physical volume knows its own position relative to the coordinate system of its parent.

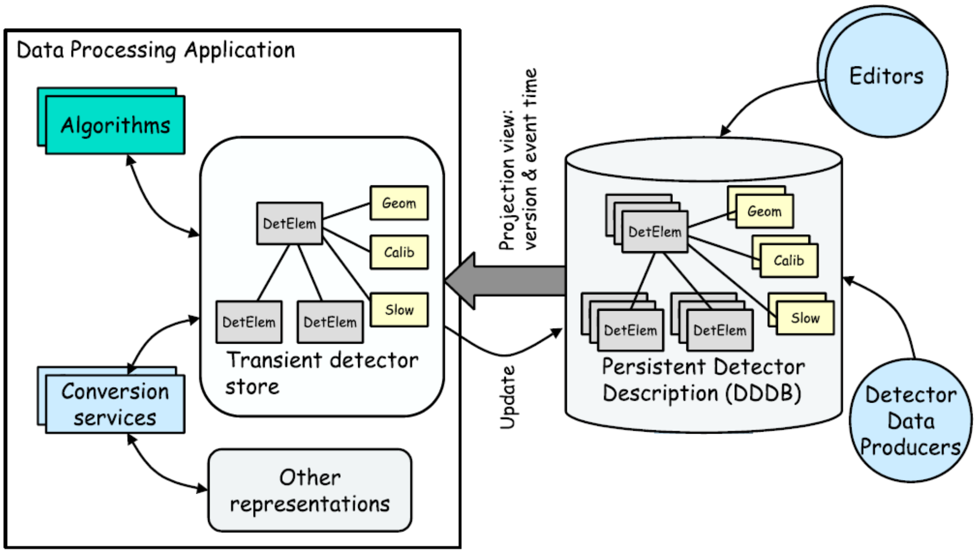

Figure 5.1: *Detector description overview.*

- **Structure.** This part contains the logical structure of the detector. It describes the tree of sensitive detector elements and their relations with the geometry and calibration of the detector.

- **Materials.** This part defines the materials and their properties (e.g density, atomic number). The materials used in the LHCb Trigger Tracker are described in Ref. [84].

More information about the LHCb detector description framework can be found in Refs. [85, 86].

5.3 The Trigger Tracker detector description in XML

After the relevant design parameters were fixed it was decided to replace the detector description of the Trigger Tracker by a more realistic version, where the volumes for the frames, readout cables, balconies, beam pipe jacket, cooling plates and cooling elements have been added in addition to a detailed description of the detector modules. The new detector description of the Trigger Tracker discussed in this dissertation is available in the XmlDDDB database from version v30r0 onwards. The geometry parameters used in this description can be found in Ref. [87].

5.3.1 Geometry tree overview

In the detector description of the Trigger Tracker there are three categories of volumes — box, module and cable. The box volumes describe the inactive elements of the Trigger Tracker box, the module volumes describe the sensitive elements of the detector and the cable volumes describe the Kapton readout cables.

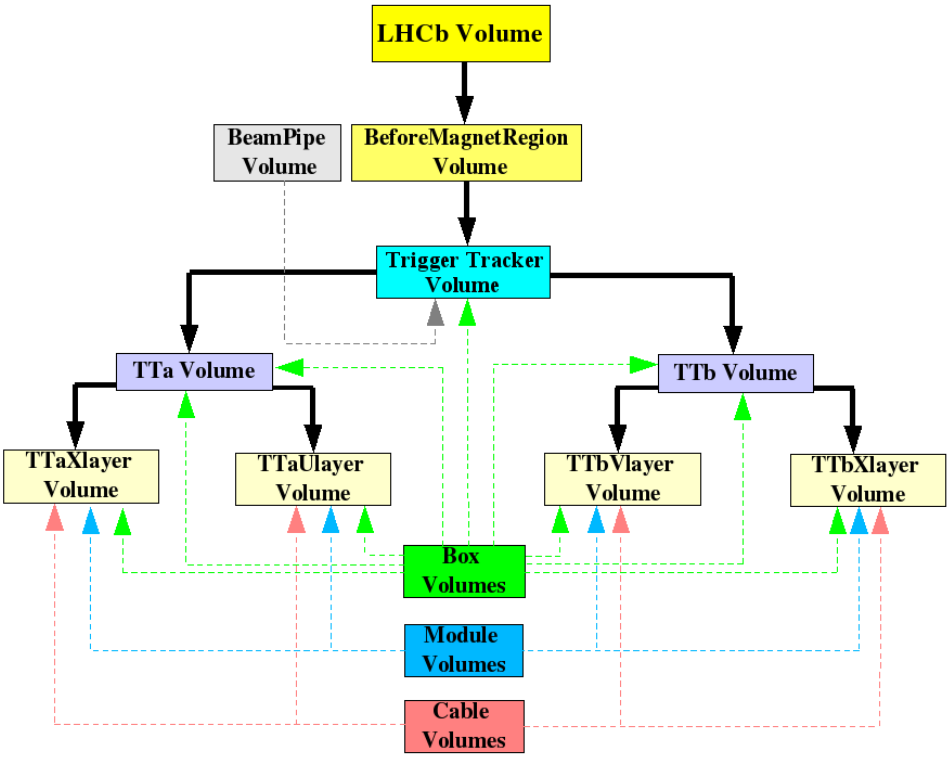

Figure 5.2: *The geometry tree for Trigger Tracker.*

The geometry tree for the Trigger Tracker is shown in Fig. 5.2, where the solid arrows show the hierarchy of volumes and the dashed arrows represent the usage of the box, module and cable volumes in the description of the top level elements of the detector tree. It can be seen that the Trigger Tracker volume is located inside the “BeforeMagnetRegion” envelope of the LHCb detector. The Trigger Tracker volume has the shape of a box and contains the volumes for TTa and TTb as well as the box volumes for the frame, the isolation walls, the cooling plates, the cooling elements and the beam pipe isolation jacket between TTa and TTb.

The volumes for TTa and TTb consist of volumes for the layers and for the beam pipe isolation jacket between the two layers and between the layers and the walls. The TTa and TTb volumes and their daughter volumes for the layers are defined as a boxes with a hole for the beam pipe.

The volumes for each detection layer consist of volumes for the half-modules, the readout cables and the balconies.

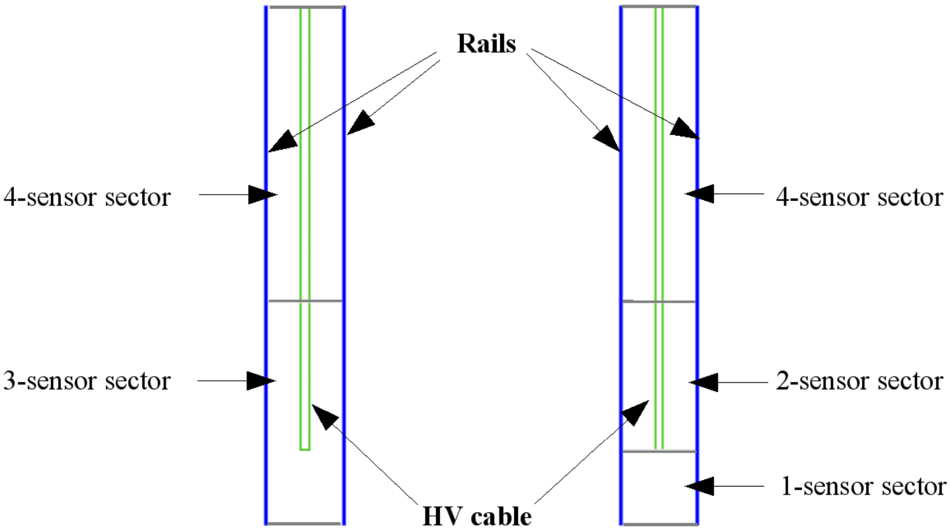

Figure 5.3: *The LM (left) and LMK (right) modules.*

The basic detector unit of the Trigger Tracker — the half-module, consisting of seven 500 μm thick silicon sensors — is the building block of the layer geometry. As described in Section 3.3.1, there are two different types of half-modules: LMK and LM modules. In the detector description a half-module is defined as an assembly of two or three physical volumes, one for each readout sector. The half-module's volume also includes passive volumes for the support rails and the high-voltage cable. The volumes for the readout sectors are defined as boxes of silicon and are the sensitive elements of the detector. The volumes for the LM and LMK half-modules are shown in Fig. 5.3. All drawings are obtained using the visualisation application PANORAMIX.

Each volume for the layers in TTa (TTb) consists of 6 volumes for the LMK half-modules surrounding the beam pipe and 24 (28) volumes for the LM half-modules. Figures 5.4 and 5.5 show a front view of the layers. The bottom half-modules were placed at their positions after a rotation of the volumes by an angle of 180 degrees around the z axis. The module volumes for the u and v layers are rotated around z axis by an angle of -5° and $+5^\circ$, respectively. As mentioned in Section 3.3.1, in order to avoid acceptance gaps, adjacent detector modules in a layer are staggered. This is taken into account in the detector description.

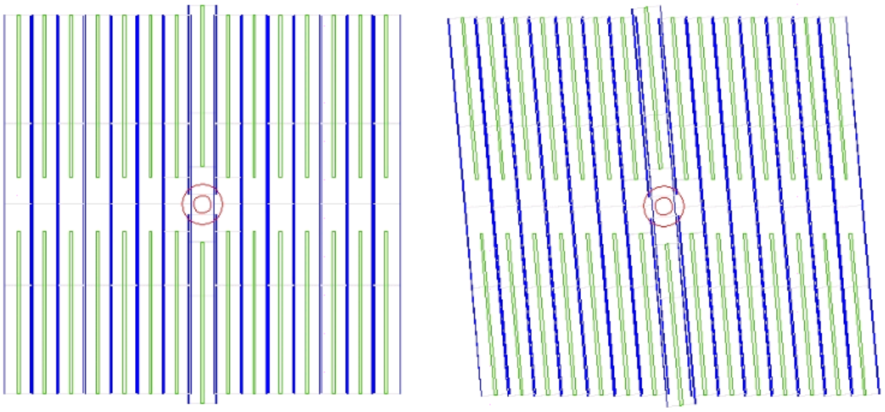

Figure 5.4: *Front view of the x (left) and u (right) layers of TTa.*

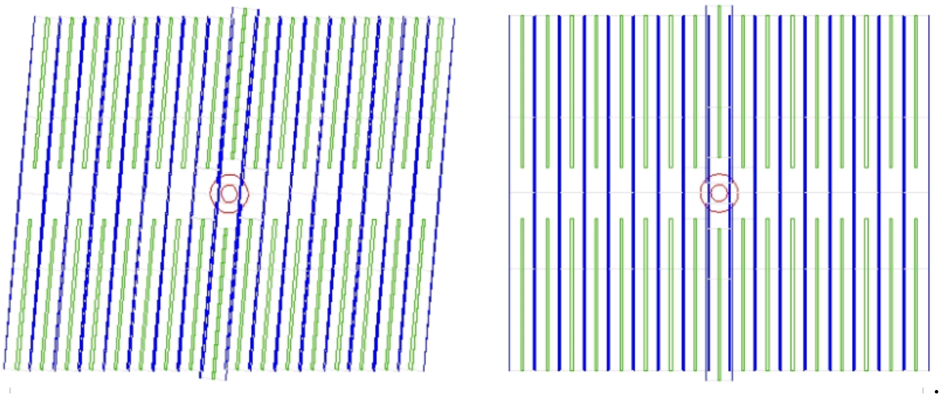

Figure 5.5: *Front view of the v (left) and x (right) layers of TTb.*

In the detector description, the 39.1 cm long interconnect Kapton cable used to connect the three-sensor and two-sensor sectors of the LM and LMK half-modules to the corresponding readout hybrids is called K-cable, while the 58 cm long interconnect Kapton cable employed to connect the inner one-sensor sectors of the LMK half-modules to their readout hybrids is called L-cable. In order to reduce the number of volumes, the width of the individual cables is set to the full width of a sensor allowing the K-cables in each quadrant of the detector to be modelled as one large volume as shown in Fig. 5.6. This simplification reduces the number of volumes needed for the K-cables from 128 to 24. For the *u* and *v* layers the cable volumes are rotated by the corresponding stereo angle.

The balconies, cooling plates, cooling elements, insulating walls, beam pipe jackets and the detector frame are inactive elements of the detector box which provide mechanical support, electrical shielding and cooling of the Trigger Tracker, as described in Sec-

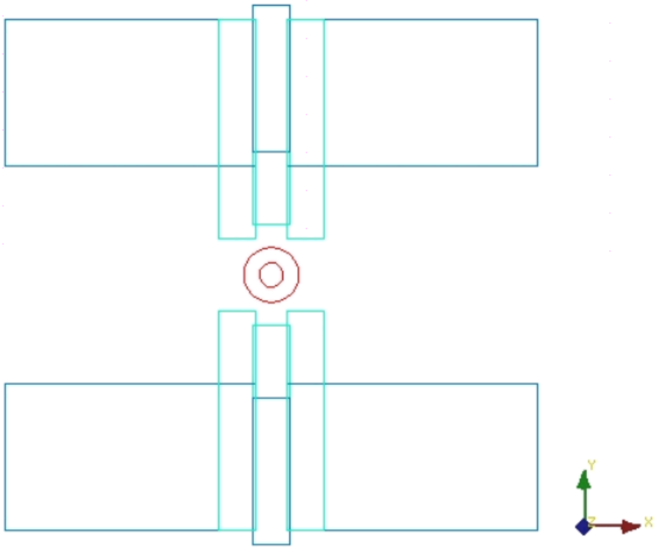

Figure 5.6: *The cable volumes for x layer of TTa. The blue colour indicates the K-cables and the light cyan colour indicates the L-cables.*

tion 3.3.2. These passive elements have been included in the detector description and are visualised in Fig. 5.7. The cooling elements and cooling plates are described as a boxes without piping to simplify the detector description. The other inactive elements are also defined as a boxes[2] except the beam pipe jacket which has the shape of a tube. Figure 5.8 shows an enlarged view of the beam pipe isolation jacket, where its different sections can be recognised.

In total, 731 physical volumes are used in the detector description of the Trigger Tracker. The list of logical volumes including their shape and material is given in Ref. [87].

5.3.2 Structure layout

The hierarchy of detector elements is described in the structure. Each detector element in the database can be converted into an instance of a corresponding C++ detector element class used in the simulation and reconstruction. The tree of the detector elements for the Trigger Tracker is shown in Fig. 5.9. As can be seen, the main detector element, the Trigger Tracker, includes two daughter detector elements, TTa and TTb. These consist of detector elements for the layers, which contain detector elements for the modules. Finally, each module, which is described separately in the database, consists of detector elements for the one-sensor, two-sensor, three-sensor and four-sensor long readout sectors.

---

[2] For the insulating walls there is a hole for the beam pipe.

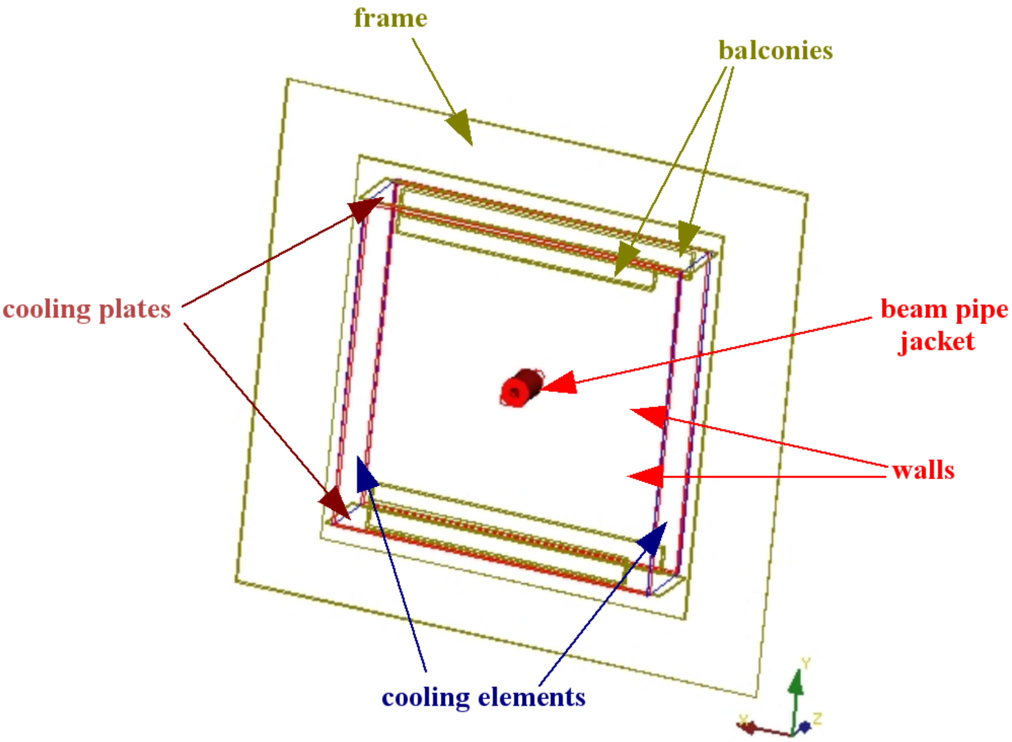

Figure 5.7: *The inactive volumes of the Trigger Tracker box.*

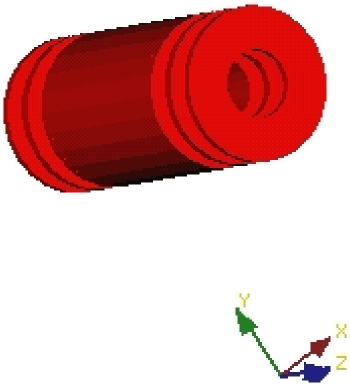

Figure 5.8: *The beam pipe isolation jacket of the Trigger Tracker box.*

By making use of a special feature in XML referred to as entities, the XML files describing the structure of the half-modules are linked to template files where the detector elements for LM and LMK half-modules are described. This allows to describe the com-

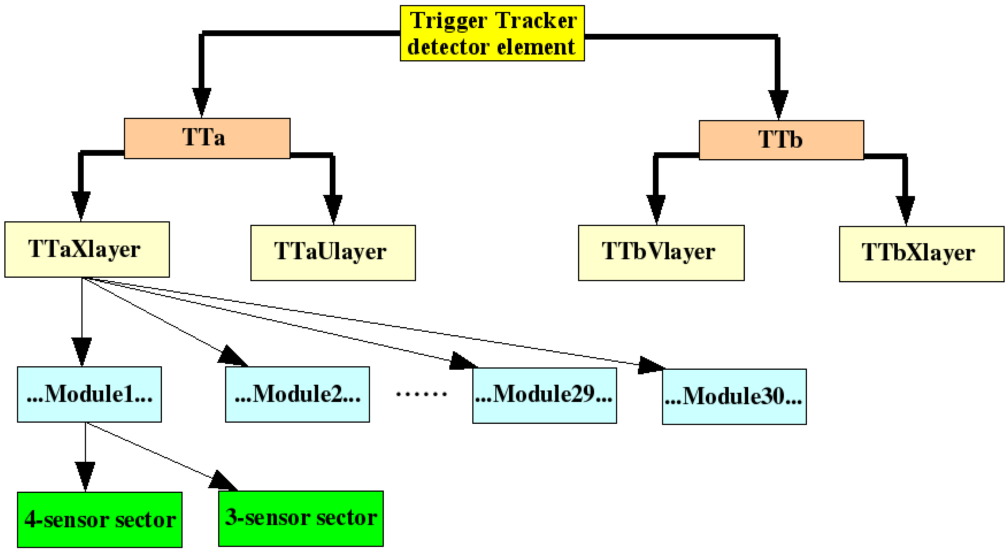

Figure 5.9: *A tree of the detector elements for Trigger Tracker.*

mon part of the modules and readout sectors only once and thus, minimise the amount of code. In these template files, different detector parameters are attached to individual detector elements. These are typically variables that are needed in the reconstruction or digitisation but not at the level of the GEANT4 based simulation. The parameters for the detector elements corresponding to the one-sensor, two-sensor, three-sensor and four-sensor long readout sectors are given in Table 5.3.2.

To provide a unique numbering for the readout channels of the Trigger Tracker, the following parameters were introduced to tag each readout sector in a given layer: "detRegion", "Module", "firstReadoutSector" and "type". As shown in Fig. 5.3.2 the layers are divided into three detection regions. The first and the third "detRegion" consists of 6 (7)

Table 5.1: *The parameters used in description of detector elements for one-sensor, two-sensor, three-sensor and four-sensor long readout sectors.*

Type	Number of sensors	Pitch [mm]	Number of strips	Capacitance [pF]	Vertical Guard Ring [mm]
TT1	1	0.18337	512	38	1.415
TT2	2	0.18337	512	44	1.415
TT3	3	0.18337	512	57	1.415
TT4	4	0.18337	512	55	1.415

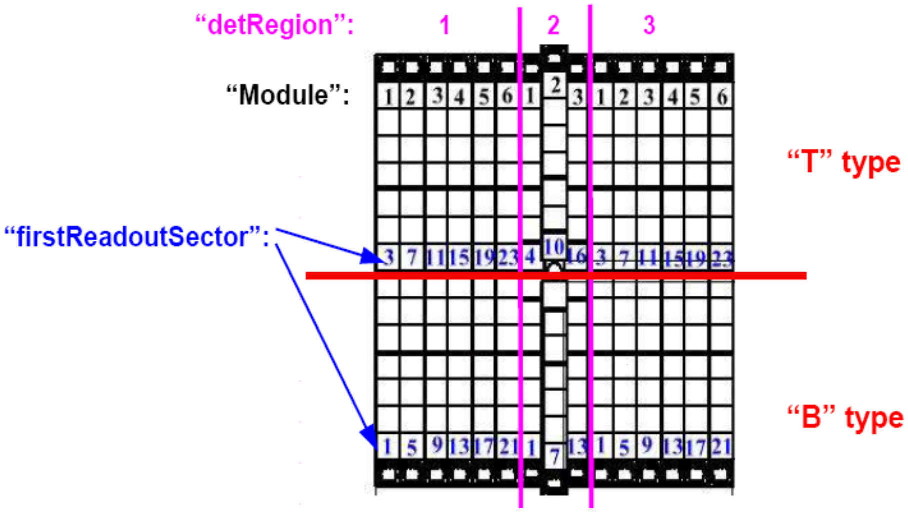

Figure 5.10: *The module numbering for TTa.*

top and 6 (7) bottom half-modules in a TTa (TTb). The second "detRegion" consists of 6 half-modules surrounding the beam pipe. The "Module" and the "firstReadoutSector" parameters give the number of the full module and the number of the readout sector within the detection region. The "type" parameter gives the position of the module, which can be top or bottom. This structure allows to identify each readout channel[3]. More information about the channel numbering and the detector element tree for Trigger Tracker can be found in Refs. [88, 89].

5.4 Validation tests

Some basic checks have been made to validate the correctness of the current description. First, it has been checked that no overlaps occur between the detector volumes. This check has been performed using the DetDescChecks tool [90], which is distributed with the LHCb software project. No overlapping volumes were found. Second, the LHCb simulation programme, GAUSS, has been used to simulate 500 minimum-bias events. Figure 5.11 shows the distribution of the impact points of the particles on the sensitive volumes of TTa and TTb. As can be seen, the physical dimensions of TTa and TTb are reproduced and the particle density distribution is as expected. The energy loss in a silicon layer and the time-of-flight of the particles obtained with the current simulation are shown in Fig. 5.12 and in Fig. 5.13. As was already seen in previous studies [91], the magnitude of the deposited energy given by GEANT is 20% higher than expected, based

---

[3] This channel numbering will be changed in the future due to inconsistency with actual partitioning.

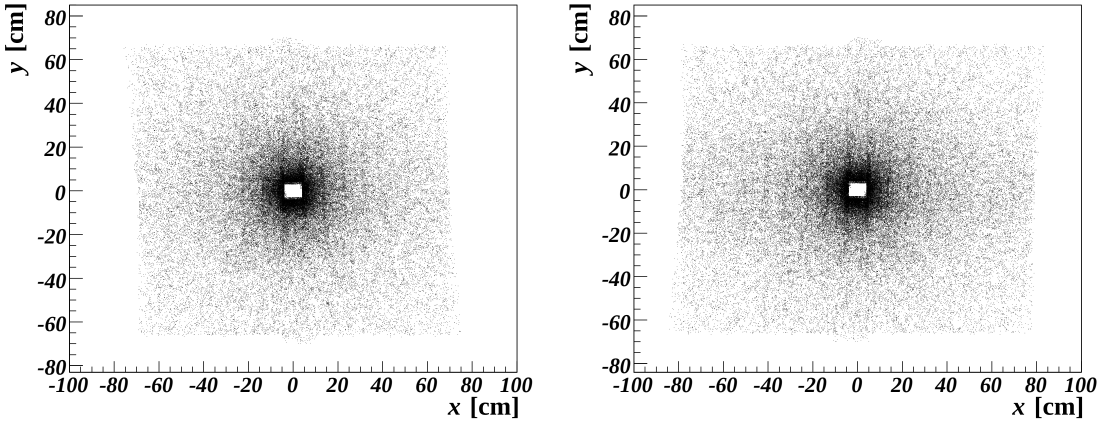

Figure 5.11: *The distribution of hits in TTa (left) and in TTb (right).*

on theoretical calculations. The average time-of-flight is consistent with the distance between the pp interaction point and the Trigger Tracker assuming that the particles travel with relativistic velocities.

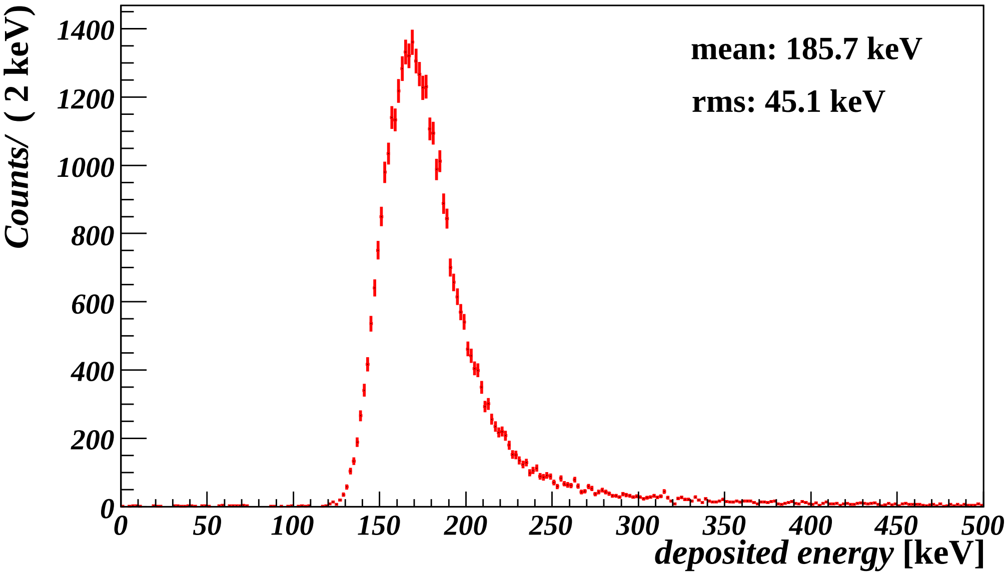

Figure 5.12: *Energy deposited by particles from the primary proton-proton interaction in a silicon sensor with a thickness of 500 μm, as simulated by* GEANT4.

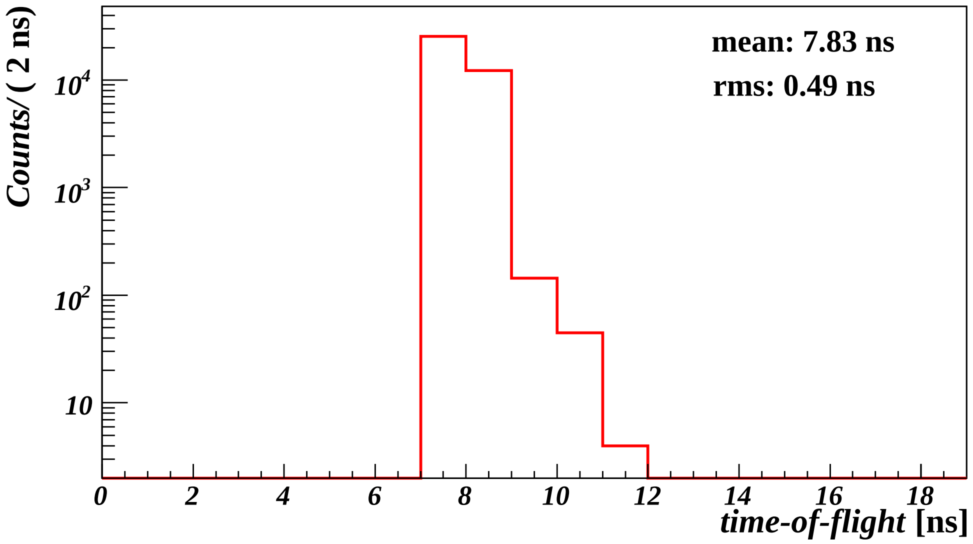

Figure 5.13: *Time at which particles from the primary proton-proton interaction traverse the TTa. The primary proton-proton interaction occurs at t=0 ns. The tail on the right of the distribution is mainly due to non-relativistic particles.*

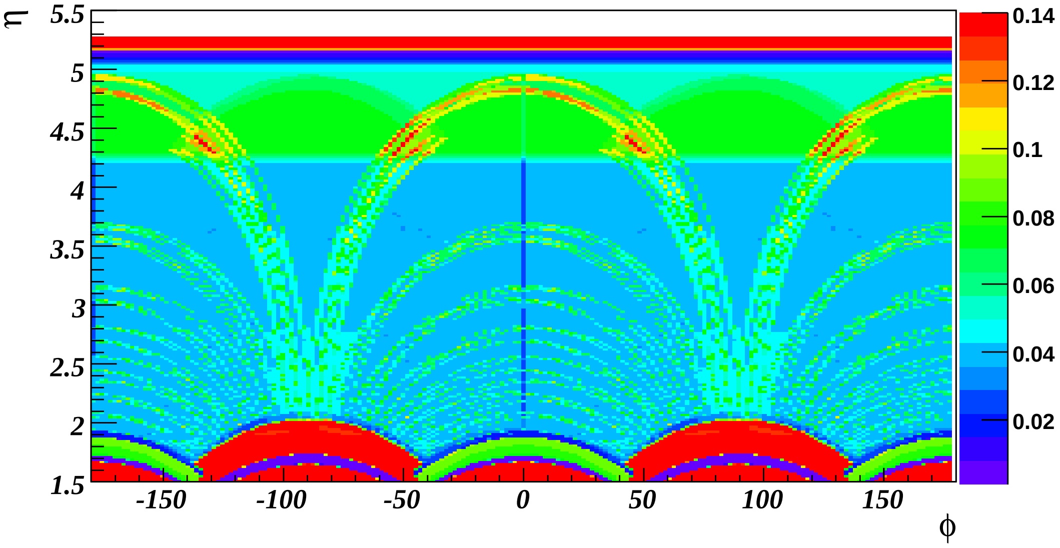

Figure 5.14: *Amount of material in terms of radiation lengths as a function of the pseudorapidity η and the azimuthal angle ϕ.*

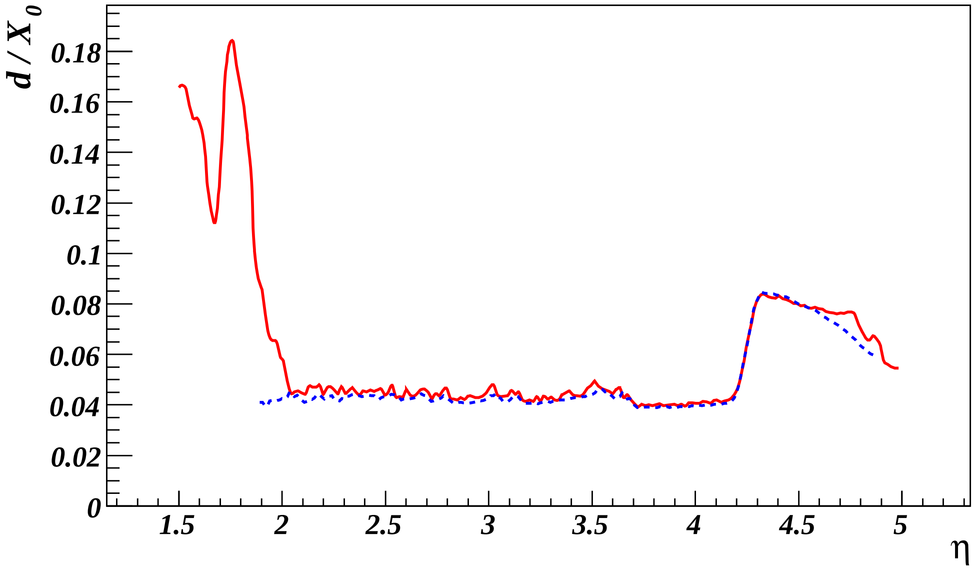

Figure 5.15: *Amount of material in terms of radiation lengths averaged over ϕ as a function of η. The solid line is with the current implementation, the dotted line represents the expectation from the studies described in [84].*

Another important test is to scan the material distribution using the Gaudi transport service. Figure 5.14 shows the amount of material in terms of radiation lengths d/X_0 as a function of the pseudorapidity η and the azimuthal angle ϕ, while Fig. 5.15 shows the amount of material averaged over ϕ as a function of η. These results are consistent with the calculation of the material budget of the Trigger Tracker described in Ref. [84]. The discrepancy at low η is outside the detector acceptance and is due to the cooling plates, the balconies and the detector frame which were not taken into account in the earlier study.

Chapter 6

Study of the $B_s^0 \to J/\psi\,\eta'$ decay at LHCb

This chapter presents the full Monte Carlo analysis of the $B_s^0 \to J/\psi\,\eta'$ decay at the LHCb detector. First, the physics of the $B_s^0 \to J/\psi\,\eta'$ decay is discussed. Second, a brief overview of the Monte Carlo data samples is given. Third, the particle identification procedure and flavour tagging are discussed. Next, the reconstruction aspects of the $B_s^0 \to J/\psi\,\eta'$ decay at LHCb are considered. Then, the $B_s^0 \to J/\psi\,\eta'$ event selection procedure and the obtained results are described in detail. Finally, the sensitivity of the LHCb detector to measure the B_s^0-$\bar{B}_s^0$ mixing phase ϕ_s with this decay mode is presented.

6.1 Physics of the $B_s^0 \to J/\psi\,\eta'$ decay

6.1.1 The $\bar{b} \to \bar{c}c\bar{s}$ quark level transition

As mentioned in Section 1.3.2, the $\bar{b} \to \bar{c}c\bar{s}$ quark-level transition is essential in the determination of the B_s^0–$\bar{B}_s^0$ weak mixing phase, ϕ_s, which is directly related to the CKM angle χ according to (1.48). The most promising decays occuring through this transition are $B_s^0 \to J/\psi\,\eta$, $B_s^0 \to J/\psi\,\eta'$, $B_s^0 \to \eta_c\,\phi$, $B_s^0 \to D_s^+\,D_s^-$ and $B_s^0 \to J/\psi\,\phi$. Only the last one is a decay of a B_s^0 into an admixture of CP eigenstates, the others are decays into a pure CP self-conjugated final state.

There are two different topologies contributing to the $\bar{b} \to \bar{c}c\bar{s}$ transition: tree and penguin processes. They can be described using Feynman diagrams with an external or internal W emission and with an external or internal W loop, respectively. Figure 6.1 illustrates the two diagrams for the tree processes.

As can be seen, the external tree diagram leads to the creation of two charged D_s mesons in the final state. In case of an internal tree process, the two mesons in the final state are formed by $c\bar{c}$ and $s\bar{s}$ quark pairs resulting into two neutral particles. When

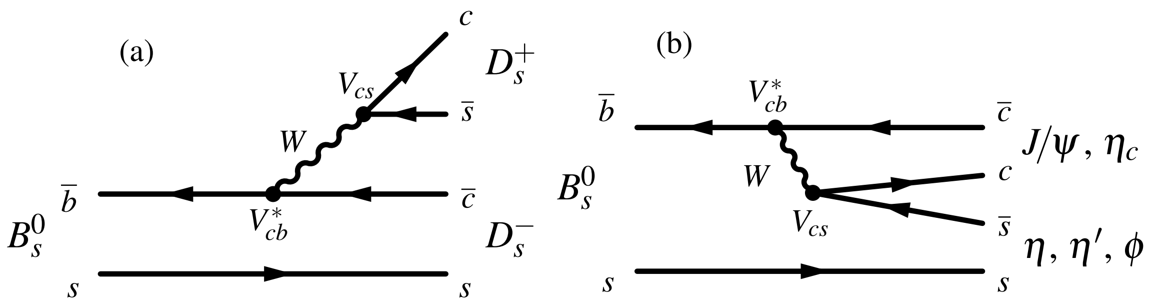

Figure 6.1: *Feynman diagrams describing the tree processes in $\bar{b} \to \bar{c}c\bar{s}$ quark-level transition: (a) with external and (b) with internal W emission. In (b), the $c\bar{c}$ quark pair can form either a J/ψ or η_c meson and the $s\bar{s}$ pair can form either a η, η' or ϕ meson.*

considering the penguin processes in the $\bar{b} \to \bar{c}c\bar{s}$ transition, then there is an opposite situation: the external diagram is responsible for the creation of two neutral mesons and the internal diagram leads to the existence of two charged D_s mesons. This means that for B_s^0 decays into two neutral mesons occuring through the $\bar{b} \to \bar{c}c\bar{s}$ transition, there are contributions from both the internal tree and external penguin diagrams.

The total amplitude for the $\bar{b} \to \bar{c}c\bar{s}$ transition can be presented as a combination of the tree and the penguin contributions:

$$A(\bar{b} \to \bar{c}c\bar{s}) = V_{cs}V_{cb}^*T + V_{cs}V_{cb}^*P_c + V_{us}V_{ub}^*P_u + V_{ts}V_{tb}^*P_t \quad , \tag{6.1}$$

where T is the amplitude of the tree contribution and P_u, P_c, P_t are the penguin amplitudes with internal u, c, t quarks, respectively. Using the unitarity relation which describes the bs squashed triangle (see (1.10)) the $V_{ts}V_{tb}^*$ term can be eliminated and the amplitude can be rewritten as:

$$A(\bar{b} \to \bar{c}c\bar{s}) = V_{cs}V_{cb}^*(T + P_c - P_t) + V_{us}V_{ub}^*(P_u - P_t) \quad . \tag{6.2}$$

Using the Wolfenstein parametrisation, it can be shown that $V_{cs}V_{cb}^*$ is of order λ^2 and $V_{us}V_{ub}^*$ of order λ^4. Therefore, the second term in (6.2) can be neglected. Thus, the total amplitude depends mainly on the CKM factor $V_{cs}V_{cb}^*$. Since the amplitude has effectively only a single CKM coefficient there is only one overall weak phase in this case [92].

6.1.2 *CP* violation in $B_s^0 \to J/\psi\eta'$

As shown in Section 1.3.2, if the B meson decays through the $\bar{b} \to \bar{c}c\bar{s}$ transition and its final state is a pure *CP* eigenstate, then *CP*-violating effects can be described in a simple way. The $B_s^0 \to J/\psi\eta'$ decay meets these requirements. The final state of this decay is a pure CP eigenstate. Its CP eigenvalue is well-defined[1]

$$(CP)\,|J/\psi\,\eta'\rangle = +|J/\psi\,\eta'\rangle \implies n_{J/\psi\,\eta'} = +1 \quad . \tag{6.3}$$

In this channel, CP asymmetry arises in the interference between the direct decay $B_s^0 \to J/\psi\,\eta'$ and the decay after oscillation $B_s^0 \to \bar{B}_s^0 \to J/\psi\,\eta'$. According to (1.37) and (1.46), the corresponding time-dependent CP asymmetry can be written in the following way:

$$\begin{aligned} A_{CP}(t) &= \frac{\Gamma(\bar{B}_s^0(t) \to J/\psi\eta') - \Gamma(B_s^0(t) \to J/\psi\eta')}{\Gamma(\bar{B}_s^0(t) \to J/\psi\eta') + \Gamma(B_s^0(t) \to J/\psi\eta')} = \\ &= -\frac{\sin\phi_s\,\sin(\Delta M_s t)}{\cosh(\Delta\Gamma_s t/2) - \cos\phi_s\,\sinh(\Delta\Gamma_s t/2)} \quad . \end{aligned} \tag{6.4}$$

As can be seen, in order to determine the weak mixing phase ϕ_s it is necessary to measure experimentally the time-dependent decay rates of an initially pure B_s^0 and $\bar{B}_s^0$ decaying into $J/\psi\eta'$. This involves very rapid B_s^0–$\bar{B}_s^0$ oscillations due to the large mass difference ΔM_s between the mass eigenstates. Therefore, in order to perform such measurements the experiment must have a good decay time resolution and excellent tagging performance. In this chapter, it will be shown that, using Monte Carlo simulation the LHCb spectrometer is expected to be an excellent detector to measure the $B_s^0 \to J/\psi\,\eta'$ decay, providing accurate measurements of the B_s^0 decay time with a high tagging efficiency.

The Standard Model prediction for ϕ_s is -0.04 rad. Clearly, the time-dependent CP asymmetry is expected to be tiny. Therefore, in order to provide a precise measurement of ϕ_s, it is very important to reconstruct a large sample of events with the $B_s^0 \to J/\psi\,\eta'$ decay.

6.1.3 Experimental aspects of $B_s^0 \to J/\psi\,\eta'$ at LHCb

It should be noted that the $B_s^0 \to J/\psi\,\eta'$ decay has never been observed up to now. It is expected to be detected at the LHC. Due to its high luminosity the LHC will generate many B hadrons which allows us study their various decays. The J/ψ and η' mesons are both resonances. Therefore, their decay vertices overlap with the decay vertex of the B_s^0. As a result, there are only two vertices — the primary vertex (where the B_s^0 meson is created) and the secondary vertex (where the B_s^0 meson decays).

---

[1] It can be shown taking into account that the J/ψ is a pseudo-vector ($J^{PC} = 1^{--}$) and the η' is a pseudo-scalar meson ($J^{PC} = 0^{-+}$) which both originate from a B_s^0 with $J^P = 0^-$. This implies that the J/ψ and η' must have a relative orbital momentum $l = 1$ due to angular momentum conservation. As a result, $CP(J/\psi\,\eta') = (-1)^l CP(J/\psi) CP(\eta') = +1$.

There are many decay modes of the J/ψ and η' mesons. However, only few of them can be used to detect these particles experimentally. For the J/ψ meson, the two main decay channels are $J/\psi \to e^+e^-$ and $J/\psi \to \mu^+\mu^-$. Both processes have a branching fraction of 6 %. Since electrons and muons are charged particles, their tracks can be reconstructed by the LHCb tracking system. However, it should be noted that electrons have a mass which is about 200 times smaller than that of muons. Therefore they suffer much higher energy losses due to bremsstrahlung. This results in a worse momentum resolution for electrons, which directly affects the invariant mass resolution for the J/ψ and B_s^0. Consequently, the muon channel is better suited to reconstruct the J/ψ.

There are also two main decay modes which can be used to detect a η' experimentally. These are the $\eta' \to \pi^+\pi^-\eta$ and the $\eta' \to \rho^0\gamma$ channels in which the η and ρ^0 mesons are again unstable particles. The dominant decay mode of the η is the $\eta \to \gamma\gamma$ channel. The ρ^0 meson decays due to the strong interaction into a $\pi^+\pi^-$ pair with a probability close to 100% and a decay width as large as 150 MeV. It should be noted that the η' meson can also decay directly into $\pi^+\pi^-\gamma$ without the resonant creation of a ρ^0. Due to the rather large decay width of the ρ^0 meson, it is quite difficult to distinguish between these two contributions. Therefore, the Particle Data Group [9] gives the branching fraction for the $\eta' \to \rho^0\gamma$ channel including the non-resonant $\eta' \to \pi^+\pi^-\gamma$. From an experimental point of view, the search of the η' decaying in the channel $\eta' \to \pi^+\pi^-\eta$ is more challenging, since it requires to reconstruct two photons instead of one. Due to interactions with the material of the detector many photons will be converted before the ECAL. Therefore, the photon reconstruction and identification is not a trivial task. In addition, in order to suppress the hadronic background in the ECAL it is necessary to apply a tight cut on transverse energy E_T of the photon candidate. This again decreases the photon reconstruction efficiency. The corresponding branching fractions are

$$\mathrm{BF}(\eta' \to \rho^0(\pi^+\pi^-)\gamma) = (29.4 \pm 0.9) \times 10^{-2} \quad ,$$

$$\mathrm{BF}(\eta' \to \pi^+\pi^-\eta(\gamma\gamma)) = \mathrm{BF}(\eta' \to \pi^+\pi^-\eta) \times \mathrm{BF}(\eta \to \gamma\gamma) = (17.5 \pm 0.6) \times 10^{-2} \,.$$

In this dissertation the reconstruction of the $B_s^0 \to J/\psi\eta'$ decay is performed using the $J/\psi \to \mu^+\mu^-$ and $\eta' \to \rho^0(\pi^+\pi^-)\gamma$ channels. In this case there are four charged particles and one photon in the final state. Figure 6.2 illustrates the topology of this decay. The main properties of the J/ψ, η' and ρ^0 mesons and their decay channels used in this study are listed in Table 6.1.

6.1.4 $B_s^0 \to J/\psi\,\eta'$ branching fraction and annual production yield

In order to be able to estimate the branching fractio (BF) of the $B_s^0 \to J/\psi\eta'$ decay it is necessary to consider the physics of the η' meson using the quark model described in

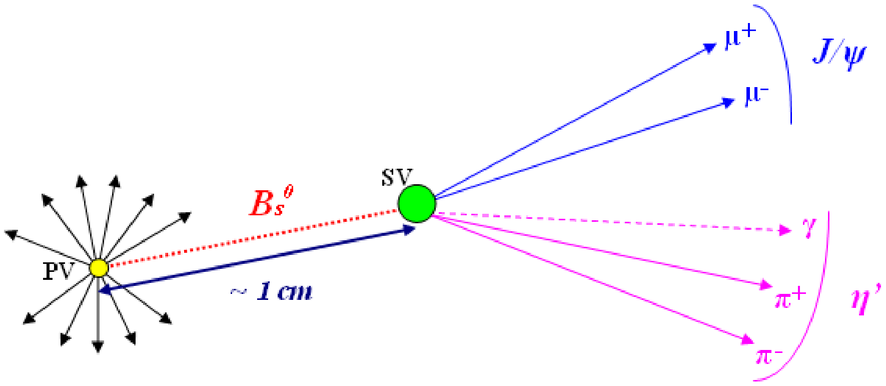

Figure 6.2: *The $B_s^0 \to J/\psi(\mu^+\mu^-)\ \eta'(\rho^0(\pi^+\pi^-)\gamma)$ decay mode. PV and SV denote the primary and the secondary vertex respectively.*

Table 6.1: *The main properties of the J/ψ, η' and ρ^0 mesons and their decay channels used in the study.*

Particle	J^{PC}	Mass (MeV/c^2)	Width (MeV/c^2)	Decay channel	BF ($\times 10^{-2}$)
J/ψ	1^{--}	3096.92 ± 0.01	0.093 ± 0.002	$J/\psi \to \mu^+\mu^-$	5.93 ± 0.06
η'	0^{-+}	957.78 ± 0.14	0.300 ± 0.090	$\eta' \to \rho^0(\pi^+\pi^-)\gamma$	29.4 ± 0.9
ρ^0	1^{--}	769.0 ± 0.9	150.9 ± 1.7	$\rho^0 \to \pi^+\pi^-$	~ 100

Ref. [9]. Due to $SU(3)$ symmetry breaking, the physical state of the η' is a mixture of the pseudoscalar $SU(3)$ octet, η_8, and pseudoscalar $SU(3)$ singlet, η_1, and can be written in the following way:

$$\eta' = \eta_8 \sin\theta_p + \eta_1 \cos\theta_p \quad , \tag{6.5}$$

where θ_p is the mixing angle. The η_8 and η_1 are defined as

$$\eta_8 = \frac{1}{\sqrt{6}}(u\bar{u} + d\bar{d} - 2s\bar{s}) \quad , \quad \eta_1 = \frac{1}{\sqrt{3}}(u\bar{u} + d\bar{d} + s\bar{s}) \quad . \tag{6.6}$$

Substituting (6.6) into (6.5) and taking into account that the η' meson is formed by a $s\bar{s}$ quark pair in the $B_s^0 \to J/\psi\eta'$ decay, one can write the η' wave function in the following way:

$$|\eta'\rangle = C(\theta_p)|s\bar{s}\rangle \quad , \quad \text{where} \quad C(\theta_p) = \frac{1}{\sqrt{3}}\cos\theta_p - \sqrt{\frac{2}{3}}\sin\theta_p \quad . \tag{6.7}$$

Unfortunately, the mixing angle θ_p is not well-defined. It needs to be determined experimentally. According to the latest experimental results θ_p varies between -10° and

$-20°$ [9]. As a result,

$$C(\theta_p) \in [0.71, 0.82] \quad . \tag{6.8}$$

The branching fraction of the $B_s^0 \to J/\psi\,\eta'$ decay is estimated using the well-measured branching fraction of the $B_d^0 \to J/\psi K^0$ channel. The decay amplitude of the $B_s^0 \to J/\psi\,\eta'$ can be presented in terms of the effective Hamiltonian as

$$A_{B_s^0 \to J/\psi\,\eta'} = < J/\psi\eta'|H_{\text{eff}}|B_s^0 > = C(\theta_p) < J/\psi\; s\bar{s}|H_{\text{eff}}|\bar{b}s > \quad . \tag{6.9}$$

This implies:

$$\text{BF}(B_s^0 \to J/\psi\eta') \sim C(\theta_p)^2 | < J/\psi\; s\bar{s}|H_{\text{eff}}|\bar{b}s > |^2 \; . \tag{6.10}$$

Analogously, in case of the $B_d^0 \to J/\psi K^0$ decay

$$A_{B_d^0 \to J/\psi K^0} = < J/\psi K^0|H_{\text{eff}}|B_d^0 > = < J/\psi\; s\bar{d}|H_{\text{eff}}|\bar{b}d > \quad , \tag{6.11}$$

$$\text{BF}(B_d^0 \to J/\psi K^0) \sim | < J/\psi\; s\bar{d}|H_{\text{eff}}|\bar{b}d > |^2 \quad . \tag{6.12}$$

The effective Hamiltonian for both processes is assumed to be the same, since both decays occur through the $\bar{b} \to \bar{c}c\bar{s}$ quark-level transition and U-spin flavour symmetry allows us to neglect the spectator quarks s and d. Dividing (6.10) by (6.12), one obtains the following relation:

$$\frac{\text{BF}(B_s^0 \to J/\psi\eta')}{\text{BF}(B_d^0 \to J/\psi K^0)} = C(\theta_p)^2 \quad . \tag{6.13}$$

With $\text{BF}(B_d^0 \to J/\psi K^0) = (8.72 \pm 0.33) \times 10^{-4}$ [9] the branching fraction for the $B_s^0 \to J/\psi\,\eta'$ varies between

$$\text{BF}(B_s^0 \to J/\psi\eta') = (4.40 \pm 0.17) \times 10^{-4} \;(\text{for } \theta_p = -10^0)$$

and

$$\text{BF}(B_s^0 \to J/\psi\eta') = (5.86 \pm 0.22) \times 10^{-4} \;(\text{for } \theta_p = -20^0) \; . \tag{6.14}$$

The total branching fraction for the $B_s^0 \to J/\psi(\mu^+\mu^-)\; \eta'(\rho^0(\pi^+\pi^-)\gamma)$ decay mode is defined as

$$\text{BF}_{\text{total}} = \text{BF}(B_s^0 \to J/\psi\eta') \times \text{BF}(J/\psi \to \mu^+\mu^-) \times \text{BF}(\eta' \to \rho^0(\pi^+\pi^-)\gamma) \, . \tag{6.15}$$

The expected annual production yield of a certain decay in the LHCb experiment can be estimated using the following relation:

$$N_{\text{signal}} = 2 \times \sigma_{b\bar{b}} \times L_{\text{year}}^{\text{int}} \times \text{BF}(\bar{b} \to B_s^0) \times \text{BF}_{\text{total}} \quad . \tag{6.16}$$

The factor 2 takes into account the possible production of both B_s^0 and $\bar{B}_s^0$ mesons from a $b\bar{b}$ pair, which has a branching fraction of $\text{BF}(\bar{b} \to B_s^0) = \text{BF}(b \to \bar{B}_s^0) = (10.4 \pm 1.4) \times$

Table 6.2: *The total branching fraction of the* $B_s^0 \to J/\psi(\mu^+\mu^-)\ \eta'(\rho^0(\pi^+\pi^-)\gamma)$ *decay channel and the expected number of the decays produced in the LHCb experiment with* $2\,\text{fb}^{-1}$ *of data.*

Mixing angle, θ_p	BF_{total} $(\times 10^{-6})$	N_{signal} $(\times 10^{6})$
$-10°$	7.67 ± 0.39	1.59 ± 0.23
$-20°$	10.2 ± 0.5	2.12 ± 0.31

10^{-2} [9]. The $b\bar{b}$ production cross section, $\sigma_{b\bar{b}}$, is expected to be about $500\,\mu$b [31]. Assuming an average nominal luminosity of $2 \times 10^{32}\,\text{cm}^{-2}\text{s}^{-1}$ and a time of data taking during one year of running of 10^7 s, the integrated luminosity, defined as $L_{\text{year}}^{\text{int}} = \int L\,dt$, is equal to $2\,\text{fb}^{-1}$. The product $\sigma_{b\bar{b}} \times L_{\text{year}}^{\text{int}} = 10^{12}$ gives the expected annual number of $b\bar{b}$ pairs produced in the experiment, as mentioned in Section 2.2. The total branching fraction of the $B_s^0 \to J/\psi(\mu^+\mu^-)\ \eta'(\rho^0(\pi^+\pi^-)\gamma)$ decay and its expected annual production yield are listed in Table 6.2. Due to the uncertainty on θ_p, the total branching fraction and the expected annual production yield vary between the two values. Therefore, in this study the selected signal yield and the background over signal ratio for this decay channel will be calculated for these two boundary cases.

6.2 Monte Carlo data samples

All of the physics results for the $B_s^0 \to J/\psi\,\eta'$ decay presented in this dissertation are obtained with the full Monte Carlo simulation of the LHCb experiment described in Section 5.1. In general, three different classes of simulated events, grouped into the data samples, can be distinguished: minimum-bias, $b\bar{b}$ inclusive and signal events. The minimum-biased sample consists of events which are recorded randomly — without bias. They are used for tuning the trigger. The $b\bar{b}$ inclusive sample includes those events, which contain at least one B hadron decay in the detector acceptance. Only a small fraction of these events contain the most interesting B meson decays, which can be used to measure CP violation, since their branching fractions typically vary between 10^{-4} – 10^{-6}. This type of events is mainly used to perform background studies. Finally, the signal events contain a specific B decay channel of interest. Nevertheless, in each event of the signal sample there may be many reconstructed tracks and neutral clusters coming from the underlying processes of the pp collison.

In each of the signal and inclusive $b\bar{b}$ samples, the particle of interest (i.e. the signal B meson, or one of the B hadrons in inclusive $b\bar{b}$ events) is required to have a polar angle smaller than 400 mrad. This is done to avoid the digitisation and reconstruction of events for which not all the B decay products are in the detector acceptance. For the signal samples, the fraction of events which obey this requirement is equal to $\varepsilon_{\theta}^{\text{signal}} = (34.7 \pm 0.3)\%$. For the inclusive $b\bar{b}$ sample, this is equal to $\varepsilon_{\theta}^{b\bar{b}} = (43.4 \pm 0.3)\%$.

The data samples used in this dissertation are presented in Section 6.6. All of them have been produced during the Data Challenge 2004 (DC04). In LHCb, the production of a Monte Carlo event uses a random number (seed), which is generated as a 32 bit number. Unfortunately, the first round of generation, DC04–v1, only used the 24 least significant bits of the seed. As a result, instead of 2^{32} = 4 294 967 296 different seeds, only 2^{24} = 16 777 216 seeds have been randomly chosen (in the best case — when all the seeds are used at least once). This results in the presence of duplicated events in all data samples produced in DC04–v1. According to Ref.[20], the number of independent events N_{indep} and its error $\sigma_{N_{\text{indep}}}$ can be estimated using the following formulas:

$$N_{\text{indep}} \approx 2^{24} \times (1 - e^{-N/2^{24}}) \quad , \quad \sigma^2_{N_{\text{indep}}} \approx N_{\text{indep}} \times e^{-N/2^{24}} \quad , \tag{6.17}$$

where N is the number of events in initial sample. The fraction of independent events in a data sample is $f_{\text{indep}} = N_{\text{indep}}/N$. For the data sample of the $B_s^0 \to J/\psi\,\eta'$ decay channel, 139 000 events have been generated in total, the corresponding number and the fraction of independent events are:

$$N_{\text{indep}} = 138410 \pm 371 \quad , \quad f_{\text{indep}} = 0.996 \pm 0.003 \quad . \tag{6.18}$$

This fraction is assumed to be the same in all subsets of an initial sample. It should be noted that, in this study, all reconstructed signal events of the $B_s^0 \to J/\psi\,\eta'$ decay that passed the selection cuts have been checked to be unique. In order to evaluate the selection efficiencies, the number of signal events generated in this study is multiplied by f_{indep}.

The problem described above does not relate to the $b\bar{b}$ inclusive sample used in this study, since this sample has been produced after this bug was fixed, during the second round of generation, DC04–v2.

6.3 Particle identification

In the LHCb experiment, the information from different subdetectors allows to assign a particle identification (PID) to the reconstructed tracks. As mentioned in Chapter 2, electrons (together with the neutral particles γ and π^0) are primarily identified using the Calorimeter system, muons with the Muon detector and hadrons (π, K, p) with the RICH detectors. However, the RICH system can also be used to identify leptons. The combined information from the various subdetectors improves the overall PID performance. For

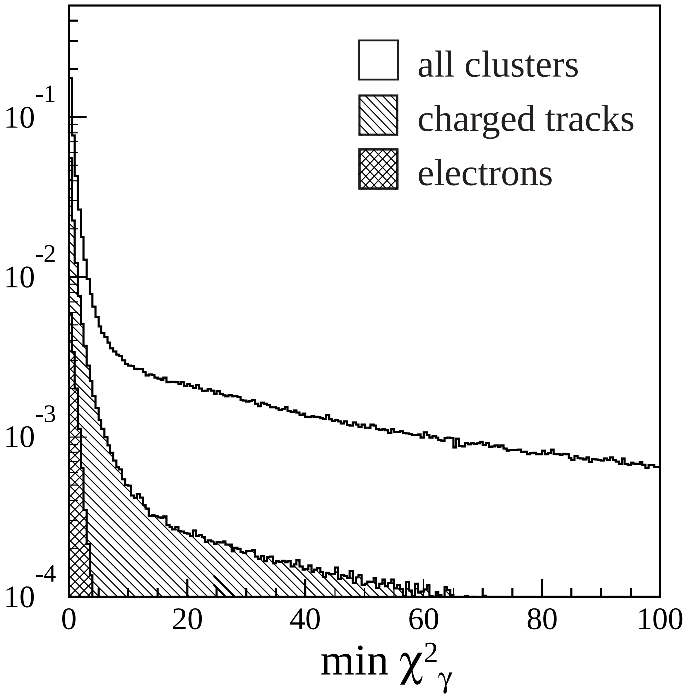

Figure 6.3: *The minimal value of the χ^2_γ estimator from the track-cluster position matching procedure for ECAL clusters.*

each particle type, this combined PID information is computed as a likelihood defined as:

$$\begin{aligned}
L(\mathrm{e}) &= L^{\mathrm{RICH}}(\mathrm{e})\,\mathrm{L}^{\mathrm{CALO}}(\mathrm{e})\,\mathrm{L}^{\mathrm{MUON}}(\mathrm{non}\,\mu) \\
L(\mu) &= L^{\mathrm{RICH}}(\mu)\,L^{\mathrm{CALO}}(\mathrm{non\,e})\,\mathrm{L}^{\mathrm{MUON}}(\mu) \\
L(h) &= L^{\mathrm{RICH}}(h)\,L^{\mathrm{CALO}}(\mathrm{non\,e})\,\mathrm{L}^{\mathrm{MUON}}(\mathrm{non}\,\mu)\ ,
\end{aligned}$$

where h represents a hadron which is either π, K or p. Each of these functions is a product of the PID likelihood estimators from the different subdetectors.

In order to compare two different particle hypotheses for the reconstructed track, the ratio of the corresponding likelihoods is calculated. The logarithm of this ratio is equivalent to a difference in the log-likelihoods:

$$\Delta\ln L_{AB} = \ln\left(\frac{L(A)}{L(B)}\right) = \ln L(A) - \ln L(B)\ \ , \qquad (6.19)$$

where $L(A)$ and $L(B)$ are the combined likelihoods for the A and B hypotheses. A particle of type A tends to have a positive $\Delta\ln L_{AB}$, while a particle of type B tends to have a negative $\Delta\ln L_{AB}$. This function is used as a selection variable.

The method described above can only be applied to charged particles. For the identification of neutral particles there is another technique. The selection of photon candidates is based on the matching of all reconstructed clusters in ECAL with all reconstructed tracks extrapolated to the ECAL reference plane. The cluster-track matching estimator, χ^2_γ, is constructed using the track impact point, the cluster barycentre, the track's covariance matrix, and the matrix of second-order cluster moments. For each cluster, the track with the minimal χ^2_γ value is determined. The minimal χ^2_γ estimator for different types of clusters is shown in Fig. 6.3. As can be seen, the peak at small values of χ^2_γ corresponds mainly to clusters produced by charged particles, including electrons. The clusters with a minimal value of χ^2_γ greater than 4 are selected as neutral clusters — photon candidates. This cut rejects the clusters due to electrons and significantly suppresses clusters due to other charged particles.

Another neutral particle, the π^0, is detected using the $\pi^0 \rightarrow \gamma\gamma$ decay. At low p_{T} (less than $3\,\mathrm{GeV}/c$), π^0's create a resolved pair of well-separated photons in the ECAL. They can be reconstructed by combining all photon candidates and applying a cut on the invariant mass. For π^0's with a higher p_{T}, there is a single, merged cluster, since the ECAL granularity does not allow to separate the two photons anymore.

6.4 Flavour tagging

In order to measure *CP* violation with neutral B mesons it is necessary to know their initial flavour state. The identification of the B meson flavour at production is called flavour tagging. The corresponding method tries to determine whether the reconstructed B meson was produced from a b or $\bar{b}$ quark. There are two different strategies to achieve this:

- **Opposite-side tagging**. This method is based on determination of the flavour of the other B hadron from the $b\bar{b}$ pair in the event. It can be determined by detecting the charge of the lepton from a semileptonic B decay or the charge of the kaon from a $b \rightarrow c \rightarrow s$ transition. The selection is done by searching for leptons and kaons with a high transverse momentum and a large impact parameter. However, there is an intrinsic dilution in case the tagging B hadron is a neutral meson, since it can oscillate before decay.

- **Same-side tagging**. In this case, the flavour of the signal meson is determined directly. This method is applied to tag B_s mesons. It takes into account the fact, that there is an extra $\bar{s}$ quark, when a B^0_s ($\bar{b}s$) meson is produced in a pp collision. Similarly, there is an extra s quark when a $\bar{B}^0_s$ meson is produced. The s or $\bar{s}$ quark hadronises into a charged kaon in about 50% of the cases. If the charge of the kaon is positive then a B^0_s has been produced and if it is negative then a $\bar{B}^0_s$ has been produced. These kaon tracks originate from the primary vertex and are correlated in phase space with the signal B_s^0. In principle, the same approach can be used to tag B_d mesons using charged pions. However, it is rather difficult to select these tagging pions due to the large pion multiplicity.

The methods described above are combined together to obtain the best tagging performance, which is determined by two parameters: the tagging efficiency, ε_{tag}, and the wrong tag fraction, w_{tag}. They are calculated as:

$$\varepsilon_{\text{tag}} = \frac{N_R + N_W}{N_R + N_W + N_U} \quad , \quad w_{\text{tag}} = \frac{N_W}{N_R + N_W} \quad , \tag{6.20}$$

where N_R, N_W, N_U are the number of correctly tagged, incorrectly tagged and untagged signal decays. Clearly, the first parameter gives the fraction of selected decays which are tagged, while the second defines the quality of tagging[2]. The observed asymmetry, A_{obs}, is diluted by the wrong tag fraction as:

$$A_{\text{obs}} = D \times A_{\text{phys}} \quad \text{with} \quad D = 1 - 2w_{\text{tag}} \quad , \tag{6.21}$$

where A_{phys} is the true asymmetry and D is the dilution factor. As can be seen, if the wrong tag fraction is equal to 50%, then no asymmetry is observed by the experiment.

The statistical uncertainty of the observed asymmetry arising from the tagging is proportional to

$$\sigma_{A_{\text{obs}}} \propto \frac{1}{\sqrt{\varepsilon_{\text{tag}} N}} \text{ , and accordingly } \sigma_{A_{\text{phys}}} \propto \frac{1}{D\sqrt{\varepsilon_{\text{tag}} N}} = \frac{1}{\sqrt{\varepsilon_{\text{tag}}^{\text{eff}} N}} \ , \tag{6.22}$$

where N is the number of selected and triggered signal decays and $\varepsilon_{\text{tag}}^{\text{eff}}$ is the effective tagging efficiency (or tagging power), which is defined as

$$\varepsilon_{\text{tag}}^{\text{eff}} = \varepsilon_{\text{tag}} \times (1 - 2w_{\text{tag}})^2 = \varepsilon_{\text{tag}} \times D^2 \quad . \tag{6.23}$$

As can be seen, a high tagging efficiency and a low wrong tag fraction are needed to obtain a large $\varepsilon_{\text{tag}}^{\text{eff}}$ and thus, have a good sensitivity to observe *CP* asymmetry. In the LHCb experiment, the tagging efficiency for the most interesting *B* meson decays varies between 55% – 65%, while a wrong tag fraction ranges between 30% – 35% [93].

6.5 $B_s^0 \to J/\psi\,\eta'$ reconstruction aspects

Before explaining the selection studies, it is important to consider the reconstruction characteristics for the final state particles of the $B_s^0 \to J/\psi\,\eta'$ decay. The quality of reconstruction of these particles dictates the selection performance of the decay.

---

[2] It gives the fraction of tagged decays that have a wrong tag assignment.

6.5.1 Charge particle reconstruction

In general, there are five different classes of tracks in the LHCb detector, depending on their origin and momentum:

- **Long tracks**: are high-momentum tracks which traverse the full LHCb tracking setup from the VELO to the T stations.
- **Upstream tracks**: are low-momentum tracks which leave hits only in the VELO and the Trigger Tracker before they are swept away by the magnetic field.
- **Downstream tracks**: traverse only the Trigger Tracker and T stations. These are typically the decay products of the K_s^0 and Λ particles which decay outside the VELO acceptance.
- **VELO tracks**: leave hits only in the VELO and are usually large-angle or backward tracks. They are useful for the primary vertex reconstruction.
- **T tracks**: are only detected in the T stations and are typically produced in secondary interactions.

A detailed description of the track reconstruction strategy and performance in the LHCb detector is given in Ref. [31, 36].

It should be noted that only long tracks are used in our study. The other types of tracks are not considered, since:

- the decay products of the $B_s^0 \to J/\psi\,\eta'$ must originate from the VELO, where the B_s^0 decay vertex is located;
- the charged particles must traverse the whole detector to perform accurate momentum and PID measurements.

The first requirement removes downstream and T tracks from the study and the second eliminates VELO and upstream tracks. The reconstruction properties for muon and pion tracks arising from the $B_s^0 \to J/\psi\,\eta'$ decay is expected not to differ from the overall reconstruction performance of long tracks described in Ref. [31, 36]. However, in this section we consider the reconstruction quality for the signal muon and pion tracks separately.

To investigate the performance of the track reconstruction for particles from the signal decay, 100 000 events of the signal sample have been used. Only the properties of reconstructed long tracks which have been correctly associated to a particle (μ^+, μ^-, π^+ or π^-) from the $B_s^0 \to J/\psi\,\eta'$ decay have been studied.

First, the accuracy of the track momentum is considered. Figure 6.4 illustrates the relative momentum residual[3], $\delta p/p$, for different types of the signal tracks. The momentum

---

[3] It is defined as $\delta p/p = (p_{\mathrm{rec}} - p_{\mathrm{true}})/p_{\mathrm{true}}$, where p_{rec} is the momentum of the reconstructed track and p_{true} is the momentum of the original particle.

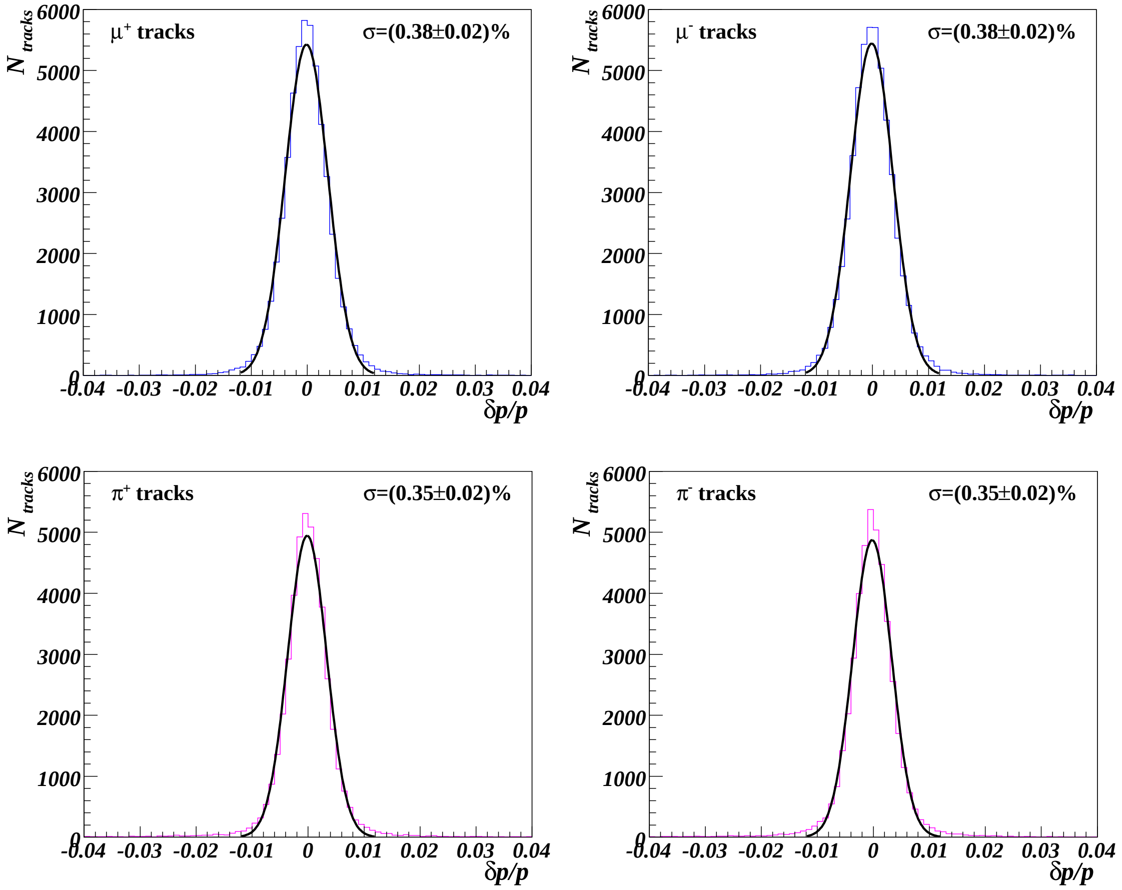

Figure 6.4: *The relative momentum residual of long tracks originating from the $B_s^0 \to J/\psi\,\eta'$ decay at the production vertex. A single Gaussian is fitted to the distributions.*

resolution is defined as a standard deviation of a Gaussian fit to the $\delta p/p$ distribution. As can be seen, the reconstructed tracks from our decay have an accurate momentum estimate, consistent with the results for long tracks described in Ref. [31, 36].

A slightly better momentum resolution for pion tracks than that for muon tracks is observed. It can be explained by the increase in curvature of the pion tracks, since they have on average a lower momentum than muons in this decay, as shown in Fig. 6.5. As can be seen in Fig. 6.6, the momentum resolution increases towards higher momentum for both pions and muons.

At the next step, the reconstruction efficiency as a function of several parameters for the signal tracks is studied. The reconstruction efficiency is defined as:

$$\varepsilon = N_{\mathrm{rec}}/N_{\mathrm{MC}} \quad ,$$

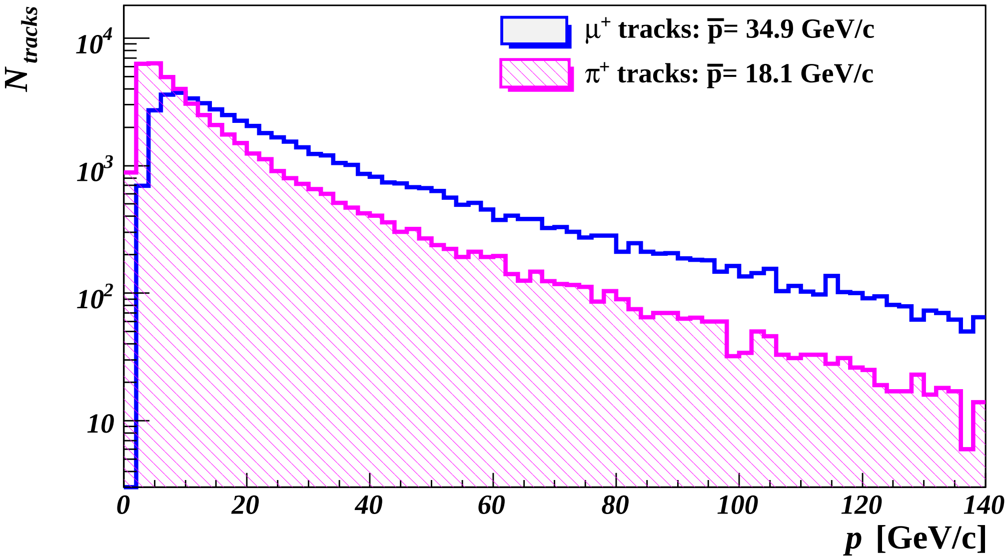

Figure 6.5: *The reconstructed momentum of the μ^+ and π^+ tracks arising from the $B_s^0 \to J/\psi\,\eta'$ decay.*

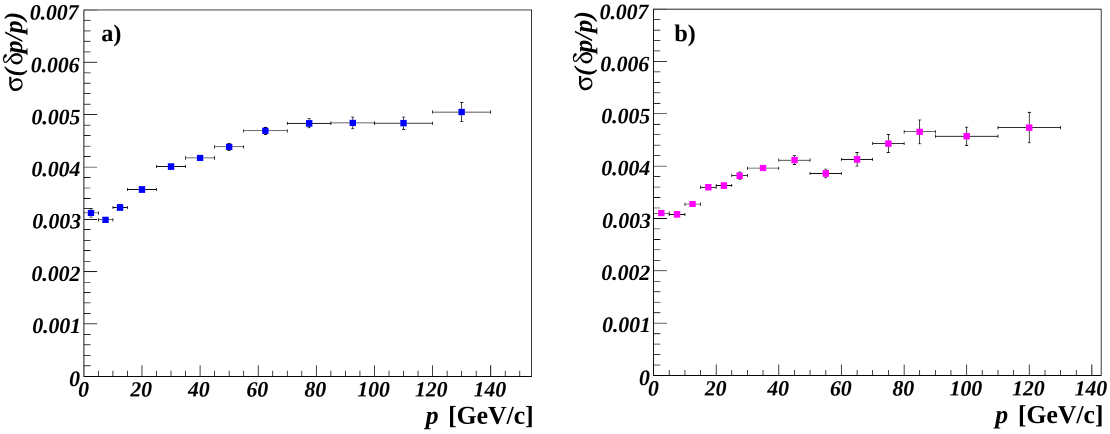

Figure 6.6: *The momentum resolution as a function of track momentum: (a) for the μ^+ tracks and (b) for the π^+ tracks originating from the $B_s^0 \to J/\psi\,\eta'$ decay. A single Gaussian fit has been used to determine the momentum resolution in each momentum bin.*

where N_{rec} is the number of reconstructed tracks which are correctly matched to a particle from the $B_s^0 \to J/\psi\,\eta'$ decay and N_{MC} is the total amount of such particles from this decay.

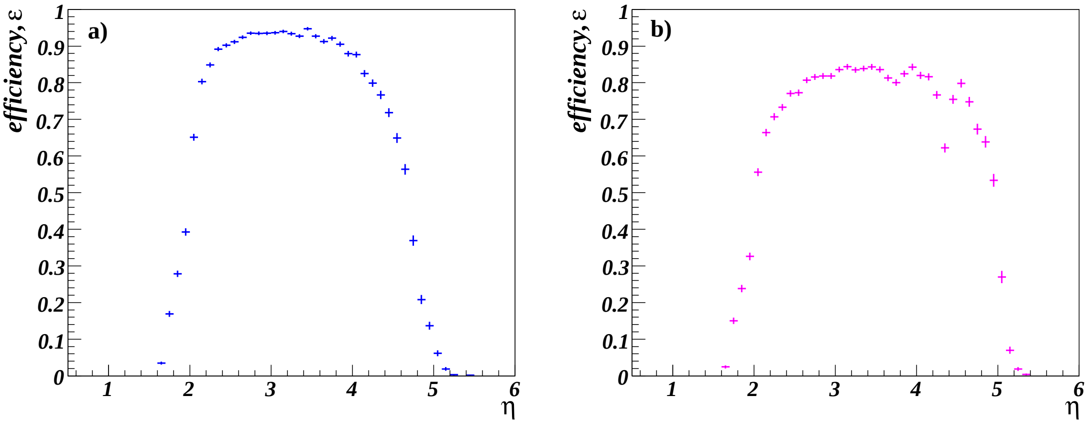

Figure 6.7: *Tracking efficiency as a function of pseudorapidity: (a) for the μ^+ tracks and (b) for the π^+ tracks arising from the $B_s^0 \to J/\psi\,\eta'$ decay.*

Figure 6.7 illustrates the efficiency of the track reconstruction as a function of the pseudorapidity η, which determined by the production angle θ of a particle relative to the beam axis. It is defined as

$$\eta = -\ln\tan\left(\frac{\theta}{2}\right) \quad . \tag{6.24}$$

In LHCb, a pseudorapidity range of $1.9 < \eta < 4.9$ will be covered by the detector. In this investigation of the reconstruction efficiency versus pseudorapidity, a cut of $p > 3$ GeV/c is applied on the true momentum of muons to ensure that they are able to reach the LHCb Muon stations and as a result, can be detected and recognised as muon tracks. For pions, only particles with momentum in the range $2 < p < 100$ GeV/c are taken into account, since only these pions can potentially be well identified by the LHCb detector. As can be seen, a reconstruction efficiency of around $91-93\%$ is achieved for the range $2.5 < \eta < 4.0$ for muons. In case of the signal pion tracks, the efficiency is about $81-84\%$ for the range $2.7 < \eta < 4.2$. The drop in efficiency outside these pseudorapidity ranges can be explained by the fact, that these tracks are produced at the edge of the detector acceptance.

The dependence of the reconstruction efficiency on the track momentum is shown in Fig. 6.8 for signal muons and pions, which are traversing the detector in a central region ($2.5 < \eta < 4.0$). As can be seen, it rises as a function of the momentum, until it reaches a plateau in both cases. An efficiency of 92–95% is achieved for muons with a momentum above $5-6\,\mathrm{GeV}/c$. For pions, it reaches approximately 82–87% for tracks with a momentum larger than $5\,\mathrm{GeV}/c$.

The total reconstruction efficiency of muons and pions originating from the $B_s^0 \to J/\psi\,\eta'$ decay is about 54% and 46%, respectively. Many of the signal tracks are lost due

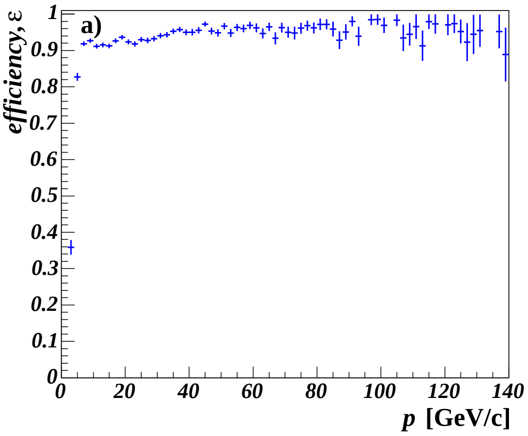

Figure 6.8: *Tracking efficiency as a function of momentum: (a) for the μ^+ tracks and (b) for the π^+ tracks originating from the $B_s^0 \to J/\psi\,\eta'$ decay.*

to the detector acceptance. In order to explain why the reconstruction efficiency is found to be less for pions than for muons, the following arguments should be taken into account:

- **Pion misidentification.** Some fraction of the pions is lost due to the wrong PID assignment, since the requirement $\Delta \ln L_{\mu\pi}\ (\pi^+,\pi^-) < 8$ was applied in this study. In LHCb, the average pion misidentification rate relative to kaons is about 3% in the momentum range of $2 < p < 100\,\mathrm{GeV}/c$ [31].

- **Hadronic interactions.** Sometimes, the original pion is lost for detection due to the nuclear interaction in the detector material. This typically results in the creation of showers of secondary pions.

- **Decays of pions.** Several percent of the signal pions decay via $\pi^+ \to \mu^+\nu_\mu$ and $\pi^- \to \mu^-\bar{\nu}_\mu$ channels before reaching LHCb tracking stations.

- **Multiple scattering.** In general, the track reconstruction for low-momentum particles is more complicated than for particles with high momentum. This is due to multiple scattering which is the result of Coulomb interaction of a charged particle traversing a medium with its nuclei or atomic electrons. This process alters the particle's original trajectory. The deflection angles are inversely proportional to the particle's momentum [9]. Since pions are less energetic particles than muons in case of the $B_s^0 \to J/\psi\,\eta'$ decay, they are more affected by multiple scattering.

It should be noted that, the multiplicity of charged pions is much larger than that of muons. In $b\bar{b}$ inclusive events, there are approximately 150 times more pions than muons reconstructed as long tracks. On average, one event of the signal sample contains 22 reconstructed pion tracks and only one reconstructed muon track. Also, 82% of all charged pions reconstructed as long tracks in the signal sample arises from the primary vertex. These are high-momentum pions produced directly in the pp collision. The rest consists of pions which are the decay products of other particles arising from the fragmentation (9.7%), pions originating from the $B_s^0 \to J/\psi\eta'$ decay channel (4.2%), and pions from the other B decay (4.1%). Therefore, in the selection it is important to reject pions originating from the primary vertex. In case of muons, the selection is much easier. Since they have a much lower multiplicity and almost 91% of all reconstructed muon tracks in the signal sample are particles from the $B_s^0 \to J/\psi\eta'$ decay.

6.5.2 Photon reconstruction

As described in Section 6.3, the photon identification and reconstruction is performed by the ECAL. The reconstruction of photons is not a trivial task because of secondary interactions. The detector material before the ECAL is a source of photon conversions ($\gamma \to e^+e^-$ process). Those photons that have converted before the magnet may be detected as two charged clusters in the ECAL (if they are not swept away by the magnetic field). However, it is very hard to identify them as photon conversion products. Photons that have converted after the magnet are detected as a single cluster and can therefore be identified by the ECAL. Usually, no corresponding electron tracks are reconstructed in this case. To recognise such clusters as converted, information from the SPD cell that lies in front of the ECAL cluster is used. As mentioned in Chapter 2, the SPD identifies charged particles, since they produce ionisation, as opposed to neutral clusters. In this study, both converted and non-converted photons are used to construct the η' candidates.

Since neutral particles do not leave hits in the tracking detectors, it is impossible to reconstruct their direction. Therefore, the selected photon candidates are assumed to originate from the B decay vertex and their four momentum is calculated accordingly. For the precise determination of the energy and position of neutral clusters it is important to take into account the following effects:

- the energy losses in the detector material before the ECAL (for converted photons only) and in the passive material between ECAL cells;
- the longitudinal and transversal shape of the electromagnetic shower.

These items as well as many other aspects of photon reconstruction in the LHCb detector are described in Ref. [94].

Figure 6.9 illustrates the number of reconstructed photon candidates per signal event. As can be seen, on average almost 40 photon candidates are reconstructed. In case of $b\bar{b}$

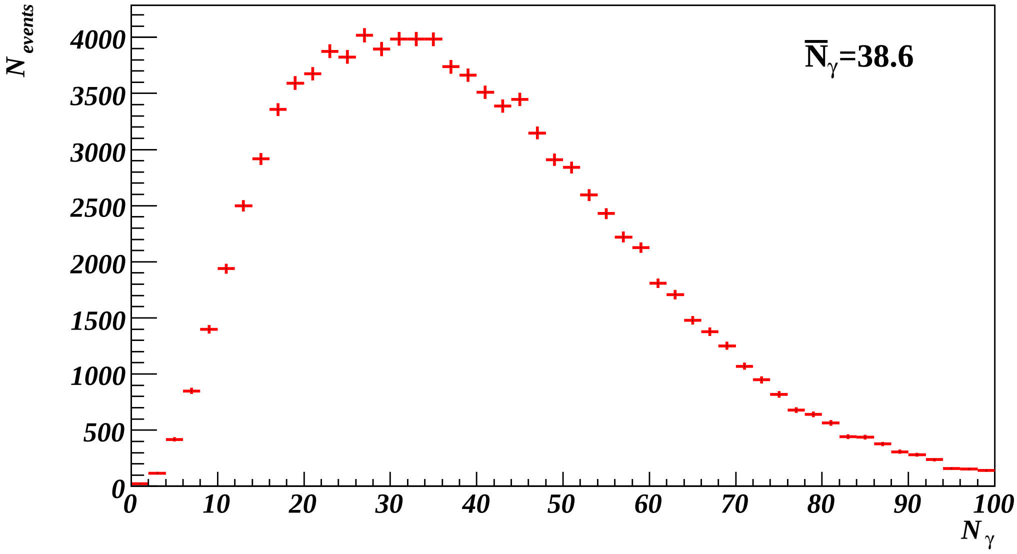

Figure 6.9: *The number of reconstructed photon candidates per signal event.*

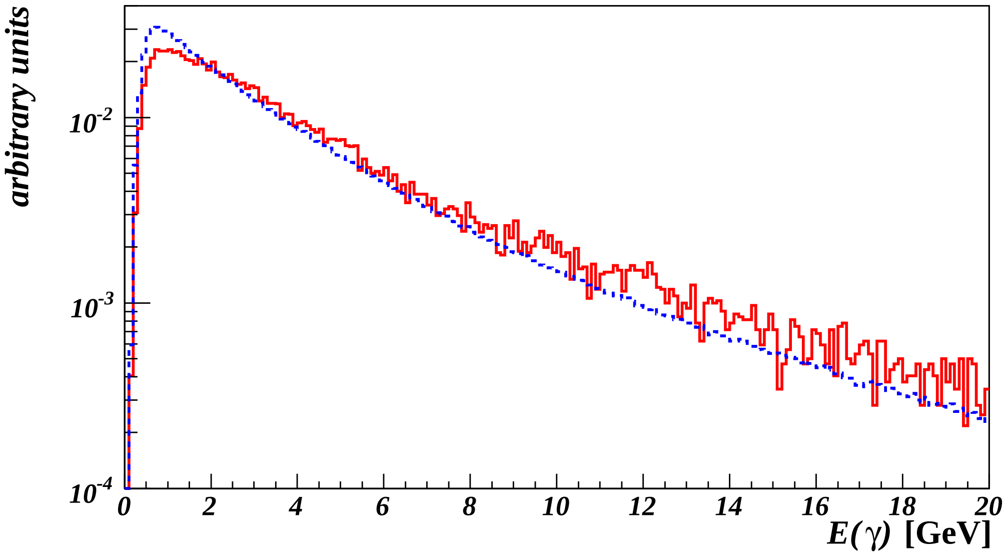

Figure 6.10: *The reconstructed energy for photons from the signal decay (red solid line), and for photons from the $b\bar{b}$ background (blue dashed lines). Signal and background distributions are normalised to the total number of entries in their histograms.*

inclusive events, this number is also approximately equal to 40. It is interesting to note that 80.5% of all photon candidates reconstructed in 100 000 events of the signal sample are matched to the correct γ. Moreover, 99% of all reconstructed photons associated to the correct γ originate from the underlying event (most of them are the decay products of π^0's) and only 1% are the signal photons coming from the $B_s^0 \to J/\psi\,\eta' \to \mu^+\mu^-\pi^+\pi^-\gamma$ decay chain. However, this 1% represents a third of all generated signal photons. As a result, the probability to reconstruct the signal photon from the $B_s^0 \to J/\psi\,\eta'$ decay is around 33%.

Due to the high multiplicity of photons, there is a high probability to select a wrong neutral cluster in the ECAL. An additional difficulty is that the energy of the reconstructed signal photons is not significantly larger than the energy of the background clusters as seen in Fig. 6.10. Therefore, the selection of signal photons is a rather complicated task.

6.6 $B_s^0 \to J/\psi\,\eta'$ event selection

In order to select the signal decays from the huge amount of pp events, it is necessary to apply tight selection cuts. The presence of high-p_{T} decay products with an invariant mass close to the nominal B mass and a decay vertex which is significantly displaced with respect to the production vertex are the main signatures of a B meson decay. The generic B decays in $b\bar{b}$ inclusive events share these properties with the specific signal decay of interest. Since the branching fraction of a specific signal decay is tiny compared to the total amount of $b\bar{b}$ inclusive events, the $b\bar{b}$ inclusive events are considered as the most dangerous background source. The different selection requirements are tuned to eliminate as much as possible the $b\bar{b}$ inclusive events while retaining a high reconstruction efficiency for $B_s^0 \to J/\psi\,\eta'$ events. Another important remark is that the reconstruction of the $B_s^0 \to J/\psi(\mu^+\mu^-)\ \eta'(\rho^0(\pi^+\pi^-)\gamma)$ channel involves a large combinatorial background due to the high photon and pion multiplicity. Therefore, the selection cuts should provide a suppression of the combinatorial background.

Furthermore, several data samples of specific B decay modes, which have a similar decay topology are used to check the performance of the selection cuts in addition. For all of them the fraction of independent events is around of 94% − 99%. The data samples used in this study are listed in Table 6.3.

The event selection algorithms are based on the DAVINCI application (version v12r18). In addition, in order to facilitate the physics analysis the event selection algorithms use the LOKI package [95] (version v3r14). This toolkit provides high-level utilities, which allow to loop over particle combinations, calculate kinematical parameters and associate reconstructed particles to the true signal decay products in a simple and uniform manner.

Table 6.3: *The data samples used in this study and the corresponding number of generated events.*

Event type	Number of generated events
$B_s^0 \to J/\psi(\mu^+\mu^-)\,\eta'(\rho^0(\pi^+\pi^-)\gamma)$	100 000
$b\bar{b}$ inclusive	33 616 466
$B_d^0 \to J/\psi(\mu^+\mu^-)\,K^*(K^\pm\pi^\mp)\gamma)$	80 000
$B_d^0 \to J/\psi(\mu^+\mu^-)\,K_s^0(\pi^+\pi^-)$	70 000
$B_d^0 \to J/\psi(\mu^+\mu^-)\,\pi^0(\gamma\gamma)$	70 000
$B_s^0 \to J/\psi(\mu^+\mu^-)\,\phi(K^+K^-)$	70 000
$B_s^0 \to J/\psi(\mu^+\mu^-)\,\eta(\gamma\gamma)$	70 000
$B_s^0 \to J/\psi(\mu^+\mu^-)\,\eta(\pi^+\pi^-\pi^0(\gamma\gamma))$	70 000
$B_u^+ \to J/\psi(\mu^+\mu^-)\,K^+$	70 000

6.6.1 Selection procedure

In general, the selection of the $B_s^0 \to J/\psi\,\eta'$ events is divided into four subsequent stages:

- **Determination of the selection variables**. At the first step, a set of reconstruction parameters is defined, which will be used as selection variables. Each of them provides a good separation between signal and background events.

- **Preselection**. At the next step, a set of loose cuts on the selection variables is applied to both the signal and $b\bar{b}$ inclusive samples. This allows to reduce the combinatorial background in the signal, and especially, in the background sample.

- **Cut optimisation**. This stage provides a final tuning of the selection cuts. It uses the event samples for the signal and background combinations which passed through the preselection cuts. An optimisation algorithm is used to determine the optimal values for the cuts on the selection variables simultaneously. It provides a selection of a large number of the signal events with the highest possible background suppression.

- **Analysis of the selection results**. The events that passed through the final selection cuts are studied. The annual signal yield and background-over-signal ratio are calculated. The quality of reconstruction in terms of mass, vertex and decay time resolutions is obtained.

Each of these stages is described in detail in the next sections of this dissertation.

6.6.2 Reconstruction strategy and selection variables

The selection of $B_s^0 \to J/\psi\,\eta'$ events starts with the reconstruction of J/ψ and η' candidates. Afterwards, they are combined together to form B_s^0 mesons. In this section, a detailed overview of the reconstruction strategy and the selection variables is given.

$\mathbf{J/\psi}$ reconstruction

The J/ψ candidates are formed by taking two tracks with opposite electric charge which are identified as muons. They should originate from a common point in space. Therefore, a vertex fit is applied to the muon pair. The invariant mass should be close to the nominal mass of the J/ψ. In this study, there are three selection variables, which are used to construct the J/ψ candidates:

- $\Delta\ln L_{\mu\pi}$ (μ^+,μ^-). This selection variable gives the difference in log-likelihood between the muon and pion hypotheses. Most charged particles that are reconstructed as long tracks in $b\bar{b}$ inclusive events are pions. Therefore, the requirement on this selection variable is used to ensure a high purity of real muons.
- χ^2 $(\mu^+\mu^-)$. The requirement on the χ^2 from the vertex fit selects only muon pairs coming from a common point in space.
- $\Delta M_{J/\psi}$ $(\mu^+\mu^-)$. This variable defines a window around the nominal mass of the J/ψ in the invariant mass spectrum of the two muon tracks.

$\boldsymbol{\eta'}$ reconstruction

The reconstruction of the η' meson is more challenging than that of the J/ψ, since it requires to reconstruct two pion tracks and one photon. These particles have a high multiplicity resulting in a large combinatorial background of η' candidates. As noted before, it is rather difficult to distinguish between signal and background photons, since the energy spectrum for both is almost identical.

The reconstruction of the η' meson is performed in two steps. First, two reconstructed tracks identified as π^+ and π^- coming from a common vertex are selected[4]. Second, a reconstructed photon candidate is selected and combined with the $\pi^+\pi^-$ pair[5] to form a η' candidate. The following set of the selection variables is used for the η' reconstruction:

---

[4] Due to the large decay width of the ρ^0 meson and the non-resonant contribution $\eta' \to \pi^+\pi^-\gamma$, there is no requirement on the invariant mass of these two tracks.

[5] At this step, the photon four-momentum is recalculated with respect to the $\pi^+\pi^-$ vertex.

- $\Delta\ln L_{\mu\pi}$ (π^+,π^-) and $\Delta\ln L_{K\pi}$ (π^+,π^-). In order to be able to elicit the pion tracks, the differences in log-likelihood between the muon and pion hypotheses and between the kaon and pion hypotheses are used. It limits the background by suppressing tracks from muons and kaons.

- χ^2 $(\pi^+\pi^-)$. The requirement on the χ^2 from the vertex fit selects pion pairs coming from a common point in space.

- $\mathrm{IP}/\sigma_{\mathrm{IP}}$ $(\pi^+,\ \pi^-)$. Many pion tracks arising from the primary vertex can be rejected by a requirement on the impact parameter significance with respect to the primary vertex. However, a rather loose requirement on this selection variable is used in this dissertation, since it distorts the decay time distribution, which is needed to study the time-dependent *CP* asymmetry.

- E_{T} (γ). This variable defines a threshold on the transverse energy of the photon candidates to reduce the high-multiplicity of low-energetic neutral background clusters.

- p_{T} (η'). The η' meson arising from the $B_s^0 \to J/\psi\,\eta'$ decay is expected to have a high transverse momentum. The η' candidates from random $\pi^+\pi^-\gamma$ combinations typically have a low p_{T}.

- $\cos\angle(p_{\rho^0}, p_\gamma)_{\mathrm{LAB}}$. This is the angle between reconstructed momentum of the ρ^0 and γ in the laboratory system. This angle is expected to be small for signal events, since the η' meson usually decays with a small opening angle between the ρ^0 and the photon. The cosine of this angle for the signal and $b\bar{b}$ events is shown in Fig. 6.11.

- $\cos\angle(p_{\eta'}, p_\pi)_{\rho^0 \mathrm{r.f.}}$. One can exploit the polarisation of pions originating from the $\eta' \to \rho^0(\pi^+\pi^-)\gamma$ decay. The η' has helicity 0, since it is a pseudoscalar meson. The ρ^0 is a vector meson with three possible helicity states: -1, 0, 1. For the γ, which is a massless vector boson, there are by definition only two helicity states: -1 and 1. Hence, the η' meson decays either to a ρ^0 with helicity 1 and a γ with helicity -1 or to a ρ^0 with helicity -1 and a γ with helicity 1. It means that in the $\eta' \to \rho^0\gamma$ decay there are no ρ^0 mesons with helicity 0. This results in an angular distribution for pions originating from the $\eta' \to \rho^0(\pi^+\pi^-)\gamma$ decay which is different from the angular distribution of pions originating from random background. The angle between the reconstructed momentum of the η' and π, calculated in the ρ^0 rest frame, is chosen as a selection variable in this analysis. Figure 6.12 illustrates the distribution of the cosine of this angle for signal and $b\bar{b}$ events.

- $\Delta M_{\eta'}$ $(\pi^+\pi^-\gamma)$. This is the window around the nominal mass of the η' in the invariant mass spectrum of the two pions and the photon.

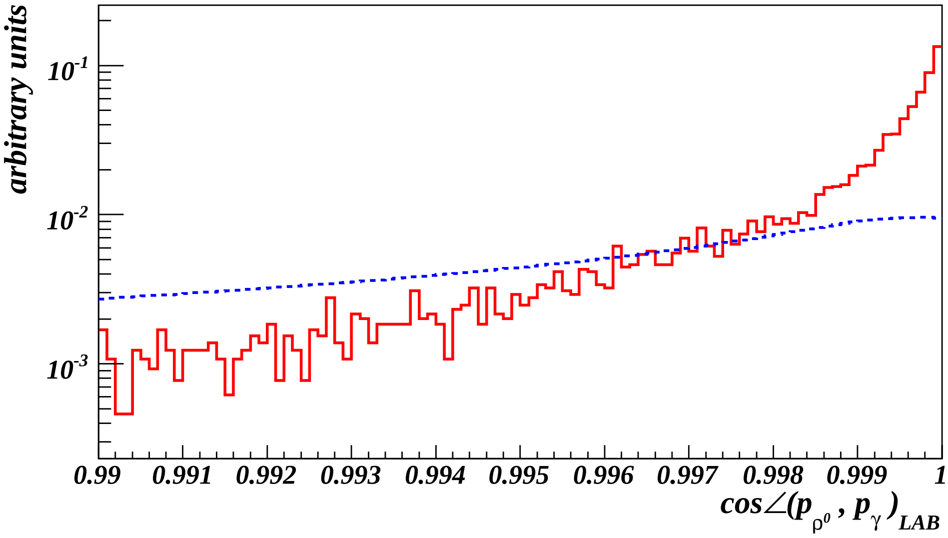

Figure 6.11: *The* $\cos\angle(p_{\rho^0}, p_\gamma)_{\mathrm{LAB}}$ *for the true signal (red solid line) and inclusive* $b\bar{b}$ *(blue dashed line) events. No cuts are applied. The signal and background distributions are normalised to the total number of entries in their histograms.*

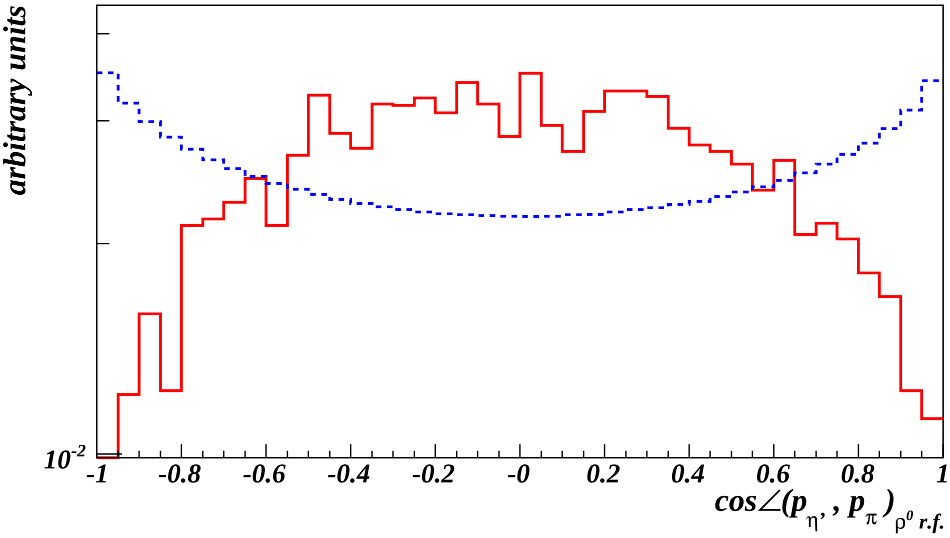

Figure 6.12: *The* $\cos\angle(p_{\eta'}, p_\pi)_{\rho^0\mathrm{r.f.}}$ *for the true signal (red solid line) and inclusive* $b\bar{b}$ *(blue dashed line) events. No cuts are applied. The signal and background distributions are normalised to the total number of entries in their histograms.*

Mass-constrained vertex fit

In this study, a mass-constrained vertex fit is used as the last step in the J/ψ and η' reconstruction. It constrains the mass of the mother particle to its nominal value by modifying the momentum of the daughter particles during the vertex fit, according to:

$$M^2 = \left(\sum_{i=1}^{N} p_i \right)^2 \quad ,$$

where M is the invariant mass, N is the number of particles and p_i is the four-momentum of these particles. This constraint is added to the geometrical vertex fit. It improves the reconstruction of the mother particle's momentum and the vertex position. Note that the χ^2 of this fit for the B itself should not be used as a selection variable, since it distorts the invariant mass distribution. The side-bins in the B invariant mass spectrum are needed to investigate the background behaviour in the signal range. More information about the vertex fit technique can be found in Ref. [96].

$\mathbf{B_s^0}$ meson reconstruction

After performing all steps described above, the selected J/ψ and η' candidates in each event are combined together to form a B_s^0 meson. First, a selection of the primary vertex with the smallest impact parameter to the reconstructed B_s^0 momentum direction is performed. Afterwards, the following selection variables are used for the B_s^0 construction:

- χ^2 $(J/\psi\ \eta')$. This variable is a measure for the coincidence of the vertices of the J/ψ and η' candidates.
- τ/σ_τ and χ^2_τ. In order to reject the background from the primary interaction, there should be a clear separation between the primary and the secondary vertices. This can be achieved by a requirement on the decay time of the B_s^0 candidate. For this purpose, the lifetime fitter, described in Ref. [97], is used. It calculates the decay time τ of the B_s^0 candidate and its error σ_τ. The decay time significance, τ/σ_τ, is used as a selection variable in this study. The χ^2 of this fit is a measure for the likelihood that the B_s^0 momentum direction points back to the primary vertex.
- $\Delta M_{B_s^0}$ $(J/\psi\ \eta')$. Finally, this variable defines a window around the nominal B_s^0 mass in the invariant mass spectrum of the J/ψ and η' candidates. It should be mentioned, that the available statistics of inclusive $b\bar{b}$ data corresponds to approximately 5 minutes of LHCb running at nominal luminosity. Clearly, this is not enough for an accurate estimation of the background contamination. Therefore, the B_s^0 mass window is significantly enlarged for background events. This trick artificially increases the background statistics. It is assumed, that the invariant mass distribution

of the background in the enlarged mass window has approximately a linear shape. Consequently, in order to estimate the background level in the tight signal mass window, it is necessary to multiply the number of selected background candidates in the loose mass window by the ratio of the two windows $f_{\text{mass}} = \Delta M_{\text{tight}}/\Delta M_{\text{loose}}$.

6.6.3 Preselection studies

As noted before, the main reason to perform a preselection is to reduce the combinatorial background in the data samples. At this step only loose cuts on the selection variables are applied to both the signal and inclusive $b\bar{b}$ events. Tight cuts may influence the optimisation of the final cuts, which is performed afterwards. The preselection cuts used in this study are listed in Table 6.4. As can be seen, some selection variables described before are not used in the preselection. These requirements are applied in the final selection. The values for preselection cuts have been determined by comparing the distributions of the selection variables for the signal and $b\bar{b}$ background. They are shown for some selection variables in Fig. 6.13. The preselection decreases the background level by a factor ~ 100.

Table 6.4: *Preselection cuts for the* $B_s^0 \to J/\psi(\mu^+\mu^-)\ \eta'(\rho^0(\pi^+\pi^-)\gamma)$ *decay.*

Selection variable	Requirement
$\Delta\ln L_{\mu\pi}\ (\mu^+,\mu^-)$	> -5
$\chi^2\ (\mu^+\mu^-)$	< 9
$\Delta\text{M}_{J/\psi}\ (\mu^+\mu^-)$	± 50 MeV/c^2
$\Delta\ln L_{\mu\pi}\ (\pi^+,\pi^-)$	< 7
$\Delta\ln L_{K\pi}\ (\pi^+,\pi^-)$	< 0
$\chi^2\ (\pi^+\pi^-)$	< 9
$\text{IP}/\sigma_{\text{IP}}\ (\pi^+\pi^-)$	> 1
$E_{\text{T}}\ (\gamma)$	> 0.25 GeV
$p_{\text{T}}\ (\eta')$	> 1.5 GeV/c
$\Delta M_{\eta'}\ (\pi^+\pi^-\gamma)$	± 50 MeV/c^2
$\chi^2\ (J/\psi\ \eta')$	< 25
$\Delta M_{B_s^0}^{\text{signal}}\ (J/\psi\ \eta')$	± 50 MeV/c^2
$\Delta M_{B_s^0}^{\text{backg}}\ (J/\psi\ \eta')$	± 500 MeV/c^2

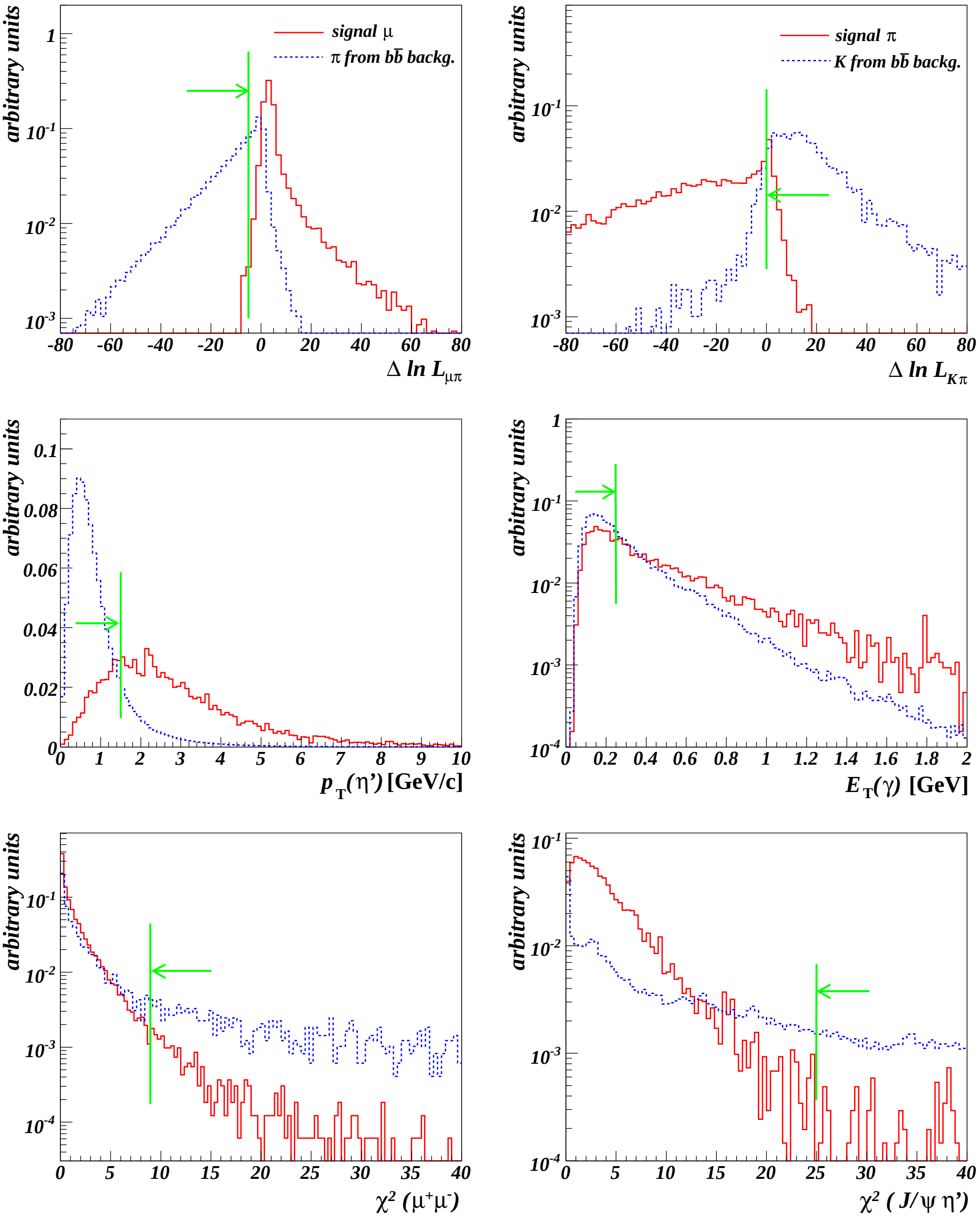

Figure 6.13: *Distributions of some selection variables used in the preselection for the signal (red solid lines) events and $b\bar{b}$ background (blue dashed lines) events. The signal and background distributions are normalised to the total number of entries in their histograms. The preselection cuts are indicated by the green vertical lines and arrows.*

6.6.4 Optimisation of the cuts

The samples of signal and background events that passed through the preselection cuts are used in the cut optimisation in the next step of the analysis. The requirements on only eight selection variables are optimised simultaneously in this study: $\Delta\ln L_{\mu\pi}(\pi^+,\pi^-)$, $E_{\mathrm{T}}(\gamma)$, $p_{\mathrm{T}}(\eta')$, $\cos\angle(p_{\rho^0},p_\gamma)_{\mathrm{LAB}}$, $\cos\angle(p_{\eta'},p_\pi)_{\rho^0 \mathrm{r.f.}}$, $\chi^2(J/\psi\,\eta')$, τ/σ_τ and χ^2_τ.

A set of the cut values is defined for each selection variable. In general, they have to cover a wide range and the distance between them should be as small as possible to guarantee a high granularity. On the other hand, a simultaneous optimisation of many selection variables with a large number of cut values consumes large amounts of CPU time. Therefore, the number of cuts can not be too large.

The set of cut values for each selection variable is determined by considering their distributions for signal and $b\bar{b}$ background events after applying the preselection cuts. The distributions are shown in Fig. 6.14 and 6.15.

In this study, the following cut values are used:

- 6 cut values for $\Delta\ln L_{\mu\pi}\,(\pi^+,\pi^-)$: $< 0,\ < 1,\ < 2,\ < 3,\ < 4,\ < 7$;
- 10 cut values for $E_{\mathrm{T}}\,(\gamma)$ (in GeV) : $> 0.25,\ > 0.3,\ > 0.35,\ > 0.4,\ > 0.45,\ > 0.5,\ > 0.55,\ > 0.6,\ > 0.65,\ > 0.7$;
- 19 cut values for $p_{\mathrm{T}}\,(\eta')$ (in GeV/c) : $> 1.5,\ > 1.7,\ > 1.9,\ > 2.0,\ > 2.1,\ > 2.2,\ > 2.3,\ > 2.4,\ > 2.5,\ > 2.6,\ > 2.7,\ > 2.8,\ > 2.9,\ > 3.0,\ > 3.2,\ > 3.4,\ > 3.6,\ > 3.8,\ > 4.0$;
- 5 cut values for $\cos\angle(p_{\rho^0},p_\gamma)_{\mathrm{LAB}}$: $> 0.995,\ > 0.997,\ > 0.999,\ > 0.9993,\ > 0.9995$;
- 6 cut values for $|\cos\angle(p_{\eta'},p_\pi)_{\rho^0 \mathrm{r.f.}}|$: $< 0.95,\ < 0.90,\ < 0.85,\ < 0.80, < 0.75,\ < 0.70$;
- 7 cut values for $\chi^2(J/\psi\,\eta')$: $< 8,\ < 9,\ < 10,\ < 12,\ < 14,\ < 16,\ < 25$;
- 11 cut values for τ/σ_τ : $> 10,\ > 12,\ > 14,\ > 16,\ > 18,\ > 20,\ > 22,\ > 24,\ > 26,\ > 28,\ > 30$;
- 9 cut values for χ^2_τ : $< 4,\ < 5,\ < 6,\ < 7,\ < 8,\ < 9,\ < 10,\ < 11,\ < 12$.

This results in 23 700 600 different combinations of cuts. These cut values span a fixed grid in the space of selection variables. For some selection variables the boundaries of this grid are determined by the preselection values.

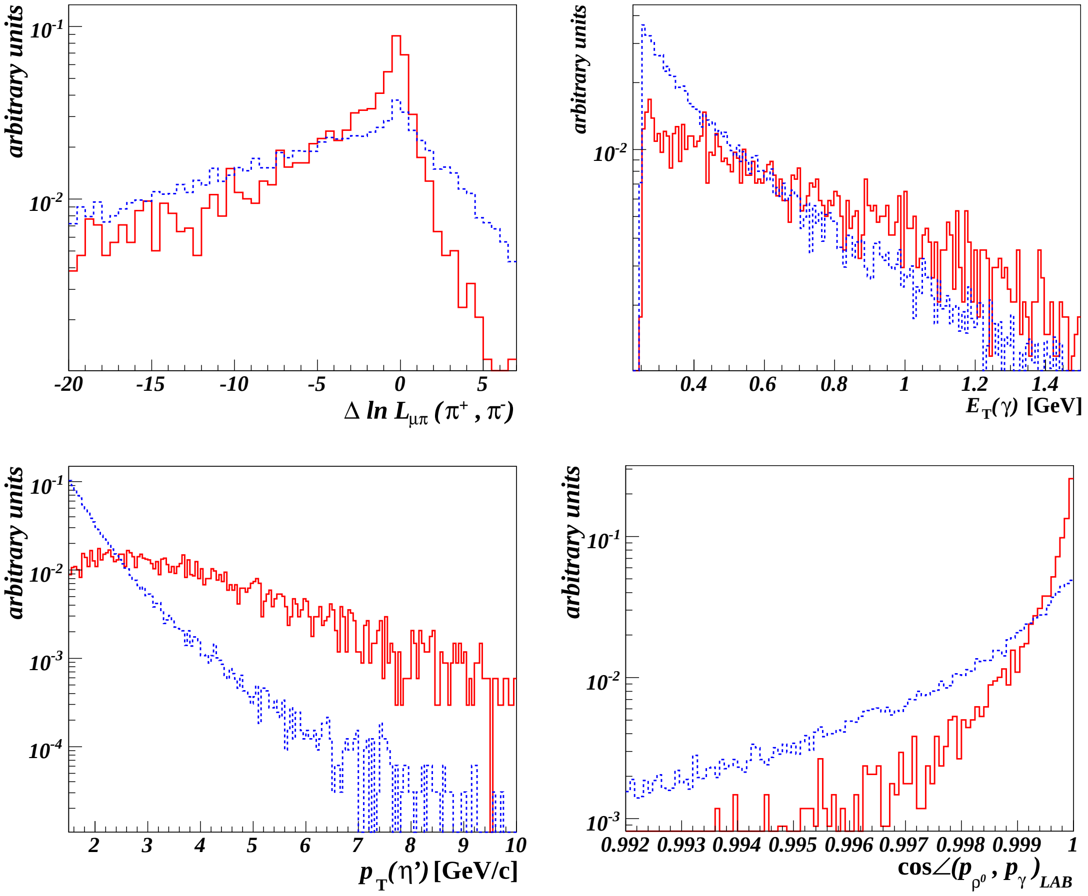

Figure 6.14: *The $\Delta \ln L_{\mu\pi}$ (π^+, π^-), E_{T} (γ), p_{T} (η') and $\cos\angle(\mathrm{p}_{\rho^0}, \mathrm{p}_\gamma)_{\mathrm{LAB}}$ distributions for the signal (red solid lines) and $b\bar{b}$ background (blue dashed lines) events after applying the preselection cuts. The signal and background histograms are normalised to their total number of entries.*

The number of selected signal (S) and background (B) events is determined for each combination of cuts and is normalised to 2 fb^{-1} of data. The statistical significance for a Poisson distribution is equal to:

$$\frac{S}{\sigma_S} = \frac{S}{\sqrt{S+B}} \quad , \tag{6.25}$$

The combination of cuts which gives the maximal value for this parameter is defined as the optimum point in the space of selection variables.

The best combination of cuts obtained from the optimisation, as it gives the maximal value for $S/\sqrt{S+B}$, is the following:

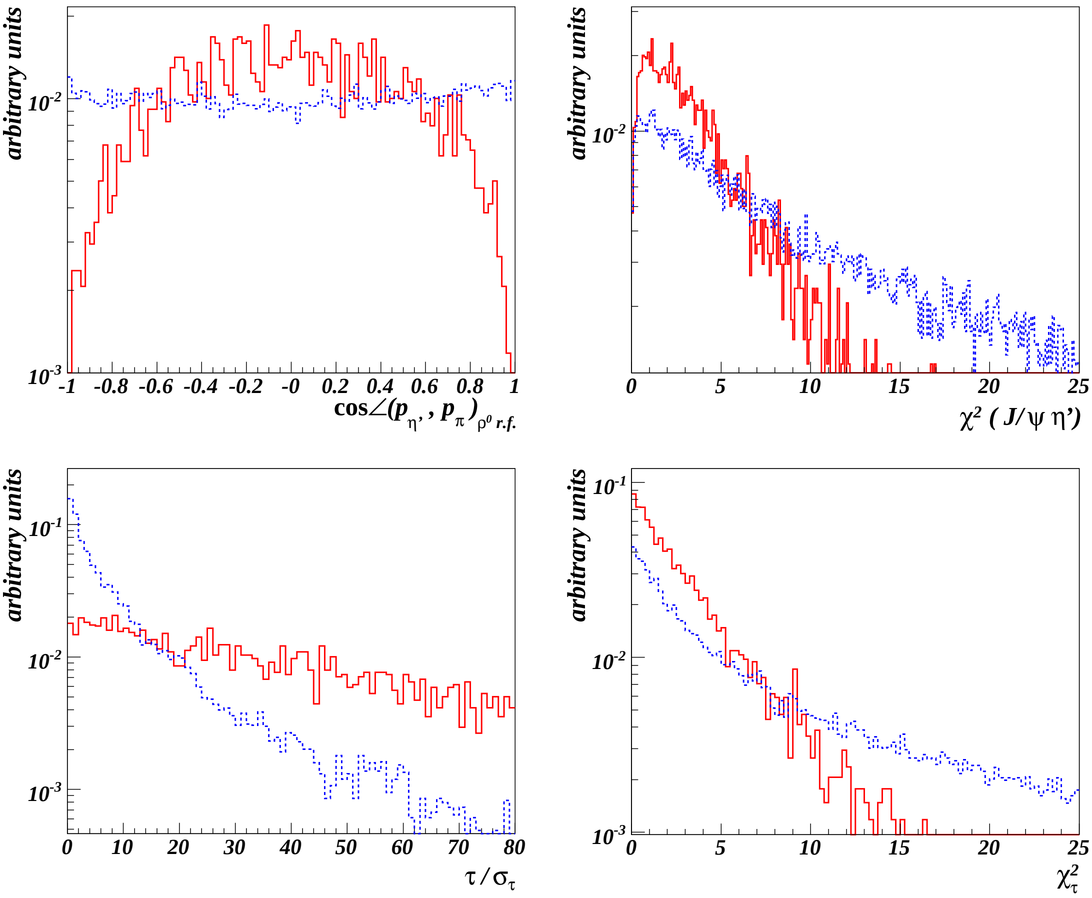

Figure 6.15: *The* $\cos\angle(p_{\eta'}, p_{\pi})_{\rho^0\mathrm{r.f.}}$, $\chi^2(J/\psi\;\eta')$, τ/σ_τ *and* χ^2_τ *for the signal (red solid lines) and* $b\bar{b}$ *background (blue dashed lines) events after applying the preselection cuts. The signal and background histograms are normalised to their total number of entries.*

- $\Delta\ln L_{\mu\pi}$ $(\pi^+,\pi^-) < 2$
- E_T $(\gamma) > 0.3\,\mathrm{GeV}$
- p_T $(\eta') > 2.8\,\mathrm{GeV}/c$
- $\cos\,\angle(p_{\rho^0}, p_\gamma)_\mathrm{LAB} > 0.9995$
- $|\cos\,\angle(p_{\eta'}, p_\pi)_{\rho^0\mathrm{r.f.}}| < 0.9$
- χ^2 $(J/\psi\;\eta') < 16$
- $\tau/\sigma_\tau > 22$

- $\chi^2_\tau < 6$

It selects a large number of signal events and rejects all the background events. Table 6.5 lists the final selection cuts used in this analysis.

Table 6.5: *Final selection cuts used for reconstruction of the* $B_s^0 \to J/\psi(\mu^+\mu^-)\ \eta'(\rho^0(\pi^+\pi^-)\gamma)$ *decay.*

Selection variable	Requirement
$\Delta\ln L_{\mu\pi}\ (\mu^+,\mu^-)$	> -5
$\chi^2\ (\mu^+\mu^-)$	< 9
$\Delta M_{J/\psi}\ (\mu^+\mu^-)$	± 50 MeV/c^2
$\Delta\ln L_{\mu\pi}\ (\pi^+,\pi^-)$	< 2
$\Delta\ln L_{K\pi}\ (\pi^+,\pi^-)$	< 0
$\chi^2\ (\pi^+\pi^-)$	< 9
$\mathrm{IP}/\sigma_{\mathrm{IP}}\ (\pi^+\pi^-)$	> 1
$E_{\mathrm{T}}\ (\gamma)$	> 0.3 GeV
$p_{\mathrm{T}}\ (\eta')$	> 2.8 GeV/c
$\cos\angle(p_{\rho^0}, p_\gamma)_{\mathrm{LAB}}$	> 0.9995
$\lvert\cos\angle(p_{\eta'}, p_\pi)_{\rho^0\mathrm{r.f.}}\rvert$	< 0.9
$\Delta M_{\eta'}\ (\pi^+\pi^-\gamma)$	± 50 MeV/c^2
$\chi^2\ (J/\psi\ \eta')$	< 16
τ/σ_τ	> 22
χ^2_τ	< 6
$\Delta M^{\mathrm{signal}}_{B_s^0}\ (J/\psi\ \eta')$	± 50 MeV/c^2

6.6.5 Event yield and background contributions

In total, 99600 ± 300 independently generated signal events were analysed. After applying the final selection cuts, 784 unique signal events containing at least one reconstructed B_s^0 candidate[6] are selected. From this sample 766 events are fully associated to the true generated signal decay. The 18 decays in the other events are not associated due to the selection of a wrong photon candidate in ECAL. Another important remark is that 644 selected signal events out of 766 have passed through the combined trigger decision of the Level-0 and HLT.

---

[6] Sometimes more than one B_s^0 candidate is reconstructed in a single event. This occurs in about 2% of all the selected events and is due to the fact that there is more than one reconstructed photon in these events which forms a η' and B_s^0 candidate that passes all selection requirements.

Signal efficiencies

The total signal efficiency, $\varepsilon_{\text{total}}$, is defined as

$$\varepsilon_{\text{total}} = \varepsilon_{\theta}^{\text{signal}} \times \frac{N_{\text{sel\&trg}}}{N_{\text{gen}}^{\text{signal}}} \quad , \tag{6.26}$$

where $\varepsilon_{\theta}^{\text{signal}} = (34.7 \pm 0.3)\%$ is the efficiency of the 400 mrad acceptance cut at generator level on the signal B_s^0, $N_{\text{sel\&trg}}$ is the number of reconstructed, selected and triggered signal events and $N_{\text{gen}}^{\text{signal}}$ is the total number of generated signal events. The total efficiency can be subdivided as:

$$\varepsilon_{\text{total}} = \varepsilon_{\text{det}} \times \varepsilon_{\text{rec/det}} \times \varepsilon_{\text{sel/rec}} \times \varepsilon_{\text{trg/sel}} \quad , \tag{6.27}$$

where:

- ε_{det} is the detection efficiency that all B decay products in the event are reconstructible (i.e. all of them are in the detector acceptance and can potentially be reconstructed). This includes the 400 mrad acceptance cut;
- $\varepsilon_{\text{rec/det}}$ is the efficiency that the reconstructible events are actually reconstructed;
- $\varepsilon_{\text{sel/rec}}$ is the efficiency that the reconstructed events are selected;
- $\varepsilon_{\text{trg/sel}}$ is the efficiency that the selected events are accepted by the Level-0 and HLT trigger algorithms.

All the above efficiencies are presented in Table 6.6, where the errors are calculated taking into account the statistical uncertainty on the fraction of independent events. As can be seen, the total signal efficiency is found to be $(0.224 \pm 0.016)\%$. This result is typical for decays with muons, pions and photons in the final state reconstructed at LHCb. For example, for the $B_s^0 \to J/\psi(\mu^+\mu^-)\ \eta(\pi^+\pi^-\pi^0(\gamma\gamma))$ decay a total signal efficiency of 0.24% is found [98].

Table 6.6: *Efficiencies for the the $B_s^0 \to J/\psi(\mu^+\mu^-)\ \eta'(\rho^0(\pi^+\pi^-)\gamma)$ decay channel.*

ε_{det} [%]	$\varepsilon_{\text{rec/det}}$ [%]	$\varepsilon_{\text{sel/rec}}$ [%]	$\varepsilon_{\text{trg/sel}}$ [%]	$\varepsilon_{\text{total}}$ [%]
5.87 ± 0.29	74.4 ± 0.3	6.11 ± 0.30	84.1	0.224 ± 0.016

Table 6.7: *The untagged selected signal yield for the* $B_s^0 \to J/\psi(\mu^+\mu^-)\ \eta'(\rho^0(\pi^+\pi^-)\gamma)$ *decay channel with* 2 *fb*$^{-1}$ *of data.*

Mixing angle, θ_p	S_{signal} [$\times 10^3$ events]
-10°	3.6 ± 0.6
-20°	4.8 ± 0.8

Selected signal yield

The selected signal yield, S_{signal}, is the number of reconstructed, selected and triggered signal decays (without tagging), which will be collected by the LHCb experiment with 2 fb^{-1} of data. This can be calculated as:

$$S_{\text{signal}} = N_{\text{signal}} \times \varepsilon_{\text{total}} \quad , \tag{6.28}$$

where N_{signal} is the expected annual production yield of the signal decay given in Table 6.2. The selected signal yield is presented in Table 6.7 for the two boundary values of the mixing angle θ_p. As can be seen, the selected signal yield is expected to range between 3.6k and 4.8k events depending on θ_p.

Background contributions

After applying the final selection cuts and without applying any trigger decision no background events are selected from 33 616 466 inclusive $b\bar{b}$ events, not even in the loose B_s^0 invariant mass window of $\pm 500\,\text{MeV}/c^2$. Hence, an upper limit for the background contribution is estimated using the Feldman and Cousins approach [9]. The background-to-signal (B/S) ratio is given by the following equation:

$$\frac{B}{S} = \frac{\varepsilon_\theta^{b\bar{b}}}{\varepsilon_\theta^{\text{signal}}} \times \frac{1}{2 \cdot \text{BF}(\bar{b} \to B_s^0) \cdot \text{BF}_{\text{total}}^{\text{signal}}} \times \frac{(N_{\text{sel}}^{\text{bkg}} \cdot f_{\text{mass}})/N_{\text{gen}}^{\text{bkg}}}{N_{\text{sel}}^{\text{signal}}/N_{\text{gen}}^{\text{signal}}} \quad , \tag{6.29}$$

where:

- $\varepsilon_\theta^{b\bar{b}} = 43.4\%$ and $\varepsilon_\theta^{\text{signal}} = 34.7\%$ are the efficiencies of the 400 mrad acceptance cut for background and signal events;
- $\text{BF}(\bar{b} \to B_s^0) = 10.7\%$ is the $\bar{b} \to B_s^0$ production fraction; The factor 2 takes into account the possible production of both B_s and $\bar{B}_s$ mesons from a $b\bar{b}$ pair;

- $\mathrm{BF}_{\mathrm{total}}^{\mathrm{signal}}$ is the total branching fraction of the B_s^0 decay into the final state given in Table 6.2;
- $N_{\mathrm{sel}}^{\mathrm{bkg}}$ is the number of selected background events in the loose B_s^0 invariant mass window of $\pm 500\,\mathrm{MeV}/c^2$. Since no background events are selected the corresponding upper limit of 2.44 events at 90% confidence level is used;
- $f_{\mathrm{mass}} = \Delta M^{\mathrm{tight}}/\Delta M^{\mathrm{loose}} = 100/1000 = 0.1$ is the mass window enlargement factor for background events;
- $N_{\mathrm{gen}}^{\mathrm{bkg}}$ is the total number of inclusive $b\bar{b}$ events generated;
- $N_{\mathrm{sel}}^{\mathrm{signal}}$ is the number of signal events selected in the tight mass window of $\pm 50\,\mathrm{MeV}/c^2$;
- $N_{\mathrm{gen}}^{\mathrm{signal}}$ is the total number of signal events generated;

Table 6.8: *The B/S ratio at 90% confidence level obtained from inclusive $b\bar{b}$ events for untagged and untriggered events.*

Mixing angle, θ_p	B/S
$-10°$	<0.47
$-20°$	<0.36

In Table 6.8 the upper limits on the B/S ratio are given for the selected untriggered and untagged events. The obtained results show a low background pollution from inclusive $b\bar{b}$ events. The B/S ratio is not be affected by the trigger decisions, since the same trigger efficiency is expected for background and signal events.

As mentioned before, several data samples of specific B decay modes, which have a similar decay topology are used in addition to check the performance of the selection cuts. They are listed in Table 6.3 together with the total number of generated events, $N_{\mathrm{gen}}^{\mathrm{spec}}$. The background contributions coming from each of them can be calculated with the following formula:

$$\left(\frac{B}{S}\right)^{\mathrm{spec}} = \frac{\mathrm{BF}(\bar{b} \to B_{d,s,u})}{\mathrm{BF}(\bar{b} \to B_s^0)} \times \frac{\mathrm{BF}_{\mathrm{total}}^{\mathrm{spec}}}{\mathrm{BF}_{\mathrm{total}}^{\mathrm{signal}}} \times \frac{N_{\mathrm{sel}}^{\mathrm{spec}}/N_{\mathrm{gen}}^{\mathrm{spec}}}{N_{\mathrm{sel}}^{\mathrm{signal}}/N_{\mathrm{gen}}^{\mathrm{signal}}}\,, \tag{6.30}$$

where:

- $\mathrm{BF}(\bar{b} \to B_{d,s,u})$ is the fraction of $\bar{b}$ quarks hadronising into a specific B hadron;
- $\mathrm{BF}_{\mathrm{total}}^{\mathrm{spec}}$ is the total branching fraction of the specific decay channel into its final state;

Table 6.9: *The background contributions from the specific decay channels given in terms of (B/S)$^{\rm spec}$ ratios for selected untriggered events at 90% confidence level.*

Decay channel	$(B/S)^{\rm spec}$ $(\theta_p = -10^0)$	$(B/S)^{\rm spec}$ $(\theta_p = -20^0)$
$B_d^0 \to J/\psi(\mu^+\mu^-)\,K^*(K^\pm\pi^\mp)$	[0.07;0.48]	[0.05;0.36]
$B_d^0 \to J/\psi(\mu^+\mu^-)\,K_s^0(\pi^+\pi^-)$	<0.07	<0.05
$B_d^0 \to J/\psi(\mu^+\mu^-)\,\pi^0(\gamma\gamma)$	<0.003	<0.002
$B_s^0 \to J/\psi(\mu^+\mu^-)\,\phi(K^+K^-)$	<0.02	<0.01
$B_s^0 \to J/\psi(\mu^+\mu^-)\,\eta(\gamma\gamma)$	<0.03	<0.01
$B_s^0 \to J/\psi(\mu^+\mu^-)\,\eta(\pi^+\pi^-\pi^0(\gamma\gamma))$	<0.02	<0.01
$B_u^+ \to J/\psi(\mu^+\mu^-)\,K^+$	<0.13	<0.10

- $N_{\rm sel}^{\rm spec}$ is the number of selected background events in the tight B_s^0 invariant mass window;

- $N_{\rm gen}^{\rm spec}$ is the total number of generated background events;

Table 6.9 lists the obtained $(B/S)^{\rm spec}$ ratios. As can be seen, the expected background contributions from the specific channels are small. The most dangerous channel for the signal decay mode is the $B_d^0 \to J/\psi(\mu^+\mu^-)\,K^*(K^\pm\pi^\mp)$, which gives the maximal value for the $(B/S)^{\rm spec}$ ratio. This can be explained by the fact that this decay has a rather large total branching fraction of about 7.9×10^{-5} and the K^* meson has a mass of $892\,{\rm MeV}/c^2$, which is rather close to the η' nominal mass. By selecting the kaon (with a wrong PID assignment) and the pion originating from the K^* decay and adding a soft photon to this particle pair one can obtain a fake η' candidate that may pass all selection requirements.

6.6.6 Reconstruction quality

The quality of reconstruction of the $B_s^0 \to J/\psi\,\eta'$ decay can be estimated by calculating the residuals, which are defined as the difference between the reconstructed value of a parameter and its true value obtained from Monte Carlo. Clearly, the residual is the absolute error of a measurement. The standard deviation of a Gaussian fit to the residual distribution is called resolution. This quantity represents the accuracy of a measurement. In this section the resolutions of the mass, vertex and B_s^0 decay time are discussed.

Mass resolutions

In the EVTGEN package, the B_s^0, J/ψ and η' mesons are generated with the following central masses (M_{MC}) and lifetimes (τ_{MC}):

- B_s^0 : $M_{\mathrm{MC}} = 5369.60\,\mathrm{MeV}/c^2$, $\tau_{\mathrm{MC}} = 1.461 \times 10^{-12}$ s ;
- J/ψ: $M_{\mathrm{MC}} = 3096.87\,\mathrm{MeV}/c^2$, $\tau_{\mathrm{MC}} = 7.565657 \times 10^{-21}$ s ;
- η' : $M_{\mathrm{MC}} = 957.78\,\mathrm{MeV}/c^2$, $\tau_{\mathrm{MC}} = 3.258476 \times 10^{-21}$ s .

The corresponding intrinsic decay widths of the particles are $\Gamma_{\mathrm{MC}} \approx \hbar/\tau_{\mathrm{MC}}$. In case of the B_s^0 meson, the width is of the order of $10^{-10}\,\mathrm{MeV}/c^2$. Therefore, all B_s^0 mesons are generated with the same mass in the simulation. For the J/ψ and η' the widths are equal to $0.087\,\mathrm{MeV}/c^2$ and $0.202\,\mathrm{MeV}/c^2$, which is very small compared to the mass resolution of the detector. Hence, in this study the J/ψ and η' mesons are considered as particles generated with a fixed mass. Figure 6.16 shows the mass resolutions of the J/ψ, η' and B_s^0 mesons obtained from the invariant mass distributions after applying all selection cuts. Note that the J/ψ and η' invariant masses are extracted before the mass-constrained vertex fit to these particles.

The J/ψ mass distribution is fitted with a single Gaussian giving a mean value of $\mu = (3097.4 \pm 0.4)\,\mathrm{MeV}/c^2$ and a resolution of $\sigma = (10.9 \pm 0.4)\,\mathrm{MeV}/c^2$. This means that the J/ψ mass window cut of $\pm 50\,\mathrm{MeV}/c^2$ corresponds roughly to a 5σ requirement on both sides of the nominal mass. If the mass window would be wider, then a small tail on the left of this distribution can be observed. This is due to the existence of $J/\psi \to \mu^+\mu^-\gamma$ radiative decays.

A double Gaussian is used to fit the η' invariant mass spectrum to describe events in the core and in the side-bins of the distribution. For the core, containing 65.8% of all events in the distribution, the mean value is $\mu = (956.8 \pm 0.5)\,\mathrm{MeV}/c^2$ with a resolution of $\sigma = (9.1 \pm 0.6)\,\mathrm{MeV}/c^2$. The second Gaussian with resolution of $\sigma = (22.3 \pm 2.6)\,\mathrm{MeV}/c^2$ describes the events belonging to the side-bins of the distribution. This is the result of the tail in the energy resolution of reconstructed photons. Most of them are concentrated on the right side of the distribution due the cut on the transverse energy of photon candidates. If the photon energy would be perfectly reconstructed (i.e. $E_{\mathrm{rec}}(\gamma) = E_{\mathrm{true}}(\gamma)$), then the η' invariant mass distribution could be well described by a single Gaussian with a resolution of $\sim 8\,\mathrm{MeV}/c^2$.

The invariant mass of the B_s^0 is calculated after applying mass-constrained vertex fits to its daughters — the J/ψ and η' mesons. This improves the B_s^0 mass resolution roughly by a factor of 2, from $\sigma = (28.7 \pm 0.7)\,\mathrm{MeV}/c^2$ to $\sigma = (14.2 \pm 0.5)\,\mathrm{MeV}/c^2$. The mean value of $\mu = (5370.3 \pm 0.5)\,\mathrm{MeV}/c^2$ is very close to the B_s^0 generated mass. The B_s^0 mass window of $\pm 50\,\mathrm{MeV}/c^2$ used in this study represents a $\sim 3.5\sigma$ requirement on both sides of the mean value, wide enough to select almost all signal events.

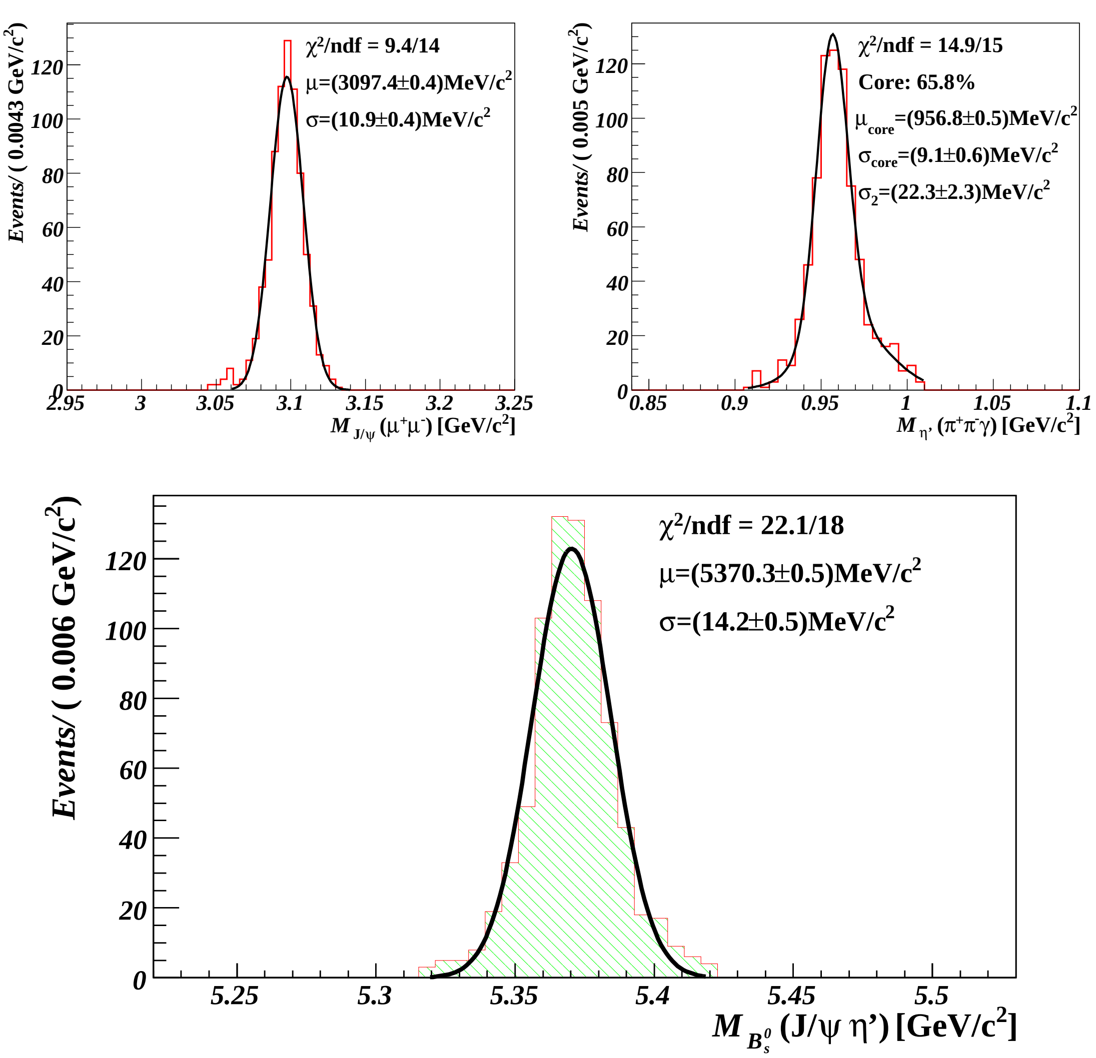

Figure 6.16: *The invariant mass of the J/ψ, η' and B_s^0 mesons for the selected signal events. The J/ψ and B_s^0 distributions are fitted with a single Gaussian and the η' mass spectrum is approximated by a double Gaussian.*

Vertex resolutions

An accurate reconstruction of the primary and secondary vertices is needed for a precise determination of the B_s^0 decay length, which is an essential parameter to measure the B_s^0 decay time. The vertex residuals in the directions transverse (x,y) and longitudinal (z) to the beam are shown in Fig. 6.17 for the selected signal events. As can be seen, the resolutions of the primary vertex are much smaller (i.e. better) than that of the secondary

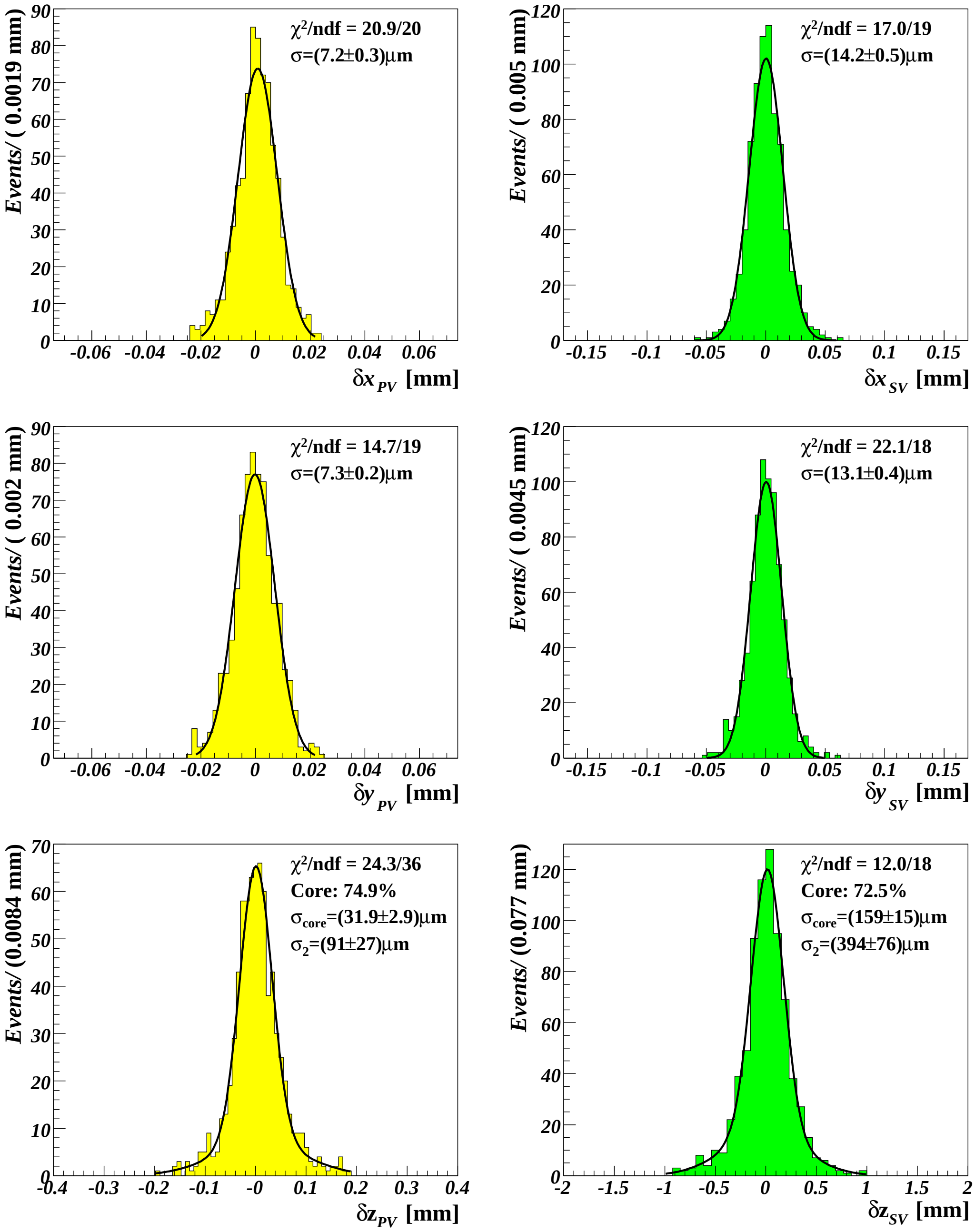

Figure 6.17: *Primary and secondary vertex residuals for the selected signal events. Distributions for the transverse components are fitted with a single Gaussian. A double Gaussian fit is applied to the distributions for the longitudinal component.*

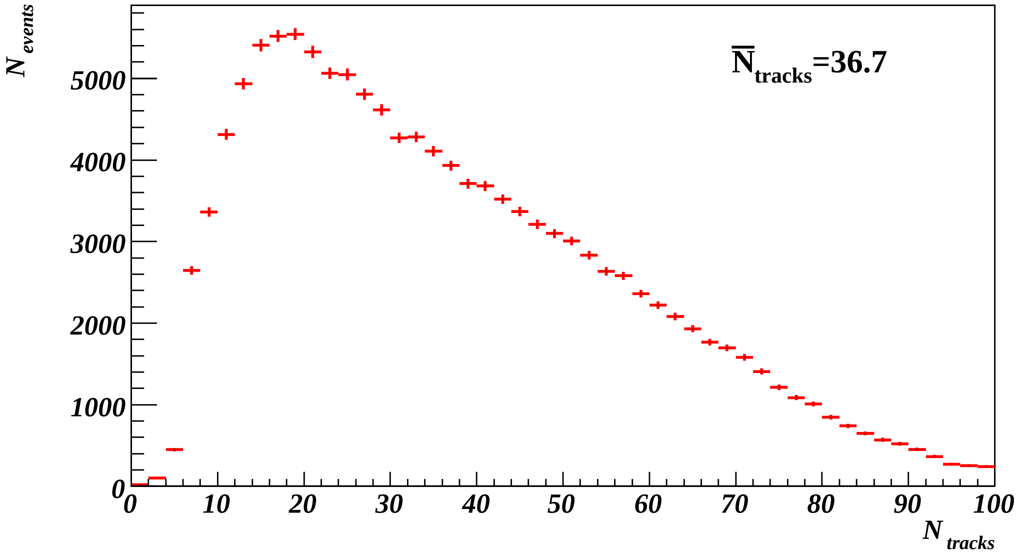

Figure 6.18: *The number of tracks used for the primary vertex reconstruction per signal event.*

vertex. It can be explained by the fact that the secondary vertex is constructed using only four charged tracks, while the primary vertex is constructed using almost 40 tracks on average, as shown in Fig. 6.18.

Also, it can be seen that the resolution for the transverse directions is much better compared to the resolution of the longitudinal direction. This can be explained by the forward acceptance of LHCb which yields few tracks in the central rapidity region. In addition, for the secondary vertices it should be taken into account that the B hadrons (and as result their decay products) at high collision energies are predominately produced at low angles with the beam axis.

B_s^0 decay time studies

In order to perform an accurate measurement of the time-dependent CP-asymmetry it is important to determine the B_s^0 decay time with high precision to resolve the fast oscillating B_s^0 mesons. In general, the B_s^0 decay time can be found from the following formula:

$$\tau = M \times \frac{\vec{p}\cdot\vec{L}}{|\vec{p}|^2} \quad , \tag{6.31}$$

where M is the nominal B_s^0 meson mass, $\vec{p}$ its reconstructed momentum vector and $\vec{L}$ the decay length vector, which is the difference between the positions of the secondary ($\vec{x}_{SV}$)

and primary ($\vec{x}_{PV}$) vertices, $\vec{L} = \vec{x}_{SV} - \vec{x}_{PV}$. Note that the B_s^0 decay time is related to the B_s^0 meson lifetime in the laboratory system t via $\tau = t/\gamma$ relation, where γ is the relativistic Lorentz factor.

In this study, the reconstructed B_s^0 decay time is obtained from the lifetime fit described in Ref. [97]. Figure 6.19 illustrates the B_s^0 decay time distribution, together with its estimated error for selected and triggered signal events. As can be seen, there are no

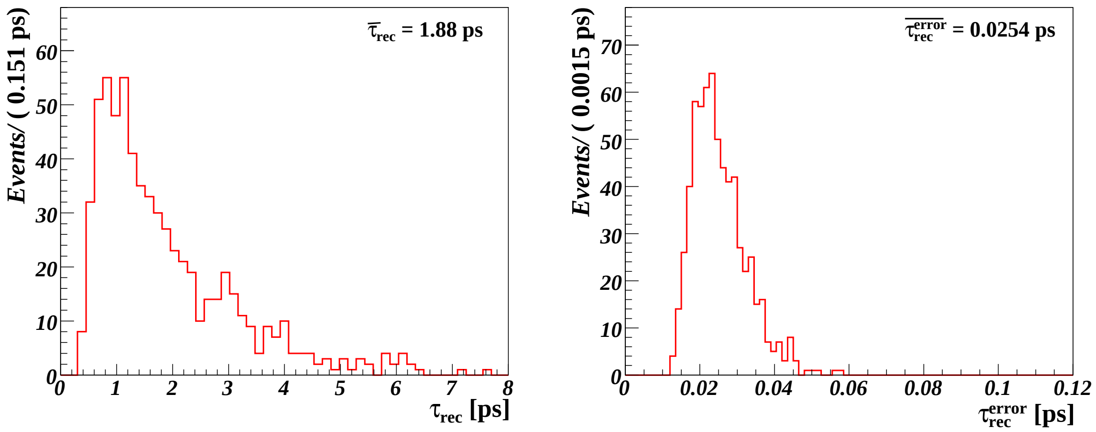

Figure 6.19: *The B_s^0 decay time (left) and its error (right) obtained from the lifetime fit for selected and triggered signal events.*

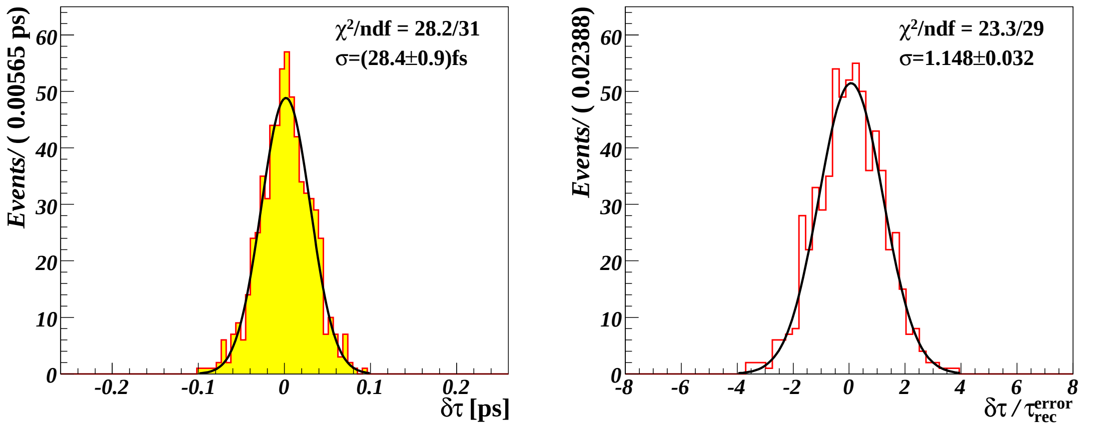

Figure 6.20: *The B_s^0 decay time residual (left) and the pull distribution (right) for the selected and triggered signal events with a single Gaussian fit.*

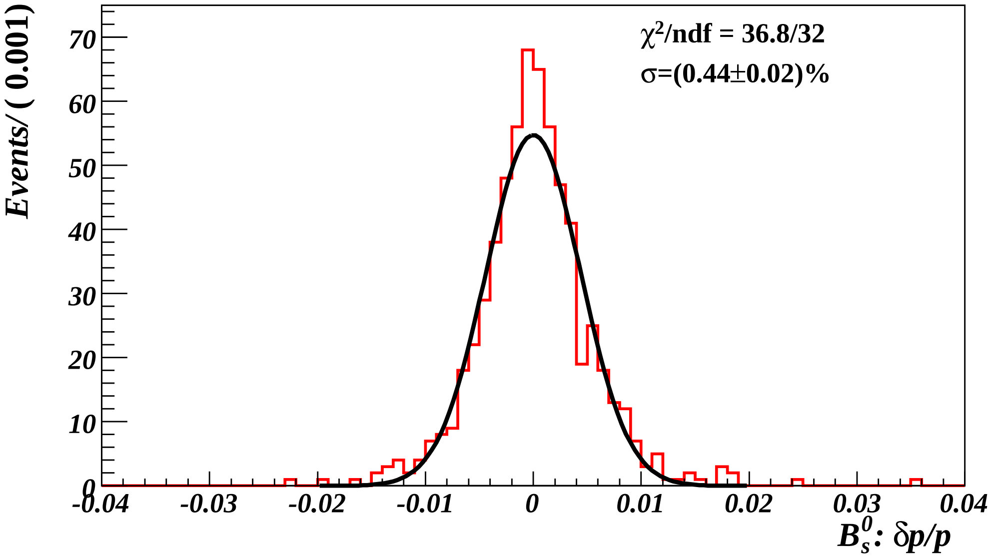

Figure 6.21: *The B_s^0 relative momentum residual for the selected and triggered signal events fitted with a single Gaussian.*

reconstructed B_s^0 mesons with a decay time below ~ 0.3 ps. This is because of the lifetime requirements which are applied in our selection. The errors on the decay time vary in a large range, which is due to the spread in the distributions of the decay distance and B_s^0 momentum. If the errors would be correctly estimated, then the B_s^0 decay time resolution would be equal to the mean value of the error distribution, which is found to be 25.4 fs. However, this is not the case, since the decay time resolution equals to 28.4 fs, as shown in Fig. 6.20. There is a 12% underestimation of the errors. This effect is confirmed by the pull distribution[7], which is also presented in Fig. 6.20. Its resolution, extracted from a single Gaussian fit, is found to be 1.148 ± 0.032.

It is interesting to note, that the decay time resolution is dominated by the error on the decay length vector $\vec{L}$. If the positions of the primary and secondary vertices would be perfectly reconstructed (i.e. $\vec{L}_{\text{rec}} = \vec{L}_{\text{true}}$), then the decay time resolution would be roughly equal to 4 fs. According to (6.31), another variable which directly affects the quality of the B_s^0 decay time determination is the reconstructed B_s^0 momentum. Its relative residual defined as $\delta p/p = (p_{\text{rec}} - p_{\text{true}})/p_{\text{true}}$ is shown in Fig. 6.21 for the selected and triggered signal events. By applying a single Gaussian fit to this distribution, the relative B_s^0 momentum resolution is found to be $\sigma = (0.44 \pm 0.02)\%$. This is much better compared to the other decays containing photons in the final state reconstructed by LHCb. For

---

[7] The pull is defined by the decay time residual normalised by its corresponding error, $\delta\tau/\tau_{\text{rec}}^{\text{error}}$.

example, it is equal to $(0.86 \pm 0.02)\%$ for the $B_s^0 \to J/\psi(\mu^+\mu^-)\,\eta(\pi^+\pi^-\pi^0(\gamma\gamma))$ decay and $(1.13 \pm 0.02)\%$ for the $B_s^0 \to J/\psi(\mu^+\mu^-)\,\eta(\gamma\gamma)$ decay [98].

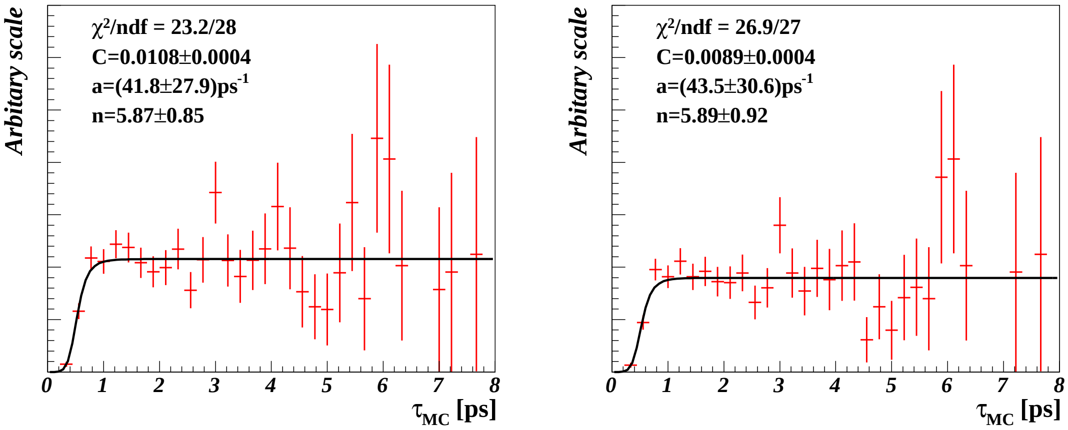

Figure 6.22: *The time-dependent selection efficiency fitted with an acceptance function for the untriggered (left) and triggered (right) signal events.*

The time-dependent selection efficiency is shown in Fig. 6.22 for untriggered and triggered events. It is parametrised by the acceptance function defined as:

$$\varepsilon_\tau(\tau) = C \times \frac{(a\tau)^n}{1 + (a\tau)^n} \quad , \tag{6.32}$$

where C is the selection efficiency at large decay times, and a and n are two parameters which govern the time dependence at small decay times. Their values are obtained from a fit to the distribution of the time-dependent selection efficiency, and shown in Fig. 6.22. For both untriggered and triggered the parameter a, which defines the slope of the rising part of the distribution, has a large error. It can be explained by the fact that the selection efficiency rises very steeply. As can be seen, it reaches a plateau already at $\sim$0.7 ps. This means that the selection requirements cut out only B_s^0 mesons with a decay time below 0.7 ps and do not distort the decay time distribution for $\tau > 0.7$ ps. It should be noted, that the determination of the acceptance function on real data is a challenging task.

6.7 LHCb sensitivity to ϕ_s with the $B_s^0 \to J/\psi\,\eta'$ decay

As already mentioned in this chapter, the $B_s^0 \to J/\psi\,\eta'$ measures directly the B_s^0 mixing phase ϕ_s from the time-dependent *CP* asymmetry arising in this channel. The determination of LHCb's sensitivity to measure ϕ_s with the $B_s^0 \to J/\psi\,\eta'$ decay is the last step in this analysis. In order to perform this task a fast Monte Carlo simulation programme has been used. A detailed description of this programme is given in Ref. [20]. For each setting of the input variables we simulate 200 LHCb "experiments" with 2 fb^{-1} per experiment. For each experiment the programme generates events taking into account the selection results obtained from the full MC simulation and performs a fit according to a likelihood function which includes the B_s^0-$\bar{B}_s^0$ mixing variables. The output of the programme consists of 200 values and corresponding errors for each of the fitted variable. The event generation and likelihood fit is performed by a toolkit for modelling expected distributions of events, called ROOFIT [99].

The fast Monte Carlo simulation includes the $B_s^0 \to D_s^- \pi^+$ decay for which no *CP* asymmetry is expected. Its selection is described in Ref. [100]. This control channel is fitted simultaneously with the $B_s^0 \to J/\psi\,\eta'$ decay to improve the determination of the mixing parameters ΔM_s, $\Delta\Gamma_s$ as well as the wrong tag fraction w_{tag} and B_s^0 lifetime τ_{B_s}. The B_s^0 mixing phase ϕ_s is completely determined by the $B_s^0 \to J/\psi\,\eta'$ decay.

In this study the sensitivity to ϕ_s is defined as the mean value of its error distribution, which contains 200 entries. It represents the average statistical error on ϕ_s. This value should be compatible with the root-mean-square of the distribution of the output values for ϕ_s. In the next subsections, a brief description of the likelihood function and the fit strategy as well as the obtained sensitivity to ϕ_s with $B_s^0 \to J/\psi\,\eta'$ are presented.

6.7.1 Likelihood function

For each simulated LHCb "experiment", the fast Monte Carlo programme generates events according to the corresponding selected signal and background yield. Every event is generated according the total likelihood function which is used again afterwards to fit the events. The mass and decay time are smeared using their estimated error. The likelihood function can be presented as the product over all events i and, in case of the decay to the pure *CP* eigenstates, it is given by the following equation:

$$L_{\text{total}} = \frac{(N_{\text{sig}} + N_{\text{bkg}})^{N_{\text{obs}}}}{N_{\text{obs}}!} e^{-(N_{\text{sig}}+N_{\text{bkg}})} \prod_{i \in B_s \to f}^{N_{\text{obs}}} L_i \left(m_i, t_i^{\text{rec}}, \tau_i^{\text{err}}, q_i\right) \ , \tag{6.33}$$

with

$$L_i(m_i, t_i^{\text{rec}}, \tau_i^{\text{err}}, q_i) = N_{\text{sig}} L_m^{\text{sig}}(m_i) L_t^{\text{sig}}(t_i^{\text{rec}}, \tau_i^{\text{err}}, q_i) + N_{\text{bkg}} L_m^{\text{bkg}}(m_i) L_t^{\text{bkg}}(t_i^{\text{rec}}) \ , \tag{6.34}$$

where:

- N_{obs} is the Poisson distributed actual number of observed events in the generated sample;

- $N_{\rm sig}$ and $N_{\rm bkg}$ are the numbers of generated signal and background events, respectively;
- $L_m^{\rm sig}(m_i)$ and $L_m^{\rm bkg}(m_i)$ are the mass probability density functions for the signal and background events for a given reconstructed mass m_i;
- $L_t^{\rm sig}(t_i^{\rm rec}, \tau_i^{\rm err}, q_i)$ is the probability density function describing the signal decay rates for the decay time $t_i^{\rm rec}$, which depends on the per-event decay time error $\tau_i^{\rm err}$ (to assign the uncertainty on the reconstructed decay time) and the tagging result q_i ($q_i = 0$ if the event is untagged, $q_i = +1$ if the signal meson is tagged as B_s^0 and $q_i = -1$ if it is tagged as $\bar{B}_s^0$);
- $L_t^{\rm bkg}(t_i^{\rm rec})$ is the probability density function used to describe the background decay rates, which do not depend on $\tau_i^{\rm err}$ and the tagging performance.

As can be seen, the total likelihood function describes two distinctive physics models for the signal and the background contribution. For both, there are two types of probability density functions which model the invariant mass distribution and the time-dependent decay rates. The probability density function used to fit and generate the B_s mass spectrum consists of the sum of two likelihood functions: a Gaussian for the signal and an exponential for the background. They take into account the mass resolution obtained from the selection results. Since the decay rates are time-dependent, it is important to take into account the effects of the decay time acceptance and the decay time errors $\tau_i^{\rm err}$ in their likelihood description. The decay time resolution is included by smearing the true decay time with $\tau_i^{\rm err}$. This probability density function also describes the effect of the wrong tagging and includes the vector of the B_s^0-$\bar{B}_s^0$ mixing parameters. The background decay rate is assumed to follow an exponential decay, while the signal decay rates are described according to their full *CP*-violating decay amplitudes.

6.7.2 Input to the fast Monte Carlo simulation

The sensitivity to ϕ_s is performed for the $\theta_p = -10^\circ$ and $\theta_p = -20^\circ$ scenarios. Table 6.10 summarises all the inputs used in the fast Monte Carlo simulation to extract ϕ_s from the $B_s^0 \to J/\psi\,\eta'$ decay, where the loose mass window ($m_{\rm loose}$) is defined as ($m_{\rm true} \pm m_{\rm loose}$), the tight mass window ($m_{\rm tight}$) as ($m_{\rm true} \pm m_{\rm tight}$), and the sideband mass window ($m_{\rm sideband}$) as ($m_{\rm sideband} < |m_{\rm true} - m_{\rm rec}| < m_{\rm loose}$). The Σ_τ parameter is the width of the decay time pull defined as the standard deviation of a single Gaussian fit to this distribution. The a and n parameters are the slope and the power of the acceptance function. The input parameters for the $B_s^0 \to D_s^- \pi^+$ channel are the following: $S_{\rm signal} = 120$k, $B/S = 0.4$, B_s^0 mass resolution of $14.0\,{\rm MeV}/c^2$, $a = 1.36\,{\rm ps}^{-1}$, $n = 3.0$ and $\Sigma_\tau = 1.21$. The same tagging performance is assumed for both the signal and the control channel in the

Table 6.10: *Input from the full MC simulation used by the fast Monte Carlo programme to extract the sensitivity to ϕ_s with the $B_s^0 \to J/\psi\,\eta'$ decay.*

Parameter	$\theta_p = -10°$	$\theta_p = -20°$
S_{signal} [events]	3.6k	4.8k
B/S	0.47	0.36
m_{tight}	$50\,\text{MeV}/c^2$	
m_{sideband}	$75\,\text{MeV}/c^2$	
m_{loose}	$150\,\text{MeV}/c^2$	
B_s^0 mass resolution	$14\,\text{MeV}/c^2$	
a	43.5 ps^{-1}	
n	5.89	
$\bar{\tau}_i^{\text{rec}}$	25.4 fs	
Σ_τ	1.15	
ε_{tag}	64%	
w_{tag}	31%	

fast Monte Carlo simulation. In addition, for the $B_s^0 \to D_s^- \pi^+$ channel the τ_i^{err} are defined by the decay time errors of the $B_s^0 \to J/\psi\,\eta'$ channel, since the present fast Monte Carlo simulation does not allow two different samples of the decay time errors. The nominal physics parameters are listed in Table 6.11.

Table 6.11: *The nominal values for the physics parameters.*

Parameter	Nominal value
ϕ_s	-0.04 rad
ΔM_s	17.5 ps^{-1}
$\Delta\Gamma_s/\Gamma_s$	0.15
τ_{B_s}	1.45 ps

6.7.3 Fit procedure

Taking into account the complexity of the likelihood function due to the large number of events and free parameters, the fit is performed in three successive steps:

1. **Mass distributions fit**: First, the mass distribution is fitted in the loose mass window. Its parameters are then kept fixed. This step allows to determine the probabilities to be signal or background for each generated event based on its reconstructed mass.

2. **Sidebands fit**: Second, the events of the sideband regions are used to determine the acceptance function parameter a, and the slope of the background time distribution τ_{bkg}. It is assumed that these parameters are independent of the reconstructed mass and that the acceptance function is identical for background and signal events. The above fitted parameters are then fixed.

3. **Signal parameters fit**: Finally, the signal observables are extracted in the tight mass window with all the parameters describing the acceptance function, the mass distributions and the background fixed. The parameters left free in this last fit are: $\Delta\Gamma_s/\Gamma_s$, ΔM_s, τ_{B_s}, w_{tag} and ϕ_s.

6.7.4 Sensitivity to ϕ_s

The obtained results are presented in Fig. 6.23 and in Fig. 6.24, where the fitted value of the ϕ_s together with its error estimated by the fit are shown. No bias is observed in the distributions of the ϕ_s output values. The sensitivity to ϕ_s is:

- 0.087 rad for $\theta_p = -10^0$;

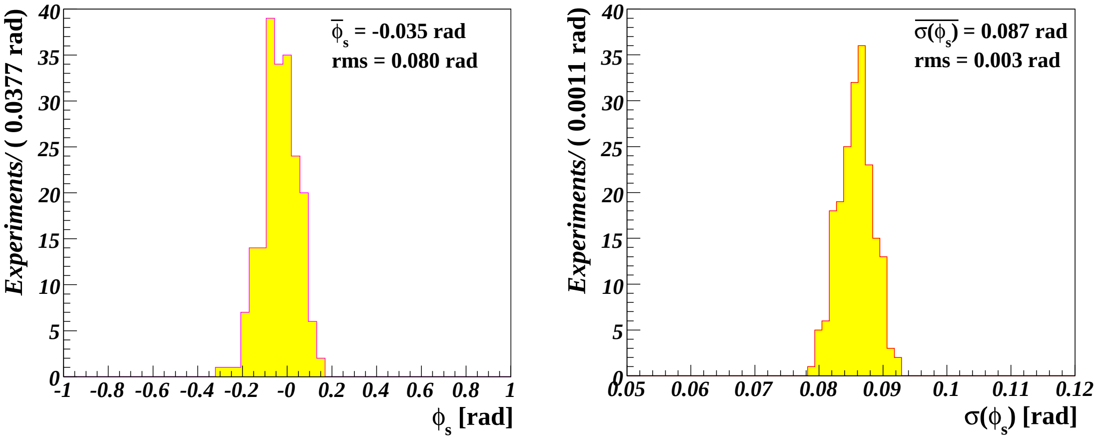

Figure 6.23: *The ϕ_s output from the likelihood fit (left) and its error distribution (right) for the $\theta_p = -10°$ scenario.*

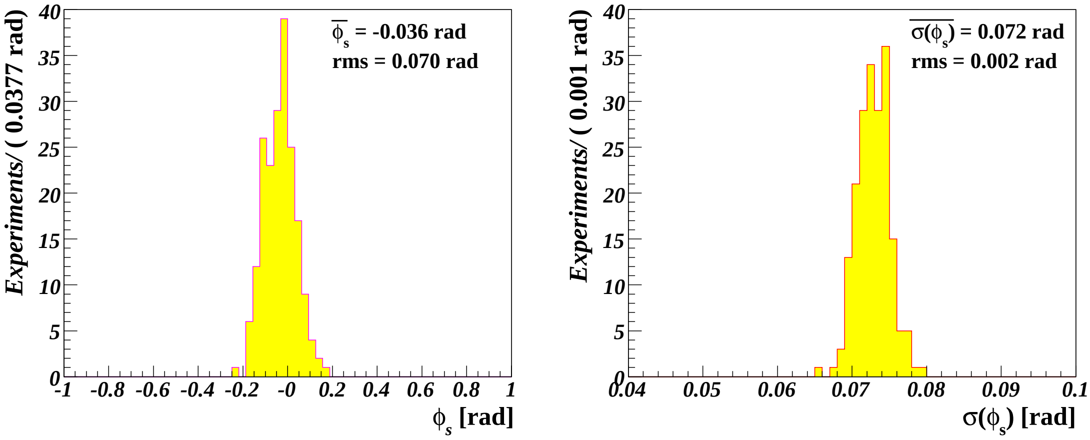

Figure 6.24: *The ϕ_s output from the likelihood fit (left) and its error distribution (right) for the $\theta_p = -20°$ scenario.*

- 0.072 rad for $\theta_p = -20^0$;
- and the average of these two values is 0.0795 rad.

The obtained sensitivity to ϕ_s is found to be better compared to the other decays into *CP*-pure eigenstates presented in Ref. [20]. This is because the shape of the time-dependent selection efficiency, which is fitted by the acceptance function, gives large values for the a and n parameters compared to the other decays. In order to test this hypothesis, a fast Monte Carlo simulation has been done for the $\theta_p = -10°$ scenario with $a = 1.25$ ps^{-1} and $n = 3$ parameters, which describe the decay time acceptance of the $B_s^0 \to \eta_c\phi$ channel. In this case, a sensitivity of 0.106 rad is found. In other words, the sensitivity depends on the decay time acceptance.

The sensitivity to ϕ_s is very well compatible with the root-mean-square of the ϕ_s distribution. The pull distributions are shown in Fig. 6.25 for $\theta_p = -10°$ and $\theta_p = -20°$.

Sensitivity to ϕ_s as a function of B/S

Figure 6.26 illustrates the sensitivity on ϕ_s as a function of the B/S ratio for $\theta_p = -10°$ and $\theta_p = -20°$. In this case, only B is varied, while S is kept fixed. As can be seen, for both scenarios the sensitivity slowly decreases for larger background levels.

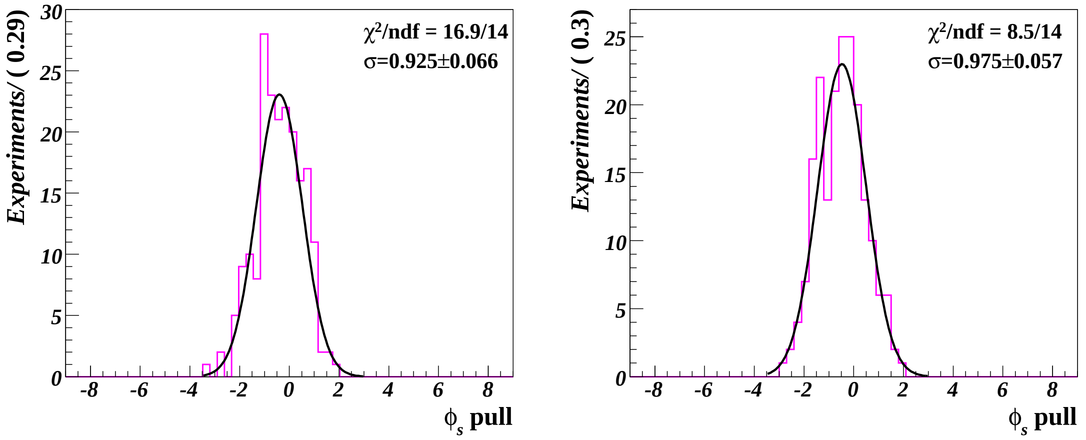

Figure 6.25: *The ϕ_s pull distribution for the $\theta_p = -10^\circ$ (left) and $\theta_p = -20^\circ$ (right) scenario. A single Gaussian is fitted to the distributions.*

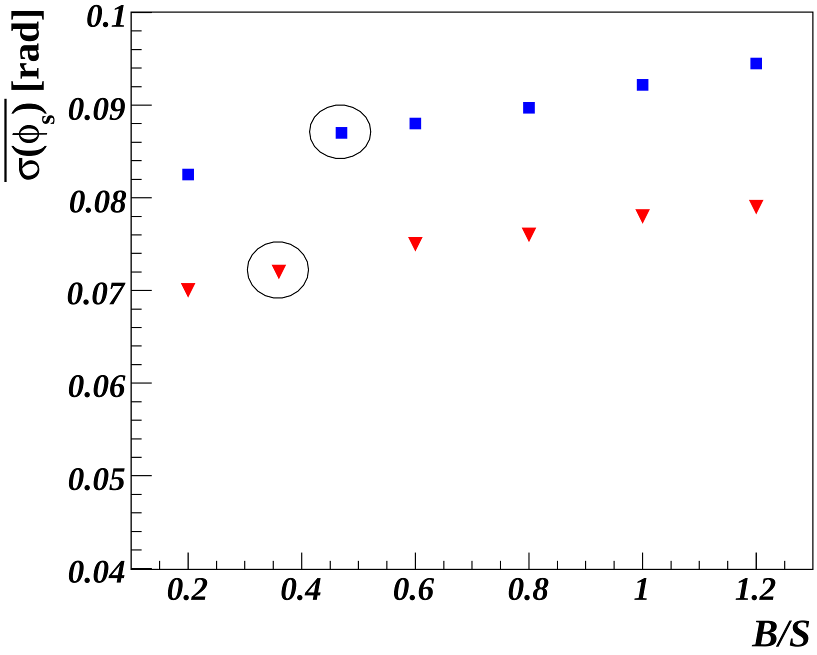

Figure 6.26: *The sensitivity to ϕ_s as a function of the B/S ratio, where the blue boxes indicate the values for $\theta_p = -10^\circ$ and the the red triangles indicate the values for $\theta_p = -20^\circ$. The results for the default setting are indicated with a circle.*

Sensitivity to ϕ_s as a function of the width of the decay time pull

In order to model the decay time resolution in a proper way, the fast Monte Carlo simulation scales the per-event decay time errors τ_i^{err} with the width of the decay time pull distribution, Σ_τ. Thus, this parameter directly affects the quality of the decay time reconstruction, and consequently, it should influence the sensitivity to ϕ_s.

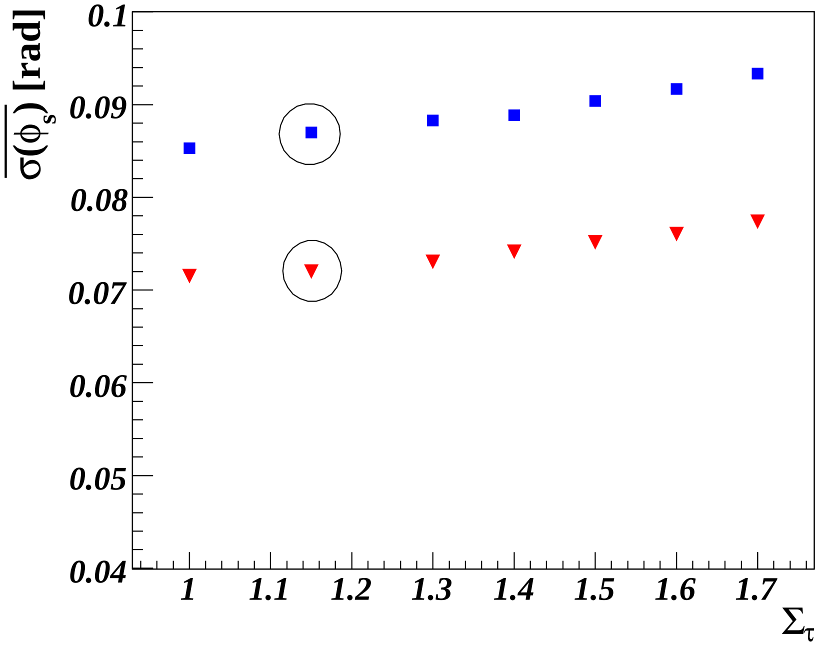

Figure 6.27: *The sensitivity to ϕ_s as a function of the width of the decay time pull Σ_τ, where the blue boxes indicate the values for $\theta_p = -10^\circ$ and the the red triangles indicate the values for $\theta_p = -20^\circ$. The results for the default setting are indicated with a circle.*

The sensitivity on ϕ_s as a function of Σ_τ is shown in Fig. 6.27 for $\theta_p = -10^\circ$ and $\theta_p = -20^\circ$. As expected the sensitivity decreases towards larger values of Σ_τ for both scenarios.

Summary

The LHCb detector will exploit the large number of B hadrons produced at the LHC to study CP violation and rare decays in the B meson system with a very high precision. The LHCb tracking system plays a crucial role in B hadron reconstruction. The Trigger Tracker is an important element of the LHCb tracking system. It covers a sensitive surface of about 7.7 m^2 with silicon microstrip detectors. In order to find the optimal detector layout and to optimise the parameters of silicon sensors and front-end electronics, an extensive R&D programme was carried out. It included tests of different prototype modules with a pulsed infra-red laser and with a test beam. The obtained results allowed to define the final design of the silicon sensors and of the detector modules and to validate the detector concept.

A rigorous quality assurance programme has been performed for the final detector modules in the burn-in test stand. Software has been developed to automate the burn-in test stand. This allowed to perform extensive and uninterrupted measurement programmes which were running even overnight and over the weekends. The obtained results demonstrate that the detectors meet the mechanical and electrical requirements for the Trigger Tracker. The overall quality of the modules is very good. The fraction of defective channels is only 0.13%. A small number of modules were graded as spares due to high leakage currents. Around two terabytes of data accumulated within the measurements in the burn-in test stand has been stored in a central production database.

A new XML-based detector description for the LHCb Trigger Tracker has been implemented. It provides a more realistic description of the active and passive elements of the detector, which is needed for both the reconstruction and the Monte Carlo simulation of the LHCb detector. A scan of the material distribution has been made and the obtained result is consistent with the expectation in the active area of the experiment.

The ability of the LHCb detector to reconstruct the $B_s^0 \to J/\psi\,\eta'$ decay using the decay channels $J/\psi \to \mu^+\mu^-$ and $\eta' \to \rho^0(\pi^+\pi^-)\gamma$ has been demonstrated. An event selection algorithm has been developed and the requirements on the selection variables have been optimised simultaneously. This provides a selection of a large number of the signal events with the highest possible background suppression. Next, the reconstruction quality of this decay has been evaluated. In particular, a good B_s^0 mass resolution is obtained, with a value of $\sim 14\,\mathrm{MeV}/c^2$. The B_s^0 decay time resolution is found to be around $28\,\mathrm{fs}$. In addition, it was observed that the time-dependent selection efficiency rises very steeply and reaches a plateau already at ~ 0.7 ps. This means that the selection requirements cut out only B_s^0 mesons with a decay time below 0.7 ps and do not distort the decay time distribution for decay times greater than 0.7 ps. The sensitivity to the B_s^0 mixing phase ϕ_s with the $B_s^0 \to J/\psi\,\eta'$ decay is found to be 0.08 rad with 2 fb^{-1} of data. Furthermore, the sensitivity to ϕ_s has been studied as a function of the background level and the B_s^0 decay time resolution. As expected, the sensitivity decreases for larger background levels and for lower B_s^0 decay time resolutions.

Bibliography

[1] R. Peccei, *Discrete and global symmetries in particle physics*, hep-ph/9807516, 1998.

[2] C. Wu *et al.*, *Experimental Test of Parity Conservation in Beta Decay*, Phys. Rev. **105** (1957) 1413.

[3] J. Christenson, J. Cronin, V. Fitch, and R. Turlay, *Evidence for the 2 π decay of the K_2^0 meson*, Phys. Rev. Lett. **13** (1964) 138.

[4] A. Sakharov, *Violation of CP invariance, C asymmetry, and baryon asymmetry in the universe*, Pisma Zh. Eksp. Teor. Fiz. **5** (1967) 32.

[5] B. Aubert *et al.*, *Observation of CP violation in the B^0 meson system*, hep-ex/0107013, 2001.

[6] K. Abe, *Observation of Large CP Violation in the Neutral B Meson System*, hep-ex/0107061, 2001.

[7] J. Ellis, *Standard Model of Particle Physics*, Encyclopedia of Astronomy Astrophysics, IOP Publishing LTD, 2006.

[8] M. Herrero, *The Standard Model*, hep-ph/9812242, 1998.

[9] W.-M. Yao *et al.*, *Review of Particle Physics*, Journal of Physics **33** (2006) .

[10] S. Glashow, J. Iliopoulos, and L. Maiani, *Weak interactions with lepton - hadron symmetry*, Phys. Rev. **D2** (1970) 1285.

[11] C. Jarlskog, *Commutator of the Quark Mass Matrices in the Standard Electroweak Model and a Measure of Maximal CP Nonconservation*, Phys. Rev. Lett. **55** (1985) 1039.

[12] L. Wolfenstein, *Parametrization of the Kobayashi-Maskawa Matrix*, Phys. Rev. Let. **51** (1983) 1945.

[13] K. Chadwick *et al.*, *Decay of b flavored hadrons to single muon and dimuon*, Phys. Rev. Lett. **46** (1981) 88.

[14] L. Spencer *et al.*, *Measurement of B-Meson Semileptonic Decay*, Phys. Rev. Lett. **47** (1981) 771.

[15] F. Abe *et al.*, *Observation of the B_c Meson in $p\overline{p}$ Collisions at $\sqrt{s}$=1.8 TeV*, Phys. Rev. Lett. **81** (1998) 2432.

[16] H. Albrecht *et al.*, *Observation of B^0 - $\bar{B}^0$ mixing*, Phys. Lett. **B192** (1987) 245.

[17] S. Giagu, *Observation of $B_s^0 - \bar{B}_s^0$ Oscillations and Measurement of Δm_s in CDF*, hep-ex/0610044, 2006.

[18] V. Abazov *et al.*, *Direct Limits on the B_s^0 Oscillation Frequency*, hep-ex/0603029, 2006.

[19] O. Schneider, *$B^0 - \bar{B}^0$ mixing*, hep-ex/0606040, 2006.

[20] L. Fernandez, *Exclusive Trigger Selections and Sensitivity to the $B_s - \overline{B}_s$ Mixing Phase at LHCb*, Ph.D. thesis, EPFL, Lausanne, 2006, CERN-THESIS/2006-042.

[21] L. Wolfenstein, *Final-state interactions and CP violation in weak decays*, Phys. Rev. **D43** (1991) 151.

[22] B. Aubert *et al.*, *Observation of CP Violation in $B^0 \to K^+\pi^-$ and $B^0 \to \pi^+\pi^-$*, hep-ex/0703016, 2007.

[23] K. Abe *et al.*, *Observation of Direct CP-Violation in $B^0 \to \pi^+\pi^-$ Decays with 535 Million BBbar Pairs*, hep-ex/0608035, 2006.

[24] L. Wolfenstein, *Final-state interactions and CP violation in weak decays*, Phys. Rev. **D43** (1991) 151.

[25] CERN public web page, *The European Organization for Nuclear Research*, `http://cern.ch`.

[26] P. Lefèvre and T. Pettersson, *The Large Hadron Collider: conceptual design*, CERN-AC-95-05-LHC, 1995.

[27] LHCb Collaboration, *LHCb Technical Proposal*, CERN-LHCC/98-4, 1998.

[28] ATLAS Collaboration, *ATLAS : Technical Proposal for a General-Purpose pp Experiment at the Large Hadron Collider at CERN*, CERN-LHCC/94-43, 1994.

[29] CMS Collaboration, *Technical Proposal*, CERN-LHCC/94-38, 1994.

[30] ALICE Collaboration, *A Large Ion Collider Experiment - Technical Proposal*, CERN-LHCC/95-71, 1995.

[31] LHCb collaboration, *LHCb Reoptimized Detector Design and Performance Technical Design Report*, CERN-LHCC/2003-030, 2003.

[32] Totem Collaboration, *Technical Proposal*, CERN-LHCC/99-7, 1999.

[33] LHCf Collaboration, *LHCf: Technical Design Report*, CERN-LHCC/2006-004, 2006.

[34] LHCb Collaboration, *LHCb VELO Technical Design Report*, CERN-LHCC/2001-011, 2001.

[35] LHCb Collaboration, *LHCb Magnet Technical Design Report*, CERN-LHCC/2000-007, 1999.

[36] J. van Tilburg, *Track simulation and reconstruction in LHCb*, Ph.D. thesis, NIKHEF, Amsterdam, 2005, CERN-THESIS/2005-040.

[37] LHCb Collaboration, *LHCb Inner Tracker Technical Design Report*, CERN-LHCC/2002-029, 2003.

[38] M. Needham, *Silicon Tracker simulation performance*, LHCb/2003-015, 2003.

[39] LHCb Collaboration, *LHCb Outer Tracker Technical Design Report*, CERN-LHCC/2001-024, 2001.

[40] G. van Apeldoorn *et al.*, *Beam Tests of Final Modules and Electronics of the LHCb Outer Tracker in 2005*, LHCb-2005-076, 2005.

[41] LHCb Collaboration, *LHCb RICH Technical Design Report*, CERN-LHCC/2000-037, 2000.

[42] LHCb Collaboration, *LHCb Calorimeter Technical Design Report*, CERN-LHCC/2000-036, 2000.

[43] LHCb Collaboration, *LHCb Muon Technical Design Report*, CERN-LHCC/2001-010, 2001.

[44] E. Rodrigues, *The LHCb Trigger System*, LHCb-2006-065, 2006.

[45] LHCb Collaboration, *LHCb trigger system: Technical Design Report*, CERN-LHCC/2003-31, 2003.

[46] R.H. Hierck, *Optimisation of the LHCb detector*, Ph.D. thesis, NIKHEF, 2003, CERN-THESIS/2003-025.

[47] M. Siegler, F. Lehner, M. Needham, and O. Steinkamp, *Expected Particle Fluences and Performance of the LHCb Trigger Tracker*, LHCb-2004-070, 2004.

[48] A. Vollhardt and U. Straumann, *An Optical Readout System for the LHCb Silicon Tracker*, Ph.D. thesis, University of Zurich, 2005, CERN-THESIS-2005-025.

[49] S. Heule and F. Lehner, *Simulation of signal generation in silicon micro-strip detectors for the Silicon Tracker of the LHCb experiment*, LHCb-2003-159, 2003.

[50] Zhong He, *Review of the Shockley-Ramo theorem and its application in semiconductor gamma-ray detectors*, Nucl. Instr. and Methods A **463** (2001) 250.

[51] J. Gassner, F. Lehner, and S. Steiner, *The mechanical Design of the LHCb Silicon Trigger Tracker*, LHCb-2004-110, 2005.

[52] J. Gassner, M. Needham, and O. Steinkamp, *Layout and Expected Performance of the LHCb TT Station*, LHCb-2003-140, 2003.

[53] S. Löchner and M. Schmelling, *The Beetle Reference Manual - chip version 1.3, 1.4 and 1.5*, LHCb-2005-105, 2005.

[54] P. Moreira *et al.*, *A radiation tolerant gigabit serializer for LHC data transmission*, Prepared for 7th Workshop on Electronics for LHC Experiments LEB 2001, Stockholm, Sweden, 10-14 Sep 2001.

[55] R. Bernhard, C. Lois, S. Heule, M. Needham, A. Vollhardt, and D. Volyanskyy, *Measurements of Prototype Ladders for the Silicon Tracker with Laser*, LHCb-2003-075, 2003.

[56] M. Agari *et al.*, *Test-beam measurements on prototype ladders for the LHCb TT station and Inner Tracker*, LHCb-2003-082, 2003.

[57] J. Gassner, M. Needham, O. Steinkamp, A. Vollhardt, and D. Volyanskyy, *Measurements of Prototype Ladders for the TT station with a Laser*, LHCb-2004-102, 2004.

[58] S. Shaheen *et al.*, *Characterization and quality control of silicon microstrip detectors with an infra-red diode laser system*, Nucl. Instrum. Meth. **A352** (1995) 573.

[59] I. Abt *et al.*, *Characterization of Silicon Microstrip detectors using an infra-red laser system*, MPI-PhE/98-13.

[60] J. Gassner, S. Heule, F. Lehner, and C. Lois, *Capacitance measurements on silicon micro-strip detectors for the TT station of the LHCb experiment*, LHCb-2003-081, 2003.

[61] M. Agari *et al.*, *Measurements of a prototype ladder for the tt station in a 120 gev/c π^- beam*, LHCb-2004-103, 2004.

[62] P.G. Rancoita, *Silicon detectors and elementary particle physics*, INFN-AE-83-7, 1983.

[63] M. Agari *et al.*, *Test Beam Results of Multi-Geometry Prototype Sensors for the LHCb Inner Tracker*, LHCb-2002-058, 2002.

[64] O. Steinkamp, *Silicon Strip Detectors for the LHCb Experiment*, LHCb-2004-054, 2004.

[65] C. Lois, *Silicon sensor probing and radiation studies for the LHCb silicon tracker*, Nucl. Instrum. Meth. **A568** (2006) 277.

[66] A. Bay *et al.*, *Hybrid Design, Procurement and Testing for the LHCb Silicon Tracker*, LHCb-2005-061, 2005.

[67] LabView programming language, *http://www.ni.com/labview/*.

[68] N. Chiapolini, *The LHCb TT production database and an overview of quality of detector modules*, Bachelor thesis, University of Zurich, 2007.

[69] V. Hangartner, *LHCb TT module properties*, Bachelor thesis, University of Zurich, 2007.

[70] R. Jacobsson, P. Koenig, A. Chlopik, and Z. Guzik, *The final LHCb readout supervisor ODIN*, Prepared for 8th Workshop on Electronics for LHC Experiments, Colmar, France, 9-13 Sep 2002.

[71] F. Bonifazi *et al.*, *The Task Manager for the LHCb On-Line Farm*, LHCb-2004-099, 1999.

[72] An Overview of Accessing DLLs or Shared Libraries from LabView programming language, *http://zone.ni.com/devzone/cda/tut/p/id/3009*.

[73] G. Haefeli, *Contribution to the development of the acquisition electronics for the LHCb experiment*, Ph.D. thesis, EPFL, Lausanne, 2004, CERN-THESIS-2004-036.

[74] G. Barrand *et al.*, *GAUDI - A software architecture and framework for building HEP data processing applications*, Comput. Phys. Commun. **140** (2001) 45.

[75] T. Sjöstrand *et al.*, *High-Energy-Physics Event Generation with PYTHIA 6.1*, Comput. Phys. Commun. **135** (2001) 238.

[76] D.J. Lange, *The EvtGen particle decay simulation package*, Nucl. Instr. and Methods A **462** (2001) 152.

[77] I. Belyaev *et al.*, *Simulation application for the LHCb experiment*, physics/0306035, 2003.

[78] S. Agostinelli *et al.*, *GEANT4: A simulation toolkit*, Nucl. Instrum. Meth. **A506** (2003) 250.

[79] M. Cattaneo, *Boole: The LHCb digitization program*, `http://lhcb-comp.web.cern.ch/lhcb-comp/Digitization`, 2004.

[80] M. Cattaneo, *Brunel: The LHCb Reconstruction Program*, `http://lhcb-comp.web.cern.ch/lhcb-comp/Reconstruction/`, 2004.

[81] P. Koppenburg, *DaVinci: The LHCb Analysis program*, `http://lhcb-comp.web.cern.ch/lhcb-comp/Analysis`, 2004.

[82] G. Barrand, *Data Visualization*, `http://lhcb-comp.web.cern.ch/lhcb-comp/Frameworks/Visualization/`, 2003.

[83] Extensible Markup Language (XML), *http://www.w3.org/xml/*.

[84] M. Needham and A. Wenger, *Material Budget Calculation for the LHCb TT Station*, LHCb-2005-020, 2005.

[85] S. Ponce *et al.*, *Detector Description Framework in LHCb*, physics/0306089, 2003.

[86] R. Chytracek *et al.*, *The LHCb detector description framework*, Proc. of CHEP 2000.

[87] M. Needham and D. Volyanskyy, *Updated geometry description for the LHCb Trigger Tracker*, LHCb-2006-032, 2006.

[88] M. Needham, *Channel Numbering and readout partitioning for the LHCb Silicon Tracker*, LHCb-2006-033, 2006.

[89] M. Needham, *The LHCb Silicon Tracker detector element tree*, LHCb-2006-034, 2006.

[90] DetDescChecks tool, *The LHCb overlap checking program*, `http://lhcb-comp.web.cern.ch/`.

[91] M. Needham, *Simulating energy loss in thin silicon detectors*, LHCb-2003-160, 2003.

[92] H. Quinn, *B Physics and CP violation*, hep-ph/0111177 (2001) .

[93] M. Calvi, O. Leroy, and M. Musy, *Flavour Tagging Algorithms and Performances in LHCb*, LHCb-2007-058, 2007.

[94] O. Deschamps *et al.*, *Photon and neutral pion reconstruction*, LHCb-2003-091, 2003.

[95] I. Belyaev, *Python-based physics analysis environment for LHCb*, Prepared for CHEP 2004, Interlaken, Switzerland, 27 September 2004.

[96] A. Amato *et al.*, *Constrained and Unconstrained vertex fitting tools for LHCb*, LHCb-2004-038, 2004.

[97] G. Raven, *Selection of* $B_s \rightarrow J/\psi\phi$ *and* $B^+ \rightarrow J/\psi K^+$, LHCb-2003-118, 2003.

[98] B. Carron, $B_s^0 \rightarrow J\psi\eta$ *decays and sensitivity to the* B_s^0 *mixing phase at LHCb*, Ph.D. thesis, EPFL, Lausanne, 2005, CERN-THESIS/2005-059.

[99] W. Verkerke and D. Kirkby, *The RooFit toolkit for data modeling*, physics/0306116, 2003.

[100] J. Borel, L. Nicolas, O. Schneider, and J. van Hunen, *The* $B_s \rightarrow D_s^- \pi^+$ *and* $B_s \rightarrow D_s^{\mp} K^{\pm}$ *selections*, LHCb-2007-017, 2007.

Acknowledgements

By completing this dissertation, I am ending an important period of my life and I will always remember this time. During these three and a half years I received help and a lot of useful recommendations from many people and I wish to thank all of them. However, first of all I am very grateful to God for everything that I ever had and perhaps, will have in my life. Nothing is possible without Him !

I am very indebted to Prof. Ulrich Straumann for giving me the outstanding opportunity to work in his research group as a Ph.D. student and for his continuous support and guidance during the Ph.D. marathon. I am also thankful to Prof. Valery Pugatch for the introduction into the LHCb experiment and collaboration.

Special thanks go to Jeroen van Tilburg and Olaf Steinkamp for all the fruitful discussions in a friendly atmosphere, many excellent advises and proof-reading this dissertation. This significantly improved the quality of my work. It has been a real pleasure to work with them.

I am truly thankful to Frank Lehner and Ralf Bernhard for their very good attitude and valuable support, both in and outside work. I am also grateful to Matthew Needham for his substantial help at the beginning of my Ph.D. thesis work.

I would like to express my gratitude to all my colleagues from Zürich, especially to Achim, Johannes and Tariel which also contributed to the work presented in this dissertation. I am also thankful to Andreas, Angela, Christophe and Cristina for our friendly relations. It was a great pleasure to work in such an international team.

Among many LHCb colleagues, I would like to thank Ivan Belyaev. I have benefited a lot from his advises concerning the LHCb software framework and physics analysis. Furthermore, I am grateful to Luis Fernandez for his help with the sensitivity studies.

It is not easy to thank my parents within just a few words. This dissertation is dedicated to them, since I very much want to thank them for their constant support and encouragement over the all years. In addition, I am thankful to my brother for his tireless concern. Finally, I am deeply and sincerely grateful to the closest person in my life – to my wife – for her love and understanding.

This work has been supported by the Swiss National Science Foundation.

DMYTRO VOLYANSKYY

E-mail: dvolyans@gmail.com

PERSONAL DATA

Born in 1981, in Ukraine

EDUCATION AND DEGREES

2007	**Doctoral degree (Ph.D.) in High Energy Physics** on *The Trigger Tracker and a Monte Carlo study of the* $B_s^0 \to J/\psi\,\eta'$ *decay in the LHCb experiment.* Physics Institute of the University of Zürich, Switzerland. Supervisor: Prof. Dr. Ulrich Straumann.
2005	European (CERN-JINR) school of High Energy Physics, Kitzbühl, Austria.
2003-2007	Ph.D. research programme in High Energy Physics at the University of Zürich and at CERN (European Organization for Nuclear Research), Geneva, Switzerland.
2003	**Master of Science degree in Physics of the Nucleus and Elementary Particles** on *The LHCb Silicon Inner Tracker. Characterization of sensors and radiation load.* National Taras Schevchenko University of Kiev, Ukraine. Diploma with honour.
2003	MS research programme at the Physics Institute of the University of Zürich.
2002	**Bachelor of Science degree in Physics**. National Taras Schevchenko University of Kiev. Diploma with honour. GPA 5(/5).
1998-2002	Studies at the Physics Faculty of National Taras Schevchenko University of Kiev.

WORK EXPERIENCE

2003-2007	Ph.D. thesis work at Physics Institute of the University of Zürich and at CERN. Research activities: ▷ *Monte Carlo analysis of the* $B_s^0 \to J/\psi(\mu^+\mu^-)\ \eta'(\rho^0\gamma)$ *decay at LHCb.* ▷ *R&D programmes for silicon microstrip detectors of the LHCb Trigger Tracker.* ▷ *Quality Assurance programme for the LHCb Trigger Tracker detector modules.* ▷ *The XML-based detector description of the LHCb Trigger Tracker.*
2003-2007	Teaching assistant at the University of Zürich.
2003-2007	Collaboration in the Silicon Tracker group and in the Proper Time and Mixing working group of the LHCb experiment at CERN.